

POLITECNICO DI TORINO

SCUOLA DI DOTTORATO

Dottorato in Ingegneria Chimica – XXIV ciclo

Tesi di Dottorato

**Computational models for  
the simulation of turbulent  
poly-dispersed flows:**

**Large Eddy Simulation and  
Quadrature-Based Moment Method**



Matteo ICARDI

**Tutore**  
Daniele MARCHISIO

**Coordinatore del corso di dottorato**  
Vito SPECCHIA

**Controrelatore**  
Giorgio MICALE

Febbraio 2012



*A Lellina e alla nostra  
piccola Elisabetta*



## **Ringraziamenti / Acknowledgments**

Questo lavoro non sarebbe stato possibile senza la preziosa supervisione del mio relatore a cui vanno i miei più profondi ringraziamenti per la sua enorme pazienza e disponibilità. Un sentito ringraziamento va a tutto il team Ascomp, soprattutto a Djamel e Chidu per il supporto e l'opportunità concessami. In questi anni ho avuto la fortuna di incontrare numerosi professori e ricercatori che ringrazio per l'enorme contributo oer la mia formazione professionale e scientifica. In particolare grazie al prof. Fox e al prof. Asinari per la loro preziosa collaborazione. Un ringraziamento speciale va anche al prof. Barresi per il supporto e i sempre validi consigli e suggerimenti. Voglio ricordare inoltre tutti le persone con cui ho vissuto e lavorato in questi anni e che hanno accettato e sopportato di buon grado un “matematico” al dipartimento di ingegneria chimica. Tra queste Antonio e Nicodemo con cui ho avuto sempre un fruttuoso dialogo scientifico e non; Cristina, Valeria, Andrea e Serena che mi hanno sopportato come vicino di ufficio; e tutti gli altri: Federica, Maria Chiara, Ilaria, Lucas, Mauricio, Roberto, Enrico, il prof. Vanni, il prof. Fissore e il prof. Baldi con cui ho condiviso tante lunghe giornate al Politecnico. Infine non posso non ringraziare tutta la mia famiglia, in particolare mia moglie Antonella, i miei genitori e i miei suoceri per la loro infinita pazienza e fiducia in me e a tutte le persone che mi sono state vicino fisicamente e spiritualmente in questi anni. Ultimo ma primo per importanza, grazie a Dio, alla sua infinita misericordia e alla sua Divina Provvidenza, per il meraviglioso progetto, talvolta misterioso, che ha preparato per ognuno dei suoi figli.



## Abstract

This work focuses on the development of efficient computational tools for the simulation of turbulent multiphase polydispersed flows. In terms of methodologies we focus here on the use of Large Eddy Simulation (LES) and Quadrature-Based Methods of Moments (QBMM). In terms of applications the work is finalised, in order to be applied in the future, to particle production processes (precipitation and crystallisation in particular). An important part of the work concerns the study of the flow field in a Confined Impinging Jets Reactor (CIJR), frequently used in particle production processes. The first part is limited to the comparison and analysis of micro Particle Image Velocimetry ( $\mu$ PIV) experiments, carried out in a previous work, and Direct Numerical Simulation (DNS), carried out in this thesis. In particular the effects of boundary and operating conditions are studied and the numerical simulations are used to understand the experimental predictions and demonstrate the importance of unavoidable fluctuations in the experimental inlets. This represents a preparatory work for the LES modelling of the CIJR. Before investigating the accuracy of LES predictions for this particular application, the model and the implementation are studied in a more general context, represented by a well-known test case such as the periodic turbulent channel flow: the LES model implementation in *TransAT*, the code used in this work, is compared with DNS data and with predictions of other codes. LES simulations for the CIJR, provided with the proper boundary conditions obtained by the previous DNS/ $\mu$ PIV study, are then performed and compared with experiments, validating the model in a more realistic test case. Since particle precipitation and crystallization often result in complex interactions between particles and the continuous phase, in the second part of the work particular attention has been paid in the modelling of the momentum transfer and the resulting velocity of the particles (relative to the fluid). In particular the possibility of describing poly-disperse fluid-solid systems with QBMM together with

LES and Equilibrium Eulerian Model (EEM) is assessed. The study is performed by comparing our predictions with DNS Lagrangian data in the turbulent channel flow previously described, seeded with particles corresponding to a realistic Particle Size Distribution (PSD). The last part of the work deals with particle collisions, extending QBMM to the investigation of non-equilibrium flows governed by the Boltzmann Equation with a hard-sphere collision kernel. The evolution of the particle velocity distribution is predicted and compared with other methods for kinetic equations such as Lattice Boltzmann Method (LBM), Discrete Velocity Method (DVM) and Grad's Moment Method (GM). The overall results of this thesis can be extended to a broad range of other applications of single-phase, dispersed multiphase and non-equilibrium flows.

## Contents

<b>Ringraziamenti / Acknowledgments</b>	v
<b>Abstract</b>	vii
<b>Contents</b>	ix
<b>1 Introduction</b>	1
1.1 CFD modelling in chemical engineering . . . . .	1
1.2 Non-dimensional numbers and flow regimes . . . . .	3
1.3 Turbulence . . . . .	6
1.4 Poly-dispersity . . . . .	7
1.5 Non-equilibrium and molecular effects . . . . .	8
1.6 Thesis outline . . . . .	10
References . . . . .	13
<b>2 Models and methods</b>	15
2.1 Single-phase flows . . . . .	15
2.1.1 Large Eddy Simulations . . . . .	16
2.2 Multiphase flow . . . . .	19
2.2.1 Mixture algebraic models . . . . .	22
2.3 Generalised Population Balance Equations . . . . .	26
2.3.1 Boltzmann Equation . . . . .	28
2.3.2 Poly-dispersity models . . . . .	29
2.4 Quadrature-based Method Of Moments . . . . .	31
2.4.1 Direct Quadrature Method Of Moments . . . . .	32
2.5 Numerical methods . . . . .	33

2.5.1	TransAT CFD code . . . . .	33
2.5.2	Convection schemes . . . . .	33
2.5.3	Time discretisation . . . . .	34
References . . . . .		39
<b>3 CFD study of a Confined Impinging Jets Reactor</b>		41
3.1	Introduction . . . . .	42
3.2	Experimental apparatus and $\mu$ PIV setup . . . . .	45
3.3	Direct Numerical Simulations and numerical details . . . . .	48
3.4	Operating conditions investigated and boundary conditions . . . . .	50
3.5	Results and discussion . . . . .	53
3.5.1	Experimental instantaneous flow field . . . . .	54
3.5.2	Mean velocity field . . . . .	56
3.5.3	Velocity fluctuations . . . . .	58
3.5.4	Spatial correlations . . . . .	58
3.5.5	Time series power spectra . . . . .	60
3.6	Conclusions . . . . .	62
References . . . . .		67
<b>4 Quality and reliability of LES models</b>		69
4.1	Introduction . . . . .	70
4.1.1	Test case description . . . . .	71
4.1.2	Numerical details . . . . .	72
4.1.3	Sub-grid Scale (SGS) modelling . . . . .	73
4.2	Results and discussion . . . . .	75
4.2.1	Mean and fluctuating velocities . . . . .	76
4.2.2	Energy spectra . . . . .	78
4.2.3	Instantaneous flow field . . . . .	82
4.3	Benchmark . . . . .	82
4.4	Conclusions . . . . .	83
References . . . . .		88
<b>5 Validation of a LES model for micro-reactor flows</b>		89
5.1	Introduction . . . . .	89
5.2	Model description . . . . .	92
5.2.1	Fluid flow equations . . . . .	92
5.2.2	Numerical methods . . . . .	93
5.3	Operating and boundary conditions . . . . .	94
5.4	Results and discussion . . . . .	98
5.4.1	Instantaneous flow field . . . . .	98
5.4.2	Flow statistics . . . . .	100

5.5	Conclusions . . . . .	107
References . . . . .		110
<b>6</b>	<b>Poly-dispersed particle-laden flow</b>	111
6.1	Introduction . . . . .	112
6.2	Fluid phase . . . . .	117
6.3	Particles phase . . . . .	118
6.4	Sub-grid scale modelling . . . . .	120
6.5	Numerical details . . . . .	121
6.6	Results and discussion . . . . .	122
6.7	Conclusions . . . . .	126
References . . . . .		134
<b>7</b>	<b>Computational models for non-equilibrium flows</b>	135
7.1	Introduction . . . . .	135
7.2	Governing equations . . . . .	138
7.3	Solution methods . . . . .	142
7.3.1	Discrete Velocity Method . . . . .	142
7.3.2	Grad's moment Method . . . . .	142
7.3.3	Quadrature Method of Moments . . . . .	144
7.3.4	Lattice Boltzmann Method . . . . .	145
7.4	Test cases and numerical details . . . . .	146
7.5	Results and discussion . . . . .	148
7.6	Conclusions . . . . .	154
References . . . . .		157
7.7	Appendices . . . . .	157
Appendices . . . . .		157
<b>8</b>	<b>Conclusions and future perspectives</b>	165



## Introduction

### 1.1 CFD modelling in chemical engineering

Computational fluid dynamics turns out to be an essential tool in the development of chemical processes as it is demonstrated by the numerous publications, books and reviews on this subject [Dudukovic, 2010, Fox, 2006, Harris et al., 1996, Kelly, 2008, Kuipers and Van Swaaij, 1997, Ranade, 2002, Trambouze, 1993]. This is due to the need of detailed simulations, that can substitute expensive and sometimes impracticable experimental campaigns, at different stages of the development of a chemical process or of the design and optimisation of a chemical reactor, as illustrated in Fig. 1.1. Many times however, the simulation context can be very challenging because of the complexity of the physical mechanisms involved and of the geometries.

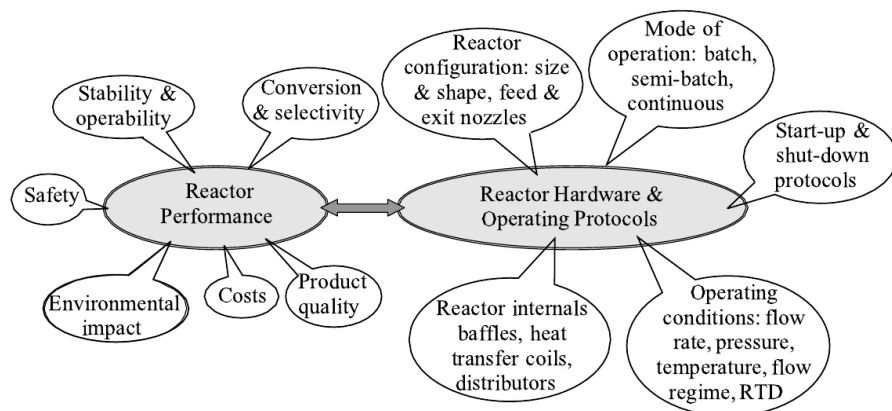


Figure 1.1: Developments stages of a chemical reactor. [Ranade, 2002].

For example, turbulent dispersed multiphase flows are often encountered in many applications, from the small scale laboratory equipments to large industrial plants: bubble columns, fluidised beds, reactors for polymer and drugs production, spray combustion, just to cite a few. These applications are not limited only to chemical engineering but, refer to a broader range of engineering applications such as energy, environment, biology, physiology and hydraulic. For a generic introduction and applications of turbulent dispersed flow simulation the reader is referred to the numerous published books and reviews [Balachandar and Eaton, 2010, Crowe et al., 1998, Curtis and Van Wachem, 2004, Loth, 2000, Mashayek and Pandya, 2003, Prosperetti, 1999, Sundaresan, 2000, Zhou, 2010]. The term “dispersed” is used to refer to a situation when it is possible to recognise a continuous phase (either gaseous or liquid) and a dispersed phase (either gaseous, liquid or solid) made by relatively small particles, droplets or bubbles (particles in a loose sense). We do not focus in this discussion on free-surface flows in which the main issue is instead represented by the motion of the interface, even if, in some applications this problem must be taken into account.

Focusing on chemical engineering, the design, scale-up and optimization of turbulent multiphase processes require deep understanding and characterisation of the critical and transitional regimes (the most famous and relatively simple among them is the transition to turbulence). Indeed the simulation of the entire range of flow conditions and regimes is a very challenging problem but practically impossible because of the huge number of physical phenomena involved, the different time and length-scales involved and the complex interactions between them. The most attractive approach is therefore represented by the so-called multi-scale methods that make use of mathematical models derived at different scales, attempting to couple them explicitly, or alternatively to pass information between them, to catch the whole physics involved, optimizing the computational costs. Various attempts have been made in this direction for the simulation of single-phase turbulence, dispersed flow modelling, mixing and reaction, etc. [Kalweit and Drikakis, 2008, Lerou and Ng, 1996, Peters, 2009, Sagaut et al., 2006, Van den Akker, 2010, Van der Hoef et al., 2006].

The key issue in the simulation of complex systems, however, is not only related to the mathematical modelling of the different scales and the links between them (the meso-scales) but also to the computational tools capable of efficiently solving those models. Three main aspects are investigated in this work: turbulence, poly-dispersity and non-equilibrium. Each of these is modelled and resolved with computational tools and models that represent a trade-off between an adequate description of the physics at competitive computational costs. The choice of these main subjects has been motivated in particular by the interest in modelling and simulating chemical reactors for particle production. In this work we are in fact interested

in computational tools capable of describing turbulent mixing of fluids with different compositions, resulting in supersaturation, which is the driving force of particle formation. The model has to be moreover capable of describing the final particle size distribution of the produced particles. It is also very important to describe molecular effects for which the particles, because of the particular flow conditions, do not fully satisfy the continuum hypothesis and the local equilibrium assumption (in other words particles velocity distribution far from the Maxwellian equilibrium). This is a very innovative and interesting field in which these three aspects must be taken into account [Kalweit and Drikakis, 2008, Karniadakis et al., 2005, Marchisio et al., 2006, Salata, 2004, Yu and Lin, 2010, Zhao et al., 2011]. However, as already pointed out, most of the topics and results of this work can be extended to the cited range of applications. In this chapter fundamentals of multiphase flows together with the objectives and motivation of this work are presented, introducing non-dimensional numbers involved in the simulation of turbulent multiphase flows and giving a general overview of the problems involved and a brief classification of flow regimes. Details about theory and models are instead postponed to Chap. 2.

## 1.2 Non-dimensional numbers and flow regimes

Multiphase flows can be conveniently described and categorised by non-dimensional numbers. The first important number is the well-known macroscopic Reynolds number ( $Re$ ):

$$Re = \frac{\rho |\mathbf{U}| L}{\mu}, \quad (1.1)$$

where  $\rho$ ,  $\mu$ ,  $|\mathbf{U}|$  and  $L$  are respectively the density, the viscosity and the mean (or characteristic) velocity and system dimension. It gives a measure of the ratio between inertial and viscous forces and consequently quantifies the importance of turbulence in the system. The transition from laminar to turbulent flows for multiphase flows is influenced by many physical parameters: the concept of turbulence itself can be defined either at the macroscopic scale of the system or locally only for one of the phase [Fox, 2012]. For this reason also a local particle Reynolds number can be defined as follows

$$Re_p = \frac{\rho |\mathbf{U}_p - \mathbf{U}| 2r}{\mu} \quad (1.2)$$

by using the relative velocity of the particle  $\mathbf{U}_p$  with respect to the surrounding fluid and the particle radius  $r$ , to classify the interaction between the fluid and the particles. An important example is represented by the drag force  $F_D$  applied by the fluid to a spherical particle that can be conveniently described by the drag coefficient

$$C_D$$

$$C_D = \frac{2F_D}{\pi r^2 \rho |\mathbf{U}_p - \mathbf{U}|^2} \quad (1.3)$$

which depends on the particle (or relative) Reynolds number, in the way depicted by Fig. 1.2. In the first part of the plot the Stokes law holds ( $C_D = \frac{24}{Re_p}$ ) while for larger relative velocity approximate formulas [Clift et al., 1978] can be used.

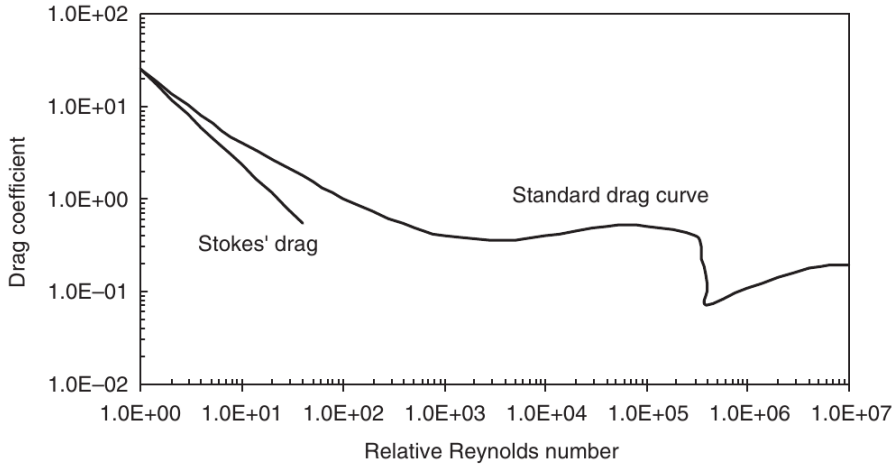


Figure 1.2: Drag coefficient  $C_D$  as a function of the particle Reynolds number [Crowe et al., 1998].

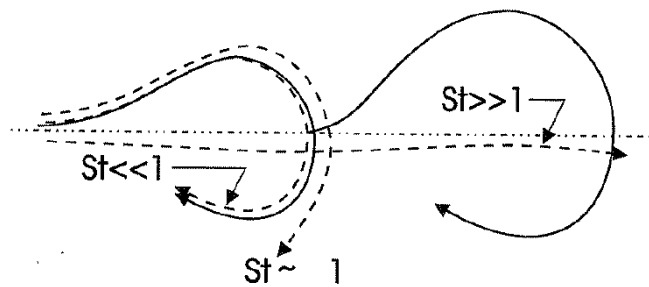


Figure 1.3: Schematic dynamics of particles with different Stokes number [Crowe et al., 1998]. Particles with  $St \ll 1$  follows the fluid while for  $St \gg 1$  they feels negligible force from the fluid. In the case of finite  $St \approx 1$  both inertial effects and fluid forcing are important.

A second important characterisation of dispersed multiphase flows can be made on the basis of the ratio between the characteristic response times of particles and fluid. This is expressed by the Stokes number ( $St$ ) defined as:

$$St = \frac{\tau_p}{\tau_f} \quad (1.4)$$

where  $\tau_p$  and  $\tau_f$  are respectively the particle response time and the characteristic time-scale of the fluid. The former can be written as

$$\tau_p = \frac{(2\rho_p + \rho)d^2}{36\mu} \quad (1.5)$$

where  $d = 2r$  is the particle diameter and  $\rho_p$  is its density, while the latter can be arbitrary chosen depending on the system scale or, in case of turbulent flows, either the turbulence integral scale or the minimum scale, giving place to different definitions of Stokes number, either global or local. The meaning of the Stokes number can be easily explained as the tendency of a particle to follow the fluid, as represented by Fig. 1.3.

The third key indicator for complex multiphase flows is represented by the Knudsen number ( $Kn$ ) that gives an estimation of the importance of particle-particle interaction. It is defined as:

$$Kn = \frac{\lambda}{L}, \quad (1.6)$$

where  $\lambda$  is the mean free path of a particle in a fluid between two successive collisions.  $L$  can be again defined globally as the system length-scale but to catch the local micro-scale behaviour of the system also a local length-scale can be used or a variational scale  $\phi |d\phi/dx|^{-1}$  considering a generic fluid variable of interest  $\phi$  [Lockerby et al., 2009]. The concept of Knudsen number behaves originally to the kinetic theory of gases but most of concepts and tools holds similarly also for gas-particle and fluid-particle flows [Gidaspow, 1994].

Other important non-dimensional numbers such as Mach number ( $Ma$ ), Damköhler number ( $Da$ ), Prandtl number( $Pr$ ), Sherwood number ( $Sh$ ) and Schmidt number ( $Sc$ ) come into play when other phenomena such as compressibility effects, chemical reactions, heat and mass transfer or scalar transport are considered. However the focus here is on the first three non-dimensional numbers introduced above. As it has been already pointed out, these numbers are usually not uniquely defined because of the multi-scale features of the flow. Nevertheless they represent fundamental concepts that give a global understanding of the physical mechanisms and allow to define criteria to choose appropriate computational models. The importance of these three numbers and the regimes that they define are explained in the next sections, with particular emphasis to applications for particle formation processes.

## 1.3 Turbulence

Most of the flows that can be observed in nature and in the process industries are turbulent and turbulence has been a very active field of research since many decades. However many problems remain open, especially when turbulence is coupled with other physical phenomena or is developed within complex geometries. This is the case, for example of multiphase flows and of mixing in micro-devices.

In principle, when considering flow and mixing in micro-devices, the turbulence effects are often neglected because the Reynolds number linearly depend on the system length-scale. However, for some particular applications (such as the production of polymeric nano-particles presented in Chaps. 3 and 5), where an adequate mixing rate is necessary, the flow can be in a transitional regime or even fully turbulent. A schematic representation of flow regimes in micro-devices is reported in Fig. 1.4.

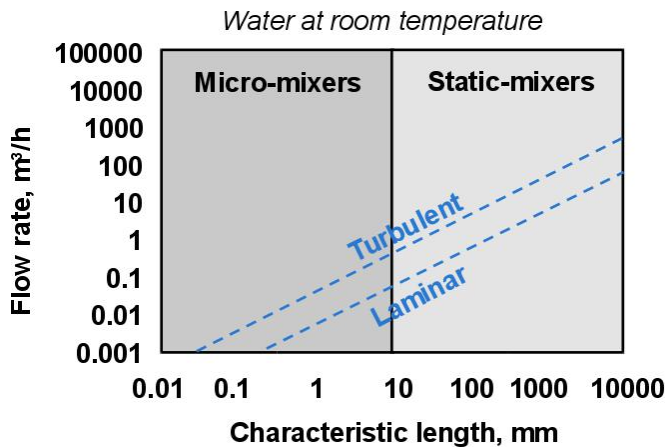


Figure 1.4: Characterisation of static and micro mixers for particle formation processes based on mean flow rate and characteristic length.

Recent hardware developments have given an important acceleration towards the use of more accurate turbulence modelling approaches such as Large Eddy Simulations (LES) and Direct Numerical Simulations (DNS). When compared with the classical Reynolds-Averaged Navier-Stokes (RANS) equation approach, these are becoming acceptable in terms of computational costs, for respectively medium and small scale industrial applications. In this work we deal with these two tools, focusing in particular on LES models. In fact, contrarily to DNS, that are no more than virtual experiments, LES requires complex modelling procedures to be applied in real flows. For example when LES is used to model turbulent multiphase reacting flows a number of issues arise. One of the most important deals with the effects of small scale fluctuations to the dynamics of dispersed inertial particles. This problem

is addressed in details in Chap. 6. Another issue that is not investigated in this work is the micro-mixing problem that come from the fact that chemical reactions occur at the molecular level [Pope, 2000] and the rate of the chemical reaction therefore depends on the local and instantaneous concentrations of the local concentration of reactants (that are not explicitly known in LES). Also the multiphase structures of the flow can be seen as a closure problem at the microscopic scale that, in LES, is not fully resolved.

## 1.4 Poly-dispersity

In many chemical engineering applications (e.g., particle production) one of the expected output from a simulation is the detailed information about the size of dispersed particles. Secondarily, since particles of different size (and different  $St$ ) behave in a very different manner, this information is crucial also to catch the correct overall dynamics of the flow. Therefore, a second important aspect we want to model is the evolution of a specific property (in this case size) for each particle. This is however a very complex problem because involves a detailed description of the single particle, giving place to an enormous number of degrees of freedom, related to the microscopic scale of the system (where each particle is represented explicitly). On the other hand, remaining at the macroscopic level force us to compute only mean quantities such as mean particle size or volume fraction. A third possibility is the so-called “Population Balance Model” [Ramkrishna, 2000, Ramkrishna and Mahoney, 2002, Rigopoulos, 2010], in which some microscopic information is retained, though in a statistical sense, with the use of a Particle Size Distribution (PSD) that describes the statistical distribution of particle size at each point of the domain in a continuous way. This can be achieved considering infinitesimal volumes of the fluid, counting the number of particles and dividing them into separate particle size classes. This results in a discrete frequency distribution, depicted in the left part of Fig. 1.5. Another averaging on the phase space (particle size) leads to a continuous PSD, also called Number Density Function (NDF) (an example is given in right part of Fig. 1.5).

More generally, a system constituted by a continuous primary phase and a dispersed secondary phase (i.e., droplets, particles or bubbles) can be conveniently described by the Generalised Population Balance Equation (GPBE) [Fox and Marchisio, 2007] that can be viewed as a generalisation of the Population Balance, Boltzmann, Williams or Particle Dynamics equation for generic dispersed multiphase flow. In this formulation in fact, not only the size of the particles come into play, but a generic set of property of the dispersed phase (e.g., velocity, chemical composition, surface area) is used instead. This approach can be regarded as a meso-scale modelling tool and has numerous links with the field of kinetic theory of rarefied

gases. Details about this approach are illustrated in details in Chap. 2.3.

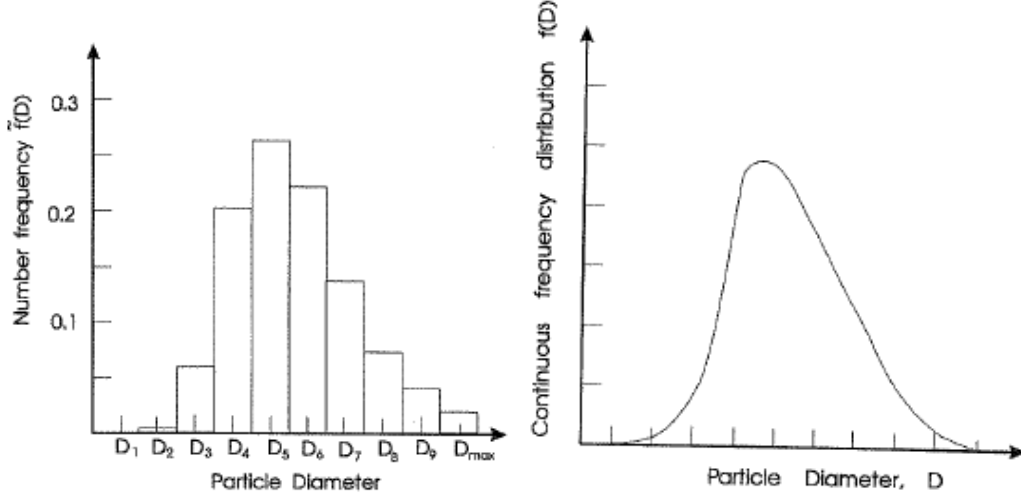


Figure 1.5: Examples of discrete (left) and continuous PSD, describing the size of particles in a certain point of the flow Crowe et al. [1998].

## 1.5 Non-equilibrium and molecular effects

The development of micro and nano-scale technology have seen a strong acceleration due mainly to the applications for biological lab-on-chip systems and electronic devices, and the scales of these systems are always decreasing. Therefore there is an increasing need of theoretical and computational models specifically designed for the simulation of micro-scale flows [Cao et al., 2009, Karniadakis et al., 2005, Reese and Zhang, 2009] One of the main differences of these models with respect to classical macroscopic fluid dynamics, is the capability of predicting non-continuum (non-equilibrium) effects. On the other hand, these effects are also observed in high-speed and rarefied flows in aerospace and vacuum technologies [Kogan, 1992, Reese et al., 2003, Sone and Onishi, 1978]. Although many differences remains between these two fields of application (e.g., in terms of  $Re$  and  $Ma$ ), they often belong to the same Knudsen regimes. With the definition given in Eq. 1.6, four regimes can be defined: continuum, slip, transitional and free molecular flows.

The continuum flow regime corresponds to a situation where the classical macroscopic balance equation (either Euler or Navier-Stokes) holds, while in the slip flow regime some molecular effects start to be relevant but they can be taken into account by the introduction of slip conditions at the walls [Sone and Onishi, 1978]. However, when  $Kn < 0.1$ , the continuum hypothesis becomes inadequate and microscopic or kinetic models have to be introduced [Hadjiconstantinou, 2006, Sone, 2002]. Finally

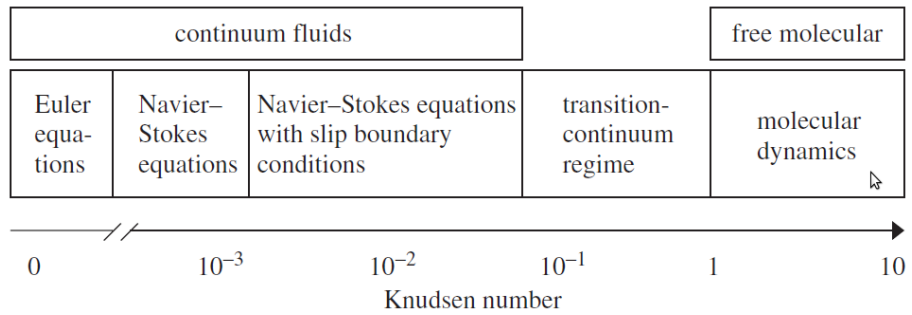


Figure 1.6: Knudsen regimes [Reese et al., 2003].

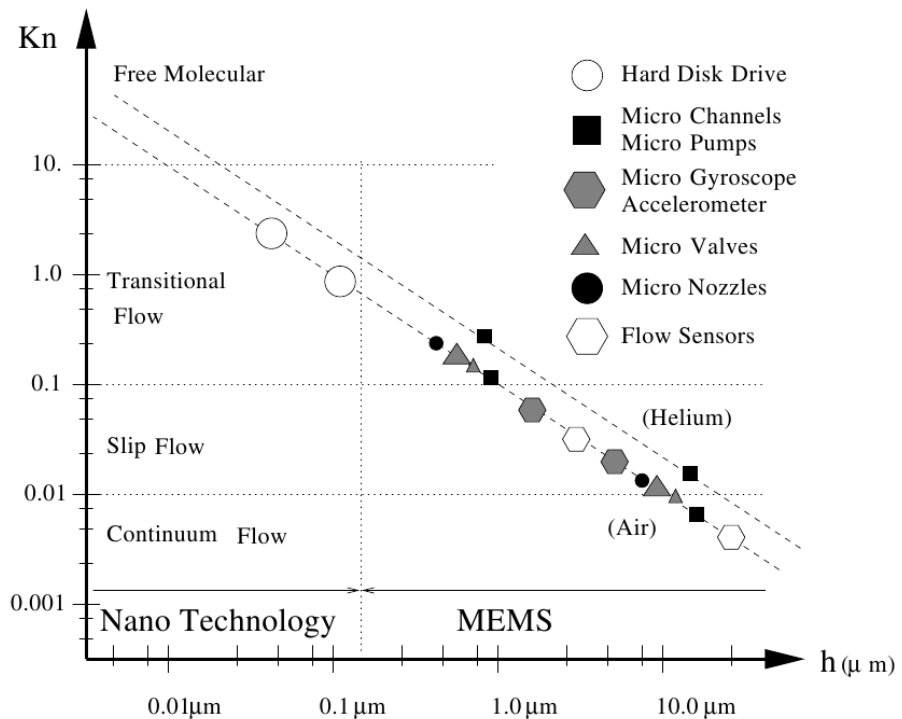


Figure 1.7: Knudsen regimes and typical applications of nano-technology and MEMS [Karniadakis et al., 2005].

$Kn \ll 1.0$  the particles flow without collisions and they can be described by Newton's laws of mechanics. They are represented in Fig. 1.6 and together with some applications in Fig. 1.7

As it has been already said, the concepts of collision and  $Kn$  regimes, originally introduced to describe dilute gases, hold similarly for liquids in micro- and

nano-devices, and dispersed multiphase or “granular flows” in general [Gidaspow, 1994], where a mean free path can be defined either for fluid or solid particles. Kinetic equations are the links between the microscopic (molecular- or particle-scale) description and the macroscopic continuum equations. The latter, in fact, can be derived rigorously from the kinetic description, like the Euler and Navier-Stokes equation that can be analytically derived from Boltzmann equation via moment expansion or asymptotic analysis. Higher order macroscopic equations can be also derived [Kogan, 1992, Shan et al., 2006, Struchtrup, 2005] to extend the validity of classical fluid dynamics equations to low  $Kn$  but many closures problems arise. Therefore it is often required the solution of the Boltzmann Equation or other similar kinetic equations.

The rarefaction effects and break down of the continuum hypothesis has important consequences on the transport coefficients such as anomalous viscosity as well as anomalous diffusivity and modified drag force on dispersed particles. The kinematic viscosity for Newtonian fluids, in fact, can be directly derived from the kinetic theory of gases for collision-dominated flows as

$$\mu \approx \lambda c \rho \quad (1.7)$$

where  $c$  is the mean molecular speed and  $\lambda$  the mean free path. For a simple gas of hard spherical molecules in thermodynamic equilibrium the mean free path is  $(\sqrt{2}\pi d^2 n)^{-1}$  [Bird, 1994], where  $n$  is the number of particles per unit volume. Combining Eq. 1.7 with Eq. 1.6, the following relation between  $Kn$ ,  $Ma$  and  $Re$  can be obtained

$$Kn \approx \frac{Ma}{Re}. \quad (1.8)$$

In Sec. 2.3 the governing kinetic equations for dispersed multiphase flows and for rarefied gases are presented as particular cases of the GPBE, while in Chap. 7, the Boltzmann Equation is solved with a QBMM.

## 1.6 Thesis outline

In this chapter an overview of problems and complex fluid regimes arising in multiphase turbulent flows has been given. In Chap. 2 an analytic description of the models and methods used in this work to deal with these problems is reported, while in the following chapters test cases and applications are presented. In particular the fluid dynamics analysis of a micro-mixer is carried out in Chap. 3, by means of  $\mu$ PIV experiments and accurate DNS simulations. In this part of the work, another important problem that has not been cited yet is also faced: the validation of CFD models and the comparison with experimental results. In fact, when considering complex models such as LES for turbulence, the comparison with experimental data

can be misleading because the experiments itself are affected by errors and limitations that cannot be simply averaged out [Grinstein, 2009]. Therefore coupling of accurate CFD simulations and experimental measures have to be considered to fully understand the behaviour of complex fluid in complex geometries. The validation of a LES model is then performed in Chap. 4 in a simple channel flow geometry. The outcomes of Chaps. 3 and 4 are then used to validate a LES model for the micro-mixer. Poly-dispersed particles are introduced in a LES framework in Chap. 6 to validate an efficient multiphase poly-dispersed turbulent flows coupled model. Non-equilibrium effects are studied in a more theoretical framework in Chap. 7 focusing on quadrature methods for the Boltzmann equation. Eventually some comments and critical analysis of the whole work are presented in Chap. 8, together with possible extensions and applications.

## References

- S. Balachandar and J. K. Eaton. Turbulent dispersed multiphase flow. *Annu. Rev. Fluid Mech.*, 42:111–133, 2010.
- G. Bird. *Molecular Gas Dynamics and the Direct Simulation of Gas Flows*. Oxford University Press (Oxford), 2nd edition, 1994.
- B.-Y. Cao, J. Sun, M. Chen, and Z.-Y. Guo. Molecular momentum transport at fluid-solid interfaces in mems/nems: A review. *Int. J. Mol. Sci.*, 10(11):4638–4706, 2009.
- R. Clift, J. R. Grace, and M. E. Weber. *Bubbles, Drops and Particles*. Academic Press, New York, 1978.
- C. Crowe, M. Sommerfeld, and Y. Tsuji. *Multiphase flows with droplets and particles*. CRC Press, Boca Raton, Florida, USA, 1998.
- J. Curtis and B. Van Wachem. Modeling particle-laden flows: A research outlook. *AIChE J.*, 50(11):2638–2645, 2004.
- M. Dudukovic. Reaction engineering: Status and future challenges. *Chem. Eng. Sci.*, 65 (1):3–11, 2010.
- R. Fox. Cfd models for analysis and design of chemical reactors. *Adv. Chem. Eng.*, 31: 231–305, 2006.
- R. Fox and D. Marchisio. *Multiphase reacting flows: modelling and simulation*. Courses and lectures. Springer, 2007.
- R. O. Fox. Large-eddy-simulation tools for multiphase flows. *Annu. Rev. Fluid Mech.*, 44 (1), 2012.
- D. Gidaspow. *Multiphase flow and fluidization: continuum and kinetic theory descriptions*. Academic Press, 1994.
- F. F. Grinstein. On integrating large eddy simulation and laboratory turbulent flow experiments. *Philos. Trans. R. Soc. A*, 367(1899):2931–2945, 2009.

- N. Hadjiconstantinou. The limits of navier-stokes theory and kinetic extensions for describing small-scale gaseous hydrodynamics. *Phys. Fluids*, 18(11), 2006.
- C. K. Harris, D. Roekaerts, F. J. J. Rosendal, F. G. J. Buitendijk, P. Daskopoulos, A. J. N. Vreenegoor, and H. Wang. Computational fluid dynamics for chemical reactor engineering. *Chem. Eng. Sci.*, 51(10):1569–&, 1996.
- M. Kalweit and D. Drikakis. Multiscale methods for micro/nano flows and materials. *J. Comput. Theor. Nanosci.*, 5(9):1923–1938, 2008.
- G. Karniadakis, A. Beşkök, and N. Aluru. *Microflows and nanoflows: fundamentals and simulation*. Interdisciplinary applied mathematics. Springer, 2005.
- W. J. Kelly. Using computational fluid dynamics to characterize and improve bioreactor performance. *Biotechnol. Appl. Biochem.*, 49:225–238, 2008.
- M. N. Kogan. Kinetic theory in aerothermodynamics. *Prog. Aerosp. Sci.*, 29(4):271–354, 1992.
- J. A. M. Kuipers and W. P. M. Van Swaaij. Application of computational fluid dynamics to chemical reaction engineering. *Rev. Chem. Eng.*, 13(3):1–118, 1997.
- J. J. Lerou and K. M. Ng. Chemical reaction engineering: A multiscale approach to a multiobjective task. *Chem. Eng. Sci.*, 51(10):1595–1614, 1996.
- D. Lockerby, J. Reese, and H. Struchtrup. Switching criteria for hybrid rarefied gas flow solvers. *Proc. R. Soc. A*, 465(2105):1581–1598, 2009.
- E. Loth. Numerical approaches for motion of dispersed particles, droplets and bubbles. *Prog. Energy Combust. Sci.*, 26(3):161–223, 2000.
- D. L. Marchisio, L. Rivautella, and A. A. Barresi. Design and scale-up of chemical reactors for nanoparticle precipitation. *AICHE J.*, 52:1877–1887, 2006.
- F. Mashayek and R. Pandya. Analytical description of particle/droplet-laden turbulent flows. *Prog. Energy Combust. Sci.*, 29(4):329–378, 2003.
- N. Peters. Multiscale combustion and turbulence. *Proceedings of the Combustion Institute*, 32:1–25, 2009.
- S. B. Pope. *Turbulent Flows*. Cambridge University Press, Cambridge, 2000.
- A. Prosperetti. Some considerations on the modeling of disperse multiphase flows by averaged equations. *Jsme International Journal Series B-fluids and Thermal Engineering*, 42(4):573–585, 1999.
- D. Ramkrishna. *Population balances: theory and applications to particulate systems in engineering*. Chemical, Petrochemical & Process. Academic Press, 2000.
- D. Ramkrishna and A. W. Mahoney. Population balance modeling. promise for the future. *Chem. Eng. Sci.*, 57(4):595–606, 2002.
- V. Ranade. *Computational flow modeling for chemical reactor engineering*. Process systems engineering. Academic Press, 2002.
- J. Reese and Y. Zhang. Simulating fluid flows in micro and nano devices: The challenge of non-equilibrium behaviour. *J. Comput. Theor. Nanosci.*, 6(10):2061–2074, 2009.
- J. Reese, M. Gallis, and D. Lockerby. New directions in fluid dynamics: Non-equilibrium

---

## REFERENCES

---

- aerodynamic and microsystem flows. *Philos. Trans. R. Soc. A*, 361(1813):2967–2988, 2003.
- S. Rigopoulos. Population balance modelling of polydispersed particles in reactive flows. *Prog. Energy Combust. Sci.*, 36(4):412–443, 2010.
- P. Sagaut, S. Deck, and M. Terracol. *Multiscale and multiresolution approaches in turbulence*. Imperial College Press, 2006.
- O. V. Salata. Applications of nanoparticles in biology and medicine. *J. Nanobiotechnol.*, 2(3):177–182, 2004.
- X. Shan, X.-F. Yuan, and H. Chen. Kinetic theory representation of hydrodynamics: A way beyond the navier-stokes equation. *J. Fluid Mech.*, 550:413–441, 2006.
- Y. Sone. *Kinetic theory and fluid dynamics*. Birkhäuser (Boston), first edition, 2002.
- Y. Sone and Y. Onishi. Kinetic theory of evaporation and condensation - hydrodynamic equation and slip boundary condition. *J. Phys. Soc. Jpn.*, 44(6):1981–1994, 1978.
- H. Struchtrup. *Macroscopic transport equations for rarefied gas flow: approximation methods in Kinetic Theory*. Springer (Berlin), 2005.
- S. Sundaresan. Modeling the hydrodynamics of multiphase flow reactors: Current status and challenges. *AICHE J.*, 46(6):1102–1105, 2000.
- P. Trambouze. Computational fluid-dynamics applied to chemical-reaction engineering. *Revue De L Institut Français Du Pétrole*, 48(6):595–613, 1993.
- H. E. A. Van den Akker. Toward a truly multiscale computational strategy for simulating turbulent two-phase flow processes. *Ind. Eng. Chem. Res.*, 49(21):10780–10797, 2010.
- M. Van der Hoef, M. Ye, M. Van Sint Annaland, A. Andrews, S. Sundaresan, and J. Kuipers. Multiscale modeling of gas-fluidized beds. *Adv. Chem. Eng.*, 31:65–149, 2006.
- M. Yu and J. Lin. Nanoparticle-laden flows via moment method: A review. *Int. J. Multiphase Flow*, 36(2):144–151, 2010.
- C.-X. Zhao, L. He, S. Z. Qiao, and A. P. Middelberg. Nanoparticle synthesis in microreactors. *Chem. Eng. Sci.*, 66(7):1463–1479, 2011.
- L. X. Zhou. Advances in studies on two-phase turbulence in dispersed multiphase flows. *Int. J. Multiphase Flow*, 36(2):100–108, 2010.



## Models and methods

In this chapter mathematical models and computational methods for multiphase turbulent flows are introduced and explained, with particular emphasis on Large Eddy Simulation (LES) as turbulence model and the Generalised Population Balance Equation (GPBE) and Quadrature based Methods of Moments (QMOM) as a general tool for multiphase and poly-disperse flows. Eventually in the last section 2.5 the CFD platform and numerical schemes and details are presented.

### 2.1 Single-phase flows

A turbulent flow at the macroscopic scale can be represented as a random field because of the unavoidable perturbation in initial conditions, boundary conditions and material properties [Pope, 2000]. This means that, when the continuum hypothesis holds and no other approximations are made, the solution of the macroscopic balance equations for mass and momentum represents a single realization of the turbulent random field, similarly to the result of an experiment without systematic error. This is what is obtained from Direct Numerical Simulations (DNS) where the balance equations are solved with numerical schemes and grids accurate enough to neglect numerical errors. Therefore, being free of modelling error, DNS are in principle fully equivalent to a single experiment realization without any error. However, as it would be explained after, this approach is computationally very expensive and is not practicable for many real applications.

The continuity and momentum equations for a Newtonian incompressible fluid are the well known Navier-Stokes equation:

$$\begin{aligned} \nabla \cdot \mathbf{U} &= 0, \\ \frac{\partial \mathbf{U}}{\partial t} + \mathbf{U} \cdot \nabla \mathbf{U} &= -\frac{1}{\rho_f} \nabla p + \nu_f \Delta \mathbf{U}, \end{aligned} \quad (2.1)$$

where  $\mathbf{U} = \mathbf{U}(\mathbf{x}, t)$  is the velocity vector field,  $p$  is the pressure,  $\rho_f$  is the fluid density and  $\nu_f = \frac{\mu_f}{\rho_f}$  and  $\mu_f$  are respectively the kinematic and dynamic viscosity.

The turbulent random fields can be decomposed into a mean and a fluctuating component, for example the velocity field can be written as:

$$\mathbf{U} = \bar{\mathbf{U}} + \mathbf{U}' . \quad (2.2)$$

The balance equations for the mean velocity and pressure are the same except for an additional stress term in the RHS of the momentum equation that is called the Reynolds stress tensor:

$$\tau_{ij} = \overline{U'_i U'_j} \quad (2.3)$$

The simplest turbulence models are based on the turbulent viscosity hypothesis that tries to mimic the Newtonian viscous stress assuming

$$\tau_{ij} = \frac{2}{3} k \delta_{ij} - \nu_t \left( \frac{\partial U_i}{\partial x_j} + \frac{\partial U_j}{\partial x_i} \right) , \quad (2.4)$$

where the first term is the isotropic part dependent on the turbulent kinetic energy  $k = \sum_i \overline{U'_i U'_i}$  and the second part is the product of the turbulent viscosity (or “eddy viscosity”)  $\nu_t$  and the mean strain rate. This assumption is however not generally valid like the Newtonian viscous stress assumption. In fact, considering a simple shear flow, the molecular viscosity is justified by the fact that the molecular time-scale,  $\lambda/c$  (where  $c$  is the mean molecular speed and  $\lambda$  is the mean free path, see also Eq. 1.7), divided by the strain time-scale is of the order of  $Kn Ma$  that is usually very small<sup>1</sup>, while this is much higher considering the turbulent fluctuations time-scale.

In Reynolds-Averaged Navier-Stokes equation (RANS) models the turbulent viscosity hypothesis is used together with the concept of time-average, i.e.: the decomposition in Eq. 2.2 is performed with an integration in time (Reynolds average). This means that the stochastic behaviour of the flow is completely lost and cannot be reconstructed. A huge number of algebraic and differential RANS models have been developed and they are widely used in many industrial and practical applications. An interesting alternative is represented by LES, discussed in the next section.

### 2.1.1 Large Eddy Simulations

LES models are based on the statistical theory of fully developed turbulence of Kolmogorov. This is derived from the scale similarities hypothesis and dimensional

---

<sup>1</sup>This could not be true for flows at the micro- and nano-scale, rarefied or and high-speed flows. In these cases in fact there could be effects like anomalous diffusion or other non-continuum effects. However similar laws can be sometimes derived with transport coefficients (e.g., viscosity, diffusivity) calculated from mesoscopic or particle methods. See Sec. 1.5, Sec. 2.3 and Chap.7.

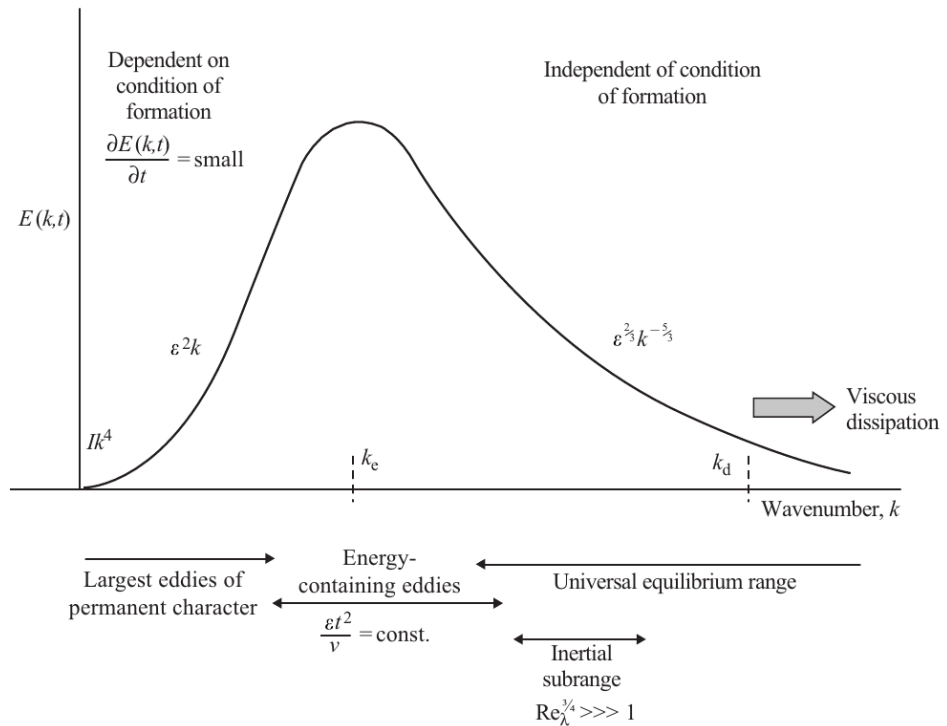


Figure 2.1: Energy spectrum for a generic fully developed turbulent flow [Hinze, 1975].

analysis and it has been verified and validated by experiments and numerical simulations [Pope, 2000]. The main result of this theory is the so-called turbulence spectrum, depicted in Fig. 2.1. It represents the kinetic energy contained at different length-scales (eddies). The first part of the spectrum for low wavenumber (very large eddies of the order of the system characteristic size) depends on boundary conditions and domain geometry, while the rest of the spectrum is universally valid for fully turbulent flows. Most of the energy is contained by large eddies and is transferred to smaller eddies until the dissipation acts to reduce their size and finally make the smallest eddies vanish at the Kolmogorov length-scale,  $\lambda_K$ .

The idea behind LES is to solve the larger scales of turbulence (eddies) and model (with the so-called sub-grid scale models, SGS) the smaller ones that are more isotropic therefore easier to model. This theoretical concept can be applied with low-pass filter in frequency space but has been practically implemented in most CFD codes (based either on finite volume or finite differences method) with a “box-filter” operation that makes use of the grid cells (of the size  $\Delta > \lambda_K$ ), volume-averaging the flow field in each cell. This is one of the most controversial points

about LES because with this type of filter (a low-pass in physical space) the strong theoretical framework of LES partially breaks down. It is worth mentioning here that a new interpretation and derivation of LES has been recently proposed by Pope [2010] that is more consistent and suitable also for multiphase extensions [Fox, 2012].

The effects of the filtering operation is represented in Fig. 2.2 and in Fig. 2.3 a schematic representation of LES together with DNS and RANS is proposed.

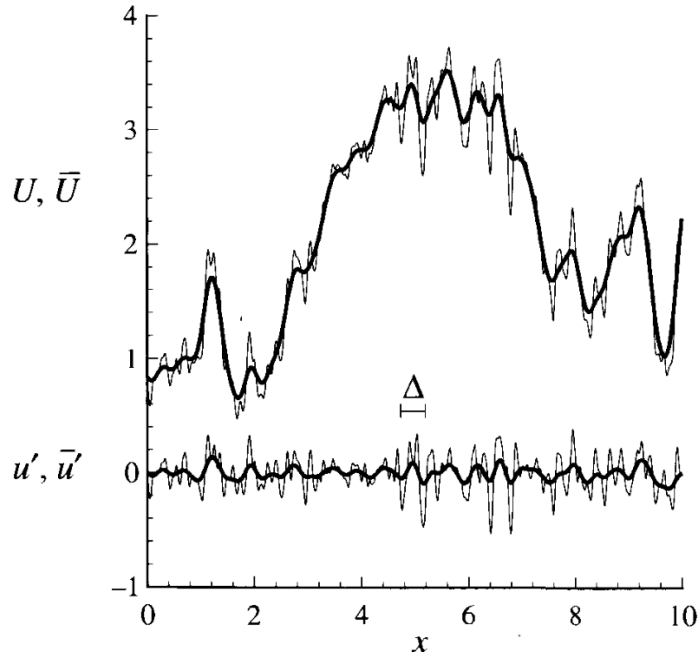


Figure 2.2: Example of a LES filter operation on the velocity  $U$  [Pope, 2000].  $\bar{U}$  is the filtered velocity,  $u'$  is equivalent to the fluctuation  $U'$  defined in Eq. 2.2 and  $\bar{u}'$  is the filtered fluctuation that is not null.

Real large scale problems (e.g., in aeronautics) are often characterised by  $Re \sim 10^5 - 10^7$ , and the use of DNS for these problems would require years to hundred of years, even with the most modern computers. The overall CPU time required for a DNS, in fact, scales as  $Re^{11/4}$ , without considering other important issues such as memory requirement. For LES the requirement in terms of grid points (and consequently on time steps) is more reasonable but still very challenging, especially if the viscous sub-layer must be solved in wall-bounded flows. For these reasons many hybrid RANS-LES approaches have also been recently developed such as V-LES, URANS, DES [Labois and Lakehal, 2011, Sagaut et al., 2006, Speziale, 1998] that couple LES equation with RANS equation in the near-wall regions.

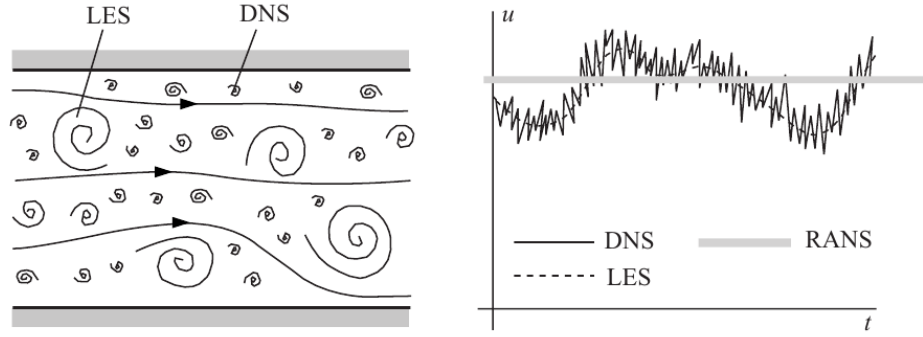


Figure 2.3: Schematic representation of the differences between DNS, LES and RANS [Ferziger and Peric, 2002, Ranade, 2002]

A more detailed discussion of LES and SGS models together with open problems, regarding accuracy and consistency are described in Chap. 4 and 5.

## 2.2 Multiphase flow

Many different models can be used for the simulation of multiphase dispersed flows, depending on the desired accuracy and the flow conditions. The first flow indicator, the Stokes number, has been already introduced in Sec. 1.2. Another distinction can be made between dense and dilute flow. This can be achieved by looking at the ratio between particle response time  $\tau_p$  and particle collision time  $\tau_C$ . The former has been defined in Eq. 1.5 while the latter can be expressed as

$$\tau_C \approx \frac{1}{\pi n d^2 \sigma} \quad (2.5)$$

where  $n$  is the particle concentration,  $d$  is the diameter and  $\sigma$  is the standard deviation of particle velocity fluctuations (the counterpart for dispersed flows of the mean particle molecular speed  $c$ , already defined for single-phase flow) that gives an estimate of the relative velocity between two particles. In Fig. 2.4 a flow map is depicted for dilute and dense multiphase flow in air, as a function of the particle diameter and the loading  $Z = \phi_v/\phi_f$  which is the ratio between the mass fractions of the continuous and the dispersed phase. In general a multiphase flow is said to be dilute when  $\tau_p/\tau_C < 1$  and it can be described with one-way coupling models. This means that particles feel the effect of the fluid but not vice-versa. A dense multiphase flow instead is characterised by an important contribution of particle-particle interaction and collisions that significantly change the particle dynamics. Therefore three-way and four-way coupling models must be used. The three-way coupling

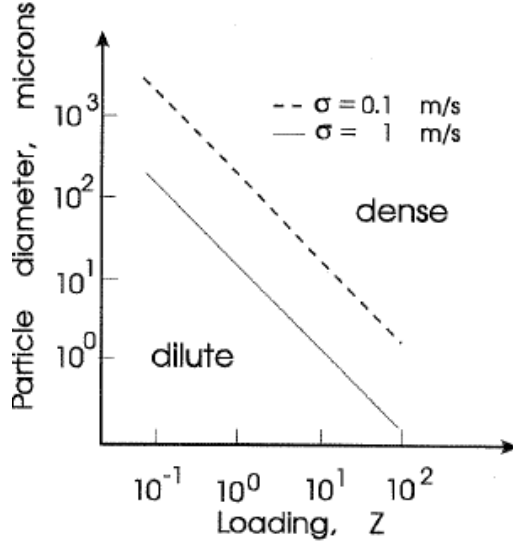


Figure 2.4: Dilute and dense flows depending on particle diameter  $d$ , particle loading  $Z$  and the standard deviation of particle velocity fluctuations  $\sigma$  [Crowe et al., 1998].

consider to the effects of the elements of the dispersed phase on each other through the continuous phase, as for example when a particle enters another particle's wake. Finally the four-way coupling regime is characterised also by interactions between particles, through direct collisions.

This distinction can be better analysed by looking at the Stokes number, as reported in Fig. 2.5. In this flow map the dilution regimes are determined by the volume fraction of particles,  $\phi_V$ , and the Stokes number based on the Kolmogorov time-scale, that represents the smallest time-scale of a turbulent flow:

$$\tau_K = \left( \frac{\nu}{\epsilon} \right)^{\frac{1}{2}} \quad (2.6)$$

where  $\epsilon$  is the dissipation rate of the turbulent kinetic energy. The two-way coupling regime is further divided into two class, depending on the size of the particles. Bigger particles, in fact, enhance the production of turbulent kinetic energy, while smaller particles enhance dissipation. Similar conclusions can be drawn with different definitions of Stokes number, based either on the LES time-scale  $\tau_\epsilon$  or other characteristic time-scales of the fluid.

Focusing on the dilute regime, many different models can be used to describe the particle motion and their accuracy are directly dependent on the particle Stokes number. As already introduced in Sec. 1.4, in fact, very small particles follow the fluid with approximately the same velocity and trajectory (see Fig. 1.3). This means that the flow can be described as a single-phase flow with variable density. This

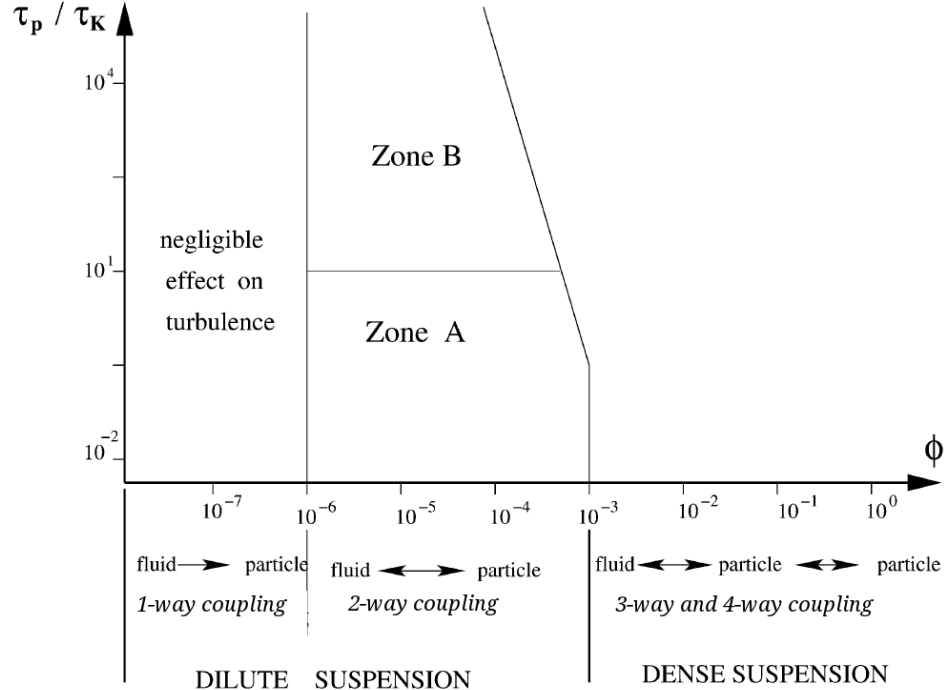


Figure 2.5: Fluid-particles coupling depending on the volume fraction of particles  $\phi_V$  and the Stokes number  $St = \frac{\tau_p}{\tau_K}$ , defined with the Kolmogorov time-scale  $\tau_K$  [Elghobashi, 1994, 2006].

model is called the Homogeneous Model or Dusty Gas Model and it can be rarely used to describe accurately real multiphase flow applications. A second and more accurate model is represented by the Equilibrium Eulerian Model (EEM) [Ferry and Balachandar, 2001, Ferry et al., 2003] or the Algebraic Slip Mixture Model (ASM or ASMM) [Ishii, 1975, Manninen and Taiavassalo, 1996]. In this case the particle velocity is linked to the fluid velocity and other flow properties with an algebraic relation. These models are based on a local equilibrium approximation and are valid for moderate  $St$ . The next step is to relax the local equilibrium assumption, by solving an independent momentum balance equation for the particles velocity. This is the common two-fluid (or multi-fluid) approach derived from volume or ensemble average for the phases [Drew and Passman, 1998].

When particles becomes larger, either a Lagrangian Particle Tracking (LPT) or a fully resolved method must be used. The former consists in following the trajectory of each single particle in a Lagrangian manner through the resolution of Newton's equations, while the latter refer to those methods, such as the Discrete

Element Method [Munjiza, 2004] or interface capturing methods like Volume-Of-Fluid , Level-Set and Front-Tracking [Hirt and Nichols, 1981, Osher and Sethian, 1988, Unverdi and Tryggvason, 1992], where the interface of the particle is captured. This is particularly important when interface phenomena must be taken into account or when the geometry of the particles is complex and far from a sphere. Except these models, all the others are based instead on point-particle approximations. The differences between Lagrangian and Eulerian methods and between point-particle and fully resolved approaches are represented in Fig. 2.6.

These models and their validity are illustrated in Fig. 2.7. In the following part of this section, we focus in particular on the ASM and its differences with the multi-fluid and the Lagrangian/fully resolved methods. The EEM equations are instead given in Chap. 6.

### 2.2.1 Mixture algebraic models

According to the derivation of Manninen and Taivassalo [1996] and Bove [2005], let us consider a multi-component fluid made of  $K$  components, each one characterised by its own density  $\rho_k$ , volume fraction  $\phi_k$  and mass weighted velocity  $\mathbf{U}_k$ <sup>2</sup>.

The mixture can be characterised by its density

$$\rho_m = \sum_{k=1}^K \phi_k \rho_k \quad (2.7)$$

and its velocity

$$\mathbf{U} = \sum_{k=1}^K \frac{\phi_k \rho_k \mathbf{U}_k}{\rho_m} \quad (2.8)$$

which can be regarded as the velocity of the mixture centre of mass. Finally the mass fraction  $c_k$  can be calculated as

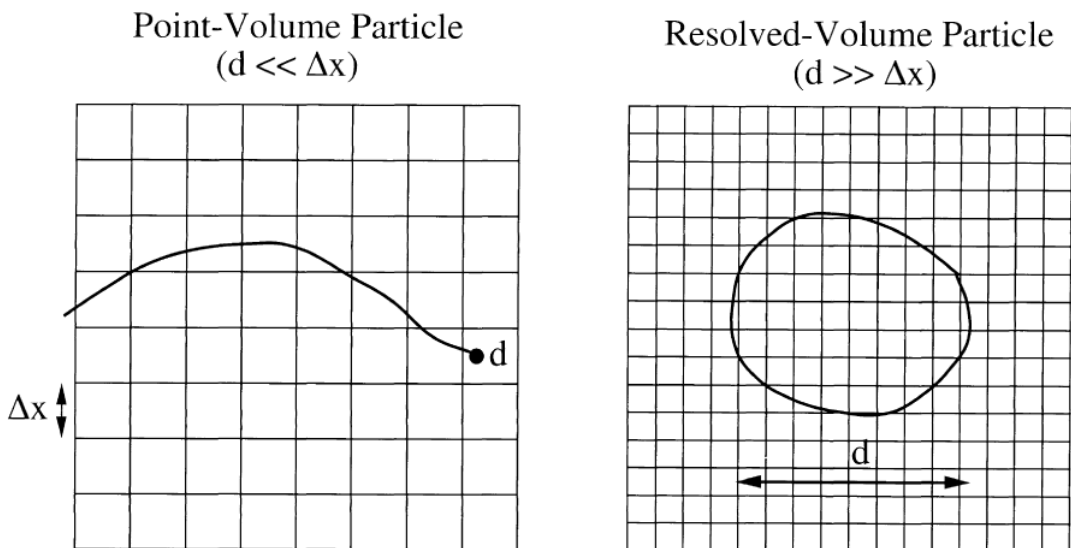
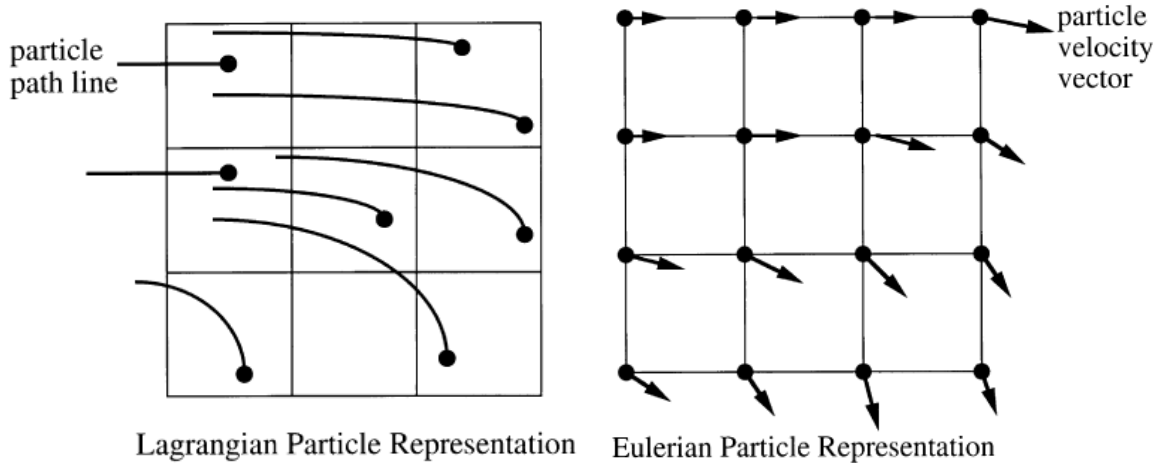
$$c_k = \frac{\phi_k \rho_k}{\rho_m} \quad (2.9)$$

The continuity equation for the mixture is

$$\frac{\partial \rho_m}{\partial t} + \nabla \cdot (\rho_m \mathbf{U}_m) = 0 \quad (2.10)$$

---

<sup>2</sup>The Favre average is used for the phase velocities  $\mathbf{U}_k = \frac{\langle \chi_k \rho \mathbf{U} \rangle}{\langle \chi_k \rangle}$ , and a phasic average for  $\rho_k = \langle \chi_k \rho \rangle / \langle \chi_k \rangle$ , where  $\rho$ ,  $\mathbf{U}$  are the local density and velocity of the fluid,  $\chi_k$  is the characteristic function of phase  $k$  and  $\langle \rangle$  represents a volume, time or ensemble average.



- > neglects particle volume effect on the continuous-fluid grid
- > ideal for many particles
- > requires models for drag, lift, etc.

- > describes particle volume/ interface as part of the continuous-fluid grid
- > ideal for complex particle shapes
- > requires high CPU per particle

Figure 2.6: Differences between Lagrangian and Eulerian fields and between point-particle and fully resolved simulations, depending on the diameter of particles  $d$  and the grid spacing  $\Delta x$  [Loth, 2000].

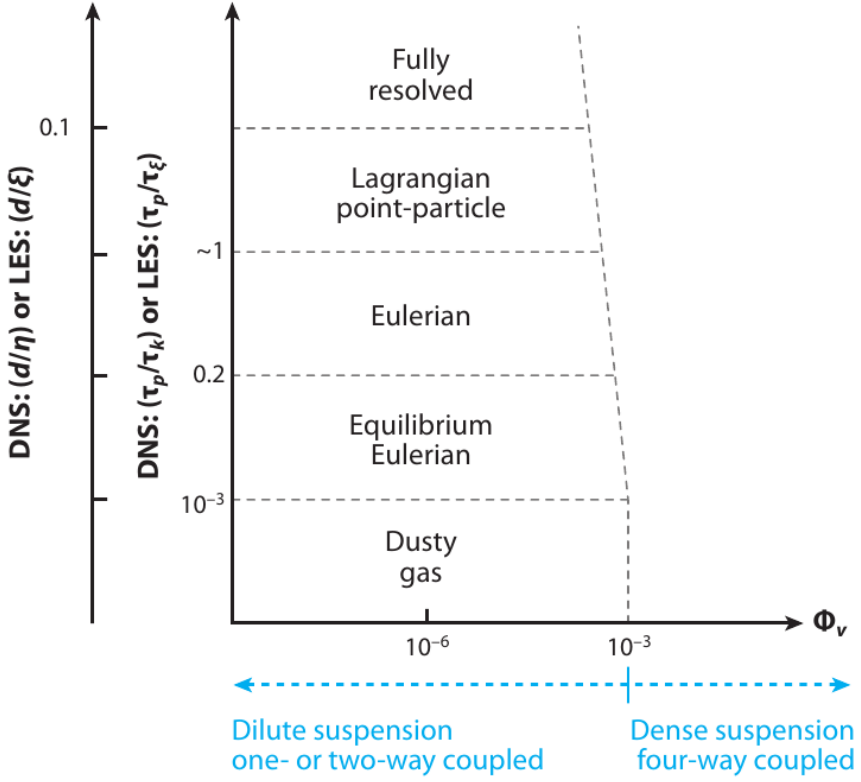


Figure 2.7: Balachandar and Eaton [2010]

while the mixture momentum balance equation is

$$\frac{\partial}{\partial t} (\rho_m \mathbf{U}_m) + \nabla \cdot (\rho_m \mathbf{U}_m \mathbf{U}_m) = -\nabla p + \nabla \cdot (\tau_m + \tau_{Tm} + \tau_{Dm}) + \rho_m \mathbf{g} + \mathbf{M}_m \quad (2.11)$$

The three stress tensors represent respectively the average viscous stress, the turbulent stress and the diffusion stress due to phase slip, while the term  $\mathbf{M}_m$  represent other momentum sources (e.g., surface tension, phase interactions).

The term  $\tau_{Dm}$  in Eq. 2.11 can be expressed as

$$\tau_{Dm} = - \sum_{i=1}^K \phi_k \rho_k \mathbf{U}_{Dk} \mathbf{U}_{Dk} \quad (2.12)$$

where  $\mathbf{U}_{Dk} = \mathbf{U}_k - \mathbf{U}_m$  is the diffusion velocity<sup>3</sup>. In the ASM diffusion velocity

<sup>3</sup>Some authors refer to this velocity as the drift velocity. However the drift velocity is usually defined with respect to the velocity of the centre of volume of the mixture, while the drift velocity is defined instead with respect to the centre of mass of the mixture [Ishii, 1975].

for phase  $k$  is not directly calculated but derived from the knowledge of the slip velocities  $\mathbf{U}_{S,ki} = \mathbf{U}_k - \mathbf{U}_i$  between phase  $k$  and the other phases as

$$\mathbf{U}_{Dk} = \sum_{i=1}^K c_k \mathbf{U}_{S,ki} \quad (2.13)$$

Equivalent models, called respectively Diffusion Mixture and Drift Flux models, are instead formulated in terms of diffusion or drift velocities [Jakobsen, 2008].

At this stage, the mixture equations are equivalent to the multi-fluid formulation and the only assumption made is the single pressure shared by the continuous and the dispersed phase. However, to have a closed set of equations, they must be coupled with equations for the volume fractions  $\phi_k$ , the slip velocities  $\mathbf{U}_{S,ki}$  and with closure relations for stress tensors and momentum source terms.

As it has been anticipated, we are interested in the use of Population Balance Model to describe the poly-dispersity of the flow, therefore we do not introduce here an explicit equation for the volume fraction  $\phi_k$ . As it is explained in the next section, in fact, in the population balance framework the volume fractions are calculated as the third order moment of the number density function multiplied by a shape factor ( $\pi/6$  for spherical particles). Also the source  $\Gamma_k$  that takes into account exchange of mass between the phases (due to birth and death terms) can be obtained directly from the population balance.

The momentum source term  $\mathbf{M}_m$  can be written as

$$\mathbf{M}_m = \sum_{i=1}^K (\Gamma_k \mathbf{U}_k + \mathbf{M}_k) \quad (2.14)$$

If  $\Gamma_k = 0$  and the surface tension is neglected  $\mathbf{M}_m = 0$  because in this case all the terms  $\mathbf{M}_k$  sum to zero.  $\mathbf{M}_k$  can be decomposed in terms of a generalised drag force and averaged interfacial terms (pressure and shear stresses). Neglecting the second ones and distinguishing the continuous (primary) phase (for  $k = 1$ ) from the dispersed phases (for  $k > 1$ ) we can write

$$\mathbf{M}_1 = \sum_{k=2}^K \mathbf{M}_k \quad (2.15)$$

$$\mathbf{M}_k = -\mathbf{M}_k^G \quad (2.16)$$

where  $\mathbf{M}_k^G$  takes into account drag, lift, gravity, pressure gradient, virtual mass, Basset force, buoyancy. These terms must be modelled with specific laws or empirical correlation.

Neglecting the surface tension and assuming a single pressure for the mixture, the general differential equation for the slip velocities is

$$\frac{\partial}{\partial t} \mathbf{U}_{S,ki} + \mathbf{U}_k \cdot \nabla \mathbf{U}_k - \mathbf{U}_i \cdot \nabla \mathbf{U}_i = \left( \frac{1}{\rho_i} - \frac{1}{\rho_k} \right) \nabla p + \frac{1}{\rho_k \phi_k} \nabla \cdot (\phi_k \tau_k) - \frac{1}{\rho_i \phi_i} \nabla \cdot (\phi_i \tau_i) + \frac{1}{\rho_k \phi_k} \mathbf{M}_k^G - \frac{1}{\rho_i \phi_i} \mathbf{M}_i^G \quad (2.17)$$

or equivalently a similar equation can be derived in terms of diffusion velocities  $\mathbf{U}_{Dk}$ .

Algebraic equation for the slip velocities can be obtained from Eq. 2.17, under local equilibrium assumptions. As a matter of fact, the classical ASM is obtained considering  $K = 2$  ( $\mathbf{U}_k = \mathbf{U}_p$  and  $\mathbf{U}_i = \mathbf{U}$ ), simplifying Eq. 2.17 neglecting the time derivative, substituting the pressure gradient from the mixture momentum balance (Eq. 2.11) and using explicit formulation for the momentum source terms  $\mathbf{M}_i$ . The ASM can be extended with a similar derivation for a generic number of dispersed phases. The multiple-phases extension is needed also for the coupling with a multiple-classes population balance approach such as the one explained in Sec. 2.4.

The EEM is another example of algebraic closure for the dispersed phase velocity. It is conceptually equivalent to the ASM but it is derived [Ferry and Balachandar, 2001] as an expansion of the Maxey-Riley equation [Maxey and Riley, 1983], which is the balance of forces acting on a dispersed particle, in terms of the fluid velocity, as follows:

$$\frac{D\mathbf{U}_p}{Dt} = \frac{D\mathbf{U}_p}{Dt} + O(\tau_p), \quad (2.18)$$

where,  $D/Dt$  is the Lagrangian derivative operator and  $\tau_p$  is the particle response time, defined in Eq. 1.5. The explicit equations of EEM are given in Chap. 6.

## 2.3 Generalised Population Balance Equations

Starting from the concepts of the Population Balance Equation (PBE) [Ramkrishna, 2000] and the Williams Spray Equation [Williams, 1958] and their solution methods, a new approach has been recently formalised by Fox and Marchisio [2007] that introduced a generalisation of PBE in a physically-consistent, full mesoscopic description of multiphase dispersed flow. The key point is the introduction of a multi-variate phase space for particles, that includes, among the other variables, also particle velocity. In this section we present this general framework, focusing in two particular cases of the GPBE: the classical mono-variate population balance written in terms of particle size and the Boltzmann Equation (BE), that is instead an equation for the evolution of the particle velocity distribution.

Let us consider a continuum phase and a dispersed phase made of particles (bubbles, droplets or solid particles) characterised by many different inhomogeneous properties (e.g., size, surface area, composition, velocity), described by a vector  $\mathbf{s} = (s_1, \dots, s_S)$  that spans the so-called “phase-space”. It is possible to describe this inhomogeneity in an Eulerian framework by using a Number Density Function (NDF)  $n(\mathbf{x}, t; \mathbf{s})$  whose meaning is the following:  $n(\mathbf{x}, t; \mathbf{s})d\mathbf{s}$  represents the infinitesimal number of particles per unit volume with properties in the interval  $(\mathbf{s}, \mathbf{s} + d\mathbf{s})$ , around the point  $\mathbf{x}$  at time  $t$ . Its evolution is dictated by the following Generalised

Population Balance Equation (GPBE):

$$\frac{\partial n}{\partial t} + \nabla_{\mathbf{x}} \cdot (\mathbf{U}_p n) + \nabla_{\mathbf{s}} \cdot (\dot{\mathbf{s}} n) = (\nabla_{\mathbf{s}} \otimes \nabla_{\mathbf{s}}) : (\mathbf{D} n) + Q \quad (2.19)$$

where  $\nabla_{\mathbf{x}}$  and  $\nabla_{\mathbf{s}}$  indicate respectively the gradient with respect to space coordinates and to internal coordinates, the colon indicates the Frobenius product and  $\otimes$  the tensor product. The second and third term in the LHS represent respectively the “real-space” advection and the “phase-space” advection. The former is the variation due to particles motion whereas the latter is the variation due to the rate of change,  $\dot{\mathbf{s}}$ , of the properties  $\mathbf{s}$  (called also internal coordinates). The RHS has a phase-space diffusion term, defined by the diffusion matrix  $\mathbf{D}$  and a collision term  $Q$ . The diffusion term is generally due to average operations or microscopic processes (such as Brownian motion or turbulent fluctuations) and in the following description it is neglected to simplify the discussion. The operator  $Q$  represents instead all the instantaneous or discontinuous events such as collisions. It can be split in three parts:

$$Q = Q_0 + Q_1(n) + Q_2(n, n) . \quad (2.20)$$

The first term,  $Q_0$  represent zero-order processes that do not depend directly on the NDF (such as nucleation of new particles).  $Q_1$  and  $Q_2$  instead are related respectively to a single-particle event (such as particle breakage) and two-particle binary processes (the real collisions of particles with their exchange of properties between the colliding particles). This dependence on the particles is expressed with a dependence on the NDF<sup>4</sup>.

The GPBE in Eq. 2.19 is a kinetic equation and resembles the structure of many important equations such as the Boltzmann Equation [Cercignani, 1988] and the Population Balance equation [Ramkrishna, 2000], which can be seen as particular cases of the GBPE. Other labels are the Smoluchowski equation (which describes the evolution of particles in space, not to be confused with the Smoluchowski coagulation equation that describes the evolution of particle size) and the Fokker-Planck equation [Risken, 1996] (which describes the evolution of particle velocity), both characterised by having a drift and a diffusion term in phase-space. As it has been already reported, two particular cases of this equation are very important and will be now introduced and discussed. Let us assume that the property of interests are limited to particle diameter  $d$  and particle velocity  $\mathbf{U}_p$ , therefore  $\mathbf{s} = (d, \mathbf{U}_p)$ .

---

<sup>4</sup>It is important to note that all the collision terms depend on  $\mathbf{x}$  and  $t$  but the dependence has been omitted to focus on the different dependences on  $n$ .

### 2.3.1 Boltzmann Equation

To derive the BE we simply assume that all the particles have the same size, reducing the phase space to the particle velocity space only, obtaining:

$$\frac{\partial n}{\partial t} + \nabla_{\mathbf{x}} \cdot (\mathbf{U}_p n) + \nabla_{\mathbf{U}_p} \cdot (\mathbf{A}_p n) = Q, \quad (2.21)$$

where  $\mathbf{A}_p$  is the sum of the external forces per unit mass acting on the particles (e.g., gravity, drag, electromagnetic forces).

The classical form of the BE is obtained in the case of no external forces, in the limit of  $St \rightarrow 0$ , when particles act as a granular gas, and for a particular form of the collisional operator, namely:

$$Q = \iint q(\mathbf{x}_1, \mathbf{U}_{p1}, \mathbf{x}_2, \mathbf{U}_{p2}) [n^{(2)}(\mathbf{x}_1, t; \mathbf{U}'_1, \mathbf{x}_2, t; \mathbf{U}'_2) - n^{(2)}(\mathbf{x}_1, t; \mathbf{U}_{p1}, \mathbf{x}_2, t; \mathbf{U}_{p2})] d\mathbf{x}_2 d\mathbf{U}_{p2}, \quad (2.22)$$

where the subscript 1,2 indicates that we are following particle 1 in its collision with particle 2,  $\mathbf{U}'_{1-2}$  indicates the velocities after the collision,  $n^{(2)}$  is the pairwise distribution function and  $q(\mathbf{x}_1, \mathbf{U}_{p1}, \mathbf{x}_2, \mathbf{U}_{p2})$  is the collision frequency. Three important hypotheses are now introduced. The first is the molecular chaos assumption (“Stosszahl Ansatz”), that is one of the key points of the BE, for which  $n^{(2)}(\mathbf{x}_1, t; \mathbf{U}_{p1}, \mathbf{x}_2, t; \mathbf{U}_{p2}) \approx n(\mathbf{x}_1, t; \mathbf{U}_{p1})n(\mathbf{x}_2, t; \mathbf{U}_{p2})$ . The second assumption is that particles are small enough that, when colliding, the NDF calculated at  $\mathbf{x}_1$  is approximately equal to the one at point  $\mathbf{x}_2$ . Finally we introduce the so-called hard-sphere potential that models the collision as instantaneous event that happens with a frequency given by

$$q(\mathbf{x}_1, \mathbf{U}_{p1}, \mathbf{x}_2, \mathbf{U}_{p2}) = \begin{cases} \frac{|\mathbf{g}| \cos \Theta}{d} & \text{if } \mathbf{g} \cdot \mathbf{x}_{12} > 0, \\ 0 & \text{elsewhere,} \end{cases} \quad (2.23)$$

where  $\mathbf{g} = \mathbf{U}_{p1} - \mathbf{U}_{p2}$  is the velocity difference,  $\mathbf{x}_{12}$  is the versor connecting the two centres of the particles and  $\Theta$  is the angle between these two vectors, as it is illustrated in Fig. 2.8.

Under these hypotheses Eq. 2.22 can be rewritten as:

$$Q = \int_{\mathbf{U}_{p2}} \int_{\mathcal{S}^+} |\mathbf{g}| \cos \Theta [n(\mathbf{x}, t; \mathbf{U}'_1)n(\mathbf{x}, t; \mathbf{U}'_2) - n(\mathbf{x}, t; \mathbf{U}_{p1})n(\mathbf{x}, t; \mathbf{U}_{p2})] d\mathbf{x}_{12} d\mathbf{U}_{p2}, \quad (2.24)$$

where the integral over  $\mathbf{x}_{12}$  is performed over an half sphere  $\mathcal{S}^+$ . Finally, simple geometrical observations and balances of momentum and energy, before and after the collision, can be used to find the relations between pre- and post-collisional velocities.

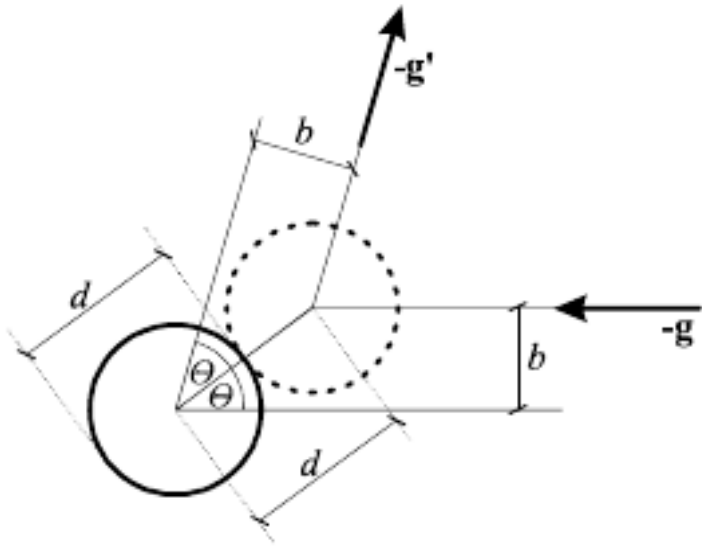


Figure 2.8: Collisions of two identical particles of diameter  $d$  [Struchtrup, 2005].

The BE is further analysed and solved in Chap. 7, in a slightly different formulation that simplify the expression, retaining the physical meaning of hard-sphere collision. It is important to highlight here that, for realistic multiphase flow, the BE is often used with linearised model for particle collisions and modification to take into account inelastic collision in a more dense regime (Boltzmann-Enskog Equation).

### 2.3.2 Poly-dispersity models

Let us consider now the size (diameter) of the particles as the only property of interest of the dispersed phase. Therefore  $\mathbf{s} = (d)$ . The function  $n = n(\mathbf{x}, t; d)$  in this case is also called Particle Size Distribution (PSD), that represents the number of particles with diameter  $d$  per unit volume at point  $\mathbf{x}$  and time  $t$ . An evolution equation for  $n(\mathbf{x}, t; d)$  can be derived from the evolution of Eq. 2.19 by integrating out particle velocity. The mesoscopic description of GPBE requires, in fact, the presence of particle velocity as internal coordinate. This means that in general a fully kinetic approach, similar to the one described in the previous section, must be used. This approach is necessary to predict multiphase flow in which the particle fluctuation collisions are important but are not the dominant effect<sup>5</sup>. This is the

---

<sup>5</sup>In the limiting case of purely collisional flows, in fact, the particle velocity distribution relaxes instantaneously to a local equilibrium.

case, for example, of particle trajectory crossing. After the integration on all the possible particle velocity the GPBE reads as follows:

$$\frac{\partial n}{\partial t} + \nabla_{\mathbf{x}} \cdot (\mathbf{U}_p(d)n) + \frac{\partial}{\partial d} (\dot{d}n) = Q. \quad (2.25)$$

The real-space advection term remains the same except that now the velocity  $\mathbf{U}_p(d)$  represents the expected velocity for particle of size  $d$  (formally it is a conditional mean particle velocity, conditioned on a particular particle size). When the particle velocity is not solved with the GPBE,  $\mathbf{U}_p(d)$  must be modelled with one of the methods discussed in Sec. 2.2, via a differential momentum equation or with simplified algebraic relation, depending on the Stokes number and the desired accuracy. The phase-space advection is now reduced to a single term that represents particle growth (due to phase change for example) with growing velocity  $\dot{d}$ . The collision term  $Q$  has been redefined to maintain the same notation and includes other phenomena such as particle breakage, coalescence and nucleation. Equation 2.25 is now exactly equivalent to the classical mono-variate PBE [Ramkrishna, 2000].

As we already mentioned, kinetic equations and PBES can be viewed as a mesoscopic (or statistical) description of the huge number of microscopic entities and events. The connection with more commonly used macroscopic quantities such as mean concentration or particle size is performed through the definition of the following moments<sup>6</sup>:

$$m_i(\mathbf{x}, t) = \int_0^\infty d^i n(\mathbf{x}, t; d) dd. \quad (2.26)$$

In this mono-variate case, it is straightforward the derivation from  $\mu_i$  of important macroscopic quantities to describe the dispersed phase such as

- total particle number density:  $m_0$ ;
- mean particle diameter:  $m_1/m_0$ ,  $m_2/m_1$  or  $m_3/m_2$  (Sauter diameter) or  $m_4/m_3$ ;
- mean particle surface area:  $c_2 m_2/m_0$ , where  $c_2$  is the two-dimensional shape factor;
- mean particle volume:  $c_3 m_3/m_0$ , where  $c_3$  is the three-dimensional shape factor;
- particle volume fraction:  $c_3 m_3$ ;
- variance of the distribution:  $m_2 - m_1^2/m_0$

<sup>6</sup>A more general definition of moments for the GPBE, that allows to recover other macroscopic quantities such as dispersed phase velocities or mixed moments of particle size and velocity, is also possible but is not reported here. The reader interested is referred to the work of Fox and Marchisio [2007].

In the next section a Quadrature-Based Moment Method for the numerical solution of GPBE are introduced. In particular the application to the mono-variate PBE is analysed while the application of this method for the Boltzmann Equation is discussed in Chap. 7.

## 2.4 Quadrature-based Method Of Moments

The Quadrature Method Of Moments (QMOM) is a general tool for solving kinetic equations and PBEs by using a Gaussian quadrature formula that can approximate exactly  $M$  selected moments of the distribution (usually the first ones). The moments  $m_i$  are solved numerically within their transport equation, obtained directly applying the moments transform to Eq. 2.25 (or to Eq. 2.19 in the more general case) and the arising unclosed terms (typically the collision term  $Q$ ) are approximated with a Gaussian quadrature formula. QMOM was first introduced by McGraw [1997], as a closure for Population Balance Equations (PBE) of particles, sprays and dispersed multiphase systems in general. In this case the internal variables of the distribution function are physical properties of the particles (usually the size of the particles). In the mono-variate case, when a single property  $d$  is tracked, the NDF  $n(\mathbf{x}, t; d)$  or if normalised, the Probability Density Function (PDF)  $f(\mathbf{x}, t; d)$  is approximated as a sum of  $M/2$  delta functions

$$n(d) \approx \sum_{i=1}^{M/2} w_i \delta(d - d_i) \quad (2.27)$$

where the dependence on external variables such as time and space is omitted.  $w_i$  and  $d_i$  are respectively the quadrature weights and nodes that can be used as a quadrature formula to calculate whatever integrals involving  $n$ . They can be obtained from the first  $M$  moments that are exactly approximated with an inversion algorithm that identifies them with the roots of the polynomials orthogonal to the distribution function. The most used ones are the Product-Difference (PD) algorithm [Gordon, 1968] and the Wheeler algorithm [Wheeler, 1974]. Quadrature weights and nodes are identified by these algorithms as the roots of the polynomial orthogonal to the distribution in the chosen phase space domain (generally  $d \in [0, \infty]$ ). QMOM and its variants (e.g., Direct Quadrature Method of Moments, DQMOM) have been successfully extended and applied also for multivariate distributions and for different types of kinetic equations in many applications such as multi-variate PBEs, micro-mixing problem, Fokker-Plank equation, Boltzmann equation [Attar and Vedula, 2008, Fox, 2006, 2003, Gavi et al., 2007, Lage, 2007, Laurent et al., 2010, Raman et al., 2006, Sidin, 2009, Upadhyay and Ezekoye, 2008, Wang and Fox, 2004, Yoon and McGraw, 2004a,b]. In general, we talk about Quadrature-Based

Moment Methods (QBMM), when the concept of adaptive quadrature nodes and weights, derived from the moments of the distribution, is used.

QBMM turns out to be a very efficient tool for PBEs, compared to other methods such as the full Probability Density Function (PDF) models or the Direct Simulation Monte-Carlo (DSMC), that however retains a good accuracy that can be controlled by the number of moments chosen for the quadrature. In particular the coupling of QBMM with Eulerian multi-fluid method has been developed in different works [Fan et al., 2004, Marchisio et al., 2003, Petitti et al., 2010] that demonstrated the efficiency and the relatively simple implementation in CFD codes. Among the numerous variants of QBMM we focus now on the DQMOM that is the method used in this thesis for the solution of PBEs (see Chap. 6 and 8).

#### 2.4.1 Direct Quadrature Method Of Moments

As already mentioned, QBMM make use of quadrature weights and nodes that are uniquely obtained from a set of moments, provided that a moment transform such as Eq. 2.26 is given. With the QBMM approximation, the moments are calculated by the following formula

$$m_i(\mathbf{x}, t) = \sum_{j=1}^{M/2} d_j^i w_j. \quad (2.28)$$

that defines the relation between the set of quadrature nodes and weights,  $(w_1, \dots, w_{M/2}, d_1, \dots, d_{M/2})$ , and the set of moments,  $\mathbf{m} = (m_1, \dots, m_M)$ <sup>7</sup>. The DQMOM [Marchisio and Fox, 2005] is a formulation in which transport equations are derived and solved for quadrature nodes and weight, collected in a vector of transported quantities  $\zeta = (w_1, \dots, w_{M/2}, w_1 d_1, \dots, w_{M/2} d_{M/2})$ , where  $w_i d_i \equiv n_i$  represents the weighted nodes. This approach presents important advantages and some serious drawbacks that are now briefly presented:

- + the inversion algorithm to obtain  $\zeta$  from  $\mathbf{m}$  is no more needed since the values  $\zeta$  are always directly accessible;
- a similar inversion must be performed for those quantities, such as moments of collision source term  $\int_0^\infty Q d^i dd$ , that are expressed in the moment (QMOM) formulation;
- + transport equations, if adequately solved, are not affected by the problem of unrealisable moment;

---

<sup>7</sup>This relation is highly non-linear and not always invertible in the desired domain (positive moments and positive nodes and weights). In fact, there exist unrealisable set of moments that give place to negative quadrature weights.

- the numerical discretisation introduces an error on high-order moments that are not exactly conserved;
- + the expected particle velocity  $\mathbf{U}_p(d_i)$  can be directly used for the advection of  $w_i$  and  $n_i$ , simplifying the coupling of DQMOM with multi-fluid or algebraic mixture models;
- the mathematical model degenerates when the distance between two quadrature nodes tends to zero

For a more detailed analysis of the different QBMM approaches and an accurate analysis of QMOM and DQMOM the reader is referred to the work of Grosch et al. [2007], Mazzei et al. [2010, 2011].

## 2.5 Numerical methods

Before discussing in the following chapters the test cases studied and the results obtained, it is important to give a brief introduction on the numerical schemes and tools used in this work, both from a mathematical and practical point of view.

### 2.5.1 TransAT CFD code

*TransAT* [Ascomp GmbH, 2009] is a finite volume code, specialised for the simulation of multiphase flows in complex geometries thanks to the coupling of interphase tracking methods (VOF and LS) and an Immersed Boundary method (explained in details in Chap. 5) and recently extended to a broad range of CFD applications. Most of the work carried out in this thesis relies on the TransAT platform, which has been integrated by ad-hoc models and modules for the specific application, thanks to a collaboration with *Ascomp GmbH* (<http://www.ascomp.ch>).

A QBMM solver for PBEs of poly-dispersed flows have been implemented and coupled with the ASM model. The EEM was also developed as an alternative model, especially for dilute passive particles that do not have a feedback on the carrier flow. In this case, in fact, the particle velocity can be explicitly calculated in a very efficient way, as explained in Chap. 6. LES and DNS simulations have been carried out with the available models, opportunely modified for the test cases under study. Finally some of the numerical schemes and resolution methods are briefly described in this section.

### 2.5.2 Convection schemes

Let us define a generic field quantities  $\phi$ , discretised in the points represented in Fig. 2.9. From the knowledge of cell centre variable  $\phi_P$ , assuming that the fluid

flows in the right direction and that the cells are equally spaced, an approximation of the downward cell faces variable  $\phi_w$  must be obtained to calculate the fluxes of  $\phi$  entering on the volume  $P$ .

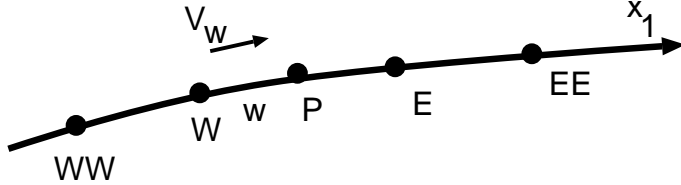


Figure 2.9: Nodes required by convection schemes in a single direction [Ascomp GmbH, 2009].

Three schemes are used in this work: the central scheme, the HLPA scheme and the QUICK scheme. The central scheme is a second order approximation based on the simple formula

$$\phi_w = \frac{\phi_W + \phi_P}{2}. \quad (2.29)$$

The QUICK scheme [Leonard, 1976] approximates the face-value  $\phi_w$  by fitting a parabolic curve through three nodal values  $\phi_P$ ,  $\phi_W$  and  $\phi_{WW}$ :

$$\phi_w = \frac{3}{8}\phi_P + \frac{3}{4}\phi_W - \frac{1}{8}\phi_{WW}. \quad (2.30)$$

Finally the HLPA scheme [Zhu, 1991] can be written as

$$\phi_w = \phi_W + \gamma_w(\phi_P - \phi_W) \frac{\phi_W - \phi_{WW}}{\phi_P - \phi_{WW}} \quad (2.31)$$

where

$$\gamma_w = \begin{cases} 1 & \text{if } |\hat{\phi}_W - 0.5| < 0.5 \\ 0 & \text{otherwise} \end{cases} \quad (2.32)$$

and

$$\hat{\phi}_W = (\phi_W - \phi_{WW}) / (\phi_P - \phi_{WW}) \quad (2.33)$$

is an upwind-biased normalised variable

### 2.5.3 Time discretisation

The time discretisation in the coupled CFD/PBE solver is performed with second order backward differencing scheme because the source term for moments  $\mathbf{m}$  or DQMOM variables  $\boldsymbol{\zeta}$  can be very stiff, causing numerical instability if the source

term is treated explicitly unless very small time steps are used. The time derivative is approximated as:

$$\frac{d\phi}{dt}^{n+1} \approx \frac{3}{2}\phi^{n+1} - 2\phi^n + \frac{1}{2}\phi^{n-1}, \quad (2.34)$$

where the superscript indicates the different time steps.

Let us consider the transport equation for quadrature weight  $i$  in the DQMOM framework:

$$\frac{\partial w_i}{\partial t} + \nabla_{\mathbf{x}} \cdot (\mathbf{U}_p w_i + D \nabla_{\mathbf{x}} w_i) = S_i. \quad (2.35)$$

The same equation holds for each component of the DQMOM vector variable  $\zeta$ .  $S_i$  represent the generic source term that, in the DQMOM formulation, is calculated from the moment source terms with an inversion algorithm. In general  $\mathbf{S}$  depends on all the flow variables. Let us focus on the dependence on the DQMOM variables, such that  $\mathbf{S} = \mathbf{S}(\zeta)$ . When the diffusivity  $D \neq 0$  the source term are corrected to include also spurious diffusion terms to maintain the equivalence between QMOM and DQMOM formulation (see the seminal work of Marchisio and Fox [2005]). After the space discretisation the semi-discrete equations for nodes and weights can be written as a system of ordinary differential equations:

$$\frac{\partial \zeta}{\partial t} + \mathbf{L}(\zeta) = \mathbf{S}(\zeta), \quad (2.36)$$

where the operator  $\mathbf{L}$  is a linear operator that represents the spatial discretisation of advection and diffusion terms. In the implicit method, the first term is approximated by Eq. 2.34 and the operator  $\mathbf{L}$  is calculated at time  $n+1$ . Since the dependence of  $\mathbf{S}$  on  $\zeta$  is highly non-linear, the source term cannot be calculated implicitly. Therefore it is decomposed as follows:

$$\mathbf{S}^{n+1} \approx \mathbf{S}(\zeta^n) + \frac{\partial \mathbf{S}}{\partial \zeta}(\zeta^{n+1} - \zeta^n), \quad (2.37)$$

splitting the source term in an explicit and an implicit part. The DQMOM variables are strongly coupled one to each other but a coupled solver, when the number of nodes and weights become high ( $> 2$ ) is computationally very demanding. Therefore the equations are solved in a decoupled way but, since the source term of a single variable depend on all the others, to ensure the unconditional stability, the maximum eigenvalue,  $\lambda_S$ , of the Jacobian  $|\partial \mathbf{S} / \partial \zeta|$  is calculated and used for all the variables as implicit part of the source term<sup>8</sup>. Each component  $S_i$  of the source term  $\mathbf{S}$  is so rewritten as

$$S_i^{n+1} = \lambda_S \zeta^{n+1} + (1 - \lambda_S) \zeta^n. \quad (2.38)$$

---

<sup>8</sup>When an iterative solver is used, this is equivalent of imposing an adaptive relaxation that makes the system of ODEs unconditionally stable

This decomposition of source terms is essential when dealing with source terms such as complex particle aggregation and breakage kernels or turbulent mixing of different PSDs.

## References

- Ascomp GmbH. *Multi-Fluid Navier-Stokes Solver TransAT User Manual*, 2009.
- P. J. Attar and P. Vedula. Direct quadrature method of moments solution of the fokker-planck equation. *J. Sound Vib.*, 317(1-2):265–272, 2008.
- S. Balachandar and J. K. Eaton. Turbulent dispersed multiphase flow. *Annu. Rev. Fluid Mech.*, 42:111–133, 2010.
- S. Bove. *Computational Fluid Dynamics of Gas-Liquid Flows including Bubble Population Balances*. PhD thesis, Aalborg University Esbjerg, 2005.
- C. Cercignani. *The Boltzmann equation and its applications*. Applied mathematical sciences. Springer-Verlag, 1988.
- C. Crowe, M. Sommerfeld, and Y. Tsuji. *Multiphase flows with droplets and particles*. CRC Press, Boca Raton, Florida, USA, 1998.
- D. A. Drew and S. L. Passman. *Theory of multicomponent fluids*. Springer-Verlag New York, Inc., 1998.
- S. Elghobashi. On predicting particle-laden turbulent flows. *Appl. Sc. Res.*, 52:309–329, 1994.
- S. Elghobashi. An updated classification map of particle-laden turbulent flows. In *IUTAM Symposium on Computational Approaches to Multiphase Flow*, volume 81. Springer, 2006.
- R. Fan, D. L. Marchisio, and R. O. Fox. Application of the direct quadrature method of moments to polydisperse gas-solid fluidized beds. *Powder Technol.*, 139(1):7–20, 2004.
- J. Ferry and S. Balachandar. A fast eulerian method for disperse two-phase flow. *Int. J. Multiphase Flow*, 27(7):1199–1226, 2001.
- J. Ferry, S. L. Rani, and S. Balachandar. A locally implicit improvement of the equilibrium eulerian method. *Int. J. Multiphase Flow*, 29(6):869–891, 2003.
- J. H. Ferziger and M. Peric. *Computational Methods for Fluid Dynamics*. Springer-Verlag, Berlin, third edition, 2002.
- R. Fox. Bivariate direct quadrature method of moments for coagulation and sintering of particle populations. *J. Aerosol Sci.*, 37(11):1562–1580, 2006.
- R. Fox and D. Marchisio. *Multiphase reacting flows: modelling and simulation*. Courses and lectures. Springer, 2007.
- R. O. Fox. *Computational Models for Turbulent Reacting Flows*. Cambridge University Press, Cambridge, 2003.
- R. O. Fox. Large-eddy-simulation tools for multiphase flows. *Annu. Rev. Fluid Mech.*, 44(1), 2012.

---

## REFERENCES

---

- E. Gavi, D. Marchisio, and A. Barresi. Cfd modelling and scale-up of confined impinging jet reactors. *Chem. Eng. Sci.*, 62(8):2228–2241, 2007.
- R. G. Gordon. Error bounds in equilibrium statistical mechanics. *J. Math. Phys.*, 9(5): 655–663, 1968.
- R. Grosch, H. Briesen, W. Marquardt, and M. Wulkow. Generalization and numerical investigation of qmom. *AICHE J.*, 53(1):207–227, 2007.
- J. O. Hinze. *Turbulence*. MacGraw-Hill, New York, USA, 1975.
- C. Hirt and B. Nichols. Volume of fluid (vof) method for the dynamics of free boundaries. *J. Comput. Phys.*, 39(1):201 – 225, 1981.
- M. Ishii. *Thermo-Fluid Dynamic Theory of Two-Phase Flow*. Eyrolles, Paris, France, 1975.
- H. Jakobsen. *Chemical reactor modeling: multiphase reactive flows*. Springer, 2008.
- M. Labois and D. Lakehal. Very-large eddy simulation (v-les) of the flow across a tube bundle. *Nucl. Eng. Des.*, 241(6):2075 – 2085, 2011.
- P. L. Lage. The quadrature method of moments for continuous thermodynamics. *Comput. Chem. Eng.*, 31(7):782–799, 2007.
- C. Laurent, G. Lavergne, and P. Villedieu. Quadrature method of moments for modeling multi-component spray vaporization. *Int. J. Multiphase Flow*, 36(1):51–59, 2010.
- B. P. Leonard. A stable and accurate convective modelling procedure based on quadratic upstream interpolation. *Int. J. Mech. Sci.*, 16:183–308, 1976.
- E. Loth. Numerical approaches for motion of dispersed particles, droplets and bubbles. *Prog. Energy Combust. Sci.*, 26(3):161–223, 2000.
- M. Manninen and V. Taivassalo. *On the mixture model for multiphase flow*. VTT Publications, Espoo, Finland, 1996.
- D. L. Marchisio and R. O. Fox. Solution of population balance equations using the direct quadrature method of moments. *J. Aerosol Sci.*, 36:43–73, 2005.
- D. L. Marchisio, R. D. Vigil, and R. O. Fox. Implementation of the quadrature method of moments in cfd codes for aggregation-breakage problems. *Chem. Eng. Sci.*, 58(15): 3337–3351, 2003.
- M. R. Maxey and J. K. Riley. Equation of motion for a small rigid sphere in a nonuniform flow. *Phys. Fluids*, 26:883–889, 1983.
- L. Mazzei, D. Marchisio, and P. Lettieri. Direct quadrature method of moments for the mixing of inert polydisperse fluidized powders and the role of numerical diffusion. *Ind. Eng. Chem. Res.*, 49(11):5141–5152, 2010.
- L. Mazzei, D. Marchisio, and P. Lettieri. A new quadrature-based moment method for the mixing of inert polydisperse fluidized powders in commercial cfd codes. *AICHE J.*, in press, 2011.
- R. McGraw. Description of aerosol dynamics by the quadrature method of moments. *Aerosol Sci. Technol.*, 27(2):255–265, 1997.
- A. Munjiza. *The combined finite-discrete element method*. Wiley, 2004.

- S. Osher and J. A. Sethian. Fronts propagating with curvature-dependent speed: Algorithms based on hamilton-jacobi formulations. *J. Comput. Phys.*, 79(1):12 – 49, 1988.
- M. Petitti, A. Nasuti, D. L. Marchisio, M. Vanni, G. Baldi, N. Mancini, and F. Podenzani. Bubble size distribution modeling in stirred gas-liquid reactors with qmom augmented by a new correction algorithm. *AICHE J.*, 56(1):36–53, 2010.
- S. Pope. Self-conditioned fields for large-eddy simulations of turbulent flows. *J. Fluid Mech.*, 652:139–169, 2010.
- S. B. Pope. *Turbulent Flows*. Cambridge University Press, Cambridge, 2000.
- V. Raman, H. Pitsch, and R. Fox. Eulerian transported probability density function sub-filter model for large-eddy simulations of turbulent combustion. *Combustion Theory and Modelling*, 10(3):439–458, 2006.
- D. Ramkrishna. *Population balances: theory and applications to particulate systems in engineering*. Chemical, Petrochemical & Process. Academic Press, 2000.
- V. Ranade. *Computational flow modeling for chemical reactor engineering*. Process systems engineering. Academic Press, 2002.
- H. Risken. *The Fokker-Planck equation: methods of solution and applications*. Springer series in synergetics. Springer, 1996.
- P. Sagaut, S. Deck, and M. Terracol. *Multiscale and multiresolution approaches in turbulence*. Imperial College Press, 2006.
- R. S. R. Sidin. *Droplet size distribution in condensing flow*. PhD thesis, University of Twente, Enschede, 2009.
- C. Speziale. Turbulence modeling for time-dependent rans and vles: A review. *AIAA J.*, 36(2):173–184, 1998.
- H. Struchtrup. *Macroscopic transport equations for rarefied gas flow: approximation methods in Kinetic Theory*. Springer (Berlin), 2005.
- S. O. Unverdi and G. Tryggvason. A front-tracking method for viscous, incompressible, multi-fluid flows. *J. Comput. Phys.*, 100(1):25 – 37, 1992.
- R. R. Upadhyay and O. A. Ezekoye. Treatment of design fire uncertainty using quadrature method of moments. *Fire Saf. J.*, 43(2):127–139, 2008.
- L. Wang and R. Fox. Comparison of micromixing models for cfd simulation of nanoparticle formation. *AICHE J.*, 50(9):2217–2232, 2004.
- J. C. Wheeler. Modified moments and gaussian quadratures. *Rocky Mt. J. Math.*, 4: 287–296, 1974.
- F. A. Williams. Spray combustion and atomization. *Phys. Fluids*, 1(6):541–545, 1958.
- C. Yoon and R. McGraw. Representation of generally mixed multivariate aerosols by the quadrature method of moments: Ii. aerosol dynamics. *J. Aerosol Sci.*, 35(5):577–598, 2004a.
- C. Yoon and R. McGraw. Representation of generally mixed multivariate aerosols by the quadrature method of moments: I. statistical foundation. *J. Aerosol Sci.*, 35(5): 561–576, 2004b.

---

*REFERENCES*

- J. Zhu. A low-diffusive and oscillation-free convection scheme. *Commun. Appl. Numer. Methods*, 7(3):225–232, 1991.



# 3

## CFD study of a Confined Impinging Jets Reactor

As it has been reported, the main scope of this work is to develop modelling tools for the simulation of particle formation processes. Since some of these processes are conducted in micro-devices, a thorough study of the flow in these devices is necessary. We are particularly interested in the Confined Impinging Jets Reactor (CIJR), commonly used for precipitation processes of micro- and nano-particles, employed in a variety of applications that include pharmaceuticals, cosmetics, dyes and pesticides. As already mentioned, in this work, with the purpose of gaining a better understanding of the main mixing mechanisms occurring in a CIJR, the flow field was studied at four inlet flow rates ranging from  $Re = 62$  to  $Re = 600$ . These conditions correspond to regimes with incipient turbulence in the chamber. Micro Particle Image Velocimetry ( $\mu$ PIV) experiments and Direct Numerical Simulations (DNS) were performed and results are compared in this chapter. MicroPIV is an innovative experimental technique that allows measurement of the instantaneous velocity fields in microfluidic devices. The coupled numerical-experimental approach was found to be essential in understanding and explaining the flow behaviour and the development of turbulence, in particular with respect to the important effects of the inlet boundary conditions. Oscillations present in the inlet flow of the device are in fact primarily responsible for the chaotic and turbulent effects in the reactor. These results provide insights that are important in the development of appropriate computational models for this type of micro-reactor or mixers.

---

Part of the contents of this chapter has been published in the work of Icardi et al. [2011].

### 3.1 Introduction

Ultra-fine or nano-particles turn out to be very useful in a growing number of applications [Horn and Rieger, 2001, Salata, 2004], in particular in biology and medicine. Many novel processes have been developed in order to produce nanoparticles with the desired properties, namely specific particle size distribution, composition and morphology. For example the process of solvent displacement can be employed to produce polymeric nano-particles carrying an active principle to be used in targeted drug delivery [Johnson and Prud'homme, 2003a, Kipp, 2004, Lince et al., 2008]. In solvent displacement the pharmaceutical active principle and the polymer are dissolved in an organic solvent and then rapidly mixed with an anti-solvent. The faster the overall mixing process occurs, the smaller and the more mono-disperse the particles will be. Moreover, efficient mixing dynamics at all scales will foster the interactions between the pharmaceutic active ingredient and the polymer carrier, preventing further particle growth and, in the case of block-co-polymers, tailoring the particle surface with the desired hydrophilic properties.

The necessity of carrying out processes in controlled conditions of rapid mixing, is the main motivation for the development of innovative mixers. A class of mixers designed to operate in turbulent conditions, characterised by dimensions of the order of millimetres, with multiple inlets and a zone of high turbulent kinetic energy dissipation rate, is currently under development. Examples of this kind of mixer configuration are the T-Mixer [Gradl et al., 2006], the Multi-Inlet Vortex Mixer [Cheng et al., 2009, Liu et al., 2008] and the Confined Impinging Jets Reactor [Gavi et al., 2007b, Johnson and Prud'homme, 2003b].

The objective of this part of the work is to investigate the flow field in a three-dimensional Confined Impinging Jets Reactor (CIJR) with a cylindrical reaction chamber. The CIJR is characterised by two inlets facing each other opening on opposite sides of the reaction chamber. The two inlets are operated at high velocity, therefore they behave as round jets that collide and form an impingement plane where turbulence is developed and the scale of segregation is rapidly reduced. The impingement plane is confined by the mixer head, that at the same time provides a volume in which mixing at the molecular level takes place through diffusion.

Various CIJR geometries and dimensions were studied experimentally by Johnson and Prud'homme [2003b] and their mixing efficiency was evaluated by means of a parallel competitive reactions scheme. Following that work, Liu and Fox [2006] applied Computational Fluid Dynamics (CFD) in order to develop a model able to predict the extent of mixing and reaction in the CIJR and found good agreement with the experimental data. They employed the Reynolds-Averaged Navier-Stokes equations (RANS) approach to model the flow field and the Interaction by Exchange with the Mean (IEM) approach coupled with a presumed Probability Density Function (PDF) method (i.e., the Direct Quadrature Method of Moments, [Marchisio

and Fox, 2005]) to model micro-mixing. Another work [Gavi et al., 2007a] extended the results by considering the effect of the choice of different turbulence models and near wall treatments on the final model predictions, as well as scale up and scale down issues and strategies. The outcome of the latter investigation showed that the choice of the turbulence model and the near wall treatment has a great effect on the final model predictions, and therefore an independent validation of flow and turbulent field is needed.

A useful technique to experimentally investigate the flow field in a CIJR is microscopic Particle Image Velocimetry ( $\mu$ PIV). MicroPIV [Santiago et al., 1998] is a novel experimental technique where instantaneous velocity fields are determined from the displacement of small seed particles. It has been increasingly employed to measure flow fields in planar microfluidic devices (see for example Li et al. [2005] and Van Steijn et al. [2007]). Recently Liu et al. [2009] published data obtained with  $\mu$ PIV for a planar CIJR, the inlet jets of which measure 0.5 mm in width. The experimental flow fields, characterised by a jet Reynolds number between 211 and 1003, were compared with CFD simulation data, obtained with a steady state RANS approach. Though the agreement between experiments and CFD was satisfactory overall, the authors observed that the measured turbulent kinetic energy was larger than CFD predictions, because in the experiments the inlet jets flap significantly at high jet Reynolds number, a phenomenon not predicted by steady state RANS simulations; the authors also suggested that an unsteady model such as Large Eddy Simulation (LES) could be used to improve model predictions.

Many studies exist on free turbulent jets. For example Landreth and Adrian [1990] measured for the first time by means of PIV the instantaneous velocity field of a turbulent circular jet impinging on a plate, thus revealing flow structures and various stages of vortex generation. The same unsteady behaviour for impinging jets that Liu et al. [2008] described for the CIJR was observed also in different geometries investigated in other studies. For example Schwertfirm et al. [2007] investigated by means of PIV the mean flow and turbulent field in a geometry similar to a T-mixer with round inlets and a square chamber section measuring  $80 \times 80$  mm at jet Reynolds number equal to 1270. The experimental measurements were compared to Direct Numerical Simulations (DNS) and, in both experiments and simulations, a flow field symmetry breakage was observed; this demonstrates that it could be a characteristic of the studied mixing device, and not only a product of non-ideal experimental conditions. Santos et al. [2008] investigated by means of PIV an axial-symmetric Reaction Injection Molding (RIM) (with inlet jet diameter 1.5 mm and chamber diameter 10 mm) in the jet Reynolds number range from 100 to 500. The study depicted the flow structures characteristic of RIM, in which the jets impingement creates vortexes, with axes perpendicular to the RIM axis.

Various studies in recent years verified the reliability and accuracy of PIV both by comparison versus analytical solutions or DNS and by comparison versus other

experimental techniques (e.g. Particle Tracking Velocimetry, Laser Doppler Velocimetry)[Feng et al., 2005], therefore PIV is now considered a mature tool for investigating the flow and turbulent fields.

Notwithstanding the proven validity of the measurement technique, its application on a small and complex geometry such as that of the CIJR is a novelty and presents many challenges. The CIJR complexity derives from its very small dimensions and from the combined effect that the walls and the impinging jets have on the flow field. In fact to our knowledge the experimental data used in this chapter are the very first of this type since there is no other published study reporting data obtained with  $\mu$ PIV on a three-dimensional CIJR. As already reported, there are many challenges in the present investigation. Firstly the precise fabrication of such a small device as a micro mixer is complex and requires specific precision machinery. Secondly, the cylindrical shape of the device and the curved walls of the mixing chamber cause laser light refraction at the interface between the wall and the fluid, a phenomenon that can be alleviated by modifying the fluid refraction index to match the walls material. Thirdly, the control over pumps flow delivery is very difficult to obtain: in particular, it is complicated to obtain equal and perfectly constant flow rates at the two inlets. Finally in  $\mu$ PIV unsteady and highly irregular turbulent flow fields are much more difficult to measure than steady flows. In steady flows accurate data can be obtained by combining the results from many instantaneous images using the sum of correlations technique [Wereley et al., 2002] but in unsteady or turbulent flow field the flow field must be sufficiently seeded so each pair of  $\mu$ PIV images yields an accurate instantaneous velocity field [Liu et al., 2009].

All these issues are addressed here by combining the experimental flow field analysis in a CIJR carried out by means of  $\mu$ PIV in a previous work [Gavi, 2009] with DNS. Nowadays in fact numerical techniques have reached a strong reliability and in particular DNS can be thought as virtual experiments since no approximations are employed when solving the governing continuity and Navier-Stokes equations (under the continuum hypothesis). Of course when working with the DNS the grid has to be fine enough to capture all the length and time-scales involved. Therefore DNS can be used also to explain the uncertainty of experimental results underlying effects related to non-ideal experimental setup. This coupled approach reveals to be essential when dealing with the already cited difficulties of  $\mu$ PIV for CIJR investigations.

The chapter is organised as follows: in the next two sections the experimental and numerical set up, respectively, are presented. The description of the operating conditions investigated in this work follows. The results are finally presented: the flow field is described, focusing on its evolution with the flow regime and fluctuations and spatial correlations are computed and commented. Eventually the main conclusions of the study are summarised.

## 3.2 Experimental apparatus and $\mu$ PIV setup

The geometry of the reactor employed in  $\mu$ PIV experiments is shown in Fig. 3.1. As can be seen, it is characterised by a cylindrical chamber with a conical head and bottom forming an angle of  $45^\circ$  with the reactor axis. An optically transparent test section was used in the experiments with two inlet pipes that had a diameter  $d_j = 1 \text{ mm}$ , a length of 10 diameters and are connected to the pumping system with flexible tubes of the same diameter. The diameters of the chamber and the outlet pipe measure  $D = 4.8 d_j$  and  $\delta = 2 d_j$  respectively. The chamber height is equal to  $H = 2 D$ . The coordinate system for the experiments is defined such that the  $x$ -axis coincides with the jets axis, while the  $y$ -axis coincides with the chamber axis and the origin is centred at the intersection of the two inlet jets.

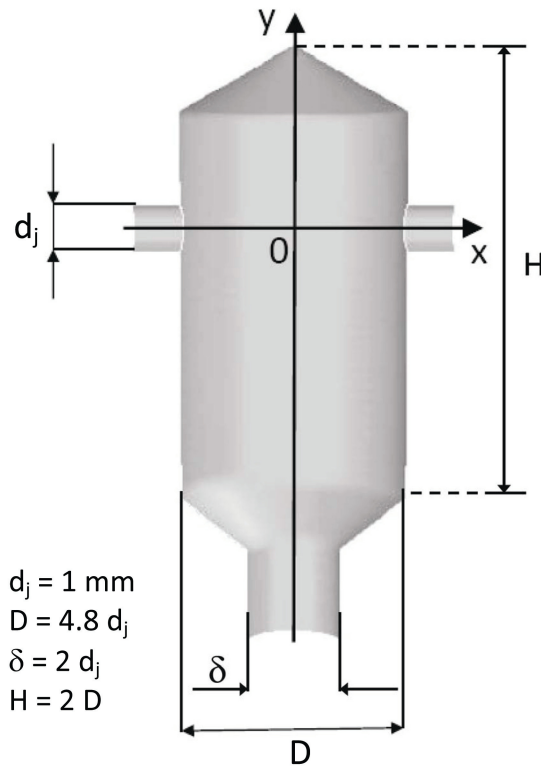


Figure 3.1: Sketch of the Confined Impinging Jets Reactor (CIJR) geometry.

Although these experiments were performed in another work, it is useful to remind the main conditions and operating parameters. The experiments were performed for jet Reynolds number ranging from 62 to 600. The jet Reynolds number is defined by the density of the fluid  $\rho_f$ , the viscosity of the fluid  $\mu_f$ , the mean velocity

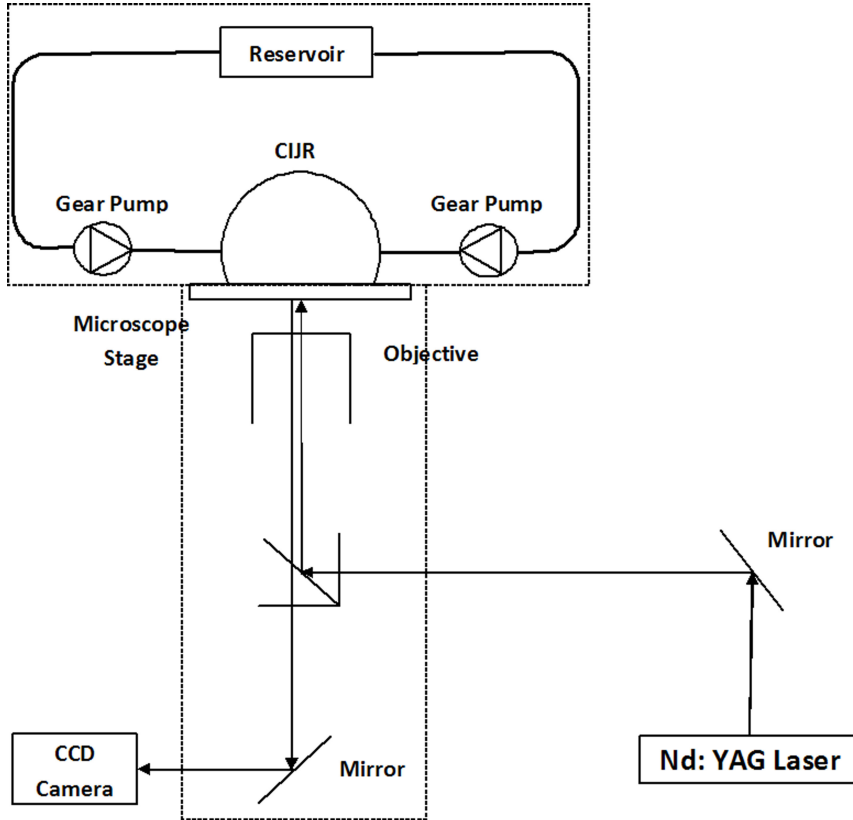


Figure 3.2: Experimental set up for  $\mu$ PIV experiments.

in the inlet pipes  $u_j$ , and the inlet pipes diameter  $d_j$  as

$$\text{Re} = \frac{u_j d_j \rho_f}{\mu_f}. \quad (3.1)$$

The experimental setup is constituted by the flow delivery facility and by the elements composing the  $\mu$ PIV apparatus, as shown in Fig. 3.2. The fluid is delivered to the test section by two micro gear pumps and pump heads (115 VAC console digital dispensing drive and 0.092 ml/rev suction shoe gear pump head, Cole Parmer Instrument Co., Vernon Hills, IL), each feeding one of the reactor inlets through pipes approximately 50 cm long with the same diameter of the reactor inlets. A reservoir of 150 ml was connected to the flow delivery system with flexible tubing. The plane surface of the test section was placed on the stage of the inverted biological microscope (Nikon, model T-300 Inverted Microscope). The light beam from the double pulsed laser passes through an optical attenuator to reduce the laser energy per pulse, the maximum energy of which is 120 mJ/pulse, and is then directed to an aperture in the back of the microscope. The laser apparatus (New Wave

Research Gemini Nd:YAG PIV laser) emits two independent 532 nm light pulses at a frequency of 4 Hz per pulse pair. Two sequential images are recorded by a CCD camera (LaVision Flowmaster 3 camera, LaVision Inc., Ypsilanti, MI). Images are analysed by the software Davis 6 (LaVision Inc., Ypsilanti, MI) with a cross correlation technique that yields the instantaneous velocity vector field [Prasad, 2000].

Since the reactor walls are round, there is a problem of refraction of the laser light at the interface between the fluid and the reactor walls that can be overcome by matching the refractive index of the fluid with that of the Plexiglas ( $RI = 1.49$ ). The option of using a sodium iodide aqueous solution was discarded because of the resulting high ionic strength, that leads to extensive aggregation of the polymer micro-particles with which the fluid is seeded. An aqueous solution of urea was chosen instead, characterised by a density of  $\rho_f = 1.14115 \text{ g/cm}^3$  and a viscosity of  $\mu_f = 1.914 \text{ cPs}$  computed by using the equations reported in Kawahara and Tanford [1966]. The refractive index of the solution was calculated by extrapolating from experimental data at 20 °C taken at wave-length of 589 nm by applying a linear correlation, that is valid for concentration of urea higher than 2.5 M [Warren and Gordon, 1966]. An urea solution of 9.38 M resulted in a refractive index of 1.41.

The flow was seeded with fluorescent melamine particles (fluorescent dye rhodamine B: excitation 540 nm; emission 625 nm) characterised by a nominal diameter of 2  $\mu\text{m}$  and density  $\rho_p = 1.51 \text{ g/cm}^3$  (G. Kisker GbR, Steinfurt, Germany). These particles have been chosen instead of more common polystyrene micro-particles because of their higher density, lower tendency to aggregation and higher emissivity. By computing the particle Stokes number  $St$  the ratio of particle response time to the flow time-scale can be quantified:

$$St = \frac{\gamma \rho_p d_p^2}{12 \mu_f}, \quad (3.2)$$

where  $\gamma$  is a characteristic rate of strain for the flow and can be approximated as  $\gamma = 2u_j/D$ . For the range of Re here considered  $St$  is approximately  $3 \times 10^{-4}$ , therefore it is ensured that particles accurately follow the flow [Samimy and Lele, 1991].

The seeding concentration was optimised by investigating one of the reactor inlets operating at low flow rate (i.e.,  $u_j = 0.105 \text{ m/s}$ ,  $Re = 62$ ). A range of different seeding concentrations was tested and for each one the root mean square of the velocity was compared to the mean velocity in the inlet, in order to minimise the noise in the measurements. The timing between laser pulses was set such that particles moved approximately one fourth of an interrogation spot between pulses.

Differently from what happens in PIV, where only a thin slice of the flow field is illuminated with a laser sheet, in  $\mu$ PIV the entire volume must be illuminated

because of the small length-scales involved. There are two consequences related to this configuration. The first one is that the diameter and intensity of a particle image are dependent on the distance from the object plane. The second one is that those particles distant from the object plane form a background glow that makes it difficult to see the near-focus particles [Olsen and Adrian, 2000a]. Since particles are flood illuminated in  $\mu$ PIV, rather than illuminated by a laser sheet as in traditional PIV, in  $\mu$ PIV the measurement volume depth (termed *depth of correlation* [Olsen and Adrian, 2000a]) depends on primarily the optics of the system [Olsen and Adrian, 2000a], but also on Brownian motion [Olsen and Adrian, 2000b], on out-of-plane motion [Olsen and Bourdon, 2003], and even on fluid shear [Olsen, 2009]. In the present experiments the depth of correlation can be calculated as [Olsen and Adrian, 2000a]

$$2Z_{corr} = 2 \left[ \frac{1 - \sqrt{\varepsilon}}{\sqrt{\varepsilon}} \left( f^2 d_p^2 + \frac{5.95(M+1)^2 \lambda^2 f^4}{M^2} \right) \right]^{1/2}. \quad (3.3)$$

In the above equation  $\varepsilon = 0.01$ ,  $M$  is the magnification,  $\lambda$  is the wavelength of fluorescence emitted by the particles,  $f$  is the focal number of the lens and can be related to the numerical aperture (NA) by the following

$$f = \frac{1}{2NA}. \quad (3.4)$$

In the present experiments, a  $4 \times 0.2$  NA objective was used with a  $0.45 \times$  coupler, yielding a depth of correlation of  $47 \mu\text{m}$ .

A multi-pass interrogation scheme with decreasingly smaller window sizes and a 50 % overlap between adjacent interrogation spots was used with a final interrogation spot size measuring  $16 \times 16$  pixels. The post-processing performed on the vector field consisted in the removal of “bad” vectors (i.e. too different from their neighbours average) that are replaced with interpolated values. Readers interested in the details of the “bad” vector removal process are referred to the specialised literature [Prasad, 2000]. The final spatial resolution was  $140 \mu\text{m}$  in both the  $x$ - and  $y$ -directions.

### 3.3 Direct Numerical Simulations and numerical details

The flow field in the CIJR is simulated by directly solving the continuity and Navier-Stokes equations for an incompressible fluid in three dimensions:

$$\nabla \cdot \mathbf{U} = 0, \quad (3.5)$$

$$\frac{\partial \mathbf{U}}{\partial t} + \mathbf{U} \cdot \nabla \mathbf{U} = -\frac{1}{\rho_f} \nabla p + \nu_f \Delta \mathbf{U}, \quad (3.6)$$

where  $\nu_f$  is the kinematic fluid viscosity. When DNS is employed the governing equations are solved without any model. Therefore, if the grid is fine enough and the numerical discretisation scheme is accurate enough, the flow is described in detail by resolving all the time and length-scales involved in the turbulent flow. In this respect, fully resolved DNS are virtual experiments that can be used to understand and interpret experimental data.

Computations are carried out with the commercial Computational Multi-Fluid Dynamics (CMFD) code *TransAT* [Ascomp GmbH, 2009]. The equations are solved with a finite volume approximation, where the pressure-velocity coupling is performed by using the SIMPLEC algorithm. Time discretisation is performed with a 2<sup>nd</sup> order implicit scheme or with a 3<sup>rd</sup> order explicit Runge-Kutta scheme. The advective terms are discretised with both the classical QUICK scheme and the HLPA scheme [Zhu, 1991], which combines a second-order upstream-weighted approximation with the first-order upwind differencing under the control of a convection boundedness criterion. Although HLPA is not the most common scheme for DNS, it assures a better convergence and stability, especially in the initial transitory part of the simulations. The simulations were performed also with the QUICK scheme and the CDS and they revealed no significant differences. Solid boundaries of the reactor are represented with the Immersed Surface Technique (IST) in which the cells near the walls are marked using a signed distance function (known as the solid level-set function) and treated in a separate way to impose no-slip condition there. By employing this technique the walls can be immersed in a Cartesian grid, which results in a reduced meshing time and a higher accuracy of the numerical schemes, since the numerical viscosity due to grid-skewness is simply eliminated [Ferziger and Peric, 2002]. These two elements make the IST approach very useful to simulate unsteady turbulent flows with DNS in complex geometries. More details about IST are explained in Chap. 5.

Grid	Cells per block	Blocks	Internal cells	$\Delta x, \mu\text{m}$	Parallel
1	40x40x80	1	$1 \times 10^5$	100-140	O-MP
2	68x60x128	1	$3.5 \times 10^5$	50-80	O-MP
3	100x84x150	1	$8.5 \times 10^5$	30-60	O-MP
4	46x42x34	36	$8 \times 10^5$	50-60	MPI
5	82x52x66	36	$8 \times 10^6$	17-25	MPI

Table 3.1: Computational grids used for simulations: grid number, number of cells per block, number of blocks, number of internal cells used for computing the flow, cells size and parallelization library

Five different grids were prepared to optimise the computing time and ensure that for each investigated case all the scales were resolved. Details about the grids

(within the IST context) are reported in Table 3.1. After a dimensional analysis, explained in the next section, and the comparison of results obtained with different grids for a test case, it was found that grid 2 was able to capture all the relevant length-scales for the two lowest flow rates, while for the two highest flow rates a more refined grid must be used. In this case grid 3 was found to be fine enough since the local ratio between the mean cell size and the approximated minimum length-scale of the flow is always between 0.5 and 2. The details about the estimation of the minimum length-scale of the flow are reported in the next section. Simulations were performed on a Linux cluster ( $10 \times 8$  CPUs AMD Opteron, 2.44 GHz) with either a shared or a distributed memory parallelism. The former was used with single-block grids (Open-MP library) and the latter with multi-block grids (MPI library). Using eight processors with shared memory and a speed-up factor of about 3.5, the total CPU time needed to simulate 1 s of real time with grid 2 was found to be between one and four days depending on the flow regime which influence the convergence and the simulation time step.

### 3.4 Operating conditions investigated and boundary conditions

The flow field was measured and simulated for four inlet jet Reynolds numbers ( $\text{Re}$ ): 62, 150, 310 and 600, corresponding to actual average inlet velocities ( $u_j$ ) of 0.105, 0.250, 0.520, 1.01 m/s. For all the four cases the flow in the inlet pipes is laminar, however inside the chamber a transition occurs; the impingement in fact, creates strong instabilities and drive the flow towards turbulence. In Table 3.2 the operating conditions are summarised reporting for each flow rate the mean inlet velocity, the mean residence time in the CIJR, the inlet jet Reynolds number and the approximated Kolmogorov micro-scale.

FR, mL/min	Mean inlet velocity, m/s	$\tau_R$ , s	Re	$\lambda_K$ , $\mu\text{m}$
10	0.105	1.05	62	-
20	0.25	0.44	150	-
40	0.52	0.21	310	-
90	1.01	0.11	600	$\geq 17$

Table 3.2: Nominal flow rates, mean velocities, mean residence times, jet Reynolds numbers and estimated Kolmogorov micro-scale lengths.

The estimation of this length-scale is a very challenging issue since the flow under study may be not under fully developed turbulence and the statistical theory of turbulence is not guaranteed to be valid here. Nevertheless this is a crucial point

to make sure that a DNS simulation is actually resolving all the time and length-scales involved. As it is well known, for high Reynolds number flows it is possible to estimate the Kolmogorov length as  $\lambda_K = \left(\frac{\epsilon}{\nu_f}\right)^{1/4}$ , where  $\epsilon$  is the dissipation rate of turbulent kinetic energy. The turbulent kinetic energy can be measured from experiments or calculated by solving an appropriate transport equation, while its dissipation rate can be estimated with a mixing length hypothesis or by solving another transport equation. This is the standard procedure of many RANS models. For the flow under study it is reasonable to apply these concepts, at least for the highest flow rate studied, corresponding to  $Re = 600$ . In particular, the results of the work of Hosseinalipour and Mujumdar [1995] in which different RANS models were compared for impinging opposing jets in a flow regime very similar to this study, show that the Abe-Kondoh-Nagano Low-Reynolds number model [Abe et al., 1994] is able to describe accurately opposing impinging jets flow. This model, in fact, was found to be the most appropriate for this type of flows and resulted in an estimation of the maximum turbulent energy dissipation rate localised in two zones on the inlet axis, 1 mm far from the centre. With these values an estimated Kolmogorov length of  $\lambda_K = 17 \mu\text{m}$  for the case of  $Re = 600$  was obtained (after reaching a grid independent solution). As already mentioned, this estimation can be applied only for the highest flow rate but we can suppose that, for lower flow rates, the minimum length-scale could not be smaller. Of course the flow condition in the CIJR under study are not “ideal” but this is still a reasonable lower limit approximation. Simulations with other RANS models in fact gives a similar or even higher estimation of this length-scale. Based on these additional arguments it is possible to conclude that the grids adopted in this DNS study are adequate

In the experiments, the objective was focused on the plane passing through the jets and the chamber axes. Before taking images, some time was allowed for the flow to reach a steady state. The inlet flow rate was adjusted from the pumps in order to obtain the balancing of the jets. For each jet Reynolds number 1000 realisations were captured and analysed. The  $\mu\text{PIV}$  images formed using the  $4\times$  objective and the  $0.45\times$  coupling cover an area of approximately  $4.6 \times 3.68 \text{ mm}^2$ , however the measured area does not cover the entire width of the reactor, but is limited to an area  $4.0 \times 2.5 \text{ mm}^2$  due to the cylindrical shape of the device, that causes the shading region near the wall and an uneven illumination that favours the measurement in the central region of the interrogation window. The images are centred at the intersection between the jets and chamber axes.

Experimental results and DNS predictions were compared in the same window captured by  $\mu\text{PIV}$  and a numerical filter equivalent to the experimental one was developed to spatially smooth data coming from the simulations, which are finer than  $\mu\text{PIV}$  resolution for all the grids. In fact, comparing the  $\mu\text{PIV}$  resolution with the size of the computational cells, one finds that simulations are characterised by

a better resolution of smallest scales. This does not affect much the comparison of first order statistics (i.e., mean velocities) but can in principle compromise the comparison of second order statistics (i.e., velocity fluctuations). In this case however it was found that the filtering operation simply reduce the mean oscillations of a small percentage (less than 5 %) so only the unfiltered results are shown.

Simulations data were saved and analysed for each time step (calculated adaptively according to stability criteria based on Courant—Friedrichs—Lewy and diffusion conditions [Ferziger and Peric, 2002]) after the transient in a time window of length equivalent to three residence times for the two lowest flow rates and six residence times for the highest ones. MicroPIV results instead are recorded with a time step of a quarter of second for a total experimental time of 250 s. It resulted that the time steps used for numerical simulations is often more than a thousand times smaller than the experimental one. Also the total time of analysis is very different. This complicates the comparison between experiments and simulations since only the latter ones can give a complete description of the transient development of the flow. MicroPIV can instead be used to image instantaneous velocity fields and to calculate statistics which are needed for the simulations setup.

Contrary to what happens with RANS, when employing DNS or LES, the results are very sensitive to boundary conditions and the proper selection of inflow boundary conditions becomes crucial. In fact, no time averaging is performed and the system is highly sensitive to the instantaneous jets behaviour. For this reason the  $\mu$ PIV data in the inlets were analysed revealing small variations in time which could not be related to natural instabilities in the system or to turbulence in the chamber. They are instead related to the pumps feeding the solution to the CIJR. Therefore to clarify the effect of the experimental inflows two types of simulations were performed with different boundary conditions.

First a set of simulations were performed with constant laminar inflow profiles:

$$\mathbf{U}(\mathbf{x}) = \begin{pmatrix} U_x|_{inlet} \\ U_y|_{inlet} \\ U_z|_{inlet} \end{pmatrix} = \begin{pmatrix} U_0(\mathbf{x}) \\ 0 \\ 0 \end{pmatrix} \quad (3.7)$$

where  $U_0(\mathbf{x})$  is the constant parabolic profile in the tubes which depends on the wall distance, then the inflows were approximated as follows:

$$\mathbf{U}(\mathbf{x}) = \begin{pmatrix} U_x|_{inlet} \\ U_y|_{inlet} \\ U_z|_{inlet} \end{pmatrix} = \begin{pmatrix} U_0(\mathbf{x}) [1 + K \cos(t\omega + \phi)] \\ 0 \\ 0 \end{pmatrix} \quad (3.8)$$

by superposing to the constant profile a single harmonic with amplitude  $K$  (ranging between zero and 0.2), and frequency  $\omega$  ( $\approx 10 \frac{u_j}{D}$ ) chosen according to experimental data. To emphasise the effects of these oscillations the phase lag between the two

inlets was set to  $\frac{\pi}{2}$  in order to result in phase opposition. Since the time interval between the experimental measurements of the inlets is relatively large and of the same order of magnitude of the total simulations time ( $\Delta t_{\mu PIV} = 0.25$  s), an exhaustive analysis of the inflow time series is not possible especially when the flow rate is high and the inflows are more unsteady. For this reason the calculation of the boundary conditions parameters was carried out for the two lowest flow rates, analysing the time spectra, and only estimated for the two highest ones. Due to this lack of data in time and to the strong feedback (for high flow rates) of the internal flow to the velocity measured at the inlet, it was not possible to investigate in more depth the experimental inflows, recovering for example more frequencies or imposing exactly the velocity measured by experiments. However, the assumption of a single frequency can be physically explained by an oscillation due to the mechanical features of the whole pumping system and it was found to be sufficient to catch the observed behaviour.

## 3.5 Results and discussion

The cylindrical geometry of the reactor creates a three-dimensional flow field which is reproduced also in the simulations. MicroPIV measurements were obtained the  $xy$ -plane with  $z = 0$  therefore all the results are analysed in this plane. However the  $z$ -component of the flow has a strong influence on the development of turbulence, as it can be seen in the results and which would be completely neglected if a planar reactor or bi-dimensional simulations were considered instead.

The flow field is first discussed qualitatively by analysing snapshots of the instantaneous and the mean flow field measured with  $\mu$ PIV to show the main feature and structures of the flow. MicroPIV asymmetry is then underlined looking at the mean  $x$ -velocity ( $U_x^{MEAN}$ ) along  $y$ -direction at the two inlets and in the centre of the reactor. After this overview of the experiments a detailed comparison between  $\mu$ PIV and simulations in terms of first (i.e., mean velocity,  $U^{MEAN}$ ) and second order statistics (i.e., root-mean-square, RMS, of velocity fluctuations,  $U'^{RMS}$ ) is presented. In particular  $x$ -velocity ( $U_x$ ) and  $y$ -velocity ( $U_y$ ) statistics are represented respectively along the  $x$  and  $y$ -axis. Finally a more detailed analysis of the turbulence inside the reactor is carried out with spatial correlations and time spectra of velocity fluctuations. Spatial correlations are normalised as follows [Olsen and Dutton, 2002]:

$$R_{ij}(\mathbf{r}) = \frac{\langle U'_i(\mathbf{x})U'_j(\mathbf{x} + \mathbf{r}) \rangle}{\sqrt{\langle U_i'^2(\mathbf{x}) \rangle \langle U_j'^2(\mathbf{x}) \rangle}} = \frac{\langle U'_i(\mathbf{x})U'_j(\mathbf{x} + \mathbf{r}) \rangle}{U_i'^{RMS}(\mathbf{x})U_j'^{RMS}(\mathbf{x})}. \quad (3.9)$$

where the brackets represent the averaging operator,  $i$  and  $j$  represent the indexes of two spatial coordinates,  $\mathbf{x} = (x, y)$  are the coordinates of the basis point and  $\mathbf{r} = (r_x, r_y)$  are the coordinates of the displacements from the basis point. The

stagnation point was chosen as base point. While in the simulations it coincides with the centre of the reactor and the axis origin, in the experiments it is slightly off the centre in the positive  $x$ -direction. Spatial correlations will be discussed here only for the highest flow rate investigated (i.e.,  $Re = 600$ ).

### 3.5.1 Experimental instantaneous flow field

The time evolution of the flow field in the CIJR at the different jets Reynolds numbers investigated is here described in terms of the experimental instantaneous velocity vector fields. For brevity only snapshots for  $Re = 310$  and 600 are here reported, as the chaotic and turbulent behaviour of the flow field in these conditions is of higher interest for the present study.

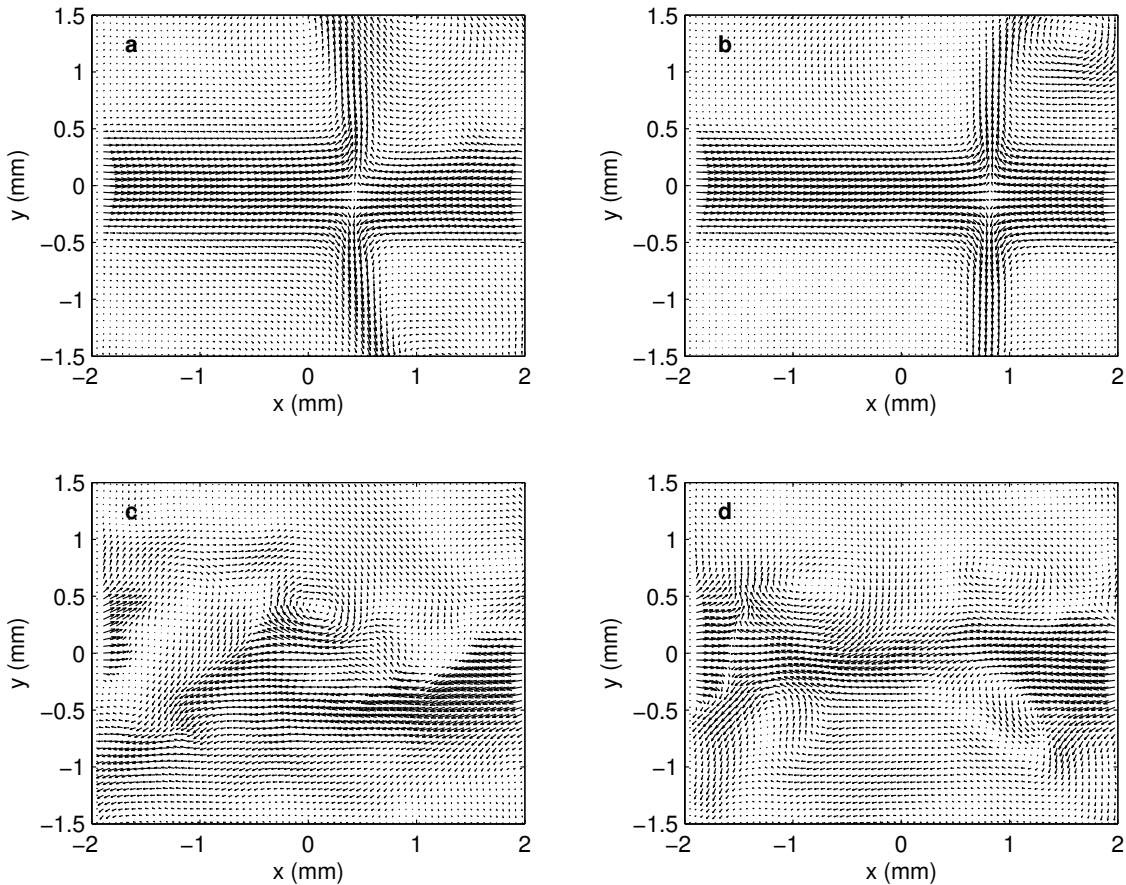


Figure 3.3: Four successive instantaneous vector fields obtained with  $\mu$ PIV for  $Re = 310$ .

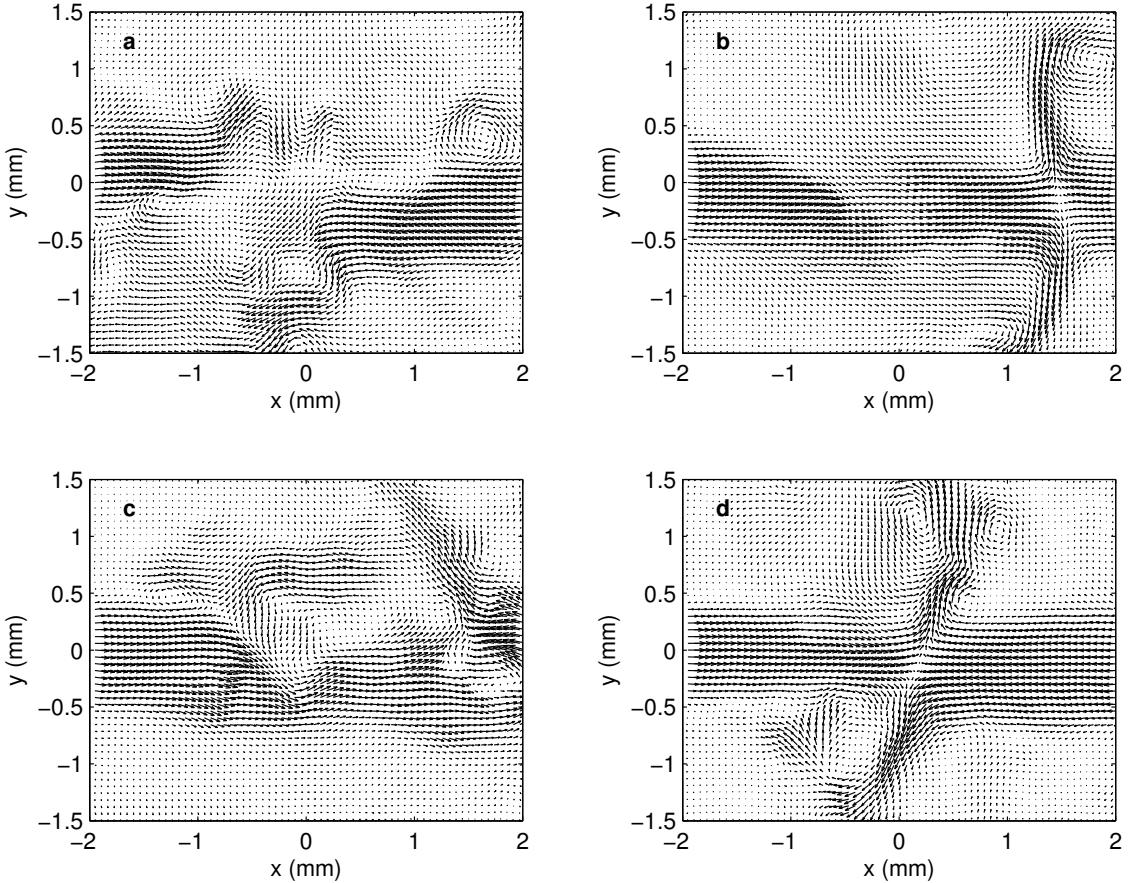


Figure 3.4: Four successive instantaneous vector fields obtained with  $\mu$ PIV for  $Re = 600$ .

For the lowest Reynolds numbers ( $Re = 62$ ) in fact, the instantaneous flow field is almost stationary, except in the centre of the chamber where a continuous but relatively slow motion of the impingement plane is detected without the creation of complicated sub-structures. In these cases, the flow field is well represented by the mean velocity discussed in the next section (see Fig. 3.5). For  $Re = 62$  the instantaneous vector fields show that the flow regime is laminar but unsteady, since the stable impingement plane oscillates from one side to the other of the chamber. At  $Re = 150$  the flow regime is still laminar, however its unsteadiness is more pronounced, because of the higher momentum belonging to the jets that causes stronger interactions between the fluid and the walls. Large eddies that interact with the incoming jet streams are created, occasionally causing the temporary disappearance of the impinging plane.

The flow begins to have a chaotic behaviour at  $Re = 310$ . Four successive snapshots for this case are shown in Fig. 3.3. The impingement plane shifts more often and more extensively and is periodically broken in many smaller eddies. Finally, as clearly evident in the four consecutive snapshots of the vector field represented in Fig. 3.4 for  $Re = 600$ , the flow is fully chaotic, the impingement plane is rarely imaged in the chamber centre, whereas in most images it is replaced by many small eddies that interact with the incoming jets streams, promoting mixing of the two feed streams. The frames reported are not correlated in time, as the 0.25 s interval between successive  $\mu$ PIV vector fields is far to capture the unsteady behaviour of the impingement zone. Their purpose is to qualitatively show the main features of the flow at increasing flow rates. For quantitative comparisons, in the next sections numerical data have been used.

### 3.5.2 Mean velocity field

In Fig. 3.5 the mean flow field measured by  $\mu$ PIV is shown for the four jet Reynolds numbers considered. For all these four conditions the jets entering from the sides of the window are clearly visible. They collide in the centre of the chamber, where the  $x$ -momentum becomes null and the flow is deviated radially in the  $y$ - and  $z$ -directions (as already said the  $z$ -direction is not visible because the  $\mu$ PIV images are purely two-dimensional). The point of collision of the jets is slightly off the centre for  $Re = 600$ , because of the great difficulty in exactly balancing the jets with the gear pumps. Unfortunately this difficulty increases as the unsteadiness and turbulence of the flow field increases. This asymmetry between the jets was also taken into account in some of the simulations by a very small difference in the mean velocity of the two jets. However in all cases, it was verified that this unbalance was smaller than 5 %.

The profiles of the  $x$ -component of the mean velocity ( $U_x^{MEAN}$ ) measured by means of  $\mu$ PIV are shown in Fig. 3.6 on three different  $x$ -planes, for  $x = -2, 2$  and 0 mm and for the four  $Re$  considered. The analysis of these data is very important because it allows the assessment of the overall accuracy of the  $\mu$ PIV approach. For the three lowest  $Re$  the  $x$ -component velocities at  $x = \pm 2$  mm are almost identical with a mismatch smaller than about 0.08–0.05 m/s, resulting in velocities for  $x = 0$  close to zero. For  $Re = 600$  instead the difference between the jets is slightly bigger causing the misalignment of the collision point.

Let us now focus on the comparison between  $\mu$ PIV experiments and DNS simulations. In Fig. 3.7 the mean velocity in the  $x$ -direction ( $U_x^{MEAN}$ ) along the jets axis normalised with respect to the maximum velocity is reported. The open symbols refer to the experimental data, the continuous line to the DNS with constant inflows (see Eq. 3.7) and the dashed line to the DNS predictions with the unsteady boundary conditions (see Eq. 3.8). The amplitude of the oscillations  $K$  is taken

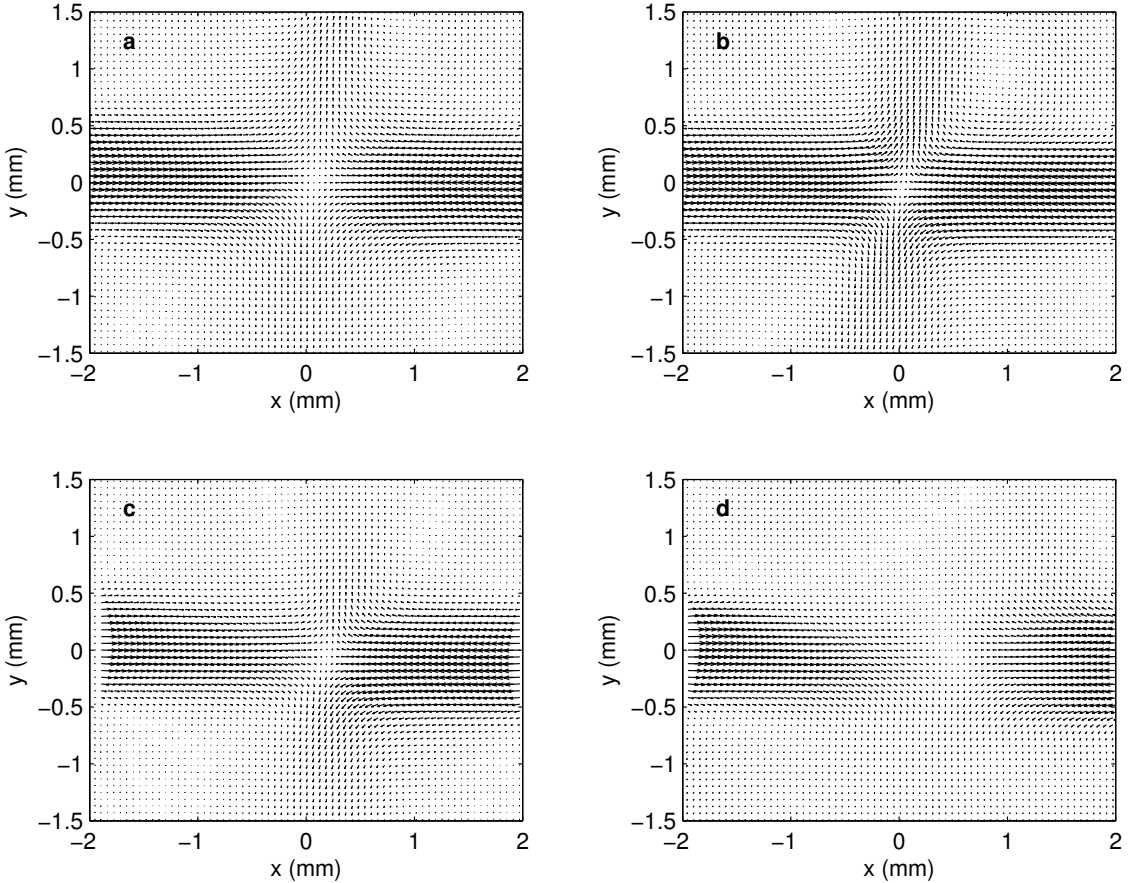


Figure 3.5: Mean velocity fields measured by  $\mu$ PIV for (a)  $Re = 62$ , (b)  $Re = 150$ , (c)  $Re = 310$ , (d)  $Re = 600$ .

here equal to  $\frac{1}{10}$ , namely the value that best approximates the experimental inlet. The data are reported for the  $x$ -coordinate ranging from  $-2$  mm to  $2$  mm, covering therefore almost the entire chamber diameter. As it is possible to see, the left and right boundaries of the plot represent the inlet jets that enter the reactor with opposite velocities and then collide in the middle. The comparison between DNS and experiments highlights that the use of unsteady inlet velocities is very important to predict experimental results, as the structure of the impingement is completely changed especially at high flow rates.

These results are particularly interesting when compared with the work of Gavi et al. [2010], where a subset of these data were used to validate RANS predictions. In that case constant and laminar inflows were adopted, resulting in satisfactory agreement, proving once again that the importance of accurate unsteady boundary conditions applies mainly to DNS. The same conclusions can be drawn also from the

comparison of the mean velocities in the  $y$ -direction ( $U_y^{MEAN}$ ) along the chamber axis, reported in Fig. 3.8. Also for these quantities, the unsteady inflows strongly influence the predictions resulting in a good agreement with experimental data. The analysis of these two velocity components in other areas of the reactor confirms these conclusions and support our hypothesis that the small instabilities related to the two inlets have a strong influence on the final flow field.

### 3.5.3 Velocity fluctuations

As a first example of second order statistics, RMS of velocity fluctuations in the  $x$ -direction ( $U_x^{RMS}$ ) along the jet axis are presented in Fig. 3.9. Also in this case  $\mu$ PIV experiments (symbols) are compared with DNS predictions with constant (continuous line) and unsteady inflows (dashed line). As it can be observed, with unsteady inflows the velocity fluctuation intensity is predicted reasonably well, while constant inflows strongly underestimate it. In particular, for the lowest flow rates, DNS with steady inflows predicts a steady laminar flow field without fluctuations in disagreement with the experiments. Also looking at the longitudinal fluctuations along the chamber axis reported in Fig. 3.10, the same consideration holds.

As a general comment it is possible to state that, especially for high flow rates, the oscillations are slightly over-predicted. This can be due to different reasons. As already reported different spatial resolutions were used in  $\mu$ PIV experiments and simulations. In fact,  $\mu$ PIV has a lower resolution and it may not capture small scales that are instead included in the numerical results. However, when the spatial filter was activated to reproduce the micro PIV resolution a small and not relevant improvement was observed. Most likely this small overestimation could be caused by the approximation of the inflow boundary conditions with a single oscillating frequency with the assumption of phase opposition.

### 3.5.4 Spatial correlations

Spatial correlations were calculated from experiments and simulations according to Eq. 3.9 in order to further investigate some specific features of the flow field in the CIJR. However, as previously mentioned, the most interesting results are observed at the highest jets Reynolds number investigated in this work and therefore the results discussed in this section are limited to  $Re = 600$ .

In Fig. 3.11  $R_{xx}$ ,  $R_{yy}$  and  $R_{xy}$  are shown both for  $\mu$ PIV experiments (left) and DNS (right).  $R_{xx}$  (top) presents a small area of high correlation around the base point, and the correlation is non-zero and positive in a wide area that contains the jet streams. This shape is confirmed by the results reported in Fig. 3.5(d). In fact, as can be seen due to the jets presence the  $x$ -component of velocity changes slowly along the jets axis, causing the correlation  $R_{xx}$  to remain high over long distances

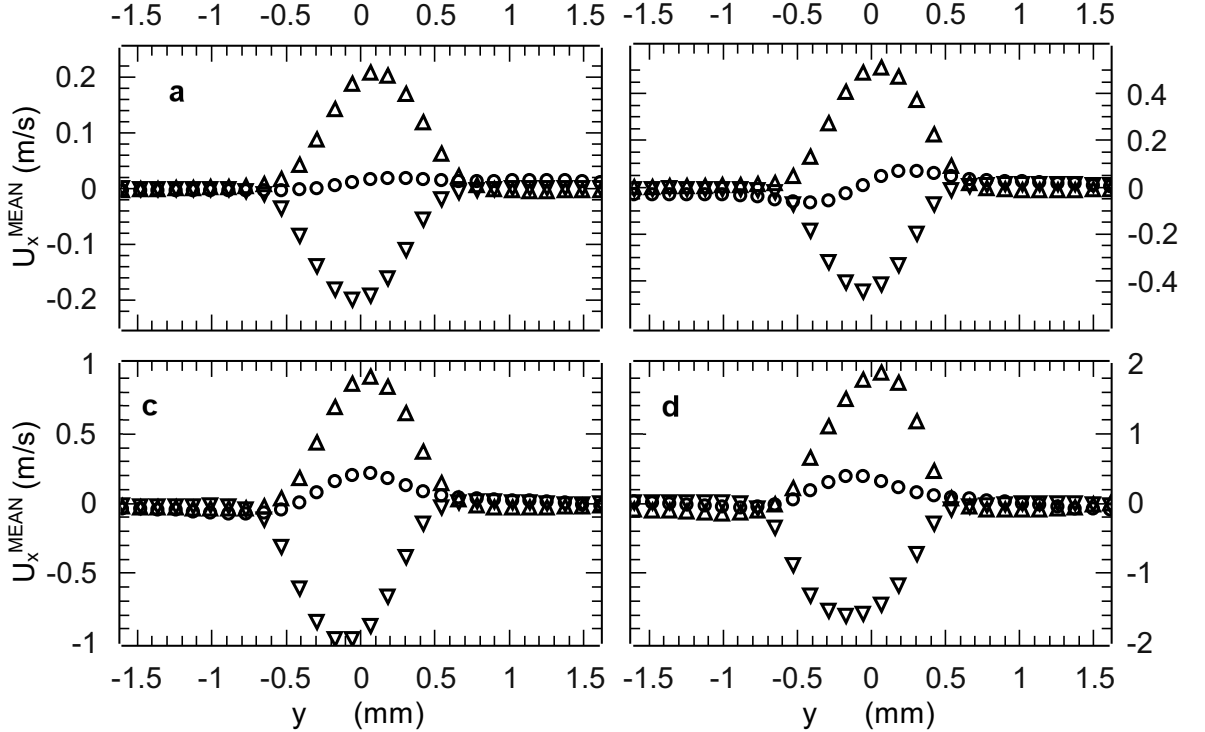


Figure 3.6: Profiles of the  $x$ -component of the mean velocity measured by  $\mu$ PIV at  $x = 0$  mm ( $\circ$ ),  $-2$  mm ( $\triangle$ ),  $2$  mm ( $\nabla$ ) for (a)  $Re = 62$ , (b)  $Re = 150$ , (c)  $Re = 310$ , (d)  $Re = 600$ .

in the  $x$ -direction. In  $\mu$ PIV measurements the correlation decrease faster along the jet axis with respect to simulations. This small difference can be explained again with the approximation of inflow conditions with a single frequency and with the different numbers and lengths of time steps. The correlation  $R_{yy}$  for both experiments and simulations is a plume centred at the base point above the jets axis, almost symmetric with respect to the chamber axis (and always positive). A second plume of low negative correlation is situated symmetrically to the first, below the jets axis, consistently with what reported in Figs. 3.5(d) and 3.4. Along the jet-axis in fact the  $y$ -component of the velocity is almost zero, whereas along the chamber axis the same component is rather high and changes only a little, determining the high  $R_{yy}$  correlation. Finally the correlation  $R_{xy}$  is symmetric with respect to an axis inclined  $45^\circ$  to the chamber and jets axes. The correlation is negative in the first and third quadrants, whereas it is positive in the second and fourth quadrants. Again the reason for this can be understood by observing the snapshots reported in Fig. 3.4. The eddies that are formed by the jet with positive  $x$ -component velocity

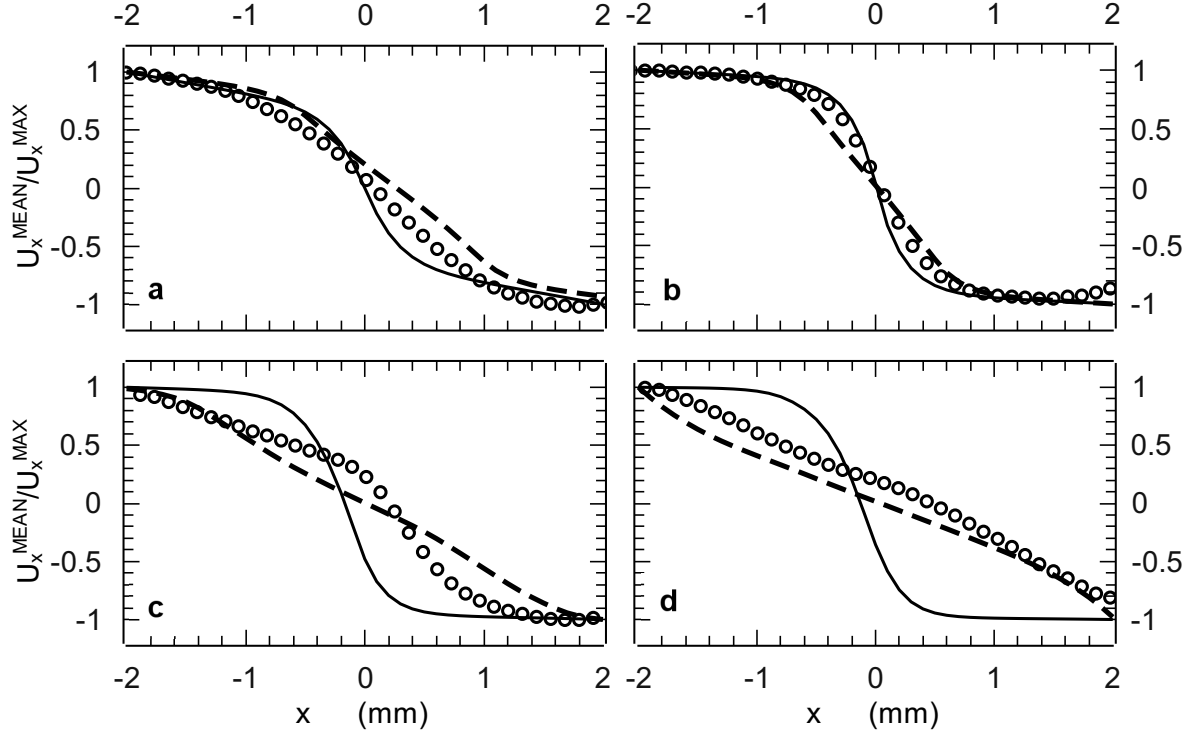


Figure 3.7: Comparison between profiles of the  $x$ -component of the mean velocity at  $y = 0$  mm measured by  $\mu\text{PIV}$ ( $\circ$ ) and predicted by DNS with constant inflows (continuous line) and DNS with variable inflows (dashed line) for (a)  $\text{Re} = 62$ , (b)  $\text{Re} = 150$ , (c)  $\text{Re} = 310$ , (d)  $\text{Re} = 600$ .

rotate anti-clock wise above the jets axis and clock wise below the jets axis, therefore originating a negative  $y$ -component velocity above and a positive  $y$ -component velocity below the jets axis. A similar situation can be described for the opposite jet with negative  $x$ -component velocity.

### 3.5.5 Time series power spectra

The important effects of imposing oscillating inflows in the simulations is also visible in Fig. 3.12 where the power spectra of  $x$ -velocity fluctuations (from DNS) in the impingement point are reported for  $\text{Re} = 310$  (dashed line) and  $\text{Re} = 600$  (continuous line). The spectra are smoothed using a 7-points moving average to remove the noise at high frequencies. As it can be seen, the imposed oscillations are very small in amplitude but they create a wide range of frequencies in the spectrum of velocity fluctuations. The spectra exhibit marked peaks reflecting the

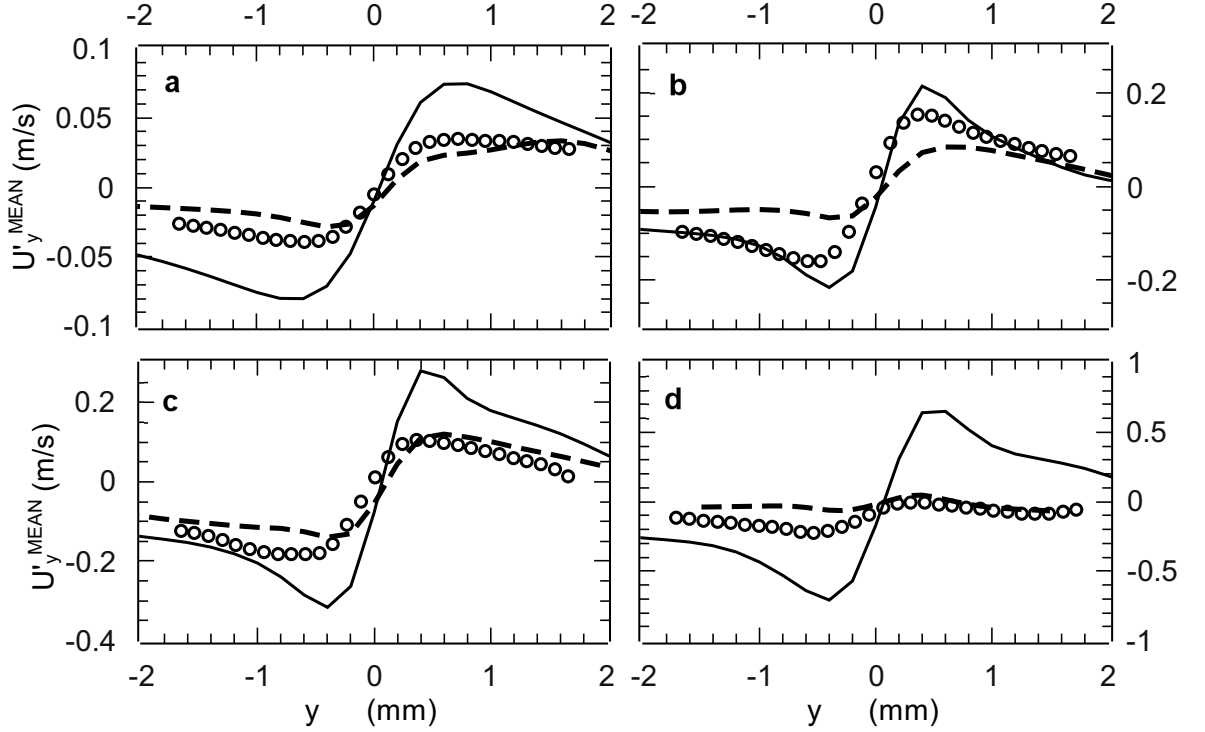


Figure 3.8: Comparison between profiles of the  $y$ -component of the mean velocity at  $x = 0$  mm measured by  $\mu\text{PIV}$ ( $\circ$ ) and predicted by DNS with constant inflows (continuous line) and DNS with variable inflows (dashed line) for (a)  $\text{Re} = 62$ , (b)  $\text{Re} = 150$ , (c)  $\text{Re} = 310$ , (d)  $\text{Re} = 600$ .

oscillations in the inflow (main mode), followed by sub-harmonics, increasing (non-linearly) in frequencies with the Reynolds number. For the two lowest flow rates the peak contains more than 90 % of the energy while for  $\text{Re} = 310$  and  $\text{Re} = 600$  the percentage decreases to 73 % and 55 % respectively. The remaining energy is transferred to smaller scales. Increasing the flow rate the power spectrum tends to approach the  $-\frac{5}{3}$  logarithmic slope, characteristic of three-dimensional turbulence. This result shows that the flow in the reactor is not fully turbulent but it is in a transitional regime. Furthermore it can be noted that the approximation of the experimental inflows with a single frequency oscillation is reasonable for the purpose of simulating the behaviour of the system. A sensitivity analysis modifying the frequency, the phase displacement between the two inlets and the amplitude of oscillations within a reasonable range revealed a weak influence of these parameters on the qualitative behaviour of the system and on the velocity statistics analysed.

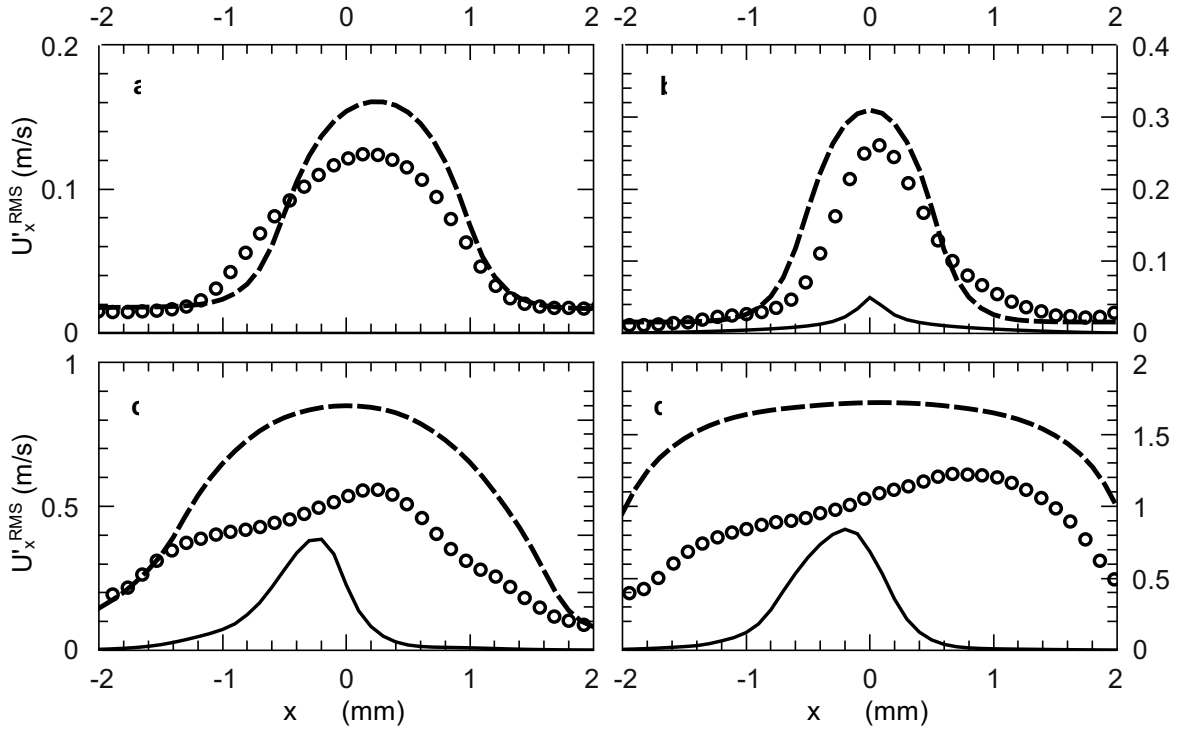


Figure 3.9: Comparison between RMS profiles of the  $x$ -component of the fluctuating velocity at  $y = 0$  mm measured by  $\mu$ PIV( $\circ$ ) and predicted by DNS with constant inflows (continuous line) and DNS with variable inflows (dashed line) for (a)  $Re = 62$ , (b)  $Re = 150$ , (c)  $Re = 310$ , (d)  $Re = 600$ .

### 3.6 Conclusions

In this chapter results concerning the flow field in a CIJR measured with  $\mu$ PIV and predicted via DNS were presented and discussed. Qualitative and quantitative comparisons in terms of first and second order statistics at four different flow regime conditions ( $Re = 62, 150, 310$  and  $600$ ) were analysed. Only the combination of the experimental and modelling approach was found to be able to address the many physical issues involved. MicroPIV data, applied for the first time to a three-dimensional axisymmetric CIJR, is able to highlight the presence of a rich variety of flow structures and instabilities. In particular it emerges that the flow field is laminar and unsteady for low jets Reynolds numbers ( $Re < 310$ ), and turbulent for and higher values. However these turbulent features increase the difficulties in the experimental setup and make it extremely hard to understand and fully explain the results. DNS can therefore be used to gain further insights in the system. Our results show that the natural instability generated by the impingement of the jets is

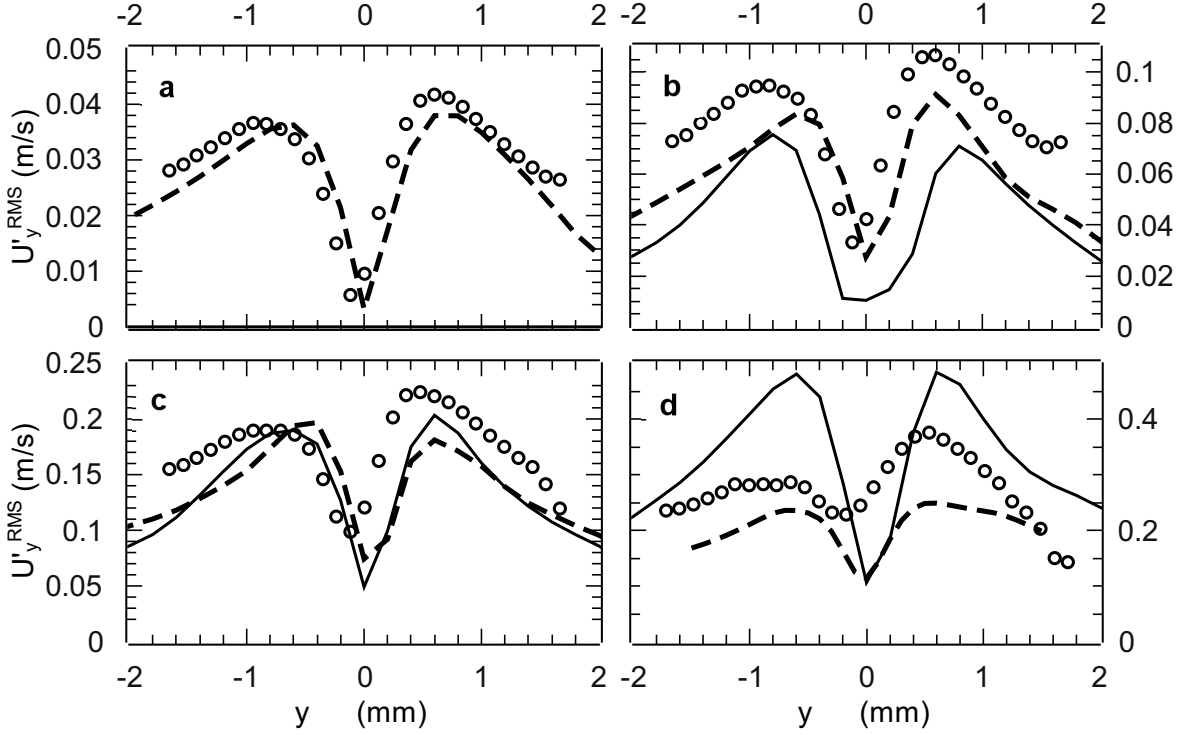


Figure 3.10: Comparison between RMS profiles of the  $y$ -component of the fluctuating velocity at  $x = 0$  mm measured by  $\mu$ PIV( $\circ$ ) and predicted by DNS with constant inflows (continuous line) and DNS with variable inflows (dashed line) for (a)  $Re = 62$ , (b)  $Re = 150$ , (c)  $Re = 310$ , (d)  $Re = 600$ .

not enough to explain the chaotic behaviour of the system. Instead, if more accurate inflow conditions are imposed in DNS, by introducing small oscillations similar to the experimental ones, a more chaotic behaviour is observed. These oscillations are not obtained with a fitting procedure but simply imposed according to the experimental data available in the inlets, which revealed small variations in time due to the feeding system. Since the main purpose of this study is to understand what happens in micro-reactors applied in industries for continuous operation, it is very important to analyse the effects of the unsteadiness acting and generated by the system, and there is no interest in artificially removing these oscillations but they must be taken into account in the computational model. DNS with a proper approximation of the boundary conditions resulted in very good agreement with experimental data and provide us with an explanation of the structures observed with  $\mu$ PIV: the breakup of the impingement plane generates many eddies of different sizes that enhance turbulence in the device and its mixing performance. These results suggest

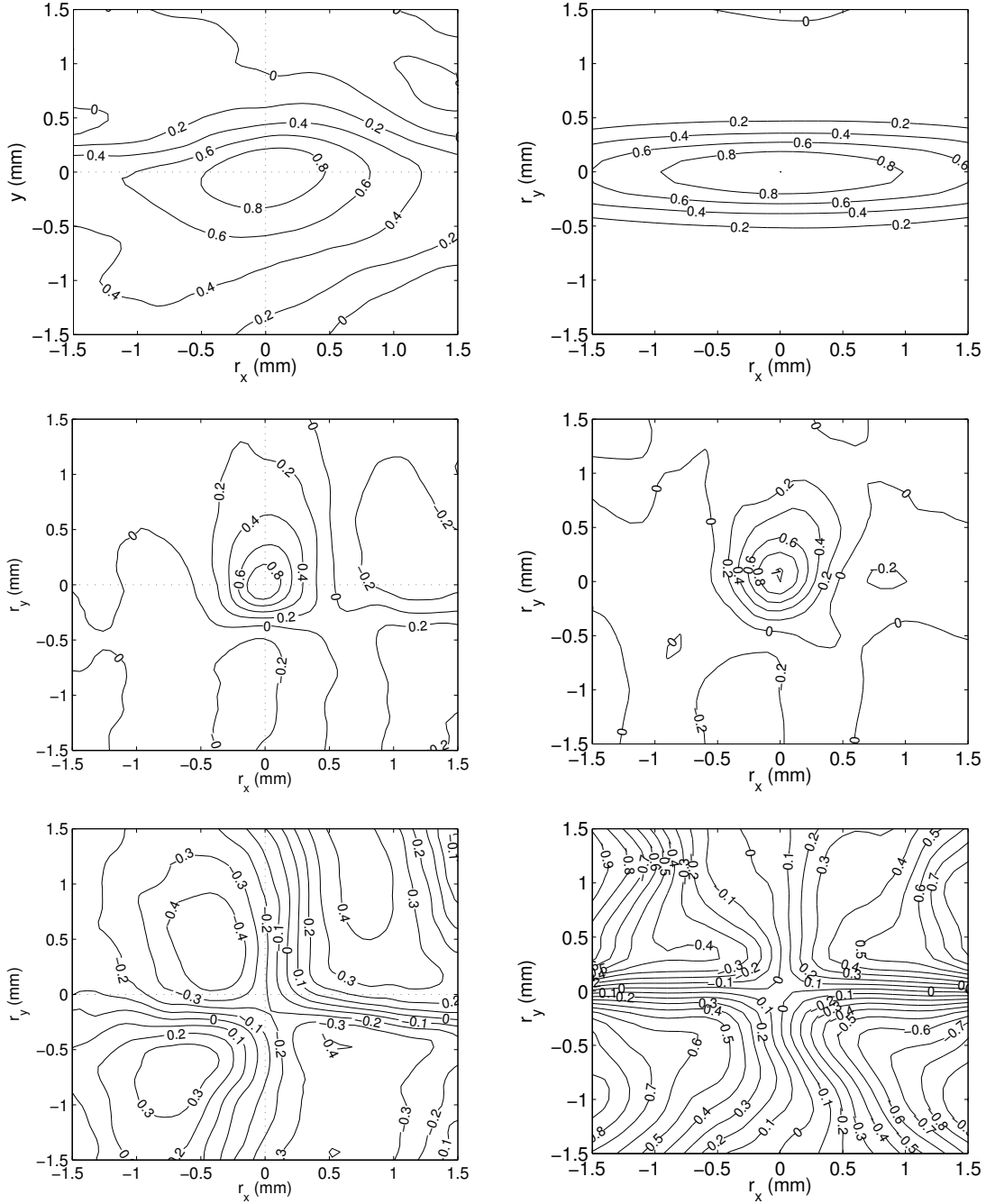


Figure 3.11: From top to bottom spatial correlation functions  $R_{xx}$ ,  $R_{yy}$  and  $R_{xy}$  as measured by  $\mu$ PIV (left) and simulations (right) for  $Re = 600$ .

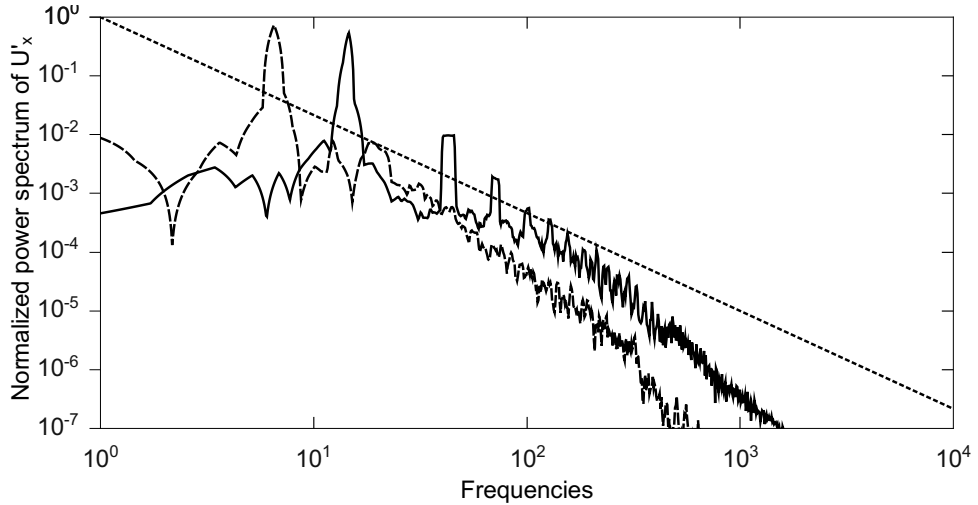


Figure 3.12: Normalised power spectra of the time series of  $x$ -velocity fluctuations in the impingement point for  $Re = 310$  (dashed line) and for  $Re = 600$  (continuous line) compared with the characteristic cascade slope for three-dimensional turbulence (dotted straight line).

also that unsteady simulations of this type of micro-mixers must be provided with accurate unsteady boundary conditions, and this gave the way for the next step of the work that includes the use of LES with appropriate sub-grid scale models for the simulations of mixing and reactions in CIJR.

## References

- K. Abe, T. Kondoh, and Y. Nagano. A new turbulence model for predicting fluid flow and heat transfer in separating and reattaching flows: I. Flow field calculations. *Int. J. Heat Mass Transfer*, 37(1):139–151, Jan. 1994.
- Ascomp GmbH. *Multi—Fluid Navier—Stokes Solver TransAT User Manual*, 2009.
- J. C. Cheng, M. G. Olsen, and R. O. Fox. A microscale multi-inlet vortex nanoprecipitation reactor: Turbulence measurement and simulation. *Appl. Phys. Lett.*, 94(20):204–104, 2009.
- H. Feng, M. G. Olsen, Y. Liu, R. O. Fox, and J. C. Hill. Investigation of turbulent mixing in a confined planar-jet reactor. *AICHE J.*, 51(10):2649–2664, 2005.
- J. H. Ferziger and M. Peric. *Computational Methods for Fluid Dynamics*. Springer-Verlag, Berlin, third edition, 2002.
- E. Gavi. *Investigation of turbulent precipitation of nanoparticles in a Confined Impinging Jets Reactor*. PhD thesis, Torino, Italy, 2009.

- E. Gavi, D. L. Marchisio, and A. A. Barresi. CFD modelling and scale-up of Confined Impinging Jet Reactors. *Chem. Eng. Sci.*, 62(8):2228–2241, 2007a.
- E. Gavi, L. Rivautella, D. L. Marchisio, M. Vanni, A. A. Barresi, and G. Baldi. CFD Modelling of nano-particle precipitation in confined impinging jet reactors. *Chem. Eng. Res. Des.*, 85(5):735–744, 2007b.
- E. Gavi, D. L. Marchisio, A. A. Barresi, M. G. Olsen, and R. O. Fox. Turbulent precipitation in micromixers: CFD simulation and flow field validation. *Chem. Eng. Res. Des.*, page in press, 2010.
- J. Gradl, H. C. Schwarzer, F. Schwertfimer, M. Manhart, and W. Peukert. Precipitation of nanoparticles in a T-mixer: coupling the particle population dynamics with hydrodynamics through direct numerical simulation. *Chem. Eng. Process.*, 45:908–916, 2006.
- D. Horn and J. Rieger. Organic nanoparticles in the aqueous phase - theory, experiment, and use. *Angew. Chem. Int. Ed.*, 40(23):4330–4361, December 2001.
- S. M. Hosseinalipour and A. S. Mujumdar. Comparative evaluation of different turbulence models for confined impinging and opposing jet flows. *Numer. Heat Transfer, Part A*, 28(6):647–666, Dec. 1995.
- M. Icardi, E. Gavi, D. Marchisio, A. Barresi, M. Olsen, R. Fox, and D. Lakehal. Investigation of the flow field in a three-dimensional confined impinging jets reactor by means of micropiv and dns. *Chem. Eng. J.*, 166(1):294–305, 2011.
- B. K. Johnson and R. K. Prud'homme. Flash nanoprecipitation of organic actives and block copolymers using a Confined Impinging Jets Mixer. *Aust. J. Chem.*, 56(10):10–21, 2003a.
- B. K. Johnson and R. K. Prud'homme. Chemical processing and micromixing in confined impinging jets. *AIChE J.*, 49(9):2264–2282, September 2003b.
- K. Kawahara and C. Tanford. Viscosity and density of aqueous solutions of urea and guanidine hydrochloride. *J. Biol. Chem.*, 241(13):3228–3232, July 1966.
- J. Kipp. The role of solid nanoparticle technology in the parenteral delivery of poorly water-soluble drugs. *Int. J. Pharm.*, 284(1-2):109–122, October 2004.
- C. C. Landreth and R. J. Adrian. Impingement of a low Reynolds number turbulent circular jet onto a flat plate at normal incidence. *Exp. Fluids*, 9:74–84, 1990.
- H. Li, R. Ewoldt, and M. G. Olsen. Turbulent and transitional velocity measurements in a rectangular microchannel using microscopic particle image velocimetry. *Exp. Therm. Fluid Sci.*, 29(4):435–446, April 2005.
- F. Lince, D. L. Marchisio, and A. A. Barresi. Strategies to control the particle size distribution of poly- $\epsilon$ -caprolactone nanoparticles for pharmaceutical applications. *J. Colloid Interface Sci.*, 322(2):505–515, 2008.
- Y. Liu and R. O. Fox. CFD predictions for chemical processing in a confined impinging-jets reactor. *AIChE J.*, 52:731–744, 2006.
- Y. Liu, J. C. Cheng, R. K. Prud'homme, and R. O. Fox. Mixing in a multi-inlet vortex mixer (MIVM) for flash nano-precipitation. *Chem. Eng. Sci.*, 63(11):2829–2842, 2008.

---

## REFERENCES

---

- Y. Liu, M. G. Olsen, and R. O. Fox. Turbulence in a microscale planar confined impinging-jets reactor. *Lab Chip*, 9(8):1110–1118, 2009.
- D. L. Marchisio and R. O. Fox. Solution of population balance equations using the direct quadrature method of moments. *J. Aerosol Sci.*, 36:43–73, 2005.
- M. G. Olsen. Directional dependence of depth of correlation due to in-plane fluid shear in microscopic particle image velocimetry. *Meas. Sci. Technol.*, 20:015402, 2009.
- M. G. Olsen and R. J. Adrian. Out-of-focus effects on particle image visibility and correlation in microscopic particle image velocimetry. *Exp. Fluids*, 29(0):S166–S174, December 2000a.
- M. G. Olsen and R. J. Adrian. Brownian motion and correlation in particle image velocimetry. *Opt. Laser Technol.*, 32:621–627, 2000b.
- M. G. Olsen and C. J. Bourdon. Out-of-plane motion effects in microscopic particle image velocimetry. *J. Fluids Eng.*, 125(5):895–901, 2003.
- M. G. Olsen and J. C. Dutton. Stochastic estimation of large structures in an incompressible mixing layer. *AIAA J.*, 40(12):2431–2438, December 2002.
- A. K. Prasad. Particle Image Velocimetry. *Current Science*, 79:51–60, 2000.
- O. V. Salata. Applications of nanoparticles in biology and medicine. *J. Nanobiotechnol.*, 2(3):177–182, 2004.
- M. Samimy and S. K. Lele. Motion of particles with inertia in a compressible free shear layer. *Phys. Fluids A*, 3(8):1915–1923, 1991.
- J. G. Santiago, S. T. Wereley, C. D. Meinhart, D. J. Beebe, and R. J. Adrian. A particle image velocimetry system for microfluidics. *Exp. Fluids*, 25(4):316–319, September 1998.
- R. J. Santos, E. Erkoç, M. M. Dias, A. M. Teixeira, and J. Carlos. Hydrodynamics of the mixing chamber in RIM: PIV flow-field characterization. *AIChE J.*, 54:1153–1163, 2008.
- F. Schwertfirm, J. Gradl, H. C. Schwarzer, W. Peukert, and M. Manhart. The low Reynolds number turbulent flow and mixing in a confined impinging jet reactor. *Int. J. Heat Fluid Flow*, 28(6):1429–1442, 2007.
- V. Van Steijn, T. M. Kreutzer, and C. R. Kleijn. MicroPIV study of the formation of segmented flow in microfluidic T-junctions. *Chem. Eng. Sci.*, 62:7505–7514, 2007.
- J. R. Warren and J. A. Gordon. On the refractive indices of aqueous solutions of urea. *J. Phys. Chem.*, 70:297–300, 1966.
- S. T. Wereley, L. Gui, and C. D. Meinhart. Advanced algorithms for microscale particle image velocimetry. *AIAA J.*, 40(6):1047–1055, June 2002.
- J. Zhu. A low-diffusive and oscillation-free convection scheme. *Commun. Appl. Numer. Methods*, 7(3):225–232, April 1991.



# 4

## Quality and reliability of LES models

Before applying LES to the CIJR described in Chap. 3, this model (and the particular implementation used in this thesis) is here studied in a more general context. In fact, the assessment and reliability of LES models is a topic that is facing increasing interest in the scientific community because of the increasing need of three-dimensional and unsteady details in practical CFD applications. Furthermore, most of the concepts used for laminar flows or RANS simulations cannot be easily translated into LES framework, where, for example, the important concept of grid independence cannot be applied. In this part of the work, the influence of Sub-Grid Scale (SGS) models, numerical schemes and wall models are analysed for a periodic turbulent channel flow, comparing the results with DNS data. The objective is to test LES models and CFD numerics commonly used for engineering applications in a simple setup where their effects and interdependency can be understood. This preliminary step is particularly important for the simulation of more complex geometries (such as the one reported in Chap. 5) and more complex problems (such as the one reported in Chap. 6).

With this objective, a periodic channel is studied with LES for a turbulent flow characterised by a friction Reynolds number  $Re_\tau = 590$ . Results are compared to DNS data of Moser et al. [1999].

---

Part of the work presented in this chapter is the result of the LESinItaly project, a collaboration of different Italian groups active in the field of LES, published in the work of Denaro et al. [2011]. The simulations have been carried out thanks to the computational resources of CASPUR.

## 4.1 Introduction

The recent and always increasing development of computational powers, thanks to new hardware and new parallelisation techniques, has given the opportunity of employing LES for small and medium scale industrial applications. LES is, in fact, more suitable than RANS for many applications in which the three-dimensional and unsteady behaviour of the flow has a greater influence on the other physical phenomena involved (e.g., chemical reactions, structure vibrations, aerodynamic wakes, etc.). However, although the main concepts of LES have been introduced in the 1970's and huge efforts have been put in the last decades for their development and study, many theoretical and practical aspects are still under a flamed debate, as it is demonstrated by some recent works [Bouffanais, 2010, Denaro, 2011, Jiménez, 2003, Jiménez and Moser, 2007, Meyers and Sagaut, 2007, Pope, 2004]. In particular, some of crucial points refer to SGS and wall models, their interactions with numerical schemes and also on the interpretation of LES itself. In this framework it is important to mention the Implicit Large Eddy Simulation (ILES) and Monotone Integrated LES (MILES) [Fureby and Grinstein, 1999, Grinstein et al., 2007, Margolin et al., 2006]. Both these approaches directly use ad-hoc numerical schemes as sub-grid models, simplifying the LES implementation but loosing the numerical independence with respect to the model.

The objective of this study is to consider a widely studied and known problem, such as the wall bounded flows in a periodic channel, and use it as a benchmark test case for an overall estimation of the prediction ability of our LES platform. This is a very challenging issue because the numerical (given by the numerical grid and schemes) and modelling errors (the SGS models and wall functions) are not easily decoupled in the LES framework and they interact in an unusual and non-linear way, giving place to a high uncertainty on the results and difficulty in applying the same conclusions for different applications.

This part of the work considers the performance of different SGS models, numerical schemes, as well as wall and SGS damping functions. A periodic channel with  $Re_\tau = 590$  is simulated with periodic boundary conditions on  $x$  and  $z$  and no-slip boundary conditions on  $y$  and results are compared against DNS data of Moser et al. [1999]. The channel flow problem has been studied by many previous works [Hoyas and Jiménez, 2006, Kim et al., 1987, Mansour et al., 1988, Mason and Callen, 1986, Moin and Kim, 1982, Piomelli et al., 1988] but, as it has been already underlined, the accuracy of LES strongly depends in a complex way to many numerical and modelling parameters, therefore it is important to test the available LES platform in simple test cases before going into more complex applications.

### 4.1.1 Test case description

The channel under study is defined by

$$L_x = 2\pi H \quad L_y = 2H \quad L_z = \pi H \quad (4.1)$$

where  $H$  is the half-height of the channel, used as characteristic dimension. The

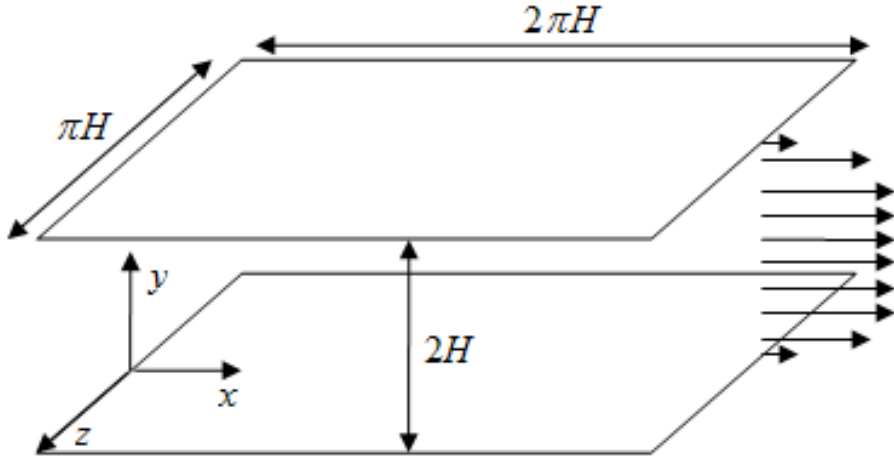


Figure 4.1: Sketch of the channel [Lampitella et al., 2011].

main flow is directed along  $x$ -direction while  $y$  is the direction normal to the walls. Therefore the boundary conditions consist in no-slip conditions at  $y$ -boundaries and periodic conditions at  $x$  and  $z$ -boundaries.

Being  $U$  the  $x$ -component of the velocity, the wall shear stress is defined as

$$\tau_w = \rho\nu \left. \frac{dU}{dy} \right|_{y=0}. \quad (4.2)$$

The friction Reynolds number  $Re_\tau$  can be defined as [Pope, 2000]:

$$Re_\tau = \frac{U_\tau H}{\nu}; \quad (4.3)$$

where  $U_\tau = \sqrt{\frac{\tau_w}{\rho}}$  is the friction velocity.

In our model, the fluid flows thank to a constant pressure forcing in  $x$ . This means that the mean flow rate is not directly imposed but it results from the balance between pressure and shear forces. This makes the model extremely sensitive to model assumptions and numerical treatment of the walls and permits a better understanding of the influence of the various model parameters.

Turbulent flows are characterised by a stochastic behaviour and therefore an instantaneous comparison of the LES results with DNS is not possible. Therefore the main quantities of importance come from statistics of the flow field. The statistics must be calculated from uncorrelated temporal samples, after that the mean flow rate and the mean resolved kinetic energy have reached a pseudo-stationary state. Averaging is performed in time and along the periodic directions. In particular, considering a generic flow field variable  $f(x, y, z, t)$  coming from a LES simulation (i.e., LES filtered quantity) we define the following spatial average:

$$\bar{f}^{xz}(y, t) = \frac{1}{L_x L_z} \int_0^{L_x} \int_0^{L_z} f(x, y, z, t) dz dx, \quad (4.4)$$

and a temporal average on top resulting in:

$$\langle \bar{f}^{xz} \rangle(y) = \frac{1}{\Delta T} \int_0^{\Delta T} \bar{f}^{xz}(y, t) dt. \quad (4.5)$$

The fluctuations with respect to LES solution are defined as:

$$f'(x, y, z, t) = f(x, y, z, t) - \bar{f}^{xz}(y, t), \quad (4.6)$$

and their RMS values as:

$$f_{RMS}(y) = \sqrt{\langle (f'(x, y, z, t))^2 \rangle^{xz}} \quad (4.7)$$

Similarly, one-dimensional energy spectra  $E_{UU}, E_{VV}, E_{WW}$  for the three velocity components can be defined at specific wall distance, calculating the Fourier transform along one of the periodic directions  $x$  or  $z$  and averaging on time and on the remaining periodic direction.

It is worth noticing that all these quantities are not exactly comparable to the DNS counterpart because they neglect the sub-grid scales fluctuations filtered out by the LES filter.

### 4.1.2 Numerical details

The desired friction Reynolds number is obtained by taking an adimensional setup with

$$H = 1 \text{ m} \quad \rho = 1 \text{ Kg/m}^3 \quad \mu = \frac{1}{Re_\tau} \quad (4.8)$$

and adding an uniform unitary pressure gradient source term in the  $x$ -momentum equation. In this work the friction Reynolds number is  $Re_\tau = 590$ .

Two numerical grids have been used to compute the flow:

1. Non-Resolved Grid (GNR),  $64 \times 32 \times 64$  cells with  $\Delta y^+ = 1.42$

## 2. Resolved Grid (GR), $64 \times 100 \times 64$ cells with $\Delta y^+ = 0.45$

The grids are uniform in  $x$  and  $z$  directions and stretched in  $y$  direction with a trigonometric law to increase the boundary layer resolution. Since these grids have a good near-wall resolution, the wall functions are not strictly needed. However, to understand the effect of the wall functions, the Werner-Wengle law [Werner and Wengle, 1991] has been tested and compared with the fully resolved simulations.

The simulations are carried out in time with an explicit third-order Runge-Kutta scheme and a second-order implicit scheme, while the advective fluxes are discretised with the central scheme, QUICK [Leonard, 1976] and HLPA [Zhu, 1991] scheme. The explicit time step was adaptively chosen to have the maximum local Courant–Friedrichs–Lowy (CFL) number below 0.2, resulting in a time step  $\Delta t = 5.0 \cdot 10^{-4}$ , while the implicit scheme has been run with  $\Delta t = 1.0 \cdot 10^{-3}$ .

The simulations have been carried out with the commercial CFD code *TransAT*, in a two-way quad-core Opteron 2.1GHz with 16 GB of RAM (hosted by CASPUR, Roma) with shared memory parallelisation paradigm (OpenMP). The total simulation time for a single run, including the initial transition before statistical stationarity, was from ten days for the coarse grid, up to sixty days for the finer one. This reduces respectively to six and fifteen days, when using two and six processors. This was found to be the best compromise between speed, scalability and accuracy. The results and the computational time were almost equal with both implicit and explicit method. Even if the explicit method is 10% faster, the implicit method is preferred because of the strict control on residuals, especially when additional physics and equations are added to the flow.

The solution has been initialised with results coming from a coarser grid and statistics are calculated from 100 samples with a sampling time  $\Delta t_{sampl} = 0.5\text{s}$  when the flow has reached that transient effects.

### 4.1.3 Sub-grid Scale (SGS) modelling

In LES the effects of the small scales of the flow are modelled as a sub-grid scale viscosity

$$\tau_{ij} = -2 \nu_t \bar{S}_{ij} \quad (4.9)$$

where the strain rate tensor  $\bar{S}_{ij}$  is determined from the large scale motion. The constant Smagorinsky model [Smagorinsky, 1963] is based on this approach and

$$\nu_t = \ell^2 |\bar{S}| \quad (4.10)$$

where  $|\bar{S}|$  is the main strain rate defined as

$$|\bar{S}| = (2 \bar{S}_{ij} \bar{S}_{ij})^{1/2} \quad (4.11)$$

and where the length-scale  $\ell = C_s \bar{\Delta}$  is based on the filter size (in our case equal to the cell size)  $\bar{\Delta}^3 = (\Delta_1 \Delta_2 \Delta_3)$ . The constant  $C_s$  is the Smagorinsky constant (commonly assumed to be between 0.10 and 0.15).

The reduction of the sub-grid length-scale  $\ell$  in low-Re number flow regions can be achieved in different ways:

- Van Driest damping function [Van Driest, 1956]:

$$\ell = C_s \bar{\Delta} \left[ 1 - \exp(-y^+/26) \right] \quad (4.12)$$

- Harmonic damping:

$$\ell = \min \left( C_s \bar{\Delta}, \left( \frac{1}{C_2 \bar{\Delta}} + \frac{1}{\kappa y} \right)^{-1} \right) \quad (4.13)$$

where  $C_2$  is a constant (in this work it is equal to  $C_s$ ),  $\kappa$  is the Von Karman constant ( $\approx 0.41$ ) and  $y$  is the distance from the wall.

- Mixing length:

$$\ell = \min \left( C_s \bar{\Delta}, \kappa y \right). \quad (4.14)$$

In the dynamic model [Ascomp GmbH, 2009, Germano et al., 1991] the eddy viscosity is determined from the information contained in the resolved velocity field. The main idea consists of introducing a test filter with a larger width than the original one, i.e.  $\tilde{\bar{\Delta}} > \bar{\Delta}$ . This test filter is then applied to the filtered Navier-Stokes equations, yielding a test-scale stress tensor  $T_{ij}$  similar in form to  $\tau_{ij}$  that takes the following form:

$$T_{ij} = \widetilde{\overline{U'_i U'_j}} - \widetilde{\overline{U_i}} \widetilde{\overline{U_j}}. \quad (4.15)$$

By virtue of the Germano identity [Germano, 1986], the two sub-grid scale (SGS) stress tensors  $\tau_{ij}$  and  $T_{ij}$  are connected through the following relation

$$T_{ij} - \tilde{\tau}_{ij} \equiv \mathcal{L}_{ij} = \widetilde{\overline{U'_i U'_j}} - \widetilde{\overline{U_i}} \widetilde{\overline{U_j}}. \quad (4.16)$$

Assuming now the Smagorinsky functional form to hold and a variable coefficient  $C_s$  to be used to close the deviatoric parts of  $\tau_{ij}$  and  $T_{ij}$ , we get

$$\tau_{ij} = -2(C_s \bar{\Delta})^2 |\bar{S}| \bar{S}_{ij} \quad (4.17)$$

$$T_{ij} = -2(C_s \tilde{\bar{\Delta}})^2 |\tilde{\bar{S}}| \tilde{\bar{S}}_{ij} \quad (4.18)$$

where  $\tilde{\overline{S}} = (\tilde{v}_{i,j} + \tilde{v}_{j,i})/2$  is the strain tensor of the test-filtered velocity field. Rearranging the last three equations results in:

$$\mathcal{L}_{ij} = -2(C_s \overline{\Delta})^2 \left[ \frac{\tilde{\overline{\Delta}}^2}{\overline{\Delta}^2} |\tilde{\overline{S}}| \tilde{\overline{S}}_{ij} - |\widetilde{\overline{S}}| \widetilde{\overline{S}}_{ij} \right] \quad (4.19)$$

In this work five different models are used to take into account sub-grid scales:

1. no model ( $\nu_t = 0$ ),
2. dynamic model,
3. constant Smagorinsky model with  $C_s = 0.10$  and Van Driest damping,
4. constant Smagorinsky model with  $C_s = 0.10$  and harmonic damping,
5. constant Smagorinsky model with  $C_s = 0.10$  and mixing length damping.

The influence of the parameter  $C_s$  has been tested, by varying it between 0.08 and 0.15 and found to be negligible.

Figure 4.2 shows the length-scale  $\ell$  calculated for the grid GNR with different damping functions and definitions of mean grid cell size. Usually the mean cell size is calculated with a geometric law  $\Delta = (\Delta_x \Delta_y \Delta_z)^{1/3}$ . Another possible definition is  $\Delta = \max(\Delta_x, \Delta_y, \Delta_z)$  that represents in slightly different way the unresolved scale when the grid stretching is high. Only the first definition was used in the simulations since the main shape of the curves does not change much with the other definition. More differences can be seen instead by varying the damping functions.

## 4.2 Results and discussion

As it has been already reported, the statistics have been compared to DNS data of [Moser et al., 1999] in terms of mean velocity, fluctuations and velocity correlations spectra.

The simulations with the Werner-Wengle wall functions resulted in negligible effects on the statistics and the flow field, confirming that the grids we used can solve the wall boundary layer. Then, among the different advection schemes tested, only the central scheme captured the correct flow behaviour. The QUICK scheme in fact creates spurious checker-board oscillations in the centre of the channel, while the HLPA, because its the boundedness criterion, introduce small numerical viscosity that laminarise the flow, predicting a very large mean flow rate. Therefore in the following results, only the simulations with the central scheme without wall functions are shown.

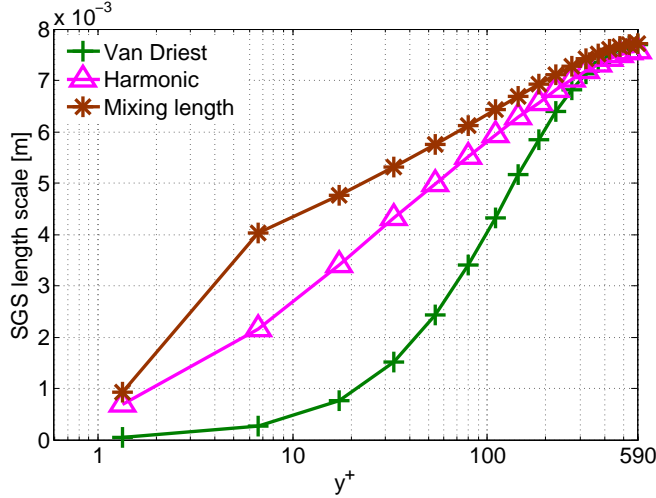


Figure 4.2: SGS length-scale used in the Smagorinsky model to calculate the SGS viscosity. Comparison of different damping functions.

It is important to highlight here that, except for the mean quantities, the comparison of LES results with DNS, is not fully equivalent, as discussed in the previous section. In fact LES fluctuations and spectra cannot account for the SGS structures of the flow. In this setup, where the mean flow rate is implicitly imposed by the pressure forcing, the main quantity of interests is therefore the mean flow profile in the  $x$  direction. Fluctuations and spectra, compared to DNS, can give however important information about the effects of the different SGS models and the LES filter.

#### 4.2.1 Mean and fluctuating velocities

Figure 4.3 represents the mean velocity profile along the wall normal direction  $y$  for the GNR and GR grid simulations with different SGS models. The case without SGS model shows an overprediction of the profile that affects the mean flow rate. The prediction seems to be even overestimated when the dynamic model is used to capture the SGS effects. It is interesting to notice that the results with the dynamic model are very similar to the Smagorinsky model with the classical Van Driest damping. The situation changes when the Smagorinsky model is used

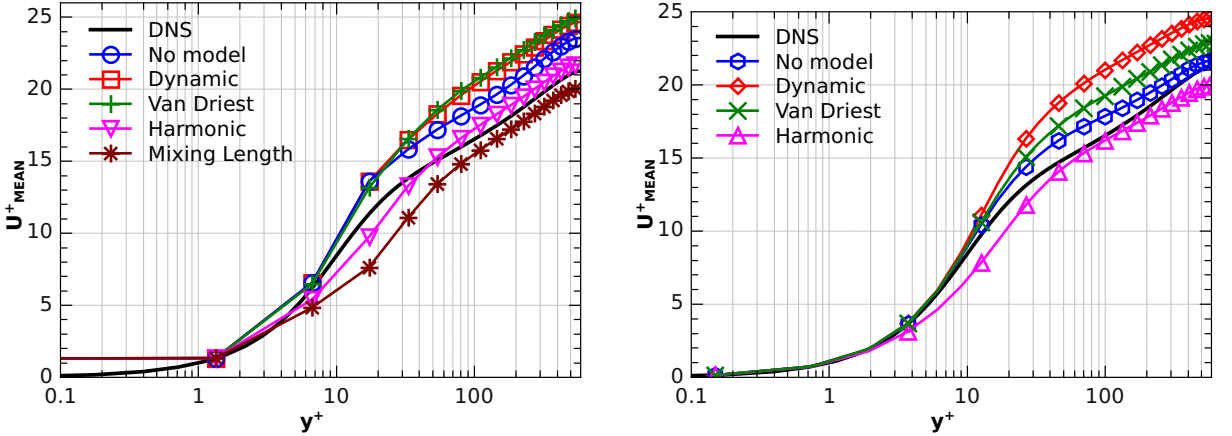


Figure 4.3: Mean velocity profiles of LES simulations with grid GNR (left) and grid GR (right). TransAT results.

together with a different damping. In fact, the best results are obtained with the harmonic damping while the mixing-length damping under-estimate the velocity profile. This seems to demonstrate that the type of SGS model is not as important as the damping functions and that the flow is very sensitive to the SGS viscosity in the near-wall region.

These conclusions are confirmed also by the results obtained with the finer grid (GR). We can conclude therefore that the overall results are not influenced much by the SGS model nor by the wall-normal resolution. This can be explained with a possible under-resolution along the stream-wise and span-wise directions that underestimate the effects of eddies and that is compensated by a higher SGS viscosity near the wall.

This means that, the development of the profile is more influenced by the sub-grid scale viscosity in the near-wall region than in the central part of the channel. Both the dynamic and the Van Driest model in fact introduce a significant SGS viscosity only quite far away from the wall (above  $y^+ > 10$ ) differently from the harmonic and mixing-length damping. This is shown in Figure 4.4 where the SGS viscosity is plotted. SGS viscosity near the wall has an opposite effect on the overall flow rate with respect to the SGS viscosity near the centre of the channel. In the first case in fact it introduces a higher dissipation near the wall which enables the development of a profile close to DNS data, while in the second case the dissipation is acting more on the central part of the channel, where the velocity profile is already partially developed, inducing an overestimation of the mean flow rate.

More information can be obtained by analysing the velocity fluctuations. In Figures 4.5 the velocity fluctuations in the three directions along the wall-normal direction are plotted. The results in the centre of the channel are always predicted

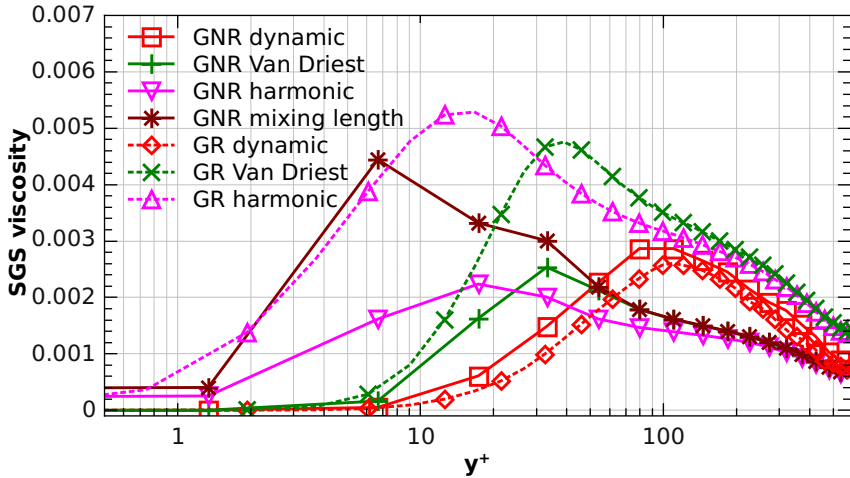


Figure 4.4: SGS viscosity profiles of LES simulations. TransAT results.

accurately by all the models but the peaks close to the wall seem to be more influenced by the choice of the models. In the stream-wise direction the predictions follows the same behaviour of the mean velocity, with good predictions obtained with the harmonic damping, while the other models over-predict the fluctuations, except the mixing length case. In the span-wise and wall-normal directions instead, the harmonic damping under-predicts the fluctuations peaks. This difference can be explained again by the fact that the grid near the wall which is more refined in the  $y$ -direction than in the others. This cause the  $x$ -fluctuations to be better predicted by the LES simulations. A post-filtering operation on the DNS data could be useful in this case to take into account the LES filter in the fluctuations.

#### 4.2.2 Energy spectra

Figure 4.6 shows the Fourier coefficients of stream-wise, span-wise and normal velocity correlations along  $x$ -direction near the wall and in the centre of the channel. In Figure 4.7 the same quantities are calculated along the  $z$ -direction. As expected, in the centre of the channel the damping functions do not influence the qualitative behaviour of the dissipative cascade. It is more interesting to notice that also different SGS models, though giving place to different flow rates and profiles, results in very similar spectra. The only exceptions are represented by the coarse simulations with the dynamic model and without model. These simulations, that are also the ones in disagreement with the DNS in terms of mean flow rate, are also characterised by low energies in the span-wise structures, and spectra that seem to be not completely developed. Differences are more evident near the wall, where the damping functions and the SGS models act in a different and stronger way. In all

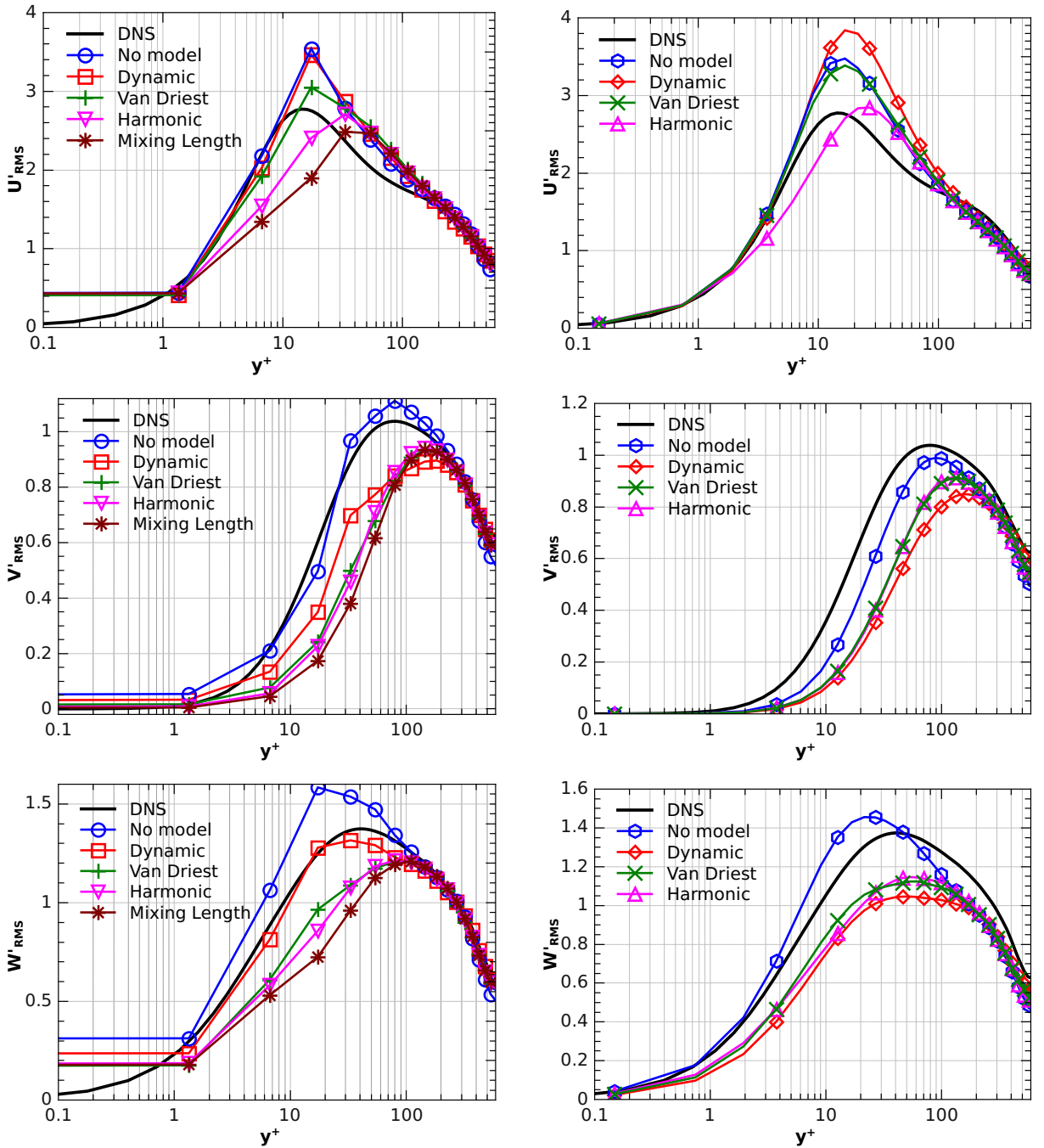


Figure 4.5: Velocity fluctuations profiles of LES simulations with grid GNR (left) and grid GR (right). TransAT results.

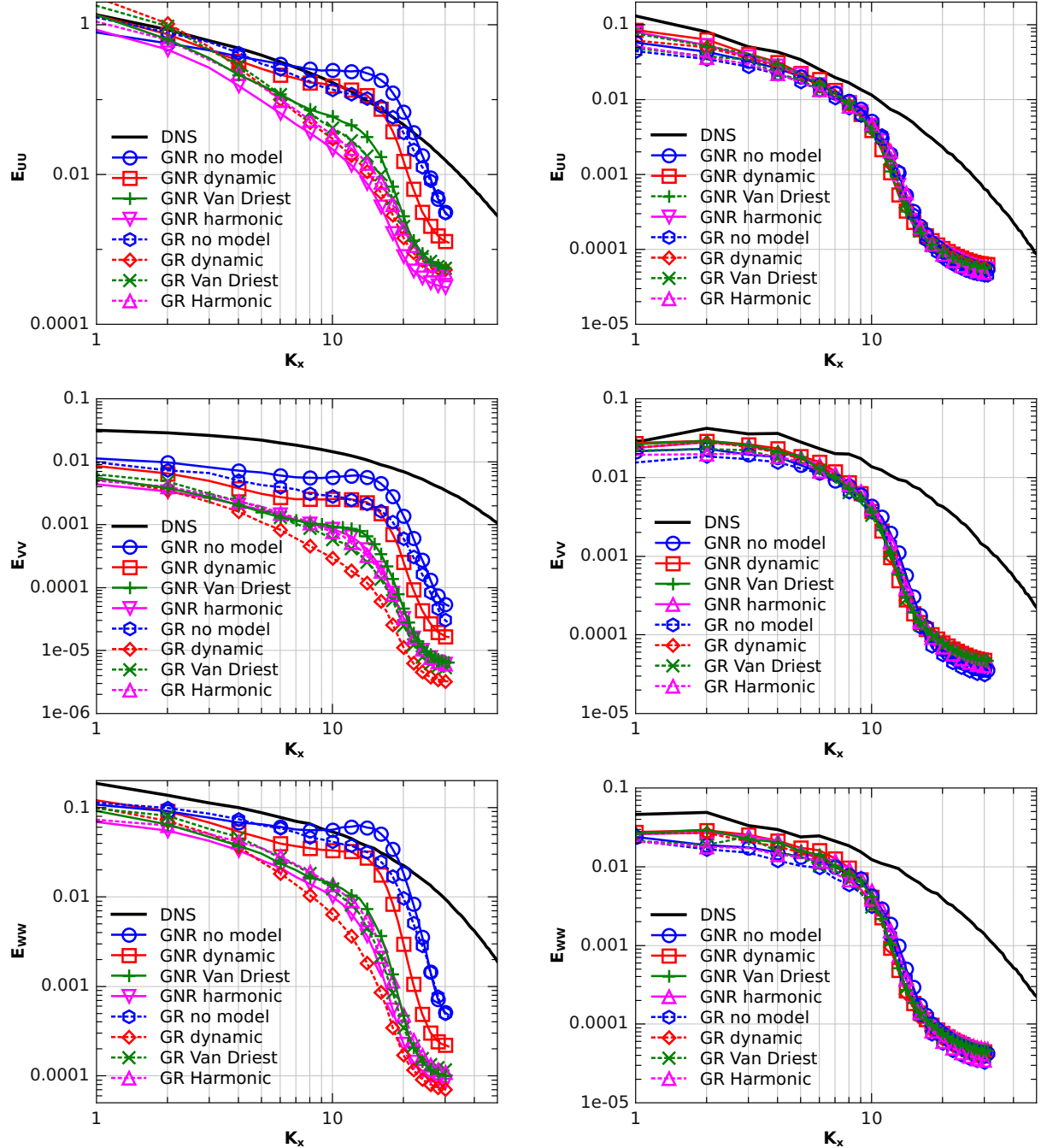


Figure 4.6: Spectra of stream-wise (up), normal (middle) and span-wise (bottom) velocities at  $y^+ = 18$  (left) and at  $y^+ = 590$  (right) along the stream-wise direction. TransAT results.

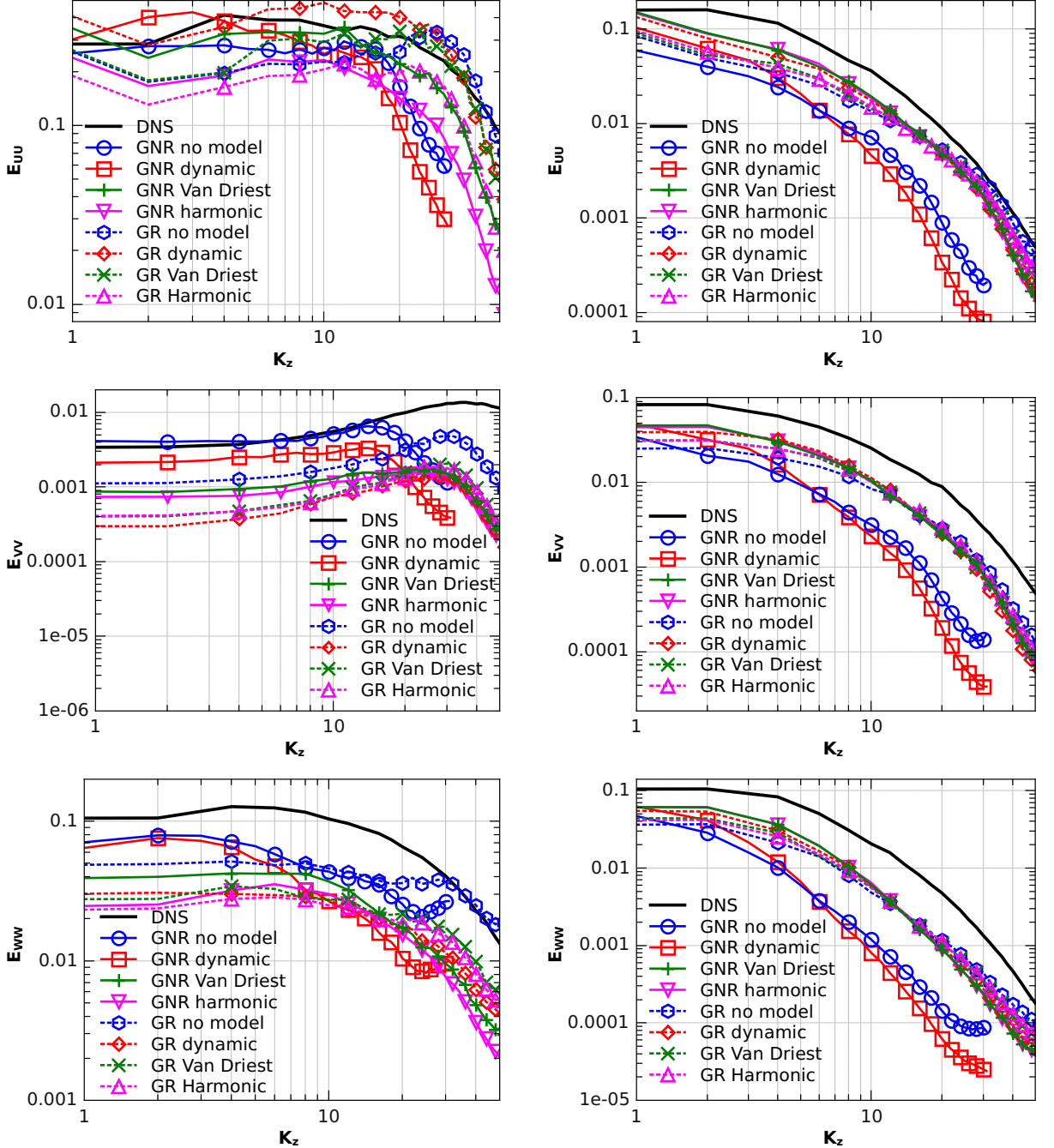


Figure 4.7: Spectra of stream-wise (up), normal (middle) and span-wise (bottom) velocities at  $y^+ = 18$  (left) and at  $y^+ = 590$  (right) along the span-wise direction. TransAT results.

the cases it is quite clear that LES are not capable to predict the frequencies above  $K_x = K_z \approx 10$ . This is a direct consequence of the filtering operation. However also for lower frequencies the results are not always well predicted. Again the coarse simulation with the dynamic model and without models perform very differently from the other simulations but in this case, they result in spectra closer to the ones from DNS. This means that the higher fluctuations and energies in smaller eddies predicted by these simulations near the wall, result in lower overall accuracy of the mean flow rate and of the structures in the centre of the channel.

### 4.2.3 Instantaneous flow field

A comparison between the different LES configurations can be carried out by looking at the instantaneous vorticity and velocity magnitude in the  $x - y$  plane of the channel, reported in Fig. 4.8. In the first two pictures in the top part of the figure, the coarser grid is used with respectively the dynamic and the harmonic damping model. In the bottom part the finer grid is used with the harmonic damping and without SGS models. The different resolution of the grids can be easily seen looking at the vorticity structures of the flow. The different mean flow rate is also visible in the centre of the channel. It is important to highlight here that the harmonic damping model seems to destroy part of the structures in the near-wall region because of its bigger SGS viscosity. The dynamic model seems to retain more structures. Therefore the approximation of this laminar near-wall region results in different shear stresses at the wall and different flow rates.

## 4.3 Benchmark

In this section the results from the collaborative test case of the *LESinItaly* group (<http://cfd.caspur.it>) are reported, from the work of Denaro et al. [2011]. The following groups have been involved in the project:

*FD-based*: spectral/finite differences code used by Abbá (Politecnico di Milano) and Germano (Politecnico di Torino).

*Fluent*: finite volumes commercial code used by Inzoli, Colombo and Lampitella (Politecnico di Milano)

*Openfoam*: finite volumes open-source code used by Aprovitola and Marra (CNR)

*FV-based*: finite volumes in-house code used by Denaro (Università di Napoli)

*Code\_Saturn*: finite volumes open-source code used by Rolfo (University of Manchester)

*Spectral-based*: in-house spectral code used by Marchioli and Soldati (Università di Udine) and Salvetti (Università di Pisa). Results not available.

*FD/Spectral-based*: mixed spectral/finite volumes code used by Iovieno and Tordella (Politecnico di Torino). Results not available.

In general a huge variability has been found in the results, in particular in the predicted mean flow rate. This demonstrates that this test case, even if it is well-known and based on a very simple geometry, can highlight the different capabilities of the codes and the models to predict the macroscopic behaviour of the flow. This is because, as already reported, the mean flow rate is not directly imposed but implicitly given by the constant pressure gradient and small errors in the approximations of small scales near the wall can highly affect the results in terms of mean flow rate.

Figure 4.9 shows the results of the simulations with the coarser grid GNR, obtained by the different codes with and without sub-grid scale models, in terms of mean velocity profiles. The same comparison is performed in Fig. 4.10 for the finer grid GR. The results clearly indicates that the global performance of finite volume codes are not as accurate as spectral or mixed-spectral codes. However the latter are generally very difficult to extend to complex flows and geometries therefore the rigorous validation of commercial finite volume codes for simple geometries is an important and issue that cannot be underestimated. This has been done in this part of the work for TransAT code and similarly other works has been carried out recently for other codes (e.g., Lampitella et al. [2011]).

## 4.4 Conclusions

Different LES models have been tested against DNS data in a periodic channel flow with  $Re_\tau = 590$ . The setup of the test case, imposing a constant pressure forcing without imposing directly a mean flow rate, is such that the drawback and the differences of LES models become evident, mainly looking at the predicted mean flow rate and mean velocity profile of the flow. This is in fact an essential quantity from an engineering point of view because it is directly related to the boundary layer approximation and, in particular, the shear stress at the wall. The results evidence that LES is very sensitive to different model parameters, as well as numerical schemes and grids. This means that, when extended for different complex test cases, a simple extrapolation of model and parameters from simpler cases is not guaranteed to perform adequately.

In these results, the central scheme was found to be able to describe the turbulent behaviour of the flow, while QUICK and HLPA schemes produces respectively spurious oscillations or high numerical viscosity. The Smagorinsky model better predicts mean velocity profiles than the dynamic model, especially when coupled

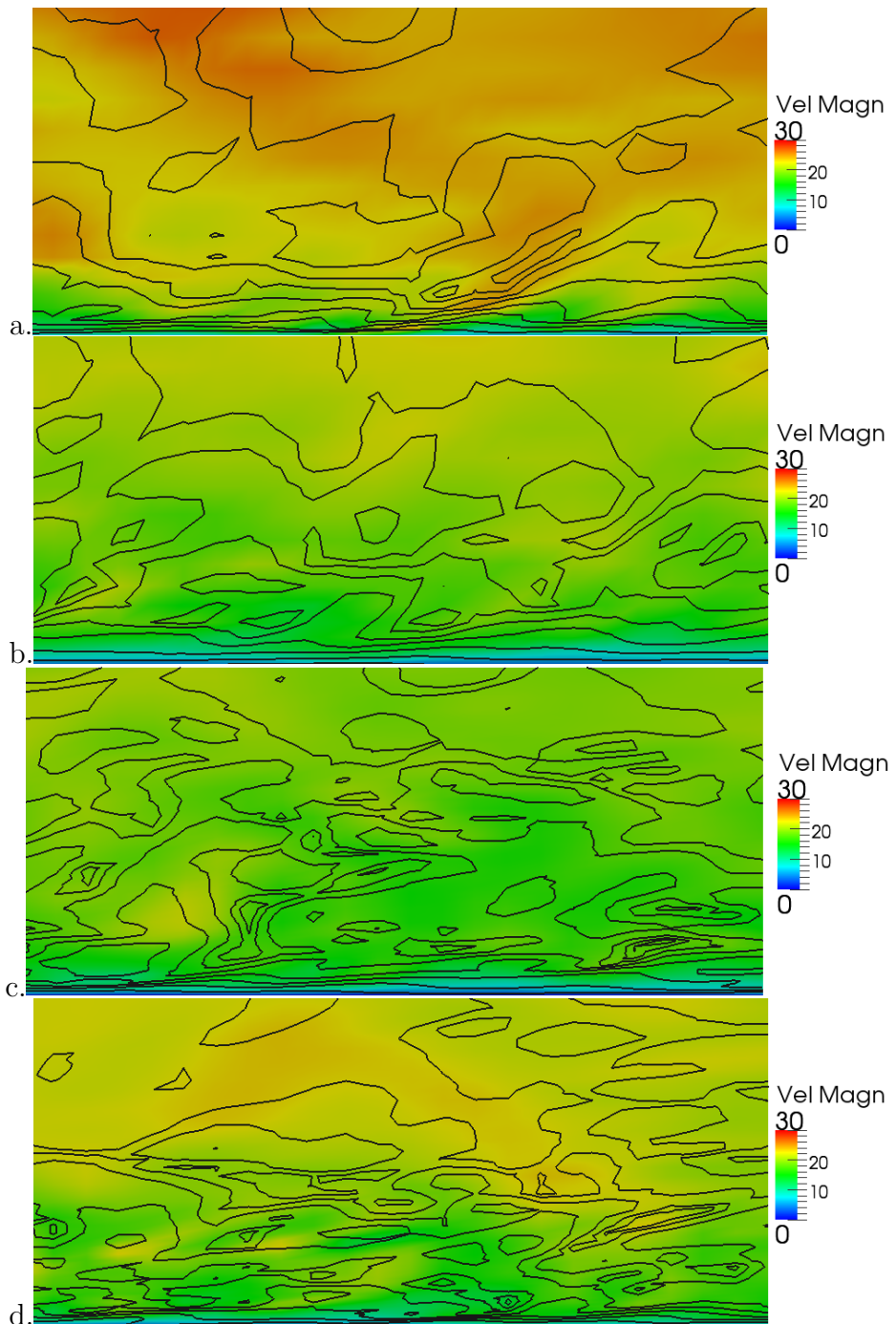


Figure 4.8: Instantaneous flow field for different simulation setups. Velocity magnitude with iso-lines of vorticity magnitude. From top to bottom: GNR with dynamic model (a), GNR with harmonic damping (b), GR with harmonic damping (c), GR without models (d).

#### 4.4 – Conclusions

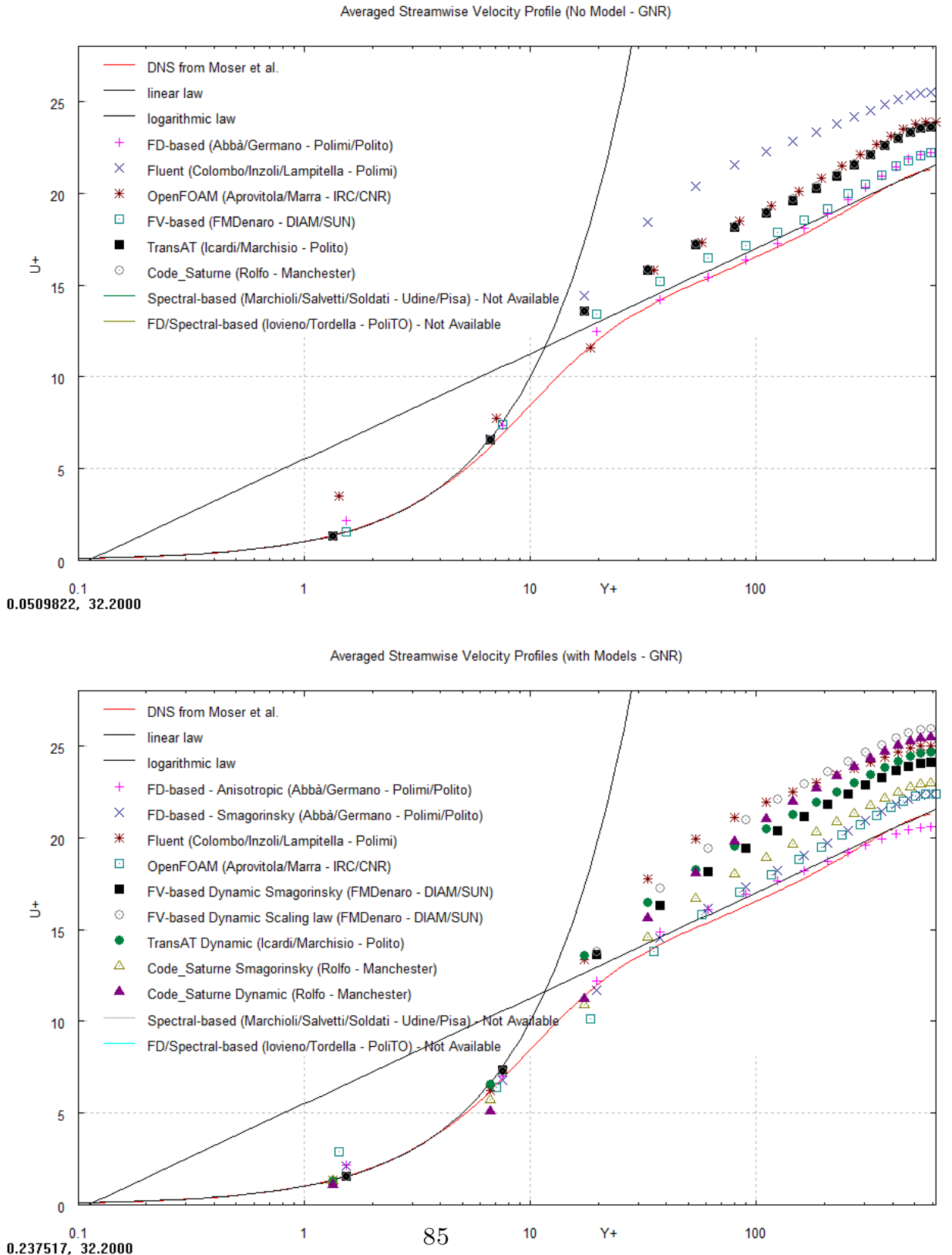


Figure 4.9: Mean velocity profiles of LES simulations with grid GNR with (bottom) and without (top) sub-grid scale models. Comparison of different codes.

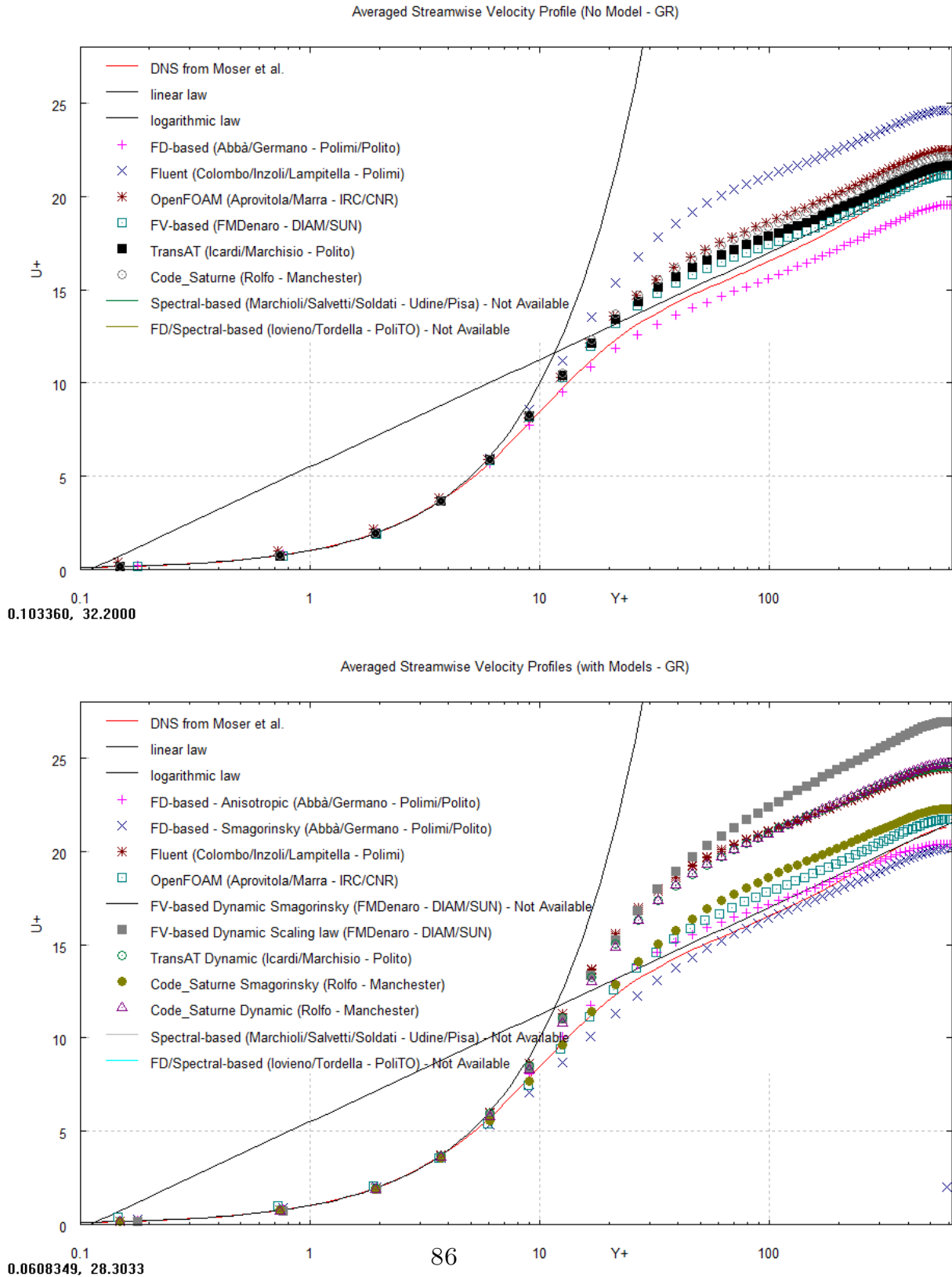


Figure 4.10: Mean velocity profiles of LES simulations with grid GR with (bottom) and without (top) sub-grid scale models. Comparison of different codes.

with an harmonic damping, that limits the SGS viscosity in the near wall region, similarly to the classical Van Driest damping but with a slower rate and without going exactly to zero at the wall. When a grid with higher resolution in the wall normal direction is used, the simulations shows qualitatively similar results. This seems to be related to the fact that the span-wise resolution can be also very important in wall bounded flows.

## References

- Ascomp GmbH. *Multi-Fluid Navier-Stokes Solver TransAT User Manual*, 2009.
- R. Bouffanais. Advances and challenges of applied large-eddy simulation. *Comput. Fluids*, 39(5):735–738, 2010.
- F. Denaro. What does finite volume-based implicit filtering really resolve in large-eddy simulations? *J. Comput. Phys.*, 230(10):3849–3883, 2011.
- F. Denaro, A. Abbá, M. Germano, M. Icardi, D. L. Marchisio, S. Rolfo, P. Lampitella, E. Colombo, F. Inzoli, A. Aprovitola, F. S. Marra, M. Iovenno, and D. Tordella. A comparative test for assessing the performances of large-eddy simulation codes. In *Atti XX Congresso dell'Associazione Italiana di Meccanica Teorica e Applicata, Bologna*, 2011.
- C. Fureby and F. Grinstein. Monotonically integrated large eddy simulation of free shear flows. *AIAA J.*, 37(5):544–556, 1999.
- M. Germano. A proposal for a redefinition of the turbulent stresses in the filtered Navier-Stokes equations. *Phys. Fluids*, 1986.
- M. Germano, U. Piomelli, P. Moin, and W. Cabot. A dynamic subgrid-scale eddy viscosity model. *Phys. Fluids A*, 3(7):1760–1765, 1991.
- F. Grinstein, L. Margolin, and W. Rider. *Implicit large eddy simulation: computing turbulent fluid dynamics*. Cambridge University Press, 2007.
- S. Hoyas and J. Jiménez. Scaling of the velocity fluctuations in turbulent channels up to  $re=2003$ . *Phys. Fluids*, 18(1):011702, 2006.
- J. Jiménez. Computing high-reynolds-number turbulence: will simulations ever replace experiments? *J. Turb.*, page N22, 2003.
- J. Jiménez and R. D. Moser. What are we learning from simulating wall turbulence? *Philos. Trans. R. Soc. A*, 365(1852):715–732, 2007.
- J. Kim, P. Moin, and R. Moser. Turbulence statistics in fully developed channel flow at low reynolds number. *J. Fluid Mech.*, 177:133, 1987.
- P. Lampitella, E. Colombo, and F. Inzoli. Sensitivity analysis on numerical parameters for large eddy simulation with an unstructured finite volume commercial code. In *Atti XX Congresso dell'Associazione Italiana di Meccanica Teorica e Applicata, Bologna*, 2011.
- B. P. Leonard. A stable and accurate convective modelling procedure based on quadratic upstream interpolation. *Int. J. Mech. Sci.*, 16:183–308, 1976.

- N. N. Mansour, J. Kim, and P. Moin. Reynolds-stress and dissipation-rate budgets in a turbulent channel flow. *J. Fluid Mech.*, 194:15, 1988.
- L. Margolin, W. Rider, and F. Grinstein. Modeling turbulent flow with implicit les. *J. Turbul.*, 7:1–27, 2006.
- P. J. Mason and N. S. Callen. On the magnitude of the subgrid-scale eddy coefficient in large-eddy simulations of turbulent channel flow. *J. Fluid Mech.*, 162:439–462, 1986.
- J. Meyers and P. Sagaut. Is plane-channel flow a friendly case for the testing of large-eddy simulation subgrid-scale models? *Phys. Fluids*, 19(4):048105, 2007.
- P. Moin and J. Kim. Numerical investigation of turbulent channel flow. *J. Fluid Mech.*, 118:341–377, 1982.
- R. Moser, J. Kim, and N. Mansour. Direct numerical simulation of turbulent channel flow up to  $re=590$ . *Phys. Fluids*, 11(4):943–945, 1999.
- U. Piomelli, P. Moin, and J. H. Ferziger. Model consistency in large eddy simulation of turbulent channel flows. *Phys. Fluids*, 31(7):1884–1891, 1988.
- S. Pope. Ten questions concerning the large-eddy simulation of turbulent flows. *New J. Phys.*, 6, 2004.
- S. B. Pope. *Turbulent Flows*. Cambridge University Press, Cambridge, 2000.
- J. Smagorinsky. General circulation experiments with the primitive equations. *Mon. Weather Rev.*, 91(3):99–164, 1963.
- E. R. Van Driest. On turbulent flow near a wall. *J. Aeronaut. Sci.*, 23(11):1007–1011, 1956.
- H. Werner and H. Wengle. Large-eddy simulation of turbulent flow over and around a cube in a plate channel. In *8th Symposium on Turbulent Shear Flows*, Munich, Germany, 1991.
- J. Zhu. A low-diffusive and oscillation-free convection scheme. *Commun. Appl. Numer. Methods*, 7(3):225–232, 1991.

## Validation of a LES model for micro-reactor flows

This part of the work focuses on the prediction of the turbulent flow in a three-dimensional Confined Impinging Jets Reactor (CIJR) with a cylindrical mixing chamber by using Large Eddy Simulation (LES). The results and conclusions derived in the previous chapters are here applied to a particular test case. Three dimensional unsteady simulations with different sub-grid scale models, numerical schemes and boundary conditions are performed for various flow rates, covering different flow regimes. The Immersed Surfaces Technique (IST), used to simulate solid wall of the reactor is here derived in details. First, a qualitative analysis of the flow field is carried out and then predictions of the mean and fluctuating velocities are compared with micro Particle Image Velocimetry ( $\mu$ PIV) data. Good agreement is found both for the mean velocity components and the fluctuations. For low to moderate Reynolds numbers the sub-grid scale model is found not to be very relevant, since small scales are of less importance, as long as scalar transport and chemical reaction are not in play. An important finding is the good prediction of the high velocity fluctuations detected in particular at higher Reynolds number due to the natural instability of the system, strongly enforced by the jets unsteadiness.

### 5.1 Introduction

In many chemical/process engineering fields (e.g., pharmaceutical, cosmetics, pesticides, etc.) there is a strong interest in micro- and nano-particles [Gesquiere et al., 2005, Horn and Rieger, 2001, Kipp, 2004, Le Roy Boehm et al., 2000, Müller, 1998, Müller et al., 2002, Qiu Zhao et al., 2003, Romanus, 2002, Salata, 2004]. These

---

Part of the contents of this chapter has been published in the work of Icardi et al. [2011].

particles are generally produced via precipitation processes in particular types of passive mixers, such as the Confined Impinging Jets Reactor (CIJR) [Liu et al., 2009] or the multi-inlet vortex reactor [Cheng et al., 2009, Lince et al., 2009, Liu and Fox, 2006, Liu et al., 2008]. CIJRs are indeed widely used nowadays and are preferred over other geometries due to their high mixing efficiency. In all these processes it is very important to control the properties of the particles, namely their Particle Size Distribution (PSD), shape and morphology, as well as composition [Johnson and Prud'homme, 2003, Lince et al., 2008, Marchisio et al., 2006, 2008]. The PSD is indeed strongly dependent on the mixing rate, and very fine particles with very narrow distributions are obtained only under extremely efficient mixing conditions. The design, optimisation and scale-up of these devices can be efficiently investigated through computational fluid dynamics (CFD). However, the simulation of the flow field and mixing dynamics is often complicated by the fact that, under typical operating conditions and due to their small geometry, the flow is usually in the transitional regime. The first important step of the CFD analysis is to obtain a deep understanding of the flow field and turbulent phenomena inside the reactors which strongly influence the chemical reactions, particles formation and their interactions. In this type of reactors, the particles have a very small size, a density very similar to the fluid (i.e. water) and they are very dilute, so that they usually have a negligible influence on the final flow and turbulent fields. Generally the results of single-phase simulations can be extended to the multiphase real system. For these reasons the results of this work are limited to the non-reactive single-phase case, which can be compared to experimental  $\mu$ PIV data, obtained with a single fluid without reactions.

Many studies on the flow field in these devices and reactors have been carried out with steady-state Reynolds-Average-Navier-Stokes (RANS) simulations [Feng et al., 2005, Gavi et al., 2010, Liu and Fox, 2006, Marchisio et al., 2006] with different turbulence models. This approach is computationally efficient and it can result in reasonably good agreement with experimental data; however it cannot capture the truly unsteady behaviour of the flow that could be very important, especially when chemical reactions are considered. In these cases this approach has to be abandoned and other more sophisticated techniques, such as Direct Numerical Simulation (DNS) and Large Eddy Simulation (LES) should be adopted instead.

DNS can be used, for example, in order to obtain reliable and detailed data on these systems [Schwertfirm et al., 2007] (see also Chap. 3). In this case, in fact, no approximation is made in the computational model and the governing Navier-Stokes equations are directly solved, therefore they can be considered as virtual experiments and can be used to develop RANS and LES closures. DNS is widely used for flows characterised by low and moderate Reynolds numbers and can be employed for both theoretical and applied research. However, since it could be very expensive in terms of simulation times, especially when it comes to the description of realistic geometries and flow conditions, it cannot be employed in many industrial

and practical applications. Another important limitation of DNS becomes apparent when scalar concentrations have to be calculated for a liquid in the turbulent regime. In this case the smallest length-scales of fluctuations in scalar concentrations (i.e., the Batchelor scale) can be much smaller than the Kolmogorov scale (i.e., the smallest scales of velocity fluctuations) [Fox, 2003] and grids that can resolve the Batchelor scale are still intractable from a practical point of view. For these reasons the research on turbulence models is still an open and interesting issue, especially when applied to turbulent reactive flows. It is in this spirit that the present work has been undertaken.

As already discussed in Sec. 2.1 and in Chap. 4, an interesting alternative to DNS is LES [Cheng et al., 2009, Gavi, 2009, Marchisio, 2009]. With this approach, only the larger scales, containing most of the energy and responsible for the main transport properties, are solved with an appropriate sub-grid scale (SGS) model. These simulations can be also very expensive compared to RANS (although less expensive than DNS) because they are inherently time-dependent and three-dimensional, but they have recently become very attractive due to increased computing capabilities.

In this chapter of the thesis the analysis of the flow field in a CIJR with LES for a single-phase non-reactive test-case is discussed and LES predictions are validated against experimental measurements. The experiments on the CIJR used here for model validation (see Chap. 3) [Gavi, 2009] were obtained with the micro Particle Image Velocimetry ( $\mu$ PIV) technique.  $\mu$ PIV is an extension of Particle Image Velocimetry (PIV) developed to study micro-devices [Meinhart et al., 1999, Santiago et al., 1998]. In a typical  $\mu$ PIV system [Li and Olsen, 2006], the microfluidic device of interest is imaged using an inverted fluorescence microscope. Fluorescent seed particles are illuminated by a double-pulsed Nd:YAG laser and the emitted light from the particles is imaged onto a CCD camera. The images are analysed using a cross-correlation technique and an instantaneous velocity vector field is obtained. For more details about  $\mu$ PIV the reader is referred to a recent review [Lindken et al., 2009]. It is important to highlight here that these measurements are conducted in a three-dimensional device in a turbulent regime. These conditions make the experimental setup extremely difficult and results cannot be simply filtered to neglect spurious fluctuations caused by experimental errors. DNS carried out on the very same system in Chap. 3 demonstrates that detailed boundary conditions are crucial to simulate the real experimental behaviour and an accurate approximation was proposed. Starting from these results, the objective of this work is to build and validate a LES tool to predict the fluid dynamics in the CIJR to avoid the use of expensive DNS. This will be of particular importance in a later stage of this work when computational models for scalar transport, chemical reactions and particles formation will be added.

The chapter is organised as follows. Firstly the theoretical background and concepts of turbulent flow simulation and numerical methods are presented, followed by

a description of the operating and boundary conditions. The results are then discussed and compared with the available experimental data. Finally some conclusions are drawn and future steps are envisioned.

## 5.2 Model description

### 5.2.1 Fluid flow equations

The single phase flow inside the CIJR is investigated by solving the incompressible Navier-Stokes equations (see Sec. 2.1).

In these flows, although the inflow conditions are laminar, the jet impingement creates strong flow instabilities and spatial variations that lead to turbulence (i.e., flow containing a wide range of time and length-scales), and when the computational grid is not fine enough to resolve all the scales arising from the interaction of the jets, a model is required to represent their effect on the macro-scale flow.

The governing equations are solved, either within the RANS framework, in which flow variables are decomposed into an average and a fluctuating term, and only the average field is described, or in a filtered form (LES), where flow variables appear as filtered quantities. In the LES framework, the filtered velocity for example becomes [Pope, 2000]

$$\bar{\mathbf{U}}(\mathbf{x}, t) = \int G(\mathbf{r} - \mathbf{x}) \mathbf{U}(\mathbf{r}, t) d\mathbf{r}, \quad (5.1)$$

where  $G$  is the filter function. The most common filter is the so-called “box filter”, which directly makes use of the finite-volume approximation of the spatial operators. The application of Eq. 5.1 to the momentum equation results in a closure problem, namely the residual stress tensor [Pope, 2000]

$$\tau_{ij}^r = \bar{U}_i \bar{U}_j - \bar{U}_i \bar{U}_j - \frac{1}{3} (\bar{U}_i \bar{U}_i - \bar{U}_i \bar{U}_i), \quad (5.2)$$

that needs to be modelled in terms of macro-scale flow variables by using a SGS model.

The simplest SGS model is the so-called “constant Smagorinsky” model [Smagorinsky, 1963] in which the residual stress terms are modelled as

$$\tau_{ij}^r = -2 (C_S \Delta)^2 |\bar{S}| \bar{S}_{ij}, \quad (5.3)$$

where  $\Delta$  is the bandwidth of the filter,  $\bar{S}_{ij}$  is the filtered strain rate,  $|\bar{S}|$  is its norm and  $C_S$  is the Smagorinsky constant. Other SGS models have been developed, and one of the most popular is the dynamic model of Germano [Germano et al., 1991], proposed to dynamically predict a wider range of flow regimes, from transitional to “fully developed” turbulence.

### 5.2.2 Numerical methods

Computations are carried out with the commercial CFD code *TransAT* [Ascomp GmbH, 2009]. The equations are solved with a finite-volume approximation and solid boundaries are represented with the Immersed Surfaces Technique (IST) [Ascomp GmbH, 2009]. In this numerical technique, similarly to the immersed boundary methods [Mittal and Iaccarino, 2005], the grid cells intersects the solid walls without fitting to them. To impose the no-slip condition, instead of using a penalty approach, it makes use of an implicit representation of the walls by defining of a level set function ( $\phi_s$ ). It is a signed distance function positive in the solid phase and negative in the fluid phase and null on the fluid-solid interface. The equations in the solid and fluid domain are combined using a smoothed Heaviside function:

$$H(\phi_s) = \frac{1}{2} \left( 1 - \tanh \left( \frac{2\phi_s}{\delta_{sf}} \right) \right), \quad (5.4)$$

which varies between one (in the fluid phase) and zero (in the solid phase) and takes intermediate values in the fluid-solid finite interface of thickness  $\delta_{sf}$ . The final density  $\rho$  and velocity  $U_i$  can be formally defined as

$$\rho = H\rho^f + (1 - H)\rho^s, \quad (5.5)$$

$$\rho U_i = H\rho^f U_i^f + (1 - H)\rho^s U_i^s, \quad (5.6)$$

where  $U_i^f$  and  $\rho^f$  are respectively the fluid velocity and density and  $U_i^s$  and  $\rho^s$  are the corresponding values for the solid.

For the solid phase the following equations are solved [Ascomp GmbH, 2009]:

$$\frac{\partial \rho^s}{\partial t} + \frac{\partial}{\partial x_j} (\rho^s U_j^s) = 0, \quad (5.7)$$

$$\frac{\partial}{\partial t} (\rho^s U_i^s) + \frac{\partial}{\partial x_j} (\rho^s U_i^s U_j^s) = 0. \quad (5.8)$$

For the case of non-moving immersed surfaces, the solid phase velocity is set equal to zero ( $U_i^s = 0$ ) whereas the standard Navier-Stokes equations are solved for the fluid phase:

$$\frac{\partial \rho^f}{\partial t} + \frac{\partial}{\partial x_j} (\rho^f U_j^f) = 0, \quad (5.9)$$

$$\frac{\partial \rho^f U_i^f}{\partial t} + \frac{\partial}{\partial x_j} (\rho^f U_i^f U_j^f) = -\frac{\partial p^f}{\partial x_i} + \frac{\partial}{\partial x_j} (2\mu^f S_{ij}^f), \quad (5.10)$$

where  $S_{ij}^f$  is the stress tensor and  $\mu^f$  si the fluid viscosity. Summing up the equations of the solid and liquid phase, multiplied by his respective Heaviside functions and

using Eq.s 5.5, the following equations are obtained:

$$\frac{\partial \rho}{\partial t} + \frac{\partial}{\partial x_j} (\rho U_j) = 0, \quad (5.11)$$

$$\frac{\partial \rho U_i}{\partial t} + \frac{\partial}{\partial x_j} (\rho U_i U_j) = -H(\phi_s) \frac{\partial p^f}{\partial x_i} + \frac{\partial}{\partial x_j} (2\mu \partial S_{ij}) - 2\mu^f S_{ij}^f n_j \delta(\phi_s). \quad (5.12)$$

The last term in the RHS is a viscous shear stress at the interface (i.e., the solid wall), where  $n_j$  is the normal to the fluid-solid interface and  $\delta(\phi_s)$  is the Dirac delta function representing the location of the interface. The wall shear itself is modelled as [Beckermann et al., 1999],

$$2\mu^f S_{ij}^f n_j = 2\mu^f \left( \frac{\rho}{\rho^f} \right) \frac{U_i}{H} \delta(\phi_s). \quad (5.13)$$

Since the walls are immersed in a cartesian grid, meshing time is considerably reduced and the accuracy of the numerical scheme can be preserved since the grid-skewness induced diffusion is simply eliminated. These two elements make the IST approach very useful to simulate unsteady turbulent flows in complex geometries.

The pressure-velocity coupling is performed by using the SIMPLEC algorithm [Ferziger and Peric, 2002]. Time discretization is performed with a 3rd order explicit Runge-Kutta scheme. The advective terms are discretised with the HLPA scheme [Zhu, 1991], which combines a second-order upstream-weighted approximation with the first-order upwind differencing under the control of a convection boundedness criterion. This scheme assures good convergence and stability properties but was demonstrated to be not the most suitable for DNS and LES [Denev et al., 2008] where the algorithms must be accurate enough to avoid numerical viscosity/diffusion [Ferziger and Peric, 2002], which represents an additional viscosity “artificially introduced” by discretization errors. For this reason simulations with the QUICK scheme [Leonard, 1976] were also performed.

Two SGS models are used: the Smagorinsky model with a model constant  $C_S = 0.08$ , to limit diffusion in the near-wall region and the dynamic Germano model in its standard formulation. In the wall flow-regions, the Werner-Wengle wall functions [Werner and Wengle, 1989] are used, together with the van Driest damping function [Van Driest, 1956].

### 5.3 Operating and boundary conditions

Figure 5.1 represents the meridian section of the three-dimensional geometry of the CIJR used both for simulations and experiments. It consists of a cylindrical reaction chamber and rounded inlet and outlet tubes. The flow enter the reactor

through two opposing tubes of diameter  $d_j = 1$  mm with a mean velocity  $u_j$ , and then exit through the lower tube of diameter  $2d_j = 2$  mm. The diameter of the reactor is  $D = 4.8$  mm and the total volume of the chamber is approximately  $V = 1.73 \cdot 10^{-7}$  m<sup>3</sup> resulting in very short mean residence times. The flow regime in the reactor can be generally characterised by the jet Reynolds number, based on the inlet jet diameter and the average inflow velocity as

$$Re_j = \frac{u_j d_j \rho^f}{\mu^f}. \quad (5.14)$$

FR, mL/min	$u_j$ , m/s	$\tau_R$ , s	$Re_j$	$\lambda_K$ , $\mu\text{m}$
10	0.105	1.05	62	45
20	0.25	0.44	150	23
40	0.52	0.21	310	14
90	1.01	0.11	600	8
150	1.5	0.074	900	6

Table 5.1: Nominal flow rates, measured mean velocities, mean residence times, jet Reynolds numbers and estimated Kolmogorov micro-scale lengths.

Grid	Cells	Internal cells	$\Delta x$ , $\mu\text{m}$
1	40x40x80	$1 \times 10^5$	100-140
2	68x60x128	$3.5 \times 10^5$	50-80
3	100x84x150	$8.5 \times 10^5$	30-60

Table 5.2: Computational grids used for simulations: grid number, number of internal cells used for computing the flow and cell size.

Fluid properties are selected by reference to the experiments, which employed an aqueous solution of urea with a density  $\rho^f = 1.141$  g/cm<sup>3</sup> and a viscosity  $\mu^f = 1.914$  cPs (this fluid was selected due to its index of refraction which more closely matched the index of refraction of the reactor walls). Five different flow rates were investigated and inlet conditions are reported together with the mean residence time and the estimated Kolmogorov length-scale in Tab. 5.1. The first four conditions are identical to those analysed in Chap. 3. The Reynolds numbers calculated using the inlet diameters and the mean velocities show that the flow regime in the inlet tubes is laminar, thus parabolic velocity profiles have been imposed. Experimental data are available only for the first four Flow Rates (FR = 10, 20, 40, 90 mL/min) and the additional case (FR = 150 ml/min) was included to investigate the effects of numerical schemes and SGS models at higher Reynolds numbers. Due to the

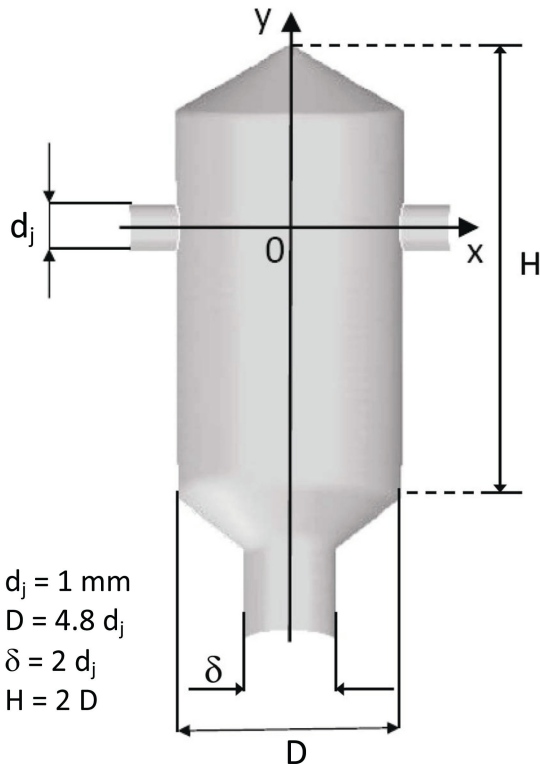


Figure 5.1: Schematic geometry of the CIJR under study.

unavoidable experimental inaccuracies, these flow rates do not correspond exactly to the velocities observed in the inlets, therefore we refer to them as “nominal flow rates”.

In Chap. 3 it has been demonstrated that in the simulations the constant laminar inflows must be modified, superposing a small oscillation proportional to the laminar profile. This was due to the impossibility of maintaining purely steady velocities at the reactor inlets in the experiments. This unsteadiness at the reactor inlets is due to a number of factors, including inherent pump unsteadiness and varying pressure within the reactor due to the unsteady motion of the impingement zone feeding back to cause unsteady inlet flow conditions. Therefore in the present simulations the same oscillating inflows, solely determined by the experimental data, are imposed by using a single harmonic oscillation in both the inflows. They are set to be in phase opposition in order to emphasise the effects of unsteady asymmetric flows. The oscillation was set proportional to the original parabolic profile (to avoid a negative inflow velocity) with amplitude equal to one tenth of the constant velocity to fit the standard deviation obtained in the experiments with  $FR = 10 \text{ mL/min}$ , which is the case where the external instabilities are more evident.

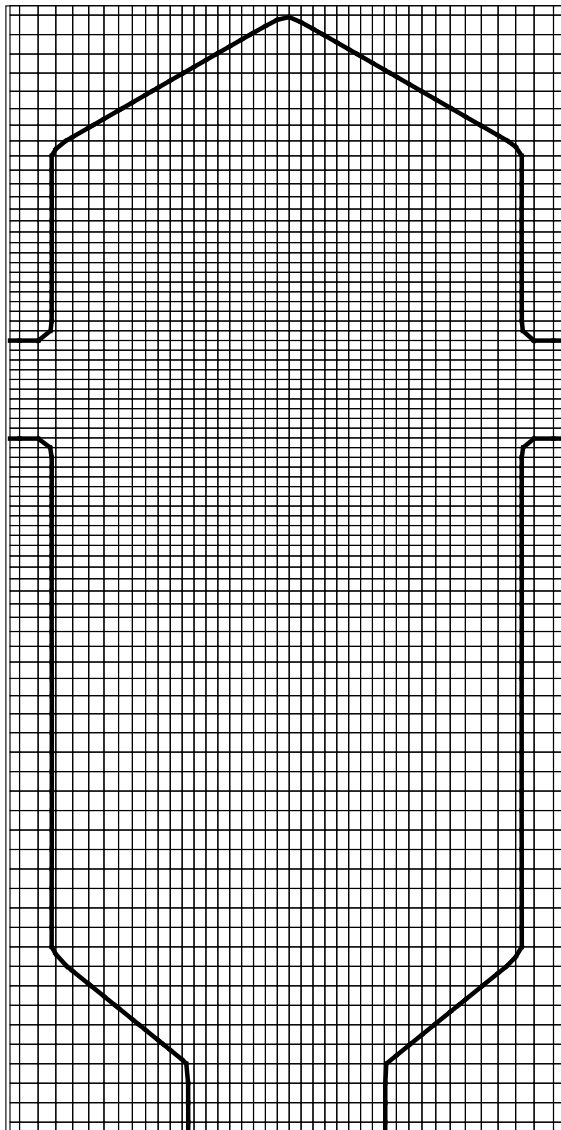


Figure 5.2: The grid used for LES.

Simulations were performed on a Linux workstation ( $4 \times$  Intel(R) Xeon(R) CPU 5160 3.00 GHz) with shared memory parallelism (Open-MP library). Using four processors the speed-up factor was found to be between 2 and 2.5 and approximately one or two days of CPU time were needed to simulate six residence times depending on the FR investigated.

An initial set of simulations was carried out with three different non-uniform Cartesian grids with a total factor of refinement between the smallest and the biggest cell equal to two. The number of total and internal cells (i.e., the grid actually used

in the IST context to compute the flow) and the minimum cell size of the the different grids are reported in Table 5.2. Dimensional analysis and grid sensitivity studies revealed that grid 1 can resolve most of the energy containing scales. In fact the results for this grid in terms of mean and fluctuating velocity are almost equal to the results obtained with grid 2 and grid 3. In particular if  $FR \leq 40$  mL/min, most of the involved scales are resolved and the LES can almost be considered as a DNS. In this case in fact the SGS viscosity is very low and the flow is not fully turbulent. At the higher FR values investigated instead, the SGS model becomes more important. The results reported in this chapter were obtained with grid 1 and a meridian section of the grid is displayed in Fig. 5.2.

Results were compared in the same window captured by  $\mu$ PIV and simulations data were saved and analysed at each time step after that the influence of initial conditions disappeared (i.e, three mean residence times) for a time interval equivalent to three mean residence times for the two lowest FR. For the two highest FR when the flow is more chaotic, the time interval length was chosen longer (six mean residence times) to obtain more accurate statistics. Time steps were chosen adaptively according to convergence conditions and resulted approximately in  $10^4$  time steps for each mean residence time. The spatial resolution in  $\mu$ PIV is defined by the dimensions of the interrogation volume. In the present experiments, the in-plane velocity vector spacing in the PIV measurements was  $140 \mu\text{m}$ , and the out-of-plane dimension of the measurement volume, defined as the depth of correlation [Bourdon et al., 2004, Olsen and Adrian, 2000], was  $47 \mu\text{m}$ . For comparison, the grid cell size in the large eddy simulations was approximately  $100 \mu\text{m}$  in the region investigated.

## 5.4 Results and discussion

Similarly to what reported in Chap. 3 and Chap. 4, simulations are statistically analysed only after transient effects decay, so that the influence of the initial condition has disappeared. First snapshots of the instantaneous flow field from the simulations with  $FR = 90$  ml/min are reported to emphasise the importance of imposing the proper boundary conditions. Then detailed comparisons of the mean velocity  $U_x^{MEAN}$  along the  $x$ -axis, mean velocity  $U_y^{MEAN}$  along the  $y$ -axis and the root mean square (RMS) of fluctuating velocities  $U_x'^{RMS}$  and  $U_y'^{RMS}$  are analysed for each FR with different SGS models and numerical schemes.

### 5.4.1 Instantaneous flow field

Figures 5.3 and 5.4 show two instantaneous velocity magnitude fields with  $FR = 90$  mL/min obtained with different inflow conditions. On the left the simulation is performed by using constant inlet flow rates equal to the nominal one. As it is seen,

a quasi-steady behaviour with large scale fluctuations is observed. On the right the results obtained with the more realistic oscillating inlet flow rates, mimicking the experimental conditions, as shown in DNS in Chap. 3, are shown. As it is possible to see, the variable asymmetric inflow conditions drastically change the flow behaviour, developing more scales, which are not created with constant inflows, even after refining the grid. These different scales are clearly identifiable when looking at the vorticity magnitude reported in Fig. 5.5.

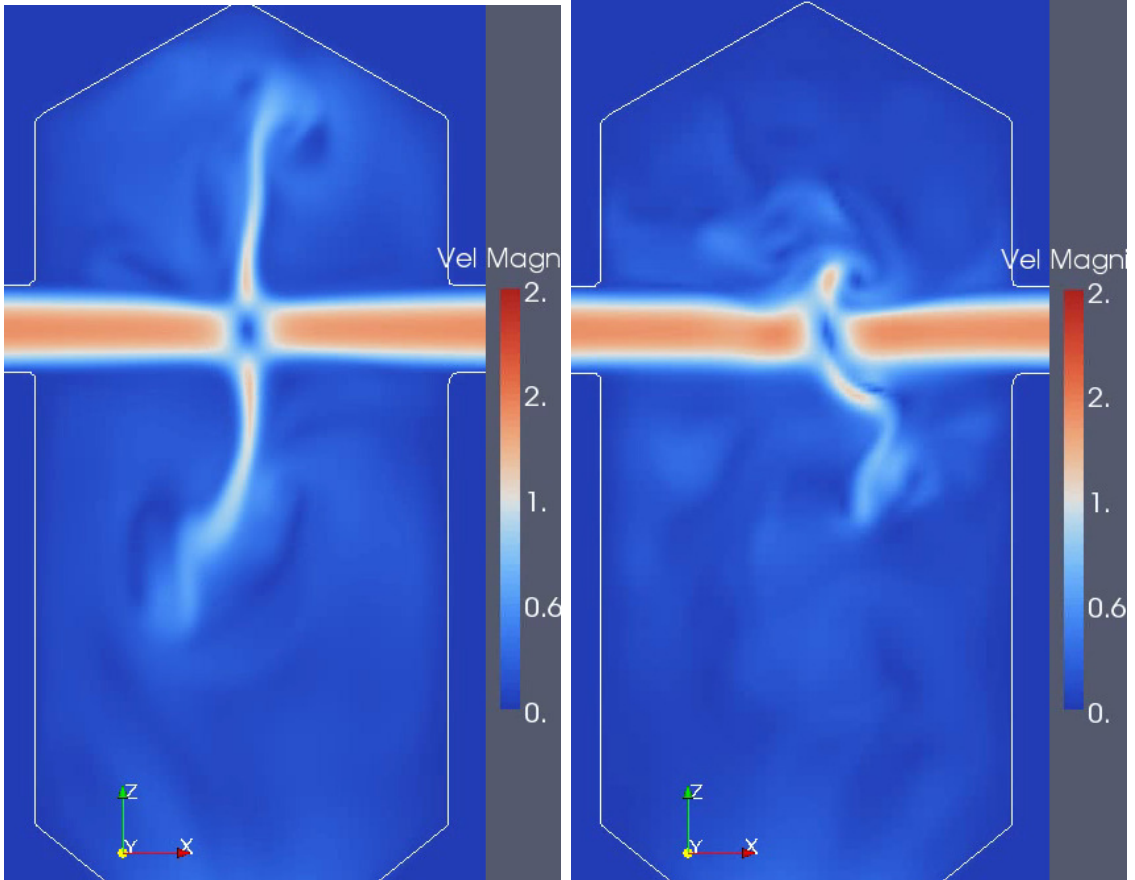


Figure 5.3: Instantaneous velocity magnitudes with  $FR = 90 \text{ mL/min}$  and constant symmetric inflows ( $\Delta t = 0.1$ ).

Vorticity is a good indicator of the flow structures and scales created and dissipated and their interaction with the local shear. The image on the left, taken from the constant inflow simulation, shows the onset of large structures created at impingement. The image on the right, taken from the variable inflows simulation, reveal the existence of smaller scales, generated from the breakup of the larger ones, responsible for the dissipation mechanism of turbulence. As will be highlighted later, this process of creation/destruction of flow scales followed by small

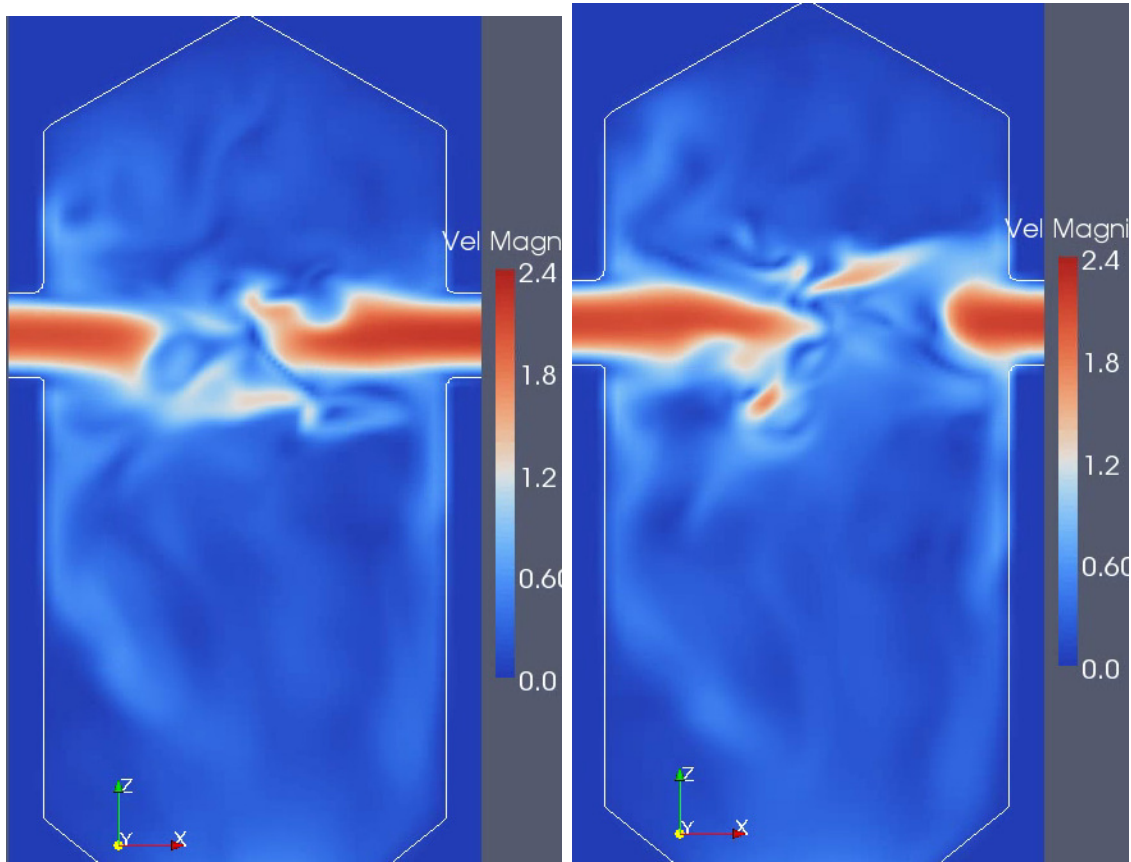


Figure 5.4: Instantaneous velocity magnitudes with FR = 90 mL/min and constant symmetric inflows ( $\Delta t = 0.1$ ).

scale vorticity generation is very important to guarantee good mixing conditions. This analysis shows the importance of using accurate boundary conditions. As already mentioned, our previous work (based on comparison between DNS and  $\mu$ PIV) showed that only by employing these boundary conditions with small oscillations, good agreement with experimental data is obtained. Therefore in what follows only results obtained with oscillating inflows are reported.

### 5.4.2 Flow statistics

The comparison with experiments can be carried out by analysing the statistics of the flow along the inlet and outlet axes near the impinging point. This is in fact the region where the most important phenomena occur. Figure 5.6 shows the mean  $x$ - and  $y$ -velocity components and the root-mean-square (RMS) of fluctuations along the  $x$  and  $y$  directions. LES predictions obtained with the constant SGS

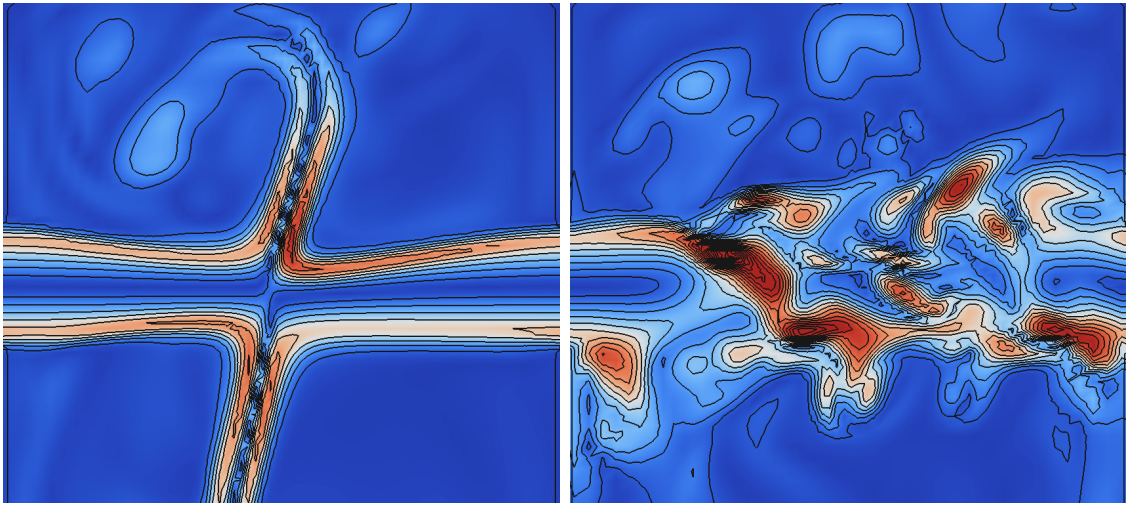


Figure 5.5: Details of instantaneous vorticity magnitudes in the center of the reactor with  $FR = 90 \text{ mL/min}$ : comparison between constant inflows (left) and unsteady asymmetric inflows (right).

model together with the HLPA scheme (continuous line) are compared with the predictions obtained with constant Smagorinsky with the QUICK scheme (dashed line) and with predictions obtained with the dynamic SGS model by Germano with the HLPA scheme (dotted line). No significant differences were observed within the three modelling and numerical options because at this FR the flow is quite uniform. However, as can be observed by comparing simulations with experimental results (represented with open symbols), LES is capable to approximate both first order (i.e., mean velocities) and the second order (i.e., RMS of velocity fluctuations) statistics.

An increase in the inflow velocity triggers the onset of a more unsteady flow regime and a weakly turbulent behaviour can be observed. In particular with intermediate flow rates ( $FR = 20\text{-}40 \text{ mL/min}$ ) the flow starts to naturally oscillate but the amplitude and positions of oscillations would not be captured if constant boundary conditions were used. These operating conditions result in a transitional regime (between laminar and turbulent). The energy-containing cascade is not fully developed and this results in less accurate predictions.

In Fig. 5.7, predictions are compared to experiments for  $FR = 20 \text{ mL/min}$ . Although  $x$ -fluctuations are overestimated, causing big fluctuations of the impingement plane and therefore smaller mean  $y$ -velocity at  $x = 0$ , the overall behaviour of the system is decently predicted. At this FR the difference between HLPA and QUICK schemes seems to be more evident in the propagation of oscillations along the  $x$ -direction, that the latter one seems to preserve, diffusing less than the former.

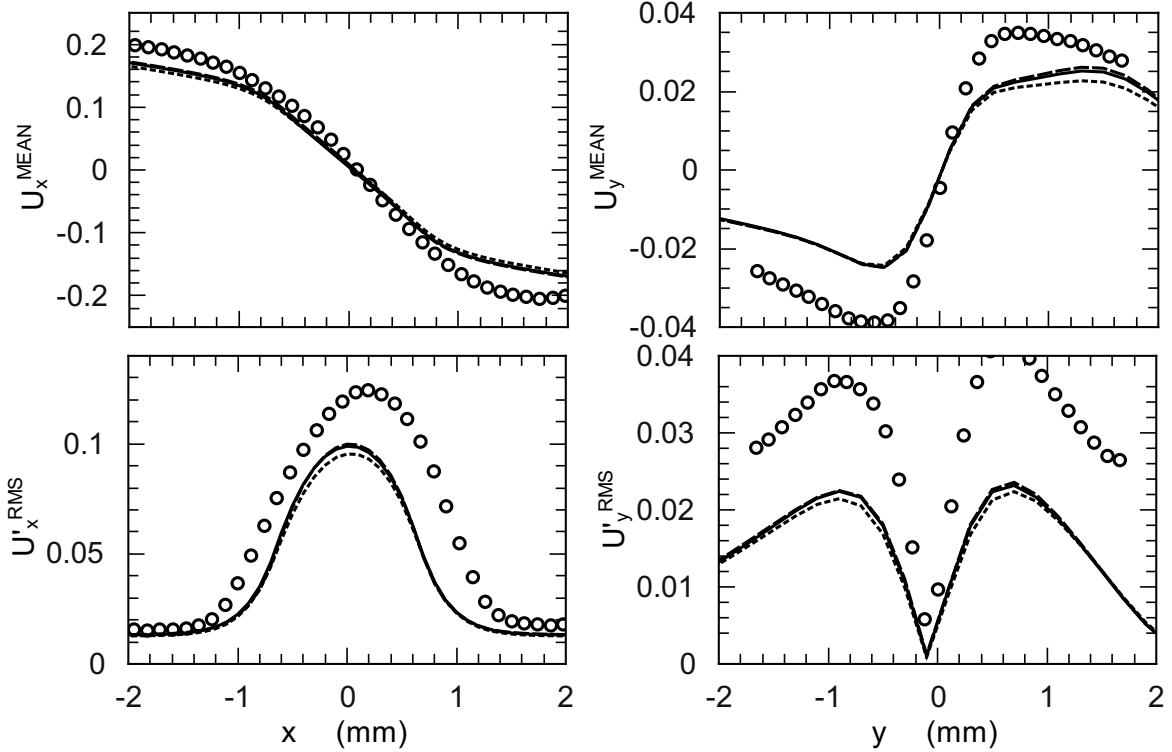


Figure 5.6: Flow statistics with  $FR = 10 \text{ mL/min}$ : Comparison between  $\mu\text{PIV}$  experiments (symbols), LES with HLPA scheme and constant SGS model (continuous line), LES with QUICK scheme and constant SGS model (dashed line), LES with HLPA scheme and dynamic SGS model (dotted line). From left to right and top to bottom: mean  $x$ -velocity along the  $x$ -axis at  $y = 0 \text{ mm}$ , mean  $y$ -velocity along the  $y$ -axis at  $x = 0 \text{ mm}$ , RMS of  $x$ -velocity fluctuations along the  $x$ -axis at  $y = 0 \text{ mm}$ , RMS of  $y$ -velocity fluctuations along the  $y$ -axis at  $x = 0 \text{ mm}$ .

It should be mentioned that for  $FR$  values greater than  $40 \text{ mL/min}$ , the experimental uncertainties starts to become more and more important. This is partially related to the curved shape of the reactor walls as well as the small dimension of the device that make it very difficult to perfectly centre the observation plane. For example, one side of the piece of Plexiglas in which the reactor chamber is embedded is machined flat to rest on the microscope stage. Any misalignment of this machined side with the centre plane of the reactor where the inlet jets impinge will cause some discrepancies when the data are compared with centre-plane simulation data. Moreover, as the  $FR$  is increased, it becomes more difficult for the pumps to guarantee perfectly constant and balanced flow rates. As a matter of fact, although the experimental data were obtained with state of the art equipments and

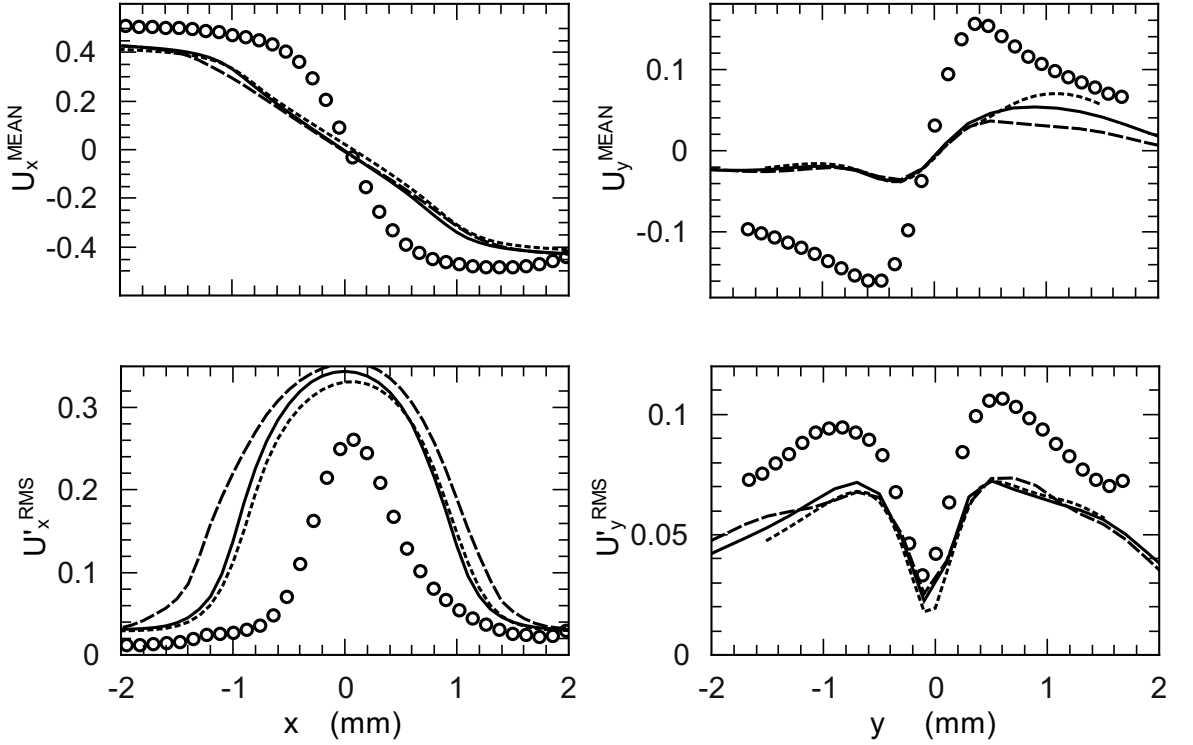


Figure 5.7: Flow statistics with  $\text{FR} = 20 \text{ mL/min}$ : Comparison between  $\mu\text{PIV}$  experiments (symbols), LES with HLPA scheme and constant SGS model (continuous line), LES with QUICK scheme and constant SGS model (dashed line), LES with HLPA scheme and dynamic SGS model (dotted line). From left to right and top to bottom: mean  $x$ -velocity along the  $x$ -axis at  $y = 0 \text{ mm}$ , mean  $y$ -velocity along the  $y$ -axis at  $x = 0 \text{ mm}$ , RMS of  $x$ -velocity fluctuations along the  $x$ -axis at  $y = 0 \text{ mm}$ , RMS of  $y$ -velocity fluctuations along the  $y$ -axis at  $x = 0 \text{ mm}$ .

carefully selected operating conditions, some asymmetry and misalignment in the experimental profiles are still detectable (see Figs. 5.8 and 5.9). For example, the stagnation point is no more centred in the chamber therefore the  $y$ -velocity profiles are also misaligned. More details on the experimental work can be found in [Gavi, 2009].

In Fig. 5.8 comparisons for  $\text{FR} = 40 \text{ mL/min}$  are reported. As can be seen, also in this case (as for  $\text{FR} = 20 \text{ mL/min}$ ) the RMS is slightly overpredicted, whereas the predictions for the mean velocities result in better agreement with experiments. This could be due to the approximation of the fluctuating boundary conditions that emphasises the collision instability. The agreement, both for first and second order statistics, significantly improves for the last case for which experimental data are

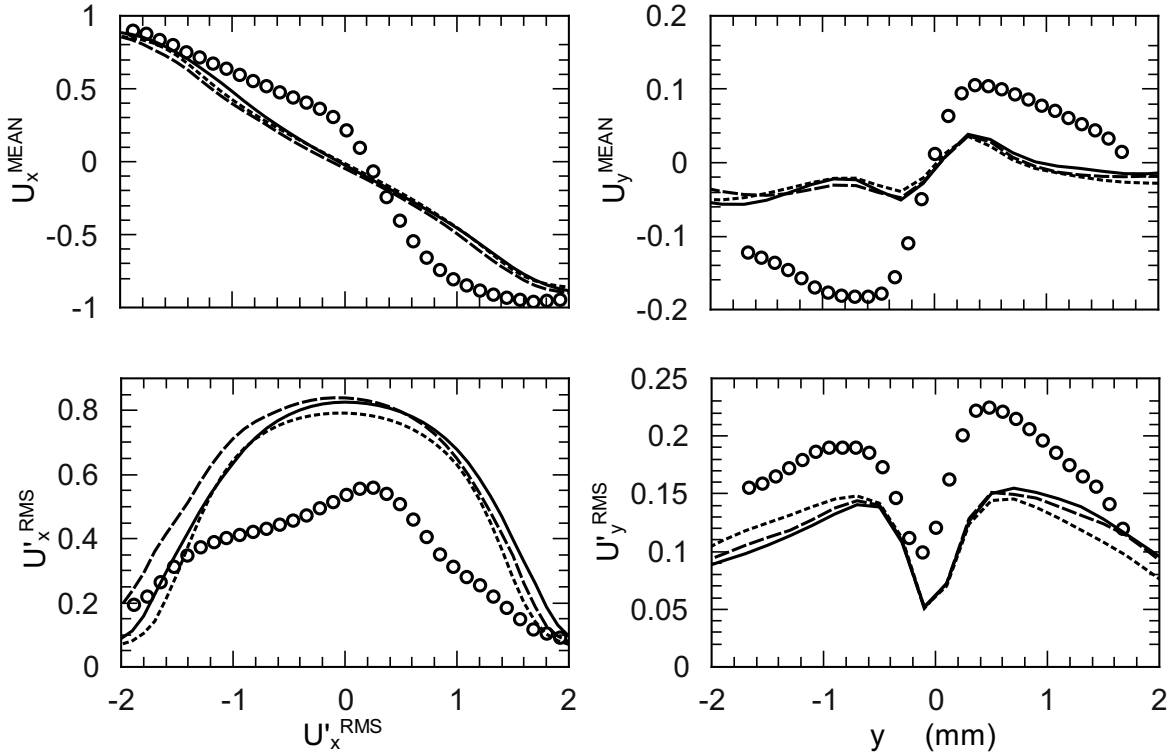


Figure 5.8: Flow statistics with  $\text{FR} = 40 \text{ mL/min}$ : Comparison between  $\mu\text{PIV}$  experiments (symbols), LES with HLPA scheme and constant SGS model (continuous line), LES with QUICK scheme and constant SGS model (dashed line), LES with HLPA scheme and dynamic SGS model (dotted line). From left to right and top to bottom: mean  $x$ -velocity along the  $x$ -axis at  $y = 0 \text{ mm}$ , mean  $y$ -velocity along the  $y$ -axis at  $x = 0 \text{ mm}$ , RMS of  $x$ -velocity fluctuations along the  $x$ -axis at  $y = 0 \text{ mm}$ , RMS of  $y$ -velocity fluctuations along the  $y$ -axis at  $x = 0 \text{ mm}$ .

available. The case for  $\text{FR} = 90 \text{ mL/min}$  approaches “fully turbulent” behaviour and LES can accurately predict the smooth  $x$ -velocity profile and the relatively high fluctuations along the entire  $x$ -axis. Also the predictions for the  $y$ -velocity component (both mean value and RMS of fluctuations) result in very good agreement with experimental data. However it should be remembered here that the experiments reveal a shifted position of the impingement point that is not predictable in the simulations where symmetric inflows were imposed. In fact, the impingement point can be recognised (at least by null mean velocities) even if it moves chaotically in the chamber. This shifting is further confirmed in the  $y$ -velocity experimental profiles that, for this reason, do not represent exactly the plane where the jets collide.

For high FR the  $y$ -velocity profiles are indeed very sensitive to the jets alignment,

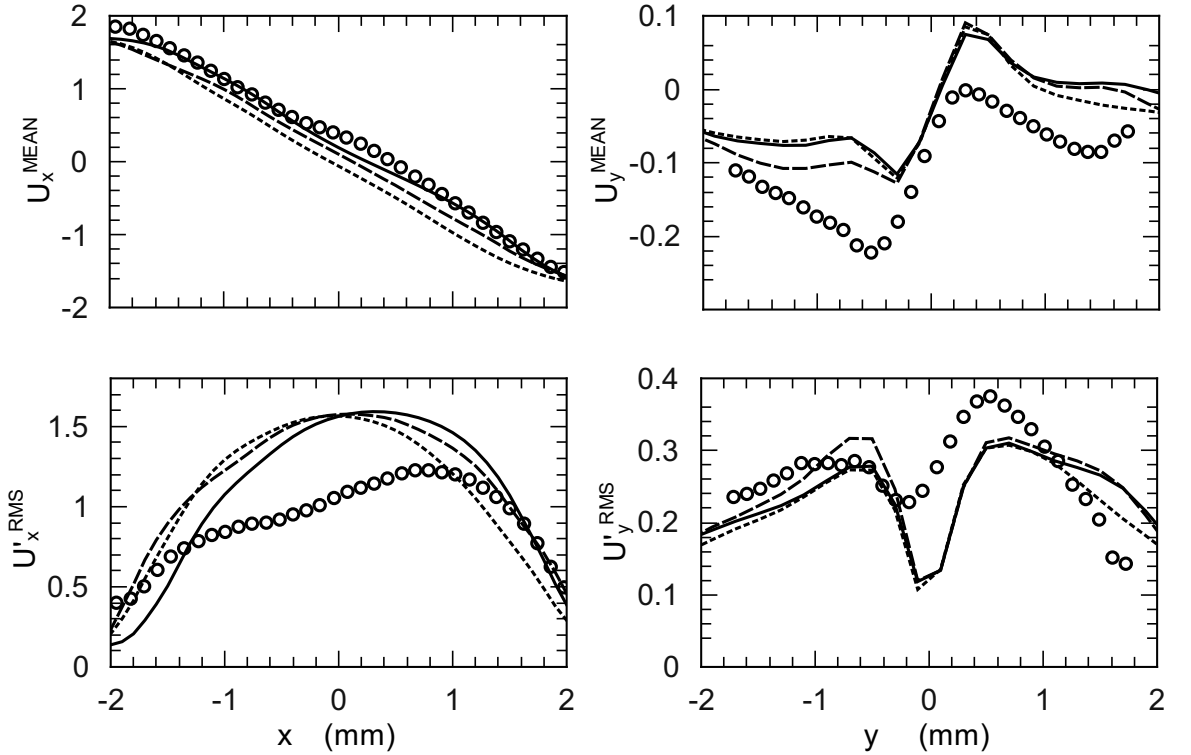


Figure 5.9: Flow statistics with  $FR = 90 \text{ mL/min}$ : Comparison between  $\mu\text{PIV}$  experiments (symbols), LES with HLPA scheme and constant SGS model (continuous line), LES with QUICK scheme and constant SGS model (dashed line), LES with HLPA scheme and dynamic SGS model (dotted line). From left to right and top to bottom: mean  $x$ -velocity along the  $x$ -axis at  $y = 0 \text{ mm}$ , mean  $y$ -velocity along the  $y$ -axis at  $x = 0 \text{ mm}$ , RMS of  $x$ -velocity fluctuations along the  $x$ -axis at  $y = 0 \text{ mm}$ , RMS of  $y$ -velocity fluctuations along the  $y$ -axis at  $x = 0 \text{ mm}$ .

symmetry and oscillations because the  $y$ -velocity is everywhere small compared to the  $x$ -component except at the impingement point where it can be relatively large. So the  $y$ -velocity profiles are not always well predicted because the impingement fluctuations are slightly overpredicted in the simulations (as shown in  $x$ -velocity fluctuations) and the  $y$ -fluctuations result to be more distributed along the  $x$ -axis instead of being more concentrated at the measurement position  $x = 0$ . However this effect do not have a strong influence the overall turbulence and mixing efficiency in the reactor.

As a general comment it is possible to state that the comparison with experimental data showed little influence of the numerical scheme adopted. In fact, for the operating conditions investigated in this work, predictions obtained with HLPA were

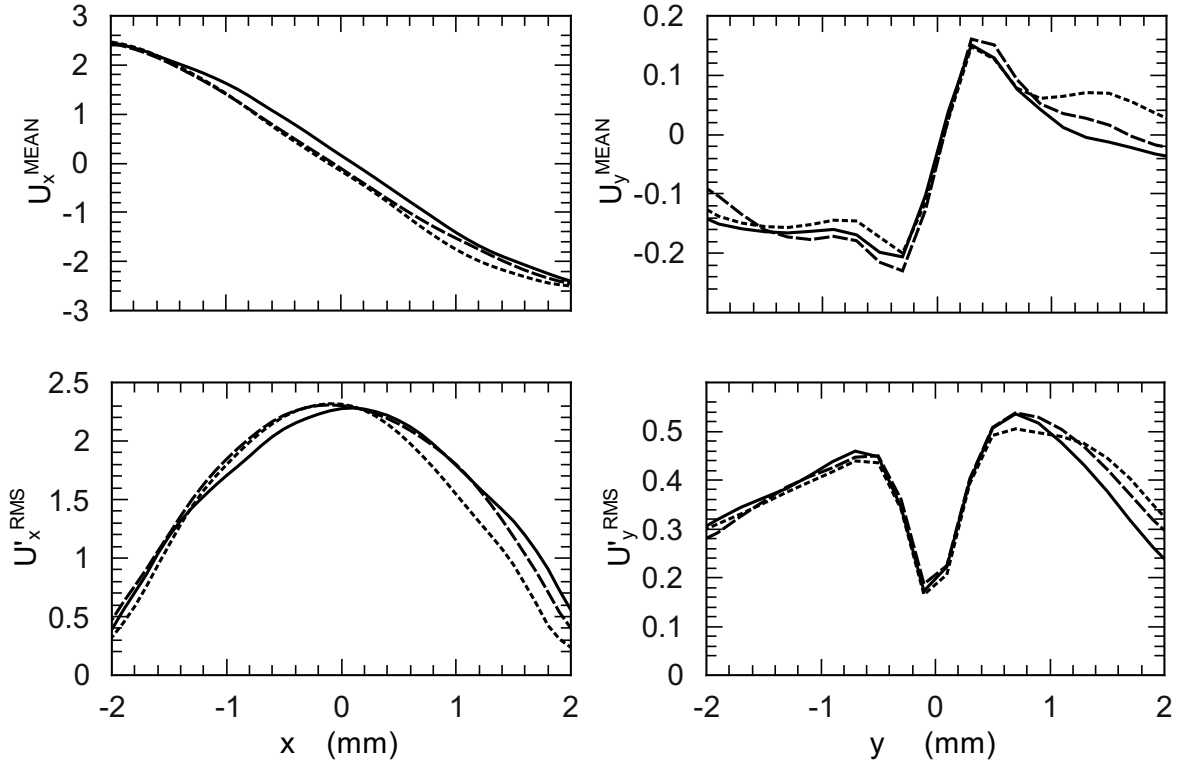


Figure 5.10: Flow statistics with  $\text{FR} = 150 \text{ mL/min}$ : Comparison between LES with HLPA scheme and constant SGS model (continuous line), LES with QUICK scheme and constant SGS model (dashed line), LES with HLPA scheme and dynamic SGS model (dotted line). From left to right and top to bottom: mean  $x$ -velocity along the  $x$ -axis at  $y = 0 \text{ mm}$ , mean  $y$ -velocity along the  $y$ -axis at  $x = 0 \text{ mm}$ , RMS of  $x$ -velocity fluctuations along the  $x$ -axis at  $y = 0 \text{ mm}$ , RMS of  $y$ -velocity fluctuations along the  $y$ -axis at  $x = 0 \text{ mm}$ .

found to be very close to those obtained with QUICK. This could be a consequence of the very regular grid used, that are already characterised by a small numerical diffusion, notwithstanding the numerical scheme adopted. The effect of the SGS seems to be slightly more important, although no significant difference is detected, proving probably that for the geometry and the operating conditions investigated the constant Smagorinsky model is adequate.

Figure 5.10 reports the predictions for  $\text{FR} = 150 \text{ mL/min}$  for which no experimental data are available. It is however interesting to compare predictions obtained with different modelling options. As it is seen, also for this case vary small differences are detected when improving the numerical scheme and/or the SGS model,

confirming the conclusions drawn for  $FR = 90$  mL/min.

Moreover, as already reported, for the considered flow regimes the turbulent behaviour of the system is not only due to the impingement of the jets, which induces a strong unsteady behaviour limited to a small region in the centre of the reactor, but also to the non-constant inlet flow rates. This suggests that, although the results are very close to the experimental data, the remaining mismatch between predictions and experiments is probably not coming from inadequate turbulence modelling or numerical issues, but most likely from the inlet flow rate approximation with the adopted boundary conditions. To improve the agreement more detailed  $\mu$ PIV measurements at the inlets should be produced and analysed.

As a final comment it is interesting to point out that similar conclusions were formulated when  $\mu$ PIV data was employed with DNS in Chap. 3. This proves that the most challenging issue is the proper modelling of the real operating conditions (in particular the inflow conditions) and once this is achieved, also LES is capable of describing properly the turbulent flow field inside the CIJR, at least under the operating conditions investigated here. It is interesting to remember here that these predictions, resulting in good agreement with experimental data, are obtained here via LES with grids that are at least ten times less refined than those used in DNS. This typically results in a reduction of the CPU time of about ten times. Last but not least, LES allows also for the simulation of liquid turbulent scalar transport and chemical reactions simply by using the same grids (and appropriate SGS mixing models) whereas DNS requires the use of much finer grids, making the DNS approach intractable for the simulation of real liquid reacting systems.

## 5.5 Conclusions

In this part of the thesis, LES has been employed to simulate the flow field in a CIJR and predictions are validated against experimental data. The DNS results obtained in Chap. 3 demonstrated the importance of properly imposing the inflow boundary and therefore this approach is here extended to the LES framework. In fact, contrary to what happens with RANS, where simulations generally result in good agreement with experimental data simply employing the time averaged inlet flow rates, more details are required to run a successful LES. For the present application and under the range of operating conditions investigated the spatial discretization schemes and the SGS models were found not to be crucial for a good prediction of the turbulent behaviour of the system. However, it has been shown that the QUICK scheme, in particular at intermediate FR values performs slightly better than the HLPA. No significant differences were instead noted between the constant Smagorinsky SGS model and the dynamic model of Germano. In conclusion LES

can be used instead of expensive DNS (and  $\mu$ PIV experiments) to obtain fast and reliable predictions, that are of particular importance when the computational model is extended to consider mixing and reactive processes. The computational model that has been validated will be extended to the simulation of turbulent precipitation processes and validated against experimental data.

## References

- Ascomp GmbH. *Multi—Fluid Navier—Stokes Solver TransAT User Manual*, 2009.
- C. Beckermann, H. J. Diepers, I. Steinbach, A. Karma, and X. Tong. Modeling melt convection in phase-field simulations of solidification. *J. Comput. Phys.*, 154(2):468–496, 1999.
- C. J. Bourdon, M. G. Olsen, and a. D. Gorby. Validation of an analytical solution for depth of correlation in microscopic particle image velocimetry. *Meas. Sci. Technol.*, 15(2):318–327, 2004.
- J. C. Cheng, M. G. Olsen, and R. O. Fox. A microscale multi-inlet vortex nanoprecipitation reactor: Turbulence measurement and simulation. *Appl. Phys. Lett.*, 94(20):204–104, 2009.
- J. Denev, J. Frohlich, H. Bockhorn, F. Schwertfimer, and M. Manhart. DNS and LES of scalar transport in a turbulent plane channel flow at low Reynolds number. *Lect. Notes Comput. Sci.*, 4818:251, 2008.
- H. Feng, M. G. Olsen, Y. Liu, R. O. Fox, and J. C. Hill. Investigation of turbulent mixing in a confined planar-jet reactor. *AIChE J.*, 51(10):2649–2664, 2005.
- J. H. Ferziger and M. Peric. *Computational Methods for Fluid Dynamics*. Springer-Verlag, Berlin, third edition, 2002.
- R. O. Fox. *Computational Models for Turbulent Reacting Flows*. Cambridge University Press, Cambridge, December 2003.
- E. Gavi. *Investigation of turbulent precipitation of nanoparticles in a Confined Impinging Jets Reactor*. PhD thesis, Torino, Italy, 2009.
- E. Gavi, D. L. Marchisio, A. A. Barresi, M. G. Olsen, and R. O. Fox. Turbulent precipitation in micromixers: CFD simulation and flow field validation. *Chem. Eng. Res. Des.*, page in press, 2010.
- M. Germano, U. Piomelli, P. Moin, and W. H. Cabot. A dynamic subgrid-scale eddy viscosity model. *Phys. Fluids A*, 3(7):1760, 1991.
- A. J. Gesquiere, T. Uwada, T. Asahi, H. Masuhara, and P. F. Barbara. Single molecule spectroscopy of organic dye nanoparticles. *Nano Lett.*, 5(7):1321—1326, 2005.
- D. Horn and J. Rieger. Organic nanoparticles in the aqueous phase - theory, experiment, and use. *Angew. Chem. Int. Ed.*, 40(23):4330–4361, December 2001.
- M. Icardi, E. Gavi, D. Marchisio, M. Olsen, R. Fox, and D. Lakehal. Validation of les

---

## REFERENCES

---

- predictions for turbulent flow in a confined impinging jets reactor. *Appl. Math. Model.*, 35(4):1591–1602, 2011.
- B. K. Johnson and R. K. Prud’homme. Chemical processing and micromixing in confined impinging jets. *AICHE J.*, 49(9):2264–2282, September 2003.
- J. Kipp. The role of solid nanoparticle technology in the parenteral delivery of poorly water-soluble drugs. *Int. J. Pharm.*, 284(1-2):109–122, October 2004.
- A. L. Le Roy Boehm, R. Zerrouk, and H. Fessi. Poly  $\varepsilon$ -caprolactone nanoparticles containing a poorly soluble pesticide: formulation and stability study. *J. Microencapsulation*, 17(2):195–205, 2000.
- B. P. Leonard. A stable and accurate convective modelling procedure based on quadratic upstream interpolation. *Int. J. Mech. Sci.*, 16:183—308, 1976.
- H. Li and M. G. Olsen. MicroPIV measurements of turbulent flow in square microchannels with hydraulic diameters from  $200\mu\text{m}$  to  $640\mu\text{m}$ . *Int. J. Heat Fluid Flow*, 27(1):123–134, 2006.
- F. Lince, D. L. Marchisio, and A. A. Barresi. Strategies to control the particle size distribution of poly- $\varepsilon$ -caprolactone nanoparticles for pharmaceutical applications. *J. Colloid Interface Sci.*, 322(2):505–515, 2008.
- F. Lince, D. L. Marchisio, and A. A. Barresi. Smart mixers and reactors for the production of pharmaceutical nanoparticles: Proof of concept. *Chem. Eng. Res. Des.*, 87(4):543–549, 2009.
- R. Lindken, M. Rossi, S. Grosse, and J. Westerweel. Micro-Particle Image Velocimetry (microPIV): recent developments, applications, and guidelines. *Lab Chip*, 9(17):2551–2567, September 2009.
- Y. Liu and R. O. Fox. CFD predictions for chemical processing in a confined impinging-jets reactor. *AICHE J.*, 52:731–744, 2006.
- Y. Liu, J. C. Cheng, R. K. Prud’homme, and R. O. Fox. Mixing in a multi-inlet vortex mixer (MIVM) for flash nano-precipitation. *Chem. Eng. Sci.*, 63(11):2829–2842, 2008.
- Y. Liu, M. G. Olsen, and R. O. Fox. Turbulence in a microscale planar confined impinging-jets reactor. *Lab Chip*, 9(8):1110–1118, 2009.
- D. L. Marchisio. Large Eddy Simulation of mixing and reaction in a Confined Impinging Jets Reactor. *Comput. Chem. Eng.*, 33(2):408–420, 2009.
- D. L. Marchisio, L. Rivautella, and A. A. Barresi. Design and scale-up of chemical reactors for nanoparticle precipitation. *AICHE J.*, 52:1877–1887, 2006.
- D. L. Marchisio, F. Omegna, A. A. Barresi, and P. Bowen. Effect of mixing and other operating parameters in sol-gel processes. *Ind. Eng. Chem. Res.*, 47(19):7202–7210, October 2008.
- C. D. Meinhart, S. T. Wereley, and J. G. Santiago. PIV measurements of a microchannel flow. *Exp. Fluids*, 27(5):414–419, October 1999.
- R. Mittal and G. Iaccarino. Immersed Boundary Methods. *Annu. Rev. Fluid Mech.*, 37(1):239–261, 2005.
- R. H. Müller. Nanosuspensions for the formulation of poorly soluble drugs I. Preparation

- by a size-reduction technique. *Int. J. Pharm.*, 160(2):229–237, January 1998.
- R. H. Müller, M. Radtke, and S. a. Wissing. Solid lipid nanoparticles (SLN) and nanostructured lipid carriers (NLC) in cosmetic and dermatological preparations. *Adv. Drug Delivery Rev.*, 54 Suppl 1:131–155, November 2002.
- M. G. Olsen and R. J. Adrian. Out-of-focus effects on particle image visibility and correlation in microscopic particle image velocimetry. *Exp. Fluids*, 29(0):S166–S174, December 2000.
- S. B. Pope. *Turbulent Flows*. Cambridge University Press, Cambridge, January 2000.
- Q. Qiu Zhao, A. Boxman, and U. Chowdhry. Nanotechnology in the Chemical Industry – Opportunities and Challenges. *J. Nanopart. Res.*, 5(5/6):567–572, December 2003.
- E. Romanus. Magnetic nanoparticle relaxation measurement as a novel tool for in vivo diagnostics. *J. Magn. Magn. Mater.*, 252:387–389, November 2002.
- O. V. Salata. Applications of nanoparticles in biology and medicine. *J. Nanobiotechnol.*, 2(3):177–182, 2004.
- J. G. Santiago, S. T. Wereley, C. D. Meinhart, D. J. Beebe, and R. J. Adrian. A particle image velocimetry system for microfluidics. *Exp. Fluids*, 25(4):316–319, September 1998.
- F. Schwertfirm, J. Gradl, H. C. Schwarzer, W. Peukert, and M. Manhart. The low Reynolds number turbulent flow and mixing in a confined impinging jet reactor. *Int. J. Heat Fluid Flow*, 28(6):1429–1442, 2007.
- J. Smagorinsky. General circulation experiments with the primitive equations. *Mon. Weather Rev.*, 91(3):99—164, 1963.
- E. R. Van Driest. On turbulent flow near a wall. *J. Aeronaut. Sci.*, 23(11):1007–1011, 1956.
- H. Werner and H. Wengle. Large-eddy simulation of turbulent flow over a square rib in a channel. *Thin Solid Films*, 1, 1989.
- J. Zhu. A low-diffusive and oscillation-free convection scheme. *Commun. Appl. Numer. Methods*, 7(3):225–232, April 1991.

# 6

## Poly-dispersed particle-laden flow

In this chapter we focus on the possible model reductions that can be operated when working with multiphase systems (such as particle precipitation) that need fast computations and robust models and that can rarely be fully resolved (e.g., in a Lagrangian way). We are particularly interested in Eulerian multi-phase models for the description of poly-disperse systems. Among them the multi-fluid Eulerian model coupled with the full description of the particle size distributions (e.g., with full Probability Density Function or Direct Simulation Monte-Carlo methods) can be computationally very expensive. Furthermore the coupling of these models with a full resolution of turbulence (i.e. DNS) is practically impossible. On the other hand, most of the currently practical and highly simplified approaches, based on strict hypothesis for multiphase flows (e.g., single-phase or homogeneous model) and averaged models for turbulence (e.g., RANS modelling) are not predictive enough for many relevant applications. A possible alternative proposed in this work, is represented by the use of LES models coupled with algebraic models for the phase interactions and Quadrature-Based Moment Methods (QBMM) for poly-dispersity.

In this framework, the chapter represents a validation of the proposed model for the simulation of preferential concentration (or turbophoresis) phenomenon in a periodic channel with  $Re_\tau = 150$ , seeded with inert poly-dispersed particles tracked with the Eulerian equilibrium model and the Direct Quadrature Method Of Moments (DQMOM). The sub-grid scale (SGS) motion of particles is reconstructed through an Approximate Deconvolution Method (ADM). The simulations are carried out with ad-hoc routines developed in the commercial CFD platform *TransAT* [Ascomp GmbH, 2009]. Results are compared to DNS Lagrangian data of Marchioli et al. [2008b].

---

Part of the contents of this chapter has been presented at the 8<sup>th</sup> International Conference on

## 6.1 Introduction

The dynamics of particles in a turbulent fluid flow has been widely studied in the last decades, both experimentally and numerically, from various points of view and applications such as particles deposition [Brooke et al., 1992, Cleaver and Yates, 1975, Friedlander and Johnstone, 1957, Kaftori et al., 1995, Kallio and Reeks, 1989, Lavezzo et al., 2009, Liu and Agarwal, 1974, Marchioli et al., 2003, McCoy and Hanratty, 1975, McLaughlin, 1989, Narayanan et al., 2003, Shams et al., 2000, Slater et al., 2003, Tang and Guo, 2011, Uijtewaal and Oliemans, 1996, Van Haarlem et al., 1998, Wang and Squires, 1996a, Young and Leeming, 1997], dispersion in shear flow and mixing layers [Burns et al., 2004, Cerbelli et al., 2001, Chein and Chung, 1987, Elghobashi and Truesdell, 1992, Hishida et al., 1992, Hu et al., 2002, Lazaro and Lasheras, 1992, Marcu and Meiburg, 1996, Parthasarathy and Faeth, 1990b, Pascal and Oesterlé, 2000, Soteriou and Yang, 1999, Stock and Wang, 1993, Wen et al., 1992, Yang et al., 2000] or settling and accumulation in homogeneous isotropic turbulence [Aliseda et al., 2002, Chun et al., 2005, Collins and Keswani, 2004, Maxey, 1987, Salazar et al., 2008, Wang and Maxey, 1993, Yen and Lei, 1991]. We refer to the review of Guha [2008] for a complete description of particles deposition problem and to Geurts et al. [2007], Mashayek and Pandya [2003], Sinaiski and Zaichik [2008], Zaichik et al. [2008] for an overview of the different methods available.

This problem can be also extended to solve other related problems such as the turbulence modulation by particles studied by two-way coupling models [Boivin et al., 1998, Druzhinin, 1995, Elghobashi and Truesdell, 1993, Meiburg et al., 2000, Narayanan, 2004, Parthasarathy and Faeth, 1990a, Schreck and Kleis, 1993, Squires and Eaton, 1990, Sundaram and Collins, 1999, Yuan and Michaelides, 1992] or particle collisions studied by population balance and kinetic theory models [Li et al., 2001, Reade and Collins, 2000, Sommerfeld and Huber, 1999, Sundaram and Collins, 1997, Wang et al., 2000, 2009, Yamamoto et al., 2001, Zhou et al., 1998].

The motion of inertial particles in turbulent flows is mainly characterised by the so-called “preferential concentration” [Eaton and Fessler, 1994, Fessler et al., 1994, Rouson and Eaton, 2001, Shaw et al., 1998, Squires and Eaton, 1991, Wood et al., 2005, Zaichik and Alipchenkov, 2003] caused by the tendency of particles to accumulate in low-vorticity regions. This tendency has been called “turbophoresis”, in analogy to what happens in thermo-phoresis and electro-phoresis, and it is a very important phenomenon for many physical events such as clouds formation, particles deposition (in turbines, engines or biological systems), fuel droplet combustion, etc. Different models can be used for the particle phase and the turbulence description.

The most accurate one is the Lagrangian tracking of particles coupled with a DNS description of the fluid. This approach is typically too expensive for large scale industrial problem so many efforts have focused on the development of more efficient models.

A much faster alternative to the Lagrangian tracking of particles is represented by a concentration field advected in an Eulerian way. This approach consists in an average operation (either volume-average or ensemble-average) and is commonly used in many applications, from dilute to dense granular flows, and has been introduced in different formulations [Drew and Passman, 1998, Guha, 1997, Ishii, 1975, Prosperetti and Zhang, 1995]. However, dilute inertial particles (with finite  $Kn$  and  $St$ ) behave like a non-equilibrium highly compressible fluid, therefore the overall accuracy and validity of the continuum hypothesis for the dispersed phase in the different flow conditions is still an open point. Recently models have been developed, based on a mesoscopic or PDF approach where the average operations is performed by the moment transform of kinetic equations [Février et al., 2005, Fox, 2012, Minier and Peirano, 2001, Passalacqua and Fox, 2011, Reeks, 1992, Zaichik and Alipchenkov, 2003]. This means that statistical mesoscopic closures, kinetic equations or additional stress term equations have to be solved to correctly predict the particle motion and dispersion. Nevertheless, if the effects at the particle-scale such as particle-particle collisions, particle-wall collisions and particle trajectory crossing are neglected, the macroscopic formulation is still a practicable and faster approach to predict particles accumulation especially when it is dominated by the drag as in very dilute particle-laden channel flows with moderate  $St$ .

Accepting the compromise of the Eulerian mean field approximation, the two-fluid approach is the standard approach, that consists in solving separate continuity and momentum balance equations for each phase. This is the most accurate approach, valid in principle for arbitrary Stokes number (under the continuum hypothesis), but is characterised usually by a system of equations linearly unstable [Arai, 1980, Jones and Prosperetti, 1985, Prosperetti and Jones, 1987, Vreman, 2011], often resulting in a computational time comparable to Lagrangian methods for medium scale applications. In particular, when additional physical models must be later taken into account (e.g., PBE model), this approach can become computationally inefficient. Therefore in this work we focus on algebraic models for computing the concentration field of particle velocity [Ferry and Balachandar, 2001, Guillard and Duval, 2007, Ishii, 1975].

For the sake of computational efficiency, to avoid expensive DNS, turbulence can be described by LES, filtering out the smallest scales of turbulence. This approach has many advantages with respect to RANS and has been used by several studies of particle-laden flows [Berrouk et al., 2007, Boivin et al., 2000, Gobert, 2010, Kuerten, 2006, Kuerten and Vreman, 2005, Moreau et al., 2010, Pandya and Mashayek, 2002, Shotorban and Balachandar, 2009, Wang and Squires, 1996a,b, Zaichik et al., 2009]

with or without SGS models for the unresolved scale of particles velocity. When the LES approach is coupled with an Eulerian formulation, the filtering operation can be applied conceptually before or after the averaging operation, giving place to slightly different models. In fact the fluctuations neglected by the averaging procedure are conceptually different from the ones filtered out by LES. Some recent works [Armenio et al., 1999, Marchioli et al., 2008a] that compare DNS results with a posteriori (post-filtered) LES in a Lagrangian settings for particles, demonstrated the importance of SGS fluctuations to predict the particles preferential concentration and accumulation at the wall, especially when using coarse LES. The use of simple turbulent dissipation approaches, through the eddy viscosity coefficient given by the fluid SGS model, is not suitable to predict the turbophoresis phenomenon that is due to the gradient of fluctuating velocities. Therefore the unresolved scales for particles do not act only as an uniform dispersion force. More complex models must be introduced such as additional forces, stochastic forcing or deconvolution methods.

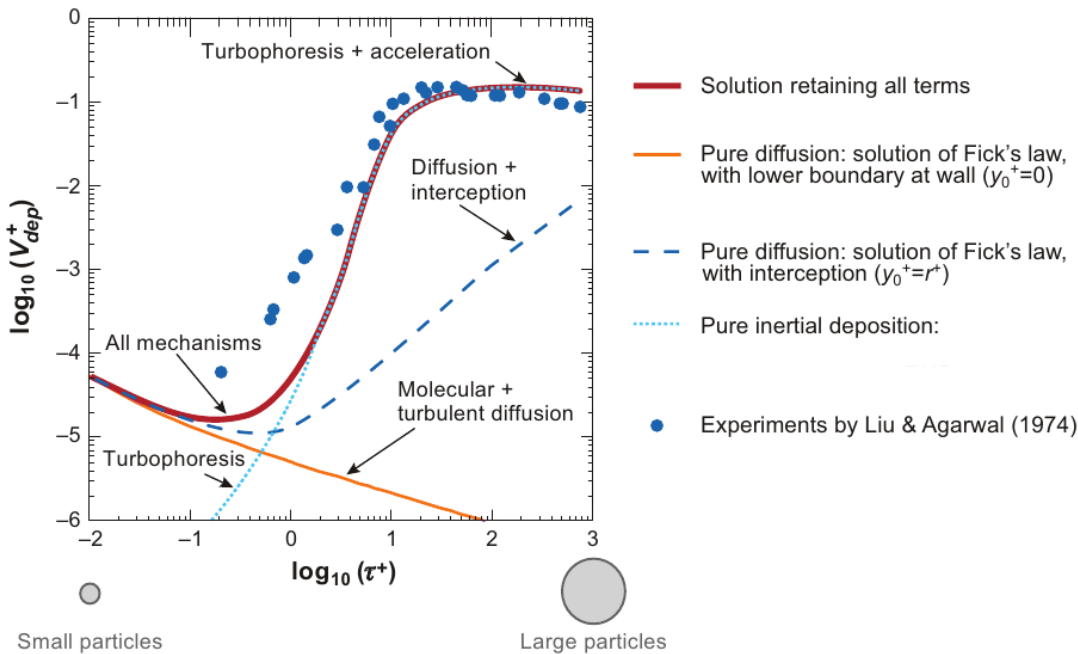


Figure 6.1: The variation in deposition rate versus normalised particle relaxation time in fully developed vertical pipe flow [Guha, 2008]. Full model (red line), pure diffusion (orange line), pure diffusion with modified wall value (dark blue dashed line), pure inertial deposition (light blue line) and experiments by Liu and Agarwal [1974] (blue dots).

A third challenge (beside turbulence and particle motions) is represented by poly-dispersity. In fact, as it has been already mentioned, the turbophoresis and

the deposition velocity is highly influenced by the particle relaxation time (i.e., the size of the particles). This dependence is illustrated in Fig. 6.1 in terms of particle deposition rate  $V_{dep}^+$  in a vertical pipe flow varying the fluid mean flow rate and consequently the particle Stokes number (indicated here as a normalised particle relaxation rate  $\tau^+$ ). Guha [1997] proposed a macroscopic equation for particle deposition (red line), based on RANS models, valid only for fully developed pipe flow, and compared it with experimental data of Liu and Agarwal [1974]. This figure, even if it is referred to a very specific case, is important to highlight the 3 different regimes that similarly holds for particles in turbulent flows. In the first regime, illustrated in the first part of the graph, small particles characterised by  $St < 1$  are moving and deposit towards wall mainly because of particle and turbulent diffusion. The deposition rate increases very fast in the central part of the graph, that represents the regime dominated by turbophoresis and inertial effects, when the Stokes number range between one and ten. In the final part there is a plateau and deposition rate stabilise.

# nodes	DQMOM nodes [ $\mu\text{m}$ ]					PSD moments [ $\text{m}^i$ ]	
	2	4	6	8	10	$i$	$i^{th}$ moment
node 1 [ $\mu\text{m}$ ]	15.4	17.9	10.1	9.1	8.4	0	1.0
weight 1	1.0	0.80	0.60	0.46	0.36	1	$1.54 \cdot 10^{-5}$
node 2 [ $\mu\text{m}$ ]	×	29.2	22.5	19.1	17.0	2	$2.85 \cdot 10^{-10}$
weight 2	×	0.20	0.39	0.49	0.54	3	$6.40 \cdot 10^{-15}$
node 3 [ $\mu\text{m}$ ]	×	×	49.9	38.3	32.2	4	$1.74 \cdot 10^{-19}$
weight 3	×	×	0.01	0.04	0.09	5	$5.71 \cdot 10^{-24}$
node 4 [ $\mu\text{m}$ ]	×	×	×	80.6	60.8	6	$2.27 \cdot 10^{-28}$
weight 4	×	×	×	0.001	0.001	7	$1.09 \cdot 10^{-32}$
node 5 [ $\mu\text{m}$ ]	×	×	×	×	120.4	8	$6.30 \cdot 10^{-37}$
weight 5	×	×	×	×	0.0001	9	$4.39 \cdot 10^{-41}$

Table 6.1: Moments and quadrature approximations of the log-normal PSD.

Let us analyse now the dependence of turbophoresis on particle Stokes number in the turbulent channel flow under study for heavy particles (with density  $\rho_p = 1000 \text{ kg/m}^3$ ) dispersed in air with an initially uniform unitary particles concentration and let us assume that the particles dynamics could be exactly simulated. In this case, if the population of particles is approximated with fixed and constant mean diameter, the predicted accumulation can be affected by a large error due to the wrong approximation of the PSD. To better understand the importance of polydispersity, let us consider a population of particles characterised by a log-normal PSD with a mean size of  $15 \mu\text{m}$ , corresponding to  $St = 0.6$  (for this particular test case) and a standard deviation of  $10 \mu\text{m}$ , meaning that there exists a significant

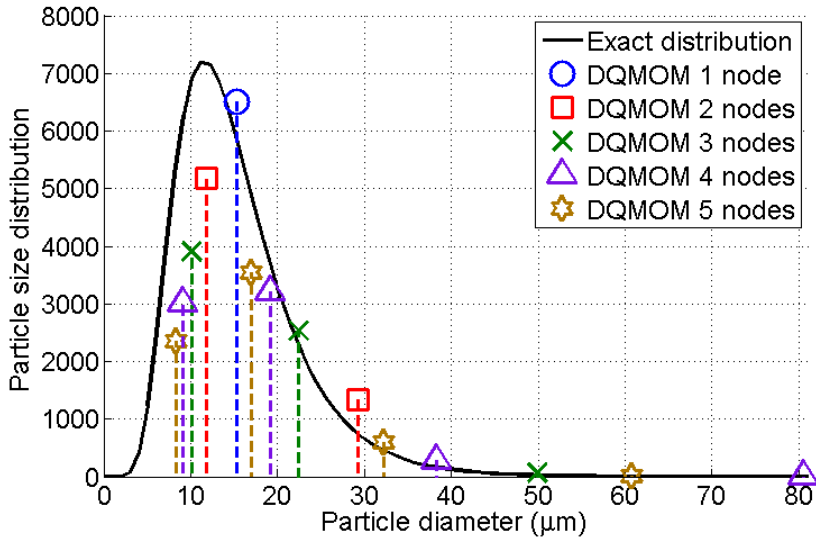


Figure 6.2: Log-normal PSD and DQMOM approximations.

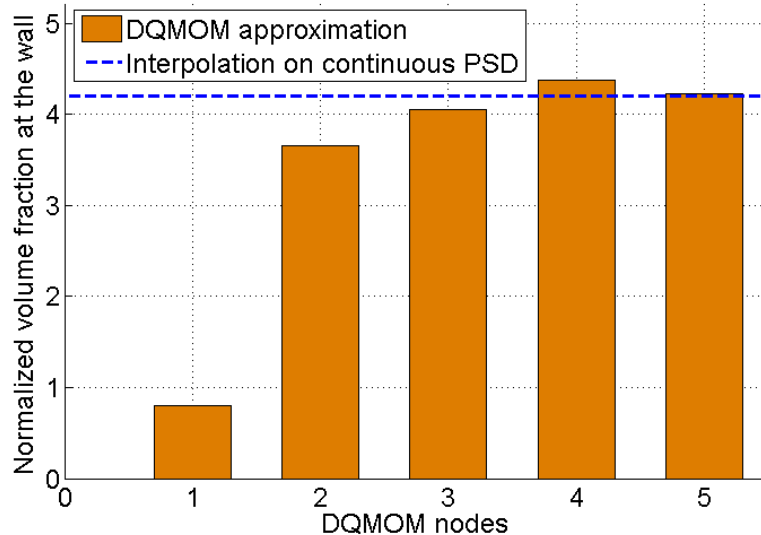


Figure 6.3: QMOM/DQMOM approximation of particle concentration at the wall in a turbulent channel flow for a realistic log-normal distribution. Results are expressed in terms of volume fraction, normalised by the initial value and compared with theoretical finding for a continuous PSD description.

number of particles between  $5 \mu\text{m}$  and  $40 \mu\text{m}$  (corresponding to Stokes number approximately between 0.2 and 5). For this distribution the moments are reported

in Tab. 6.1 together with the different quadrature representations used in QMOM or DQMOM. Fig. 6.2 reports instead the distribution along with the quadrature representation.

Data from DNS results of Marchioli et al. [2008b] of particles concentration near the wall when the profiles is fully developed are interpolated in the whole size range of this realistic PSD. The results, reported in Fig. 6.3, represent a theoretical estimated value of particle volume fraction at the wall. This is compared with the different estimations made by a global approximation with QMOM/DQMOM, with the assumptions of no other sources of error except the PSD approximation and constant quadrature nodes and weights in the whole domain. With QMOM/DQMOM in fact it is possible in principle to approximate the distribution with an arbitrary number of nodes and weights that dynamically adapt according to the local PSD (see Sect. 2.4 for more details about quadrature approximations). As it is possible to see, the approximation with one node (mean particle size) gives a very rough estimate of the accumulation while starting from three nodes the resulting predictions quickly reach a physically acceptable error. This demonstrates to importance of an accurate description of poly-dispersity and the capability of QBMM.

The objective of this part of the work is to assess the possibility of combining this quadrature approximation with a simplified algebraic Eulerian LES model. The novelty is represented by the coupling of fast and efficient methods for particles evolution, LES and population balance. In Sec. 6.2, the test case is introduced and the carrier phase model is described. In Sec. 6.3 the dispersed phase is considered and the DQMOM approximation is introduced. Sec. 6.4 deals with the particles SGS model and Sec. 6.5 presents all the numerical details of the simulations. Eventually results and concluding remarks are reported in Sec. 6.6 and Sec. 6.7.

## 6.2 Fluid phase

The periodic channel problem already introduced in Chap. 4 is used also in this chapter. It represents an infinite non-dimensional channel modelled by two periodic boundary conditions on the stream-wise and span-wise directions and a no-slip conditions on the walls. The main flow is directed in  $x$ -direction and it is driven by a constant pressure forcing, imposed directly in the momentum equation. Among the wall-bounded flow problems, this is one of the most famous configuration that can better show the property and effects of fully developed turbulent behaviour and study to analyse numerical schemes and SGS models.

The size of the domain in the periodic directions (i.e.,  $x$  and  $z$ ) is such that the periodicity conditions do not influence the flow structures. This means that it must be larger than the biggest scale of turbulence. For  $Re_\tau = 150$  the dimension

commonly used in literature are the following:

$$L_x = 4\pi H \quad L_y = 2H \quad L_z = 2\pi H \quad (6.1)$$

where  $H$  is the half-height of the channel, used as characteristic dimension.

### 6.3 Particles phase

The particles are described via a NDF  $n(L; \mathbf{x}, t)$ , representing the infinitesimal number of particles of diameter  $L$  at point  $\mathbf{x}$  and time  $t$ . The evolution of  $n$  is dictated by a population balance equation. The DQMOM (details about the method are reported in Sec. 2.4) has been used to represent  $n(L; \mathbf{x}, t)$  and to describe its evolution, by selecting six moments or, equivalently, three nodes (abscissas) and the three corresponding weights. The test case under study is mainly devoted to the validation and analysis of the multiphase and LES models therefore particles collisions have been neglected, resulting in fixed nodes. This model however can be easily extended to the mixing of different particle populations or to other particulate processes (see Chap. 6.7).

This choice is also motivated by the fact the existing DNS Lagrangian data in literature are mainly based on mono-disperse non-colliding particles so, for the sake of comparison, we selected initially uniform weights (equal to one) and three nodes representing three classes of particles corresponding to a Stokes number equal respectively to 0.2, 1 and 5. The Stokes number  $St$  is defined as

$$St = \frac{\tau_p}{\tau_f}, \quad (6.2)$$

where the particle relaxation time is:

$$\tau_p = \frac{(2\frac{\rho_p}{\rho} + 1)d_p^2}{36\nu} = \frac{(\rho_p + \frac{1}{2}\rho)d_p^2}{18\mu}, \quad (6.3)$$

and the fluid relaxation time is referred to the viscous scale (wall units):

$$\tau_f = \frac{\nu}{u_\tau^2}. \quad (6.4)$$

The particle concentrations are transported with a velocity given by the Equilibrium Eulerian Model (EEM) [Ferry and Balachandar, 2001, Ferry et al., 2003]:

$$\mathbf{U}_p - \mathbf{U} = -\tau_p (\mathbf{I} + \tau_p \nabla \mathbf{U})^{-1} \left( \frac{D\mathbf{U}}{Dt} - g \right) \quad (6.5)$$

that represents the first-order expansion of the Maxey-Riley equation [Maxey and Riley, 1983], for small  $St$  neglecting all the forces but the drag.

The particle Reynolds number can be calculated from the relative velocity and it can have a feedback on the drag force, if we consider the high Reynolds number effects [Clift et al., 1978]. These can be taken into account either with an iterative procedure or by using a modified particle relaxation number proposed by Ferry and Balachandar [2002] defined as

$$\tau_p^* = \tau_p \left( 1 + 0.76 Re_p^* \left( 1 + 0.025 Re_p^* \right) \right)^{-0.18} \quad (6.6)$$

where

$$Re_p^* = \frac{|\rho_p - \rho| d^3}{18 \nu^2} \left| \frac{D\mathbf{U}}{Dt} - g \right|. \quad (6.7)$$

This model is based on a analytical expansion based on local equilibrium between the fluid and the particle phase but, unlike the Drift Flux or Algebraic Slip Models (ASM), that are more often used for gas-liquid systems, it is written in terms of the Lagrangian derivatives  $\frac{D\mathbf{U}}{Dt}$ . This results in a formulation particularly convenient to model passive particles whose velocities can be calculated with an explicit algebraic relation instead of using a separate momentum balance equation or a non-linear Newton solver, typically used respectively in the two-fluid model adn in the ASM.

According to Balachandar [2009], the EEM approach is strictly valid up to  $St_\kappa = 0.2$ , even if it can be reasonably used up to  $St_\kappa = 1$ ; where  $St_\kappa$  is defined with a fluid relaxation time based on the Kolmogorov time-scale  $\tau_\kappa$ . For this test case the ratio  $\frac{\tau_\kappa}{\tau_f}$  range from 2 (in the near-wall region) to 13 in the centre of the channel [Marchioli et al., 2006, Soldati and Marchioli, 2009]. This means that for  $St = 0.2$  the model should be able to accurately predict the particles motion, while for the other two Stokes numbers there could be inaccuracies, especially near the wall, where the term  $\tau_p \nabla \mathbf{U}$  in Eq. 6.5 can be locally close or above unity. The stated validity condition for the EEM can be relaxed when LES is used because the Kolmogorov time-scale is substituted by the a time-scale,  $\tau_\epsilon$ , referred to the smallest resolved scale of turbulence [Balachandar and Eaton, 2010].

Although the Eulerian equilibrium model can be easily extended to take into account other forces and the particles-fluid feedback coupling, we limit our analysis to a one-way coupling model without gravity and considering only the drag force. This is, in fact, enough to catch the preferential concentration of particles as demonstrated by Elghobashi and Truesdell [1992] and other previous works. In particular the works of Wang et al. [2007], Arcen et al. [2006] and Marchioli et al. [2007] demonstrated that the lift and gravity forces are not relevant issues for the turbophoresis phenomenon, when particles are small enough.

Also the classical ASM [Ishii and Zuber, 1979, Manninen and Taiavassalo, 1996] has been tested with a modification proposed by Guillard and Duval [2007], that makes use of the pressure gradient as the driving force balanced by the drag forces. This approach would be exactly identical to the EEM in the case of inviscid fluid

since the Lagrangian derivatives in Eq. 6.5 is exactly equivalent in the momentum equation to the pressure gradient plus the viscous term. The ADM, described in the next section, in this case should be applied to the pressure that is also a filtered quantity in LES.

## 6.4 Sub-grid scale modelling

The SGS model chosen for the fluid is the standard Smagorinsky model with the harmonic dumping function for the turbulent viscosity near the wall. This model was found to give good predictions for the main quantities of interests, (mean velocity and fluctuations), for the single-phase test case of Chap. 4,. However it is important to highlight here that, since LES is often very sensitive to many numerical parameters, this could not be true when coupled with different CFD codes (e.g., spectral codes), grids or spatial discretisations.

Generally particle concentration is transported with zero molecular diffusion and eddy diffusivity equal to

$$D = \frac{\nu_t}{\rho S_{CT}}, \quad (6.8)$$

where  $\nu_t$  is the eddy viscosity given by the Smagorinsky model and  $S_{CT}$  is the turbulent Schmidt number. To balance the unavoidable numerical dissipation introduced by the advection schemes different tests have also been performed without eddy diffusivity and with different turbulent Schmidt numbers. As we already pointed out, the eddy diffusivity can describe the turbulent dispersion of particles but is not capable to describe the particle fluctuations responsible for turbophoresis.

The particles are advected with the velocity given by Eq. 6.5, where in the LES framework  $\mathbf{U} = \bar{\mathbf{U}}$  is the filtered velocity. The same equation can be used, replacing  $\mathbf{U}$  with the de-filtered fluid velocity  $\mathbf{U}^*$ , which is based on a reconstruction of the unresolved scale.

Different models have been proposed to estimate  $\mathbf{U}^*$ . In this work we have used the model proposed by Stolz et al. [2001]:

$$u_i^* = \sum_{k=0}^N (\mathbf{I} - \mathbf{G})^k u_i, \quad (6.9)$$

where  $\mathbf{G}$  is the filter function. Choosing  $k = 1$  the above expression gives a rough estimate of the unresolved scales:

$$u_i^* = u_i + (u_i - \mathbf{G}u_i). \quad (6.10)$$

This model has been recently applied to approximate the unclosed stress term in the momentum equation for the fluid in the work of Stolz et al. [2001] and

later extended to the particle Lagrangian equation [Kuerten, 2006, Shotorban and Mashayek, 2005, Shotorban et al., 2007]. In this work we have used it to model the non-linear term  $\mathbf{U} \cdot \nabla \mathbf{U}$  and the time derivatives  $D\mathbf{U}/Dt$  in Eq. 6.5 respectively with  $\mathbf{U}^* \cdot \nabla \mathbf{U}^*$  and  $D\mathbf{U}^*/Dt$ . The deconvolution order  $k$  has been set to 1 or 5, as in the previously cited works. When the deconvolution model is used there is no need to include a SGS diffusivity in the concentration equations, therefore in this case the turbulent Schmidt number appearing in Eq. 6.8, has been set to infinity. The filter function  $\mathbf{G}$  chosen is equal to the test filter used in the dynamic model (27-points Gaussian filter).

## 6.5 Numerical details

As it has been already mentioned, the desired friction Reynolds number  $Re_\tau = 150$  is obtained by taking the following dimensionless quantities:

$$\rho = 1 \text{ Kg/m}^3 \quad \mu = \frac{1}{Re_\tau} \quad (6.11)$$

and adding a unitary pressure gradient source term in the  $x$ -momentum equation.

The grids described in Chap. 4 have been scaled in  $z$  and  $x$  direction to match the actual domain size, without changing the wall-normal resolution. As in Chap. 4 the grids are labelled as:

1. GNR,  $64 \times 32 \times 64$  cells with  $\Delta y^+ = 0.36$ ,
2. GR,  $64 \times 100 \times 64$  cells with  $\Delta y^+ = 0.11$ .

However, contrarily to Chap. 4, since the the Reynolds number is lower here, both the grids have the first cell below  $y^+ = 1$  therefore we can state that both the grid are fully resolving the wall boundary layer, at least in wall normal direction.

From the results of the single-phase study (see Chap. 4), the optimal schemes and parameters have been selected to use in this test case. In particular the simulations are carried out in time with an implicit second-order backward Euler scheme, and the advective fluxes are discretised with the central scheme for velocities. The same scheme for particle concentrations cannot be used because it turned out to be unstable. Particle fluxes are discretised with the HLLPA scheme [Zhu, 1991] that is characterised by a boundedness property together with a good accuracy and strong stability. The concentrations are in fact advected with a pure transport equation with small or null diffusivity and they are characterised by high gradients that can easily give spurious numerical oscillations. So bounded and oscillations-free schemes typical of conservation laws, could also be used (e.g., TVD, ENO, WENO).

The particles are inserted in the channel with a turbulent flow field fully developed and particle statistics are calculated when the statistically steady state is

reached for particle concentration. This steady state is completely physical but it is important because it is naturally reached with Lagrangian and Eulerian models and it is fully determined by the simulation parameters In real cases instead when the particle deposit to the wall, complex interactions between wall, particles and fluid can happen. However what is important in this case is not the deposition itself but the turbophoresis phenomenon that is the main driving force for deposition.

The simulations have been carried out with the commercial CFD code *TransAT*, in a two-way quad-core Opteron 2.1GHz with 16 GB of RAM with shared memory parallelisation paradigm (OpenMP). The total simulation time for a single run was from twenty days for the coarse grid, up to a hundred days for the finer one. These reduce respectively to ten and thirty days, when using two processors and six processors.

## 6.6 Results and discussion

The results obtained with the code TransAT have been compared to DNS data of the benchmark of Marchioli et al. [2008b], in terms of mean particle concentrations, mean particle velocity, fluctuations and velocity correlation spectra.

To recognise the statistical steady state the mean concentration of particles in the region with  $y^+ < 1$  has been analysed in time. The steady state for particle concentration is reached approximately after 20,000 adimensional time units, depending on the different simulation and Stokes number, that corresponds to a developing length of approximately 1000 channel heights. This is much more than the developing-length of a single-phase flow and can give an idea of the very high computational costs of these simulations. For  $St = 0.2$  Lagrangian DNS data are only partially available and for a shorter period of time, because this case was not included in the benchmark. Therefore the statistical steady state is not completely reached and the mean concentration results lower than expected.

The concentration of particles with  $St = 5$  was found to be subjected to stability problems, especially when ADM is used. This can be explained by the fact that very large fluctuations are predicted causing locally an elevate CFL number. This could be avoided by taking very small time steps but this would reflect in impracticable simulation times. Finally the simulations with ASM resulted, as expected, in results almost identical to the EEM. This demonstrates the equivalence of the two formulations in this case therefore in the following discussion only the results with EEM will be presented. Due to limited computational resources, simulations with the finer grid, are reported only for the case without ADM. The simulations with ADM, in fact, were not carried out for the whole time needed for statistics. However, analysing the first part of the simulations, we can state that the influence of ADM is not important as for the coarser grid. This can be explained by the fact

that more scales are solved in the wall-normal direction and the ADM acts more only in the remaining directions.

Assuming that the fluid phase is adequately solved (as demonstrated in Chap. 4), four main sources of errors can be present in the simulation of the dispersed phase: numerics, Eulerian formulation, unresolved scales and equilibrium model formulation. Therefore it is important to understand which of these affects more the overall deposition rate. In particular it is worth noticing that, to extract particle statistics from the Lagrangian data, a volume average must be applied and, depending on the choice of the control volume, slightly different results can be obtained. In the following Lagrangian DNS data, taken from the benchmark study of Marchioli et al. [2008b], are averaged over 193 wall-parallel slabs, distributed non-uniformly along the wall.

Let us first analyse Fig. 6.4 where results are reported for  $St = 1.0$ . This is the case with more data available and where the most important conclusions can be drawn. In the top left the evolution in time of mean concentration of particles accumulated near the wall (in the region  $y^+ < 1$ ) clearly shows the accumulation of particles near the wall that is particularly fast, in the first part of the simulations. However very different results are obtained with the different models used. The simulation with the coarse grid without ADM shows a very low accumulation, far from the reference DNS results. The prediction significantly improves when the ADM is included. In particular, the simulation with ADM of order  $k = 5$  results in a curve very close to the DNS, at least in the initial part. After 4000 time unit, in fact, the LES results seem to reach the steady state, while the DNS curve continues to grow up to 10000 time units. This can explained by the numerical dissipation of the grid and the schemes that a certain point smooth the concentration gradient. This is confirmed by the top right plot where the mean concentration profile is represented along the wall-normal direction, where the DNS is characterised, not only by a higher peak in concentration but also by a steeper curves. LES results instead tend more to diffuse the concentration in the region  $y^+ < 10$ . Also the results with the fine grid (available only for the case without ADM) seem to confirm this hypothesis. In this case, in fact, the wall-normal resolution is very high, resulting in lower numerical errors and predicting a steeper concentration profile, with a peak similar to the DNS one, and a concentration at the wall that grows for more time. No significant differences instead are reported for the mean particle velocity profile in the central left panel. The good agreement found by LES with high order ADM is confirmed also looking at RMS of particle fluctuations in  $x$ -direction in the central right panel, while an overestimation is present for the  $y$ - and  $z$ -directions.

Figure 6.5 shows the results for  $St = 0.2$  and  $St = 5$ . As already reported, these results are not complete because DNS data are not available for  $St = 0.2$ , except for a mean concentration profile obtained in non completely developed flow, and LES simulations with ADM are not reported because affected by some numerical

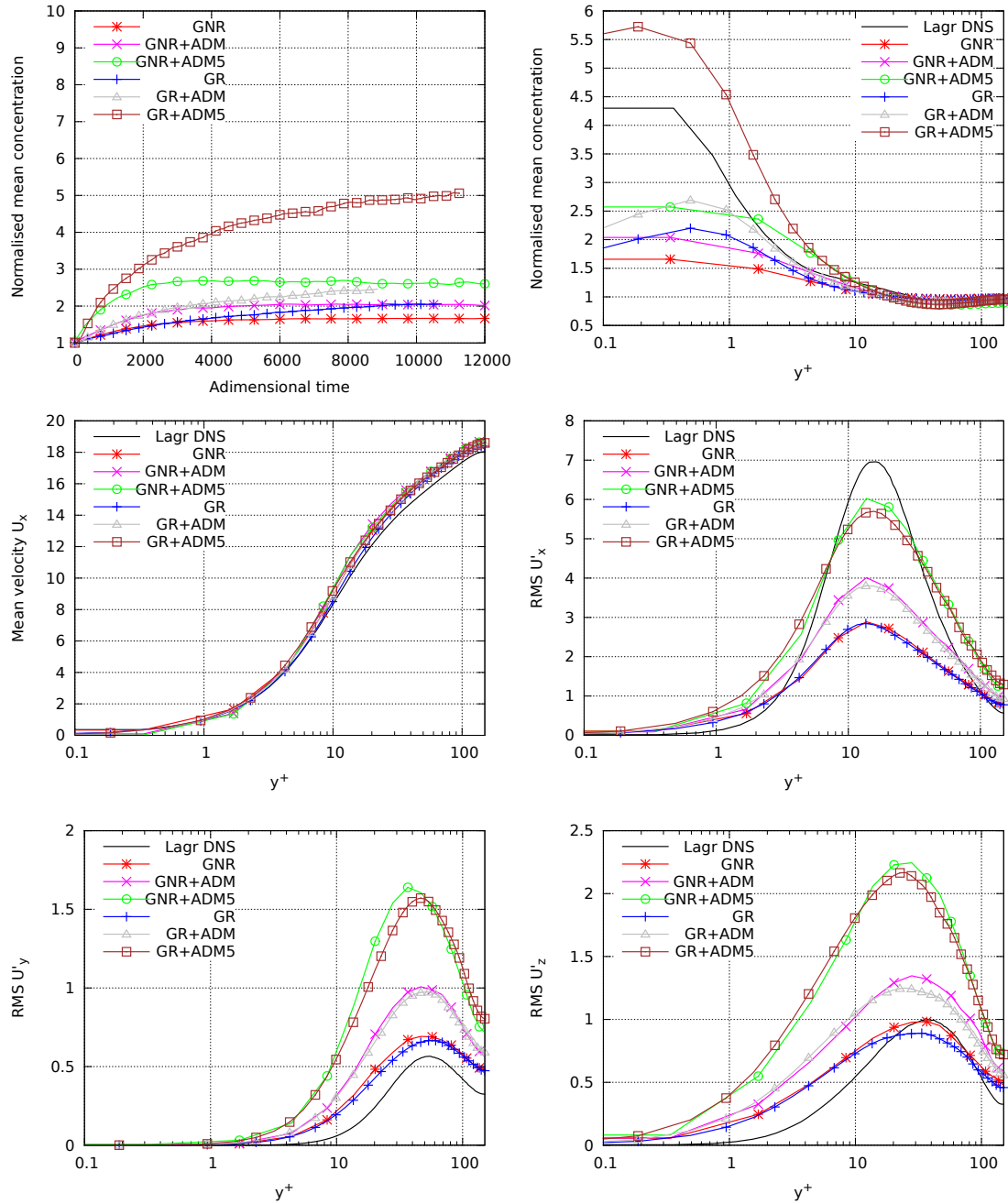


Figure 6.4: Time evolution of the mean particle concentration near the wall (top left), mean concentration profile (top right), mean stream-wise particle velocity (centre left) and RMS of stream-wise (centre right), wall-normal (bottom left) and span-wise (bottom right) fluctuations for  $St = 1.0$ .

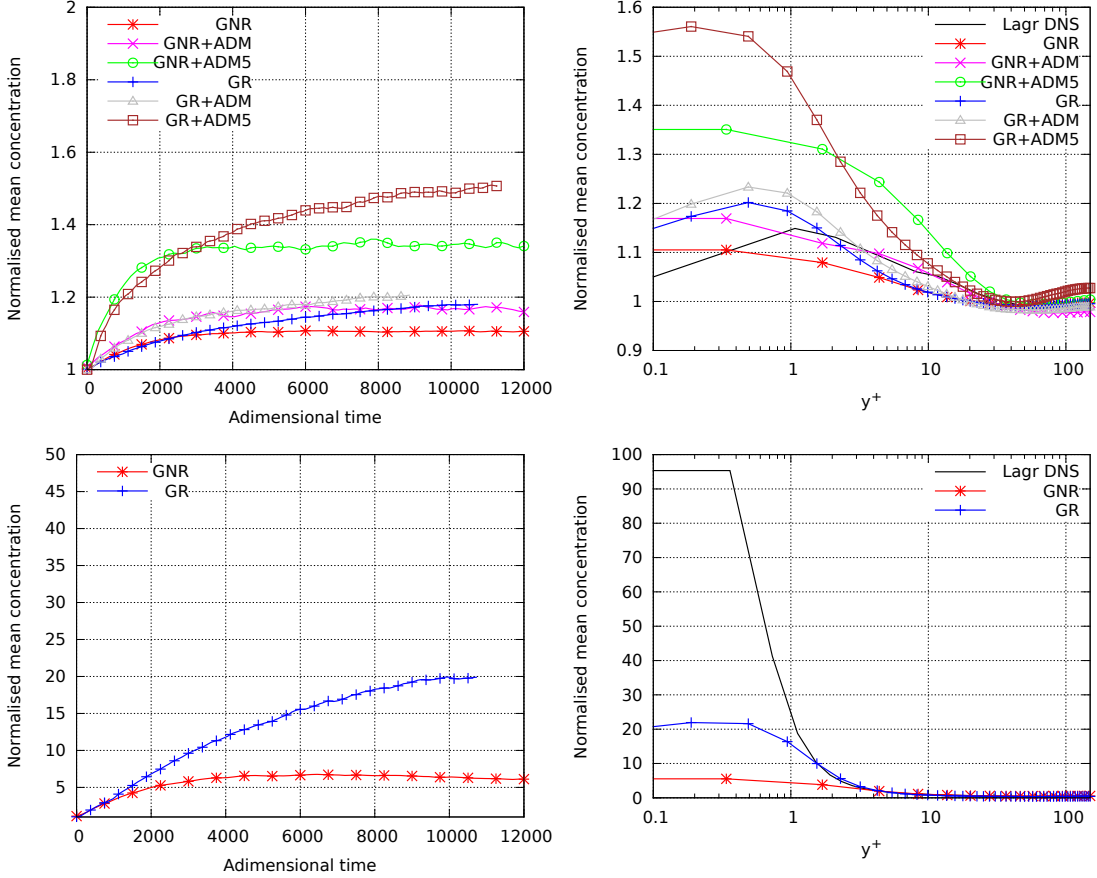


Figure 6.5: Time evolution of the mean particle concentration near the wall (left) and steady-state concentration profile (right) for  $St = 0.2$  (top),  $St = 1.0$  (middle) and  $St = 5.0$  (bottom).

instabilities. However from the top of Fig. 6.5, where the results for  $St = 0.2$  are shown, in terms of accumulation over time and concentration profile, it can be stated again that the ADM is crucial to obtain a stronger effect of turbophoresis, even if in this case, where the approximation made by EEM, can be considered small, the ADM with  $k = 1$  or the finer grid without deconvolution seem to be enough to predict the correct concentration profile. The case with  $St = 5.0$  in the bottom part of Fig. 6.5 shows instead, as expected, the inaccuracy of the EEM model in predicting the dynamics of bigger particles that, because of their high inertia, cannot be approximated with the equilibrium assumption.

Eventually these simulations are combined together to describe the evolution of the PSD for a population of particles initially distributed with a log-normal distribution of Tab. 6.1. Results are summarized in Fig. 6.6, where the contour plots

of the mean particle size are reported at three different sections of the channel. The mean particle size is quantified by the Sauter diameter, defined as the ratio between the moments of order three and two of the PSD:

$$d_{32} = \frac{m_3}{m_2} = \frac{\sum_{\alpha=1}^{N=3} w_{\alpha} L_{\alpha}^3}{\sum_{\alpha=1}^{N=3} w_{\alpha} L_{\alpha}^2}, \quad (6.12)$$

where the nodes of the quadrature approximation  $L_1$ ,  $L_2$  and  $L_3$  are constant and equal to the values reported in Tab. 6.1 for  $N = 3$ , whereas the weights  $w_1$ ,  $w_2$  and  $w_3$  are the particle concentration profiles previously discussed. As it is seen, starting from an uniform PSD (and mean particle size) throughout the channel, bigger particles tend to accumulate at the wall, causing an increase in the mean particle size. By using the first six predicted moments:

$$m_k = \sum_{\alpha=1}^{N=3} w_{\alpha} L_{\alpha}^k, \quad \text{with } k = 0, \dots, 5, \quad (6.13)$$

the PSD can be reconstructed. The reconstructed PSDs are reported (blue line), for two points in the center of the channel and near the wall, together with the quadrature approximation (red line).

## 6.7 Conclusions

In this work a fast LES model is proposed for the simulation of dilute poly-dispersed multiphase flow with moderate Stokes number, based on an Eulerian approach and algebraic relations for the relative velocity of the dispersed phase. The unresolved scales are reintroduced in the particles phase with the ADM.

The model is validated for the turbophoresis phenomenon in a turbulent periodic particle-laden channel flow with  $Re_{\tau} = 150$  and particles Stokes number ranging from 0.2 to 5. Results show good agreement with reference Lagrangian DNS data for moderate  $St$  ( $\leq 1$ ) and demonstrate the importance of an adequate SGS model for particles. In particular, the correct deposition is predicted only when the ADM is applied for the particles velocity. As expected, the different sources of error (numerics, Eulerian formulation, EEM and LES) interact in a complex way and must be accurately analysed. In particular the ADM seem to compensate the loosing of small scales fluctuations but it must be controlled, according the grid resolution in the three dimensions, to control the overestimation of fluctuations. Among the other causes of errors, the Eulerian formulation seem to be adequate for the simulation of particular type of dispersed phase, as long as particle collisions are not important. The numerical error instead can be relevant when approximating the high concentration gradients near the wall and more accurate high-order ENO/WENO schemes could be used to alleviate this error.

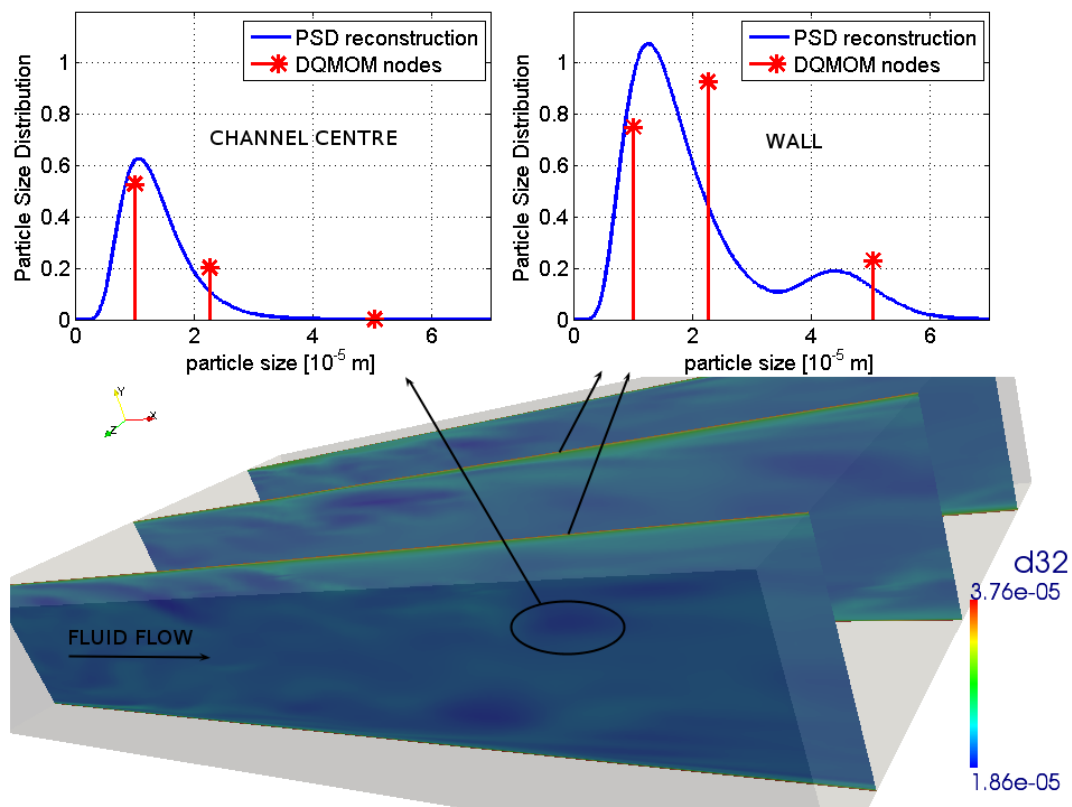


Figure 6.6: Turbophoresis phenomenon in the turbulent channel flow under study: contour plots of the mean particle size  $d_{32}$  and PSD in the centre of the channel and near the wall (DQMOM approximations, red line, and reconstructed PSD, blue line).

Finally this model represent an efficient solution for the simulation of turbulent multiphase dispersed flow with moderate Stokes number, resulting in a computational time much lower than Lagrangian DNS or multi-fluid simulations and coupled with a detailed description of the Particle Size Distribution through the use of DQ-MOM formulation. It can be easily extended to the simulation of micro- and nanoparticles in micro-devices characterised by a high mixing rate, such as the Confined Impinging Jets Reactor of Chap. 3 and 5. Other interesting applications such as environmental dispersion can be solved with this model.

## References

- A. Aliseda, A. Cartellier, F. Hainaux, and J. Lasheras. Effect of preferential concentration on the settling velocity of heavy particles in homogeneous isotropic turbulence. *J. Fluid Mech.*, 468:77–105, 2002.
- M. Arai. Characteristics and stability analysis for two-phase flow equation systems with viscous terms. *Nucl. Sci. Eng.*, 74(2):77–83, 1980.
- B. Arcen, A. Taniére, and B. Oesterlé. On the influence of near-wall forces in particle-laden channel flows. *Int. J. Multiphase Flow*, 32(12):1326–1339, 2006.
- V. Armenio, U. Piomelli, and V. Fiorotto. Effect of the subgrid scales on particle motion. *Phys. Fluids*, 11(10):3030–3042, 1999.
- Ascomp GmbH. *Multi-Fluid Navier-Stokes Solver TransAT User Manual*, 2009.
- S. Balachandar. A scaling analysis for point-particle approaches to turbulent multiphase flows. *Int. J. Multiphase Flow*, 35(9):801–810, 2009.
- S. Balachandar and J. K. Eaton. Turbulent dispersed multiphase flow. *Annu. Rev. Fluid Mech.*, 42:111–133, 2010.
- A. Berrouk, D. Laurence, J. Riley, and D. Stock. Stochastic modelling of inertial particle dispersion by subgrid motion for les of high reynolds number pipe flow. *J. Turb.*, 8:1–20, 2007.
- M. Boivin, O. Simonin, and K. D. Squires. Direct numerical simulation of turbulence modulation by particles in isotropic turbulence. *J. Fluid Mech.*, 375:235–263, 1998.
- M. Boivin, O. Simonin, and K. Squires. On the prediction of gas-solid flows with two-way coupling using large eddy simulation. *Phys. Fluids*, 12(8):2080–2090, 2000.
- J. W. Brooke, K. Kontomaris, T. J. Hanratty, and J. B. McLaughlin. Turbulent deposition and trapping of aerosol at the wall. *Phys. Fluids*, A 4:825, 1992.
- A. D. Burns, T. Frank, I. Hamill, and J.-M. Shi. The favre averaged drag model for turbulent dispersion in eulerian multi-phase flow. In *Fifth Int. Conference on Multiphase Flow, ICMF 04*, Yokohama, Japan, 2004.
- S. Cerbelli, A. Giusti, and A. Soldati. Ade approach to predicting dispersion of heavy particles in wall-bounded turbulence. *Int. J. Multiphase Flow*, 27:1861, 2001.

---

## REFERENCES

---

- R. Chein and J. N. Chung. Effects of vortex pairing on particle dispersion in turbulent shear flows. *Int. J. Multiphase Flow*, 13:785–802, 1987.
- J. Chun, D. Koch, S. Rani, A. Ahluwalia, and L. Collins. Clustering of aerosol particles in isotropic turbulence. *J. Fluid Mech.*, 536:219–251, 2005.
- J. W. Cleaver and B. Yates. A sublayer model for the deposition of particles from a turbulent flow. *Chem. Eng. Sci.*, 30:983, 1975.
- R. Clift, J. R. Grace, and M. E. Weber. *Bubbles, Drops and Particles*. Academic Press, New York, 1978.
- L. Collins and A. Keswani. Reynolds number scaling of particle clustering in turbulent aerosols. *New J. Phys.*, 6:1–17, 2004.
- D. A. Drew and S. L. Passman. *Theory of multicomponent fluids*. Springer-Verlag New York, Inc., 1998.
- O. Druzhinin. On the two-way interaction in two-dimensional particle-laden flows: the accumulation of particles and flow modification. *J. Fluid Mech.*, 297:49–76, 1995.
- J. Eaton and J. Fessler. Preferential concentration of particles by turbulence. *Int. J. Multiphase Flow*, 20(SUPPL. 1):169–209, 1994.
- S. Elghobashi and G. Truesdell. Direct simulation of particle dispersion in a decaying isotropic turbulence. *J. Fluid Mech.*, 242:655–700, 1992.
- S. Elghobashi and G. C. Truesdell. On the two-way interaction between homogeneous turbulence and dispersed solid particles. i. turbulence modification. *Phys. Fluids A*, 5: 1790–1801, 1993.
- J. Ferry and S. Balachandar. A fast eulerian method for disperse two-phase flow. *Int. J. Multiphase Flow*, 27(7):1199–1226, 2001.
- J. Ferry and S. Balachandar. Equilibrium expansion for the eulerian velocity of small particles. *Powder Technol.*, 125(2-3):131–139, 2002.
- J. Ferry, S. L. Rani, and S. Balachandar. A locally implicit improvement of the equilibrium eulerian method. *Int. J. Multiphase Flow*, 29(6):869–891, 2003.
- J. R. Fessler, J. D. Kulick, and J. K. Eaton. Preferential concentration of particles in a turbulent channel flow. *Phys. Fluids*, 6:3742, 1994.
- P. Février, O. Simonin, and K. Squires. Partitioning of particle velocities in gas-solid turbulent flows into a continuous field and a spatially uncorrelated random distribution: Theoretical formalism and numerical study. *J. Fluid Mech.*, 533:1–46, 2005.
- R. O. Fox. Large-eddy-simulation tools for multiphase flows. *Annu. Rev. Fluid Mech.*, 44 (1), 2012.
- S. Friedlander and H. Johnstone. Deposition of suspended particles from turbulent gas streams. *Ind. Eng. Chem.*, 49(7):1151–1156, 1957.
- B. Geurts, H. Clercx, and W. Uijttewaal. *Particle-laden flow: from geophysical to Kolmogorov scales*. ERCOFTAC series. Springer, 2007.
- C. Gobert. Analytical assessment of models for large eddy simulation of particle laden flow. *J. Turbul.*, 11:1–24, 2010.

- A. Guha. A unified eulerian theory of turbulent deposition to smooth and rough surfaces. *J. Aerosol Sci.*, 28(8):1517–1537, 1997.
- A. Guha. Transport and deposition of particles in turbulent and laminar flow. *Annu. Rev. Fluid Mech.*, 40(1):311–341, 2008.
- H. Guillard and F. Duval. A darcy law for the drift velocity in a two-phase flow model. *J. Comput. Phys.*, 224:288–313, 2007.
- K. Hishida, A. Ando, and M. Maeda. Experiments on particle dispersion in a turbulent mixing layer. *Int. J. Multiphase Flow*, 18:181–194, 1992.
- Z. Hu, X. Luo, and K. H. Luo. Numerical simulation of particle dispersion in a spatially developing mixing layer. *Theoret. Comput. Fluid Dyn.*, 15:403–420, 2002.
- M. Ishii. *Thermo-Fluid Dynamic Theory of Two-Phase Flow*. Eyrolles, Paris, France, 1975.
- M. Ishii and N. Zuber. Drag coefficient and relative velocity in bubbly, droplet or particulate flows. *AIChE J.*, 25:843–855, 1979.
- A. Jones and A. Prosperetti. On the suitability of first-order differential models for two-phase flow prediction. *Int. J. Multiphase Flow*, 11(2):133–148, 1985.
- D. Kaftori, G. Hetsroni, and S. Banerjee. Particle behaviour in the turbulent boundary layer: motion, deposition and entrainment. *Phys. Fluids*, 7:1095–1106, 1995.
- G. Kallio and M. Reeks. A numerical simulation of particle deposition in turbulent boundary layers. *Int. J. Multiphase Flow*, 15(3):433–446, 1989.
- J. Kuerten. Subgrid modeling in particle-laden channel flow. *Phys. Fluids*, 18(2), 2006.
- J. Kuerten and A. Vreman. Can turbophoresis be predicted by large-eddy simulation? *Phys. Fluids*, 17(1):011701–011701–4, 2005.
- V. Lavezzo, A. Soldati, S. Gerashchenko, Z. Warhaft, and L. Collins. Direct numerical simulation of inertial particle accelerations in near-wall turbulence: Comparison with experiments. *Chem. Eng. Trans.*, 17:579–584, 2009.
- B. J. Lazaro and J. C. Lasheras. Particle dispersion in the developing free shear layer. part 1. unforced flow. *J. Fluid Mech.*, 235:143–178, 1992.
- Y. Li, J. McLaughlin, K. Kontomaris, and L. Portela. Numerical simulation of particle-laden turbulent channel flow. *Phys. Fluids*, 13(10):2957–2967, 2001.
- B. Y. Liu and J. K. Agarwal. Experimental observation of aerosol deposition in turbulent flow. *J. Aerosol Sci.*, 5(2):145–155, 1974.
- M. Manninen and V. Taivassalo. *On the mixture model for multiphase flow*. VTT Publications, Espoo, Finland, 1996.
- C. Marchioli, A. Giusti, M. Salvetti, and A. Soldati. Direct numerical simulation of particle wall transfer and deposition in upward turbulent pipe flow. *Int. J. Multiphase Flow*, 29(6):1017–1038, 2003.
- C. Marchioli, M. Picciotto, and A. Soldati. Particle dispersion and wall-dependent turbulent flow scales: Implications for local equilibrium models. *J. Turb.*, 7:1–12, 2006.
- C. Marchioli, M. Picciotto, and A. Soldati. Influence of gravity and lift on particle velocity

---

## REFERENCES

---

- statistics and transfer rates in turbulent vertical channel flow. *Int. J. Multiphase Flow*, 33(3):227 – 251, 2007.
- C. Marchioli, M. Salvetti, and A. Soldati. Some issues concerning large-eddy simulation of inertial particle dispersion in turbulent bounded flows. *Phys. Fluids*, 20(4), 2008a.
- C. Marchioli, A. Soldati, J. Kuerten, B. Arcen, A. Tanière, G. Goldensoph, K. Squires, M. Cargnelutti, and L. Portela. Statistics of particle dispersion in direct numerical simulations of wall-bounded turbulence: Results of an international collaborative benchmark test. *Int. J. Multiphase Flow*, 34(9):879–893, 2008b.
- B. Marcu and E. Meiburg. The effect of streamwise braid vortices on the particle dispersion in a plane mixing layer. i. equilibrium points and their stability. *Phys. Fluids*, 8:715–732, 1996.
- F. Mashayek and R. Pandya. Analytical description of particle/droplet-laden turbulent flows. *Prog. Energy Combust. Sci.*, 29(4):329–378, 2003.
- M. R. Maxey. The gravitational settling of aerosol-particles in homogeneous turbulence and random flow-fields. *J. Fluid Mech.*, 174:441–465, 1987.
- M. R. Maxey and J. K. Riley. Equation of motion for a small rigid sphere in a nonuniform flow. *Phys. Fluids*, 26:883–889, 1983.
- D. D. McCoy and T. J. Hanratty. Rate of deposition of droplets in annular two-phase flow. *Int. J. Multiphase Flow*, 3:319, 1975.
- J. McLaughlin. Aerosol particle deposition in numerically simulated channel flow. *Phys. Fluids A*, 1(7):1211–1224, 1989.
- E. Meiburg, E. Wallner, A., A. Riaz, C. Haertel, and F. Necker. Vorticity dynamics of dilute two-way-coupled particle-laden mixing layers. *J. Fluid Mech.*, 421:185, 2000.
- J. P. Minier and E. Peirano. The pdf approach to turbulent polydispersed two-phase flows. *Phys. Reports*, 352(1-3):1–214, 2001.
- M. Moreau, O. Simonin, and B. Bédat. Development of gas-particle euler-euler les approach: A priori analysis of particle sub-grid models in homogeneous isotropic turbulence. *Flow, Turbulence and Combustion*, 84(2):295–324, 2010.
- C. Narayanan. *Numerical analysis of particle transport and flow modification in temporally evolving mixing layers*. PhD thesis, ETH Zurich, Switzerland, 2004.
- C. Narayanan, D. Lakehal, L. Botto, and A. Soldati. Mechanisms of particle deposition in a fully-developed turbulent open channel flow. *Phys. Fluids*, 15:763–775, 2003.
- R. Pandya and F. Mashayek. Two-fluid large-eddy simulation approach for particle-laden turbulent flows. *Int. J. Heat Mass Transfer*, 45(24):4753–4759, 2002.
- R. N. Parthasarathy and G. M. Faeth. Turbulence modulation in homogeneous dilute particle-laden flows. *J. Fluid Mech.*, 220:485–514, 1990a.
- R. N. Parthasarathy and G. M. Faeth. Turbulent dispersion of particles in self-generated homogeneous turbulence. *J. Fluid Mech.*, 220:515–537, 1990b.
- P. Pascal and B. Oesterlé. On the dispersion of discrete particles moving in a turbulent shear flow. *Int. J. Multiphase Flow*, 26:293–325, 2000.

- A. Passalacqua and R. Fox. Advanced continuum modelling of gas-particle flows beyond the hydrodynamic limit. *Appl. Math. Modell.*, 35(4):1616–1627, 2011.
- A. Prosperetti and A. Jones. The linear stability of general two-phase flow models-ii. *Int. J. Multiphase Flow*, 13(2):161–171, 1987.
- A. Prosperetti and D. Z. Zhang. Finite-particle-size effects in disperse two-phase flows. *Theoret. Comput. Fluid Dyn.*, 7:429–440, 1995.
- W. Reade and L. Collins. Effect of preferential concentration on turbulent collision rates. *Phys. Fluids*, 12(10):2530–2540, 2000.
- M. W. Reeks. On the continuum equations for dispersed particles in nonuniform flows. *Phys. Fluids A*, 4:1290–1303, 1992.
- D. W. I. Rouson and J. K. Eaton. On the preferential concentration of solid particles in turbulent channel flow. *J. Fluid Mech.*, 428:149–169, 2001.
- J. Salazar, J. D. Jong, L. Cao, S. Woodward, and H. C. L. Meng. Experimental and numerical investigation of inertial particle clustering in isotropic turbulence. *J. Fluid Mech.*, 600:245–256, 2008.
- S. Schreck and S. J. Kleis. Modification of grid-generated turbulence by solid particles. *J. Fluid Mech.*, 249:665–688, 1993.
- M. Shams, G. Ahmadi, and H. Rahimzadeh. A sublayer model for deposition of nano- and micro-particles in turbulent flows. *Chem. Eng. Sci.*, 55:6907, 2000.
- R. Shaw, W. Reade, L. Collins, and J. Verlinde. Preferential concentration of cloud droplets by turbulence: Effects on the early evolution of cumulus cloud droplet spectra. *J. Atmos. Sci.*, 55(11):1965–1976, 1998.
- B. Shotorban and S. Balachandar. Two-fluid approach for direct numerical simulation of particle-laden turbulent flows at small stokes numbers. *Phys. Rev. E*, 79(5), 2009.
- B. Shotorban and F. Mashayek. Modeling subgrid-scale effects on particles by approximate deconvolution. *Phys. Fluids*, 17(8):1–4, 2005.
- B. Shotorban, K. Zhang, and F. Mashayek. Improvement of particle concentration prediction in large-eddy simulation by defiltering. *Int. J. Heat Mass Transfer*, 50(19-20): 3728–3739, 2007.
- E. Sinaiski and L. Zaichik. *Statistical microhydrodynamics*. Wiley-VCH, 2008.
- S. Slater, A. Leeming, and J. Young. Particle deposition from two-dimensional turbulent gas flows. *Int. J. Multiphase Flow*, 29(5):721–750, 2003.
- A. Soldati and C. Marchioli. Physics and modelling of turbulent particle deposition and entrainment: Review of a systematic study. *Int. J. Multiphase Flow*, 35(9):827–839, 2009.
- M. Sommerfeld and N. Huber. Experimental analysis and modelling of particle-wall collisions. *Int. J. Multiphase Flow*, 25:1457–1489, 1999.
- M. C. Soteriou and X. Yang. Particle dispersion in variable density and viscosity shear flows. *Phys. Fluids*, 11:1373–1386, 1999.
- K. Squires and J. Eaton. Preferential concentration of particles by turbulence. *Phys.*

- Fluids A*, 3(5):1169–1178, 1991.
- K. D. Squires and J. K. Eaton. Particle response and turbulence modification in isotropic turbulence. *Phys. Fluids A*, 2:1191, 1990.
- D. E. Stock and L.-P. Wang. Dispersion of heavy particles by turbulent motion. *J. Atmosph. Sc.*, 50(13):1897–1913, 1993.
- S. Stolz, N. Adams, and L. Kleiser. An approximate deconvolution model for large-eddy simulation with application to incompressible wall-bounded flows. *Phys. Fluids*, 13(4):997–1015, 2001.
- S. Sundaram and L. Collins. Collision statistics in an isotropic particle-laden turbulent suspension. part 1. direct numerical simulations. *J. Fluid Mech.*, 335:75–109, 1997.
- S. Sundaram and L. Collins. A numerical study of the modulation of isotropic turbulence by suspended particles. *J. Fluid Mech.*, 379:105–143, 1999.
- Y. Tang and B. Guo. Computational fluid dynamics simulation of aerosol transport and deposition. *Frontiers of Environmental Science & Engineering In China*, 5(3):362–377, 2011.
- W. S. J. Uijtewaal and R. V. A. Oliemans. Particle dispersion and deposition in direct numerical and large eddy simulations of vertical pipe flows. *Phys. Fluids*, 8(10):2590–2604, 1996.
- B. Van Haarlem, B. J. Boersma, and F. M. T. Nieuwstadt. Direct numerical simulation of particle deposition onto a free-slip and no-slip surface. *Phys. Fluids*, 10:2608, 1998.
- A. Vreman. Stabilization of the eulerian model for incompressible multiphase flow by artificial diffusion. *J. Comput. Phys.*, 230(4):1639–1651, 2011.
- L. P. Wang and M. R. Maxey. Settling velocity and concentration distribution of heavy particles in homogeneous isotropic turbulence. *J. Fluid Mech.*, 256:27–68, 1993.
- L. P. Wang, A. S. Wexler, and Y. Zhou. Statistical mechanical description and modelling of turbulent collision of inertial particles. *J. Fluid Mech.*, 415:117–153, 2000.
- L.-P. Wang, B. Rosa, H. Gao, G. He, and G. Jin. Turbulent collision of inertial particles: Point-particle based, hybrid simulations and beyond. *Int. J. Multiph. Flow*, 35(9):854–867, 2009.
- Q. Wang and K. Squires. Large eddy simulation of particle deposition in a vertical turbulent channel flow. *Int. J. Multiphase Flow*, 22(4):667–682, 1996a.
- Q. Z. Wang and K. D. Squires. Large eddy simulation of particle-laden turbulent channel flow. *Phys. Fluids*, 8(5):1207–1223, 1996b.
- T. Wang, J. Wang, and Y. Jin. Slurry reactors for gas-to-liquid processes: A review. *Ind. Eng. Chem. Res.*, 46(18):5824–5847, 2007.
- F. Wen, N. Kamalu, J. N. Chung, C. T. Crowe, and T. R. Troutt. Particle dispersion by vortex structures in plane mixing layers. *J. Fluids Eng.*, 114:657–666, 1992.
- A. Wood, W. Hwang, and J. Eaton. Preferential concentration of particles in homogeneous and isotropic turbulence. *Int. J. Multiph. Flow*, 31(10-11):1220–1230, 2005.
- Y. Yamamoto, M. Potthoff, T. Tanaka, T. Kajishima, and Y. Tsuji. Large-eddy simulation

- of turbulent gas-particle flow in a vertical channel: effect of considering inter-particle collisions. *J. Fluid Mech.*, 442:303–334, 2001.
- X. Yang, N. H. Thomas, and L. J. Guo. Particle dispersion in organized vortex structures within turbulent free shear flow. *Chem. Eng. Sci.*, 55:1305–1324, 2000.
- F. Yen and U. Lei. On the motion of small particles in a homogeneous isotropic turbulent flow. *Phys. Fluids A*, 3(11):2571–2586, 1991.
- J. Young and A. Leeming. A theory of particle deposition in turbulent pipe flow. *J. Fluid Mech.*, 340:129–159, 1997.
- Z. Yuan and E. E. Michaelides. Turbulence modulation in particulate flows - a theoretical approach. *Int. J. Multiphase Flow*, 18:779–785, 1992.
- L. Zaichik and V. Alipchenkov. Pair dispersion and preferential concentration of particles in isotropic turbulence. *Phys. Fluids*, 15(6):1776–1787, 2003.
- L. Zaichik, V. Alipchenkov, and E. Sinaiski. *Particles in turbulent flows*. Wiley-VCH, 2008.
- L. Zaichik, O. Simonin, and V. Alipchenkov. An eulerian approach for large eddy simulation of particle transport in turbulent flows. *J. Turb.*, 10:1–21, 2009.
- Y. Zhou, A. Wexler, and L.-P. Wang. On the collision rate of small particles in isotropic turbulence. ii. finite inertia case. *Phys. Fluids*, 10(5):1206–1216, 1998.
- J. Zhu. A low-diffusive and oscillation-free convection scheme. *Commun. Appl. Numer. Methods*, 7(3):225–232, 1991.

## Computational models for non-equilibrium flows

The model presented in Chap. 6 completely neglect particle collisions. In this part of the work we investigate the possibility of using a Quadrature-Based Moment Method (QBMM), namely the Quadrature Method of Moments (QMOM) as a closure for the collision kernels of the Homogeneous Isotropic Boltzmann Equation (HIBE) with a realistic description for particle collisions, namely the hard-sphere model. The behaviour of QMOM far away and approaching the equilibrium is studied and results are compared to other approximation techniques. Comparison with a more accurate and computationally expensive approach, considered as reference, is also carried out. Our results show that QMOM describes very well the evolution when it is far away from equilibrium, without the drawbacks or the computational costs of the other methods, but it is not able to accurately reproduce equilibrium and the dynamics close to it. Corrections to cure this behavior are here proposed and tested.

### 7.1 Introduction

Classical fluid dynamics theory, both for single- or multiphase flows, is based on the assumption of small deviations from equilibrium, which is however not always valid. In the case of single phase flows this might happen for gases characterised by very low pressures: the very few collisions occurring in some parts of the flow result in velocity distributions far away from the equilibrium. Similar situations are realised at standard pressure values, when the fluid is flowing in very small channels. In the case of dispersed multiphase flows, it is very common to have regions of high particle collision frequencies close to regions of very rare collisions, characterised by large

---

Part of the contents of this chapter will be published in the work of Icardi et al. [Submitted].

departures from the equilibrium. Furthermore, molecular effects have to be taken into account also in high-speed hydrodynamics (when shock waves appear)[Kogan, 1992] or interface processes (evaporation and condensation) [Sone and Onishi, 1978]. These situations are very common in many applications like aerodynamics, vacuum technology, micro-fluidics and freeze-drying [Rasetto et al., 2010, Reese et al., 2003], just to cite a few.

A key indicator of the importance of non-equilibrium effects is the Knudsen number defined as

$$\text{Kn} = \frac{\lambda}{L}, \quad (7.1)$$

where  $\lambda$  is the mean free path of the molecules or particles and  $L$  is the length scale of the system. When  $\text{Kn} \approx 0.01$  non-equilibrium effects start to be relevant and when it is above unity the continuum hypothesis fails and the classical governing equations are no more valid[Sone, 2002].

Kinetic models have to be used to account for these non-equilibrium effects. They are characterised by a transport equation, written in terms of a distribution function. This distribution represents the state of the system from a mesoscopic point of view, neglecting the behaviour of the single molecule or particle at the microscopic scale. The macroscopic quantities (e.g. density, mean fluid velocity, energy) can then be simply derived from the moments of the distribution function by integration. The use of kinetic models is grown in the last decades and extended to many fields such us traffic modelling, semiconductor and social human behaviour [Bellomo and Pulvirenti, 2000] but the main application remains the simulation of granular and rarefied flows. In this case the distribution function expresses the infinitesimal portion of particles with a given velocity at a given time and is generally called the number density function (NDF), or the probability density function (PDF) if it is a probability function that integrates to one. As it has been already mentioned, when the NDF refers to single-phase flows, it quantifies the velocity distribution of molecules, whereas in dispersed multiphase flows it generally quantifies the velocity distribution of particles.

The evolution of the NDF (or the PDF) is dictated by a kinetic equation (KE). The most famous example is provided by the Boltzmann equation (BE) [Cercignani, 1988]: this has been formally derived for the evolution of rarefied mono-atomic gases but has been extended for the simulation of high density gases (Boltzmann-Enskog equation) and dispersed multiphase flows with applications to fluidised suspensions [Gidaspow, 1994] and sprays [Williams, 1958]. It is important to stress here also the similarities between the BE and the population balance equation (PBE) [Ramkrishna, 2000] developed for crystallisation processes, the Smoluchowski coagulation equation [Smoluchowski, 1916] and the aerosol dynamic equation [Friedlander, 2000]. These kinetic models are characterised by different internal variables or coordinates (particle size instead of particle velocity) but the solution methods are usually very

similar.

Many approaches have been proposed to solve the BE. Discrete Velocity Methods (DVM) and the Direct Simulation Monte Carlo (DSMC) are those applied with the full non-linear integral collision operator when detailed knowledge of the NDF is needed.

DVM [Aristov, 2001, Broadwell, 1964, Gatignol, 1975] is one of the most popular deterministic method for solving the BE with non-linear integral collision operator. They encompass those methods based on the systematic discretisation of the microscopic velocity, using similar approaches than those used for the discretisation of the space.

DSMC [Bird, 1994] is the reference stochastic solution method for the BE. It is the best-known approach for very high Kn number flows. However, to reduce the noise-to-signal ratio in near-continuum flows the method becomes computationally expensive.

Other methods such as the Lattice Boltzmann Methods (LBM) [e.g. Benzi et al., 1992, Chen and Doolen, 1998, Qian et al., 1992, Succi, 2001, Wolf-Gladrow, 2000] are also employed; typically they make use of a simplified collision operator in the form of linear relaxation towards the equilibrium (i.e., Bhatnagar-Gross-Krook, BGK, approximation) [Bhatnagar et al., 1954]. From a modelling point of view the use of an integral collision operator offers a richer and more accurate description of the behaviour of the fluid far from equilibrium. However, the BGK approximation results in a simpler and easy to implement model characterised by faster computational times. LBM makes use of a restricted (and minimal) number of microscopic velocities that fulfil some lattice symmetry and spatial invariance properties and preserve some macroscopic moments (e.g. mass and momentum). LBM can be used for continuum and slightly rarefied flows (the latter characterised by large lattices).

Another class of methods is represented by the Method of Moments (MOM). In this case equations for the moments of the NDF are derived from the KE and the resulting closure problem is overcome by making an assumption on the functional form of the NDF. Among moment methods the so-called Grad's moment method [Grad, 1949] is very popular, although it suffers from some important drawbacks.

In this chapter we investigate a closure based on a quadrature approximation for the solution of moment equations. This closure results in the so-called Quadrature Method of Moments (QMOM) that has been recently introduced as an alternative method for KEs [Desjardins et al., 2008, Fox, 2008, 2009, Passalacqua et al., 2011]. In some of the other already published applications of QMOM for KEs with collisions, the BGK approximation or the Maxwellian kernel are used. The application of QMOM with more complex collision models, such as the hard-sphere kernel, has been considered for the first time in the work of Fox and Vedula [2010], where the general source terms for velocity moments are derived starting from the more

general Boltzmann-Enskog expression for the collision operator. This QMOM approximation has been then compared with the approximations given by simplified kernels (BGK and Maxwellian) in the work of Passalacqua et al. [2011] considering an inhomogeneous system.

The scope of our work is to further investigate the behaviour of QMOM compared to other methods for KEs. To do this QMOM is applied to the Homogeneous Isotropic Boltzmann Equation (HIBE) with the full non-linear elastic hard-sphere collisional integral and is used to simulate the evolution from an initial state far away from equilibrium to the steady state.

In Sec. 7.2 the equation under study is introduced and explained. Then the different methods are analysed and applied to the systems under study in Sec. 7.3. After the description of the test cases in Sec. 7.4, results are presented in Sec. 7.5. Eventually some final remarks are reported in Sec. 7.6.

## 7.2 Governing equations

In the MOM for KEs two types of closures typically arise: the convective and the collisional terms. We will focus here on the collisional term. When using simplified models for collisions this problem does not arise, instead there exist alternative models to account for particle collisions more realistically that need an accurate closure. In particular we want to consider the hard-sphere model to analyse the unsteady approach to equilibrium starting from an arbitrary distribution function.

To reduce the phase space and preserve the physical meaning of collisions, we cannot reduce to a single spatial dimension so we assume a three-dimensional spatial domain with the hypothesis of homogeneity (no spatial variation) and isotropy (no preferential direction for velocity). This means that polar coordinates can be used and, neglecting the angles, the phase space is simply represented by the velocity magnitude (or speed)  $\xi$ . Nevertheless the three-dimensional components of particles velocity are still implicitly taken into account in the collisional integral. Therefore we consider the equation that operates on a distribution  $f(t, \xi)$ , function of the time  $t \in \mathbb{R}^+$  and of the magnitude of the speed  $\xi \in \mathbb{R}^+$ . The distribution function allows one to compute the infinitesimal number of molecules or particles per unit volume at time  $t$  with a speed between  $\xi$  and  $\xi + d\xi$ , namely  $f(t, \xi)d\xi$ . Clearly the formulation of the problem in terms of velocity magnitude is equivalent to that in terms of kinetic energy  $E = \xi^2/2$ .

Under the previous assumptions the dynamics of  $f$  can be described by the following equation:

$$\frac{\partial f}{\partial t} = Q(f, f) \dot{=} N(f, f) - \nu(f) f, \quad (7.2)$$

where

$$N(f, f) = 2\pi^2 \int_0^{+\infty} \xi_*^2 \int_{-1}^{+1} \int_{-1}^{+1} f(\xi') f(\xi'_*) |\xi_* y - \xi x| dx dy d\xi_* , \quad (7.3)$$

and

$$\nu(f) = 2\pi^2 \int_0^{+\infty} f(\xi_*) \xi_*^2 \int_{-1}^{+1} \int_{-1}^{+1} |\xi_* y - \xi x| dx dy d\xi_* . \quad (7.4)$$

The variables  $x$  and  $y$  are collisional parameters (integration dummy variables), which are related to the molecular velocities as:

$$\begin{aligned} \xi' &= \xi'(\xi, \xi_*, x, y) = \sqrt{\xi^2(1-x^2) + \xi_*^2 y^2} , \\ \xi'_* &= \xi'_*(\xi, \xi_*, x, y) = \sqrt{\xi_*^2(1-y^2) + \xi^2 x^2} . \end{aligned} \quad (7.5)$$

The above equations are written considering a normalised dimensionless system with unitary particle mass and radius. The HIBE, derived and studied in different previous works [Asinari, 2010, Ernst, 1981, Preziosi and Longo, 1997], is a good platform for a general analysis of QMOM and its connections to other methods. Readers are referred to the cited literature for a detailed derivation of HIBE.

Following Asinari [2010], let us introduce a change of variables in the previous expressions, namely  $E = \xi^2/2$ ,  $E_* = \xi_*^2/2$ ,  $E' = (\xi')^2/2$  and  $E'_* = (\xi'_*)^2/2$ , resulting in:

$$N(f, f) = 4\pi^2 \int_0^{+\infty} E_*^{1/2} \int_{-1}^{+1} \int_{-1}^{+1} f(E') f(E'_*) |yE_*^{1/2} - xE^{1/2}| dx dy dE_* , \quad (7.6)$$

and in

$$\nu(f) = 4\pi^2 \int_0^{+\infty} f(E_*) E_*^{1/2} \int_{-1}^{+1} \int_{-1}^{+1} |yE_*^{1/2} - xE^{1/2}| dx dy dE_* . \quad (7.7)$$

Consequently the collision relations simplify to what follows:

$$\begin{aligned} E' &= E(1-x^2) + E_* y^2 , \\ E'_* &= E_*(1-y^2) + E x^2 . \end{aligned} \quad (7.8)$$

The HIBE (Eq. 7.2) can be written in terms of the moments of the distribution function, by defining the following quantities:

$$\Phi_p(t) = 4\pi\sqrt{2} \int_0^{+\infty} f E^{p+1/2} dE , \quad (7.9)$$

that represents the even moments of the velocity distribution and where the non-integer exponent is a consequence of the change of variable. For computing the

equilibrium distribution function, let us take the first two moments, which are the number density:

$$n = \Phi_0 = 4\pi\sqrt{2} \int_0^{+\infty} f E^{1/2} dE, \quad (7.10)$$

and specific internal energy:

$$e = \frac{\Phi_1}{\Phi_0} = \frac{4\pi\sqrt{2}}{n} \int_0^{+\infty} f E^{3/2} dE = \frac{\int_0^{+\infty} f E^{3/2} dE}{\int_0^{+\infty} f E^{1/2} dE}. \quad (7.11)$$

It is possible to prove that the operator  $Q(f, f)$  conserves the previous quantities, namely

$$\begin{aligned} \frac{d n}{dt} &= \frac{d\Phi_0}{dt} = 4\pi\sqrt{2} \int_0^{+\infty} Q(f, f) E^{1/2} dE = 0, \\ \frac{d(ne)}{dt} &= \frac{d\Phi_1}{dt} = 4\pi\sqrt{2} \int_0^{+\infty} Q(f, f) E^{3/2} dE = 0, \end{aligned} \quad (7.12)$$

which means that these quantities are constant and consequently  $n = n_0 \doteq n(0)$  and  $e = e_0 \doteq e(0)$ . The constants  $n_0$  and  $e_0$  can be computed by Eqs. 7.10 and 7.11 using the initial condition  $f_0$  instead of  $f$ , namely

$$\begin{aligned} n_0 &= 4\pi\sqrt{2} \int_0^{+\infty} f_0 E^{1/2} dE, \\ e_0 &= 4\pi\sqrt{2} \int_0^{+\infty} f_0 E^{3/2} dE, \end{aligned} \quad (7.13)$$

where  $n_0$  is the number density,  $e_0 = (3/2) k_B T_0$ ,  $k_B$  is the Boltzmann constant and  $T_0$  is the temperature. By means of the previous quantities it is possible to compute the equilibrium Maxwellian distribution function, namely:

$$f^{eq}(E) = \frac{n_0}{(2\pi E_0)^{3/2}} \exp\left(-\frac{E}{E_0}\right), \quad (7.14)$$

where  $E_0 = k_B T_0$ . Clearly the collisional operator  $Q(f, f)$  drives the initial  $f_0(E)$  towards  $f^{eq}(E)$ .

In this case the closure problem arises in the approximation of the collisional integral which is a bi-linear function of  $f$  and in the case of hard-sphere cannot be simply written in terms of  $\Phi_p$ . In order to study the dynamics of this system, generalising the expression of  $e$  for the generic distribution function  $f$  we introduce the normalised moments:

$$\bar{\Phi}_p = \frac{4\pi\sqrt{2}}{n} \int_0^{+\infty} f E^{p+1/2} dE = \frac{\Phi_p}{\Phi_0}. \quad (7.15)$$

These quantities calculated for the Maxwellian distribution function  $f^{eq}$  yields

$$\bar{\Phi}_p^{eq} = \frac{4\pi\sqrt{2}}{n} \int_0^{+\infty} f_e E^{p+1/2} dE = \frac{\Phi_p^{eq}}{\Phi_0}. \quad (7.16)$$

Let us define, for non-conserved quantities, i.e. for any  $p$  such that  $p > 1$ , the following relaxation rate, namely:

$$R_p = \frac{\bar{\Phi}_p - \bar{\Phi}_p^{eq}}{\bar{\Phi}_p^{eq}} = \frac{\Phi_p - \Phi_p^{eq}}{\Phi_p^{eq}}. \quad (7.17)$$

The dynamics of  $\Phi_p$  and  $R_p$  can be obtained applying the definitions given in Eqs. 7.15 and 7.17 to Eq. 7.2, resulting in:

$$\frac{d\Phi_p}{dt} = 4\pi\sqrt{2} \int_0^\infty Q(f, f) E^{p+1/2} dE, \quad (7.18)$$

and therefore:

$$\frac{dR_p}{dt} = \frac{1}{\Phi_p^{eq}} \frac{d\Phi_p}{dt}. \quad (7.19)$$

Each non-conserved moment evolves with the following characteristic equivalent relaxation frequency  $\nu_p$ :

$$\nu_p(t) = \frac{d\Phi_p}{dt} \frac{1}{\Phi_p^{eq} - \Phi_p}. \quad (7.20)$$

The frequency resulting from Eq. 7.20 gives us the rate of change of  $\Phi_p$  and an estimate of the error committed when using the BGK approximation (that is based on a constant relaxation frequency).

Equation 7.18 can be rewritten more explicitly in terms of the pre-collisional energies only, by applying an appropriate change of variable described in Asinari [2010], obtaining

$$\frac{d\Phi_p}{dt} = 16\pi^3 \sqrt{2} \int_0^\infty \int_0^\infty \int_{-1}^{+1} \int_{-1}^{+1} |q| [(C_p^+) - (C_p^-)] f(E) f(E_*) (EE_*)^{1/2} dx dy dE_* dE, \quad (7.21)$$

where  $q, C_p^+, C_p^-$  are the following functions

$$\begin{aligned} q &= q(x, y, E, E_*) = yE_*^{1/2} - xE^{1/2}, \\ C_p^+ &= C_p^+(x, y, E, E_*) = [E(1 - x^2) + E_*y^2]^p, \\ C_p^- &= C_p^-(E) = E^p, \end{aligned} \quad (7.22)$$

with the following properties

$$\begin{aligned} q(y, x, E_*, E) &= -q(x, y, E, E_*) , \\ q(-x, -y, E, E_*) &= -q(x, y, E, E_*) , \\ C_p^+(-x, -y, E, E_*) &= C_p^+(x, y, E, E_*) , \end{aligned} \quad (7.23)$$

from which it follows also that  $q(-y, -x, E_*, E) = q(x, y, E, E_*)$ .

## 7.3 Solution methods

Let us now analyse in details the following solution methods applied to HIBE: DVM, LBM, GM and QMOM.

### 7.3.1 Discrete Velocity Method

In DVM the internal variables of the distribution function are discretised with a large number of intervals or classes so that the shape of the distribution is accurately approximated and the integro-differential KE is solved in the discretised phase space. The main drawback of the method is the very high computational cost for realistic cases.

The closure of high-order moments is generally accurate if a large number of discretisation points is used so that the distribution reconstruction is very smooth. The closure of the collisional integral instead can present some problems because the discretisation could destroy the invariant properties of collisions. Many modifications have been proposed to ensure the conservation of collisional invariants [Aristov, 2001].

We have instead employed the DVM to solve the HIBE test case with a recently proposed version (HOMISBOLTZ by Asinari [2010]) that discretises the equation directly in the energy space. The momentum is implicitly conserved by the formulation and the discrete velocities can be adapted to conserve energy. Being this method very accurate when the number of discretisation points is very large, it has been chosen as a reference solution for all the other methods.

### 7.3.2 Grad's moment Method

The GM is a closure approach for the infinite moment-system, which is based on the expansion of the velocity distribution function into a series of Hermite polynomial. It was introduced by Grad [Grad, 1949] as an alternative for the Chapman-Enskog expansion of the Boltzmann equation. See [Struchtrup, 2005] for a modern description of GM and its applications.

The distribution is approximated with an expansion centred on the equilibrium. Moments are then computed using this expansion and coefficients are obtained equating the moments of the expansion with the instantaneous tracked moments. Using this closure, moment equations are derived up to a predefined number of moments, which is assumed to properly represent a particular system. Typically, the Grad's 13-equations model and the 26-equations model are used for the simulation of rarefied gases.

In the typical case of Gaussian equilibrium distribution, the expansion is written in terms of Hermite polynomials. Instead in the energy formulation and when the

microscopic velocity space is confined to the subspace  $[0, \infty)$ , as in our case, Hermite polynomials are replaced by Laguerre polynomial due to the structure of the integrals in the collision term. These polynomials are also called Sonine polynomials [Sone, 2002].

Similarly, considering HIBE in the energy formulation and its equilibrium distribution, the Grad's expansion of the distribution  $f(E)$  can be written in a general way as:

$$f^G(E) = f^{eq}(E) \left\{ 1 + \sum_{n=2}^M \left[ \sum_{p=2}^n \left( (-1)^p \frac{n!}{(n-p)!p!} R_p(t) \right) \mathcal{L}_n^{1/2}(E/E_0) \right] \right\}, \quad (7.24)$$

where  $\mathcal{L}_n^{1/2}(E/E_0)$  is the generalised Laguerre polynomial of order  $n$  and  $R_p(t)$  are the deviations of the macroscopic moment  $\Phi_p$  from its equilibrium value  $\Phi_p^{eq}$ .

The time evolution of the moment deviation from equilibrium, considering Eqs. 7.17, 7.9 and 7.2 is:

$$\frac{dR_p}{dt} = \frac{4\pi\sqrt{2}}{\Phi_p^{eq}} \int_0^\infty Q(f^G, f^G) E^{p+1/2} . dE \quad (7.25)$$

Equation 7.25 is solved below for non-conserved variables up to order  $M$ . In the case  $M = 2$  only  $R_2$  is considered and we call it the *one-equation model*. Equivalently, a *two-equation model* for  $M = 4$  can be solved to provide the time evolution of  $R_2$  and  $R_3$ .

The Grad's expansion of the energy distribution function for the *one-equation model* reads as follows:

$$f_1^G(E) = f^{eq} \left[ 1 + R_2 \mathcal{L}_2^{1/2} \left( \frac{E}{E_0} \right) \right] \quad (7.26)$$

An analytical solutions for the collisional integral, described in App. A of this chapter, can be performed, resulting in the following differential equation for  $R_2$

$$\frac{dR_2}{dt} = -\frac{n_0}{15} \sqrt{\pi E_0} , R_2(R_2 + 32) \quad (7.27)$$

where, as already reported,  $E_0 = k_B T_0$ . Solving analytically this equation with  $R_{2o} = R_2(t = 0)$  as the initial condition, an expression for the time evolution of  $R_2$  is obtained:

$$R_2(t) = \frac{32R_{2o}}{(R_{2o} + 32)\exp\left(\frac{32}{15}\sqrt{\pi E_0} n_0 t\right) - R_{2o}} \quad (7.28)$$

Being the *one-equation model* a very crude approximation, the number of moments  $M$  is increased up to four, resulting in the following distribution function for the *two-equation model*:

$$f_2^G(E) = f^{eq} \left[ 1 + R_2 \mathcal{L}_2^{1/2} \left( \frac{E}{E_0} \right) + (3R_2 - R_3) \mathcal{L}_3^{1/2} \left( \frac{E}{E_0} \right) \right]. \quad (7.29)$$

Following the same procedure described in App. A of this chapter, we obtain

$$\begin{aligned}\frac{dR_2}{dt} &= -\frac{1}{240} \left( 125R_2^2 + R_2(256 - 46R_3) + R_3(256 + 5R_3) \right) \sqrt{\frac{E_0\pi}{4}} n_0, \\ \frac{dR_3}{dt} &= \frac{1}{1120} \left( 981R_2^2 + R_2(19200 - 94R_3) - 3R_3(3840 + R_3) \right) \sqrt{\frac{E_0\pi}{4}} n_0.\end{aligned}\quad (7.30)$$

The solution of this system is computed numerically. It is interesting to notice that, as in the one-equation model, no linearisation of the collision operator is necessary.

### 7.3.3 Quadrature Method of Moments

The QMOM has been already introduced in Sec. 2.4 and used as a tool for polydispersity problem in Chap. 6. In this chapter the QMOM equations are derived for the particular case under study.

To approximate HIBE with QMOM, starting from Eqs. 7.2–7.9, we select  $\Phi_0, \dots, \Phi_{M-1}$  and calculate  $M/2$  quadrature nodes  $E_j$  and weights  $w_j$  with an inversion algorithm such that the following approximation:

$$4\pi\sqrt{2} \int_0^\infty P(E) f E^{1/2} dE \approx \sum_{j=1}^{M/2} w_j P(E_j) \quad (7.31)$$

is exact if the integrand  $P(E)$  is a polynomial of degree lower or equal to  $M-1$  in the variable  $E$ . It must be noted that in the energy formulation, the inversion to obtain nodes and weights from the moments is performed with non-integer moments and the constant  $4\pi\sqrt{2}$  is also considered in the inversion algorithm and goes directly into the weights  $w_i$ . This simplifies the equation and ensures that the collisional kernel is well approximated.

With this quadrature we can approximate Eq. 7.18 as follows:

$$\frac{d\Phi_p}{dt} \approx \frac{\pi}{\sqrt{2}} \sum_{i=1}^{M/2} \sum_{j=1}^{M/2} w_i w_j \Lambda_{ij,p}, \quad (7.32)$$

where

$$\Lambda_{ij,p} = \int_{-1}^{+1} \int_{-1}^{+1} |q(x, y, E_i, E_j)| [C_p^+(x, y, E_i, E_j) - C_p^-(E_i)] dx dy. \quad (7.33)$$

The integration over the collisional parameters  $x$  and  $y$  can be computed analytically, by using the symmetric properties of the integrands. The detailed derivation is given in App. B of this chapter and the explicit equations for  $M = 4$  are reported in App. C.

In the hard-sphere model, the closure of the collision integral with QMOM introduces an approximation error that influences the relaxation to equilibrium.

To cure this wrong behaviour a new correction is formulated and proposed here. New quantities  $\Lambda'_{ij,p}$  are defined as:

$$\Lambda'_{ij,p} = \Lambda_{ij,p} - \kappa_p \Lambda_{ij,p}^{eq}, \quad (7.34)$$

where  $\Lambda_{ij,p}^{eq}$  are calculated at the equilibrium and  $\kappa_p$  is a weighting factor that depends on the distance from the equilibrium.  $\kappa_p$  must be close to unity when the system is approaching the equilibrium, to preserve the correct discrete equilibrium for QMOM approximation. However it should be small enough to retain the QMOM accuracy far from equilibrium.

If  $\kappa_p = 1$  the above equation represents a "global static" correction (QMOM+SC) applied at each state of the system. Its disadvantage is that it affects also the dynamic far from equilibrium. It is possible however to build a "dynamic" correction (QMOM+DC) defining  $\kappa_p$  as a function of the moments deviations  $R_p(t)$ , that retain QMOM accuracy far from equilibrium, still preserving the correct approximation at equilibrium. For example we can define

$$\kappa_p(t) = \left| 1 - \frac{R_p(t)}{R_p(0)} \right|^h = \left| \frac{\Phi_p(t) - \Phi_p(0)}{\Phi_p^{eq}(t) - \Phi_p(0)} \right|^h, \quad (7.35)$$

where the exponent  $h$  is a tunable parameter.

### 7.3.4 Lattice Boltzmann Method

LBM can be derived from the BE [Chikatamarla and Karlin, 2006, He and Luo, 1997] by discretising the velocity space using a finite set of velocity vectors. In this work we want to use and analyse this method as a closure for high-order moments and collisional terms, focusing in particular on the basic assumptions of the method by exploiting similarities and differences with QMOM.

In general LBM is a computational method based on lattices labelled as  $DdQq$ , where  $d$  is replaced by the spatial dimension and  $q$  by the number of microscopic velocities. Typical lattices for continuum flows are  $D2Q9$  in 2D and  $D3Q19$  or  $D3Q27$  in 3D. For slightly rarefied flows in 2D the  $D2Q16$  and the  $D2Q21$  lattices are often used.

The LBM for a general KE characterised by a mono-variate distribution expresses the moments in terms of a finite set of  $M$  weights and  $M$  prescribed abscissas. Typically the prescribed abscissas come from a Gauss-Hermite quadrature (i.e. the roots of the Hermite polynomials). The employment of these quadratures can be explained purely in terms of the entropy construction [Chikatamarla et al., 2006]. This approach is not exactly equivalent to the standard LBM but is instead called

off-Lattice Boltzmann Method (oLBM) [Bardow et al., 2006], because the roots do not fall on the lattice, so they cannot be used with the standard LBM transport algorithm.

The same approach can be used in the energy formulation of HIBE, using oLBM simply as a quadrature method for unclosed integral quantities. In this case, since the distribution is described in terms of energy, the generalised Laguerre nodes are the nodes prescribed by oLBM while the weights are directly derived from the moments  $\Phi_p$  instead of using the classical two-steps LBM scheme. The approach is completely equivalent to the one used with QMOM (explained in Sec. 7.3.3 and App. B of this chapter) with the only difference that we use  $M$  prescribed nodes that are calculated as the roots of the generalised Laguerre polynomial  $\mathcal{L}_M^{1/2}(E/E_0)$ . The  $M$  associated weights are computed by preserving the first  $M$  macroscopic quantities  $\Phi_p$ . The analytical formula given in the previous section for QMOM holds for every type of quadrature rule.

## 7.4 Test cases and numerical details

The equilibrium condition is univocally determined by the condition

$$Q(f, f) = 0, \quad (7.36)$$

together with initial condition for conserved quantities and it is reached in finite time from every initial condition.

As it has been already mentioned, classical macroscopic balance equations (e.g. Navier-Stokes) can be regarded as approximations of a system in local equilibrium or slightly away from it. Therefore a good approximation of the equilibrium condition is an important requirement for every kinetic-based method to represent the late dynamics and to be consistent with classical methods. This would not be an issue if a high degree of accuracy were chosen by tracking a large number of moments, so that the distribution function is accurately tracked at each state. However, when complex three-dimensional problems are taken into account, the number of moments that can be tracked is usually small to reduce the computational costs and studying the closure accuracy, in particular at equilibrium, becomes more important.

The test case studied for HIBE represents the evolution of a set of particles in a state far away from equilibrium, interacting one with each other until the steady equilibrium state is reached. The time marching procedure is based on the forward Euler integration rule. To have a very accurate reference solution HOMISBOLTZ code was used with 400 discrete energies. This ensures a very accurate approximation of the whole distribution function and its integrals. This model, as well as the other ones, are all implemented in Matlab.

Two different functions are considered:

$$\text{T1: } f_0(E) = g_1 \exp\left(-\frac{(\sqrt{E} - \sqrt{E_{T1}})^2}{(g_2/2)}\right), \quad (7.37)$$

and

$$\text{T2: } f_0(E) = g_1 \left[ \exp\left(-\frac{(\sqrt{E} - \sqrt{E_{T1}})^2}{(g_2/2)}\right) + \exp\left(-\frac{(\sqrt{E} - \sqrt{E_{T2}})^2}{(g_2/2)}\right) \right], \quad (7.38)$$

where  $g_1 = 10^{-3}$ ,  $g_2 = 70$ ,  $E_{T1} = 612.5$  and  $E_{T2} = \frac{E_{T1}}{4}$ . These two initial conditions together with the respective equilibrium conditions are shown in Fig. 7.1. As it is seen, the first condition corresponds to molecules characterised by one single average energy  $E_{T1}$ , whereas in the second initial condition two characteristic energies  $E_{T1}$  and  $E_{T2}$  are visible. For all methods the total simulation time is  $\Delta T = 5 \times 10^{-4}$  s discretised in 200 time steps of size  $\Delta t = 2.5 \times 10^{-6}$  s.

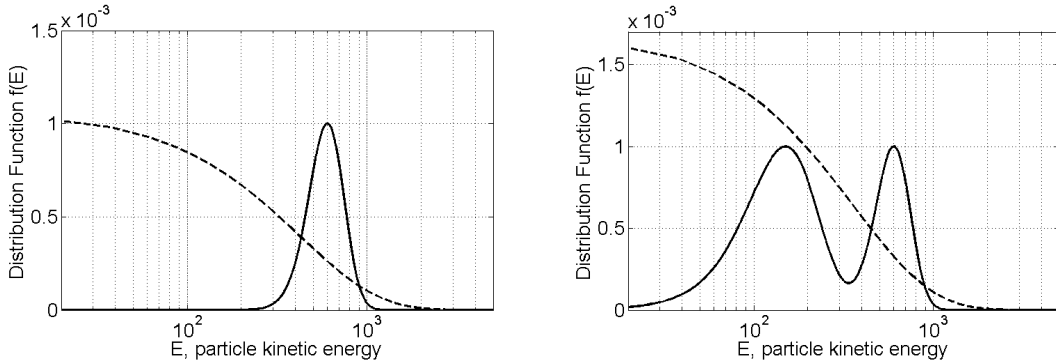


Figure 7.1: Initial (continuous lines) and equilibrium (dashed lines) distributions for test case T1 (left) and T2 (right), computed with reference DVM code HOMIS-BOLTZ.

QMOM and oLBM can be easily extended to a generic  $M$ , while the analytical equation for GM are difficult to obtain only for  $M > 4$ . Furthermore the dynamics of the system approximated with QMOM and oLBM for  $M$  ranging from four to ten were analysed without showing qualitative differences in the dynamics. Therefore dynamics results of the different methods are compared with DVM only for  $M = 4$ . This means that the first four moments are tracked and that the following approximations are used: *two-equation model* for GM, two nodes and two weights for QMOM and four discrete velocities for oLBM. In terms of velocity moments this is equivalent to solving up to the 6<sup>th</sup>-order moment. The comparison at the equilibrium is instead carried out at different  $M$  values for all methods.

## 7.5 Results and discussion

First let us analyse the closure accuracy of the collisional term with a given number  $M$  by comparing the moments of the exact equilibrium with the steady state solution obtained with QMOM, oLBM and GM. In Tab. 7.1 different orders of accuracy are investigated and the relative errors of each approximation are calculated. The QMOM error in the prediction of the equilibrium of a different system has been highlighted by Passalacqua et al. [2011] for the steady state velocity moments up to 5<sup>th</sup>-order. Our results analyse the steady state, reached by the discretised system with the initial condition T1 (see Eq. 7.37), in terms of energy moments up to 6<sup>th</sup>-order (equivalent to the 10<sup>th</sup>-order for velocities), varying the number of moments and the quadrature order and comparing it with oLBM and GM.

	$M = 4$		$M = 6$		$M = 8$	
$\times 10^8$	$\Phi_2$	%	$\Phi_2$	%	$\Phi_2$	%
GM (exact)	1.0034	0.0	1.0034	0.0	1.0034	0.0
oLBM	1.0033	0.01	1.0034	0.003	1.0034	0.001
QMOM	0.9704	3.29	0.9979	0.55	1.0022	0.12
QMOM+SC	1.0034	0.0	1.0034	0.0	1.0034	0.0
QMOM+DC	1.0034	0.0	1.0034	0.0	1.0034	0.0
$\times 10^{11}$	$\Phi_3$	%	$\Phi_3$	%	$\Phi_3$	%
GM (exact)	1.4921	0.0	1.4921	0.0	1.4921	0.0
oLBM	1.4919	0.02	1.4921	0.004	1.4921	0.002
QMOM	1.4707	1.44	1.4874	0.31	1.4910	0.08
QMOM+SC	1.4921	0.0	1.4921	0.0	1.4921	0.0
QMOM+DC	1.4921	0.0	1.4921	0.0	1.4921	0.0
$\times 10^{14}$			$\Phi_4$	%	$\Phi_4$	%
GM (exact)	×	×	2.8529	0.0	2.8529	0.0
oLBM	×	×	2.8527	0.005	2.8528	0.002
QMOM	×	×	2.8302	0.80	2.8478	0.18
QMOM+SC	×	×	2.8529	0.0	2.8529	0.0
QMOM+DC	×	×	2.8529	0.0	2.8529	0.0
$\times 10^{17}$			$\Phi_5$	%	$\Phi_5$	%
GM (exact)	×	×	6.6666	0.0	6.6666	0.0
oLBM	×	×	6.6662	0.006	6.6665	0.002
QMOM	×	×	6.6244	6.34	6.6548	0.18
QMOM+SC	×	×	6.6666	0.0	6.6666	0.0
QMOM+DC	×	×	6.6666	0.0	6.6666	0.0

Table 7.1: Exact values, approximations and relative errors of the tracked moments at steady state with different closure methods and closure order  $M$ .

GM is characterised by construction to relax to the exact equilibrium state so the approximation of the equilibrium moments is always exact. In the case of oLBM, the error is negligible since it is always less than 0.03%. This can be explained by the fact that, although the oLBM quadrature does not approximate exactly the collisional kernel (because it is not a polynomial), it makes use of prescribed nodes that are the best choice near the equilibrium. QMOM instead presents an error in the approximation of the collisional integral that drives the flow towards the wrong steady state (with an error on moments between 0.1% and 6%). Both the static (QMOM+SC) and the dynamic correction (QMOM+DC) can fix this problem and approximate exactly the equilibrium by construction.

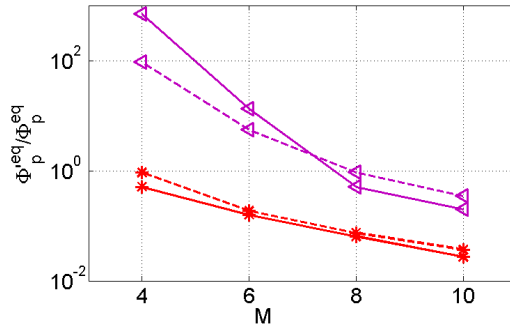


Figure 7.2: Errors committed in approximating  $\frac{d\Phi_p}{dt}$  at the exact equilibrium condition, normalised by  $\Phi_p^{\text{eq}}$  (see Eq. 7.19), for  $p = 2$  (dashed line) and  $p = 3$  (continuous line), for different  $M$ . QMOM ( $\blacktriangleleft$ ), oLBM (\*).

The quadrature accuracy in the approximation of the collisional term can be observed in Fig. 7.2 where the source term  $\frac{d\Phi_p}{dt}$ , calculated at equilibrium and normalised by  $\Phi_p^{\text{eq}}$  (see Eq. 7.19), is reported for  $p = 2$  and  $p = 3$ , as calculated by QMOM and oLBM. These terms would be null if the quadrature formula were exact. Instead, because of the non-polynomial structure of the kernel, there is an error that decreases with the number of tracked moments  $M$ . oLBM always has an error smaller than QMOM because it is based on the equilibrium assumption, however it can be highlighted that the error associated with it has a slower convergence. Furthermore we can observe in this figure that the QMOM quadrature with  $M = 8$  is equivalent to the oLBM quadrature with  $M = 4$ . This is due to the fact that QMOM is a Gaussian quadrature formula, whose nodes and weights are adapted to the macroscopic state of the system (given by the moments). So the  $M/2$  nodes calculated at equilibrium result to be exactly the roots of the Laguerre polynomials. oLBM instead prescribes  $M$  fixed Laguerre nodes by hypothesis and only the  $M$  weights are calculate with an inversion algorithm, resulting in a “double” accuracy at equilibrium. Results with GM and corrected QMOM are not reported here because

they approximate exactly the collisional term at equilibrium by construction.

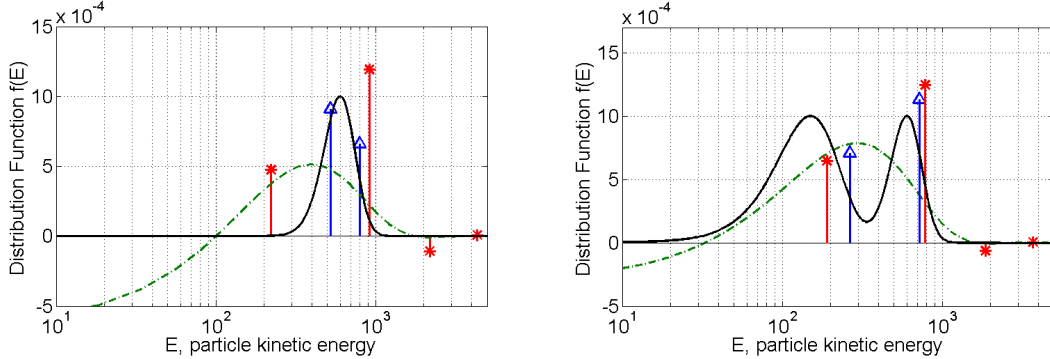


Figure 7.3: Approximations of initial conditions T1 (left) and T2 (right). Exact values (continuous line), GM (dashed-dotted line), QMOM ( $\Delta$ ), oLBM (\*).

Let us discuss the dynamical evolution of the system towards the steady state, considering the two initial conditions reported in Fig. 7.1 and focusing on the case  $M = 4$ . The main characteristics of the methods can be easily understood by looking at the approximation of the initial conditions T1 and T2 introduced in Eqs. 7.37-7.38 and Fig. 7.3. The main drawback of GM is that the positivity of the distribution function is not guaranteed. In the depicted test case for example, the distribution function becomes negative predicting negative number density (or probability) of particles with small kinetic energy  $E$ . The same problem occurs for the third node of the oLBM closure. This would be a problem when considering spatial transport terms which would yield unrealisable moments [Vikas et al., 2011]. QMOM instead intrinsically preserves the positivity of the quadrature weights for all sets of realisable moments.

Figure 7.4 represents the evolution of the second and third moments of  $f(E)$ , equivalent respectively to the 4<sup>th</sup> and 6<sup>th</sup> moments of the velocity magnitude distribution  $f(\xi)$ , in terms of the relaxation rates  $R_p$  for the test cases T1 and T2. Figure 7.5 reports the same comparison in a logarithmic scale normalising  $R_p$  with the initial value  $R_p(0)$ . This scaling makes clearly visible that the approach to equilibrium is exponential. In these results DVM has been considered the reference exact solution. All the other methods apparently seem to predict well the first part the relaxation towards equilibrium but, as this is approached, some differences become evident. In the last part of the dynamics, for example, Fig. 7.5 clearly shows that although QMOM predicts well the initial dynamics and results in positive weights, it wrongly predicts the relaxation towards equilibrium. In fact, as it has been already seen in Tab. 7.1, the moments tend to values slightly different from those expected and this error (typically less than 10%) must not be overlooked. This behaviour is

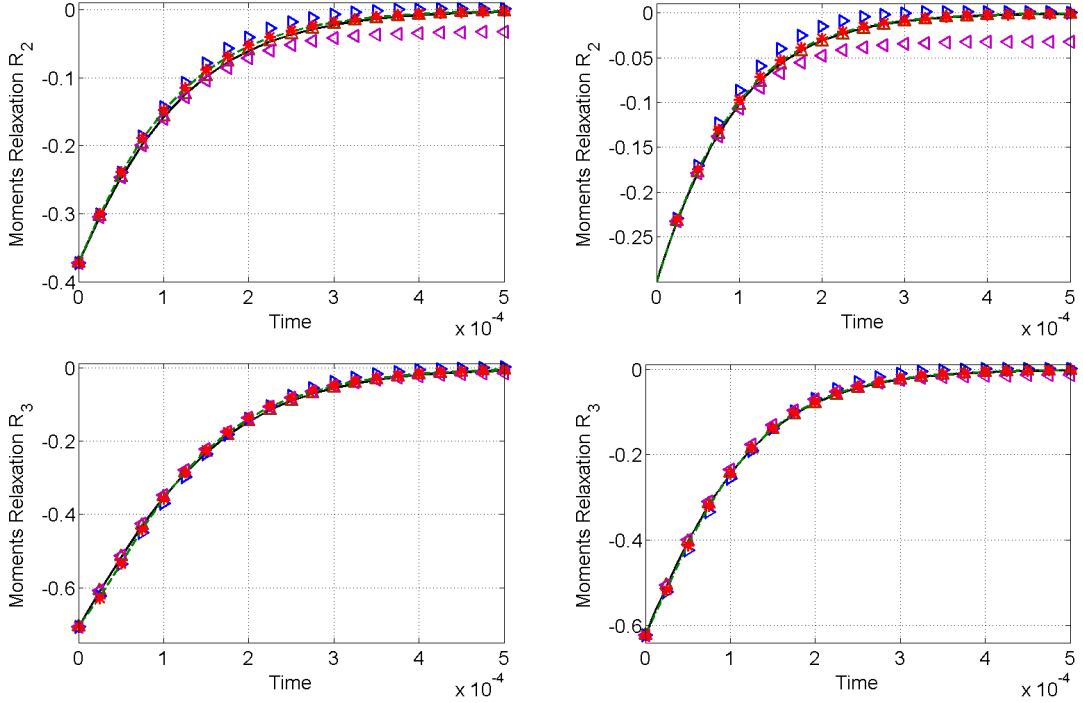


Figure 7.4: Evolution over time of the 2<sup>nd</sup> (top) and 3<sup>rd</sup> (bottom) moment relaxations for test case T1 (left) and T2 (right). Reference DVM (continuous line), GM (dashed-dotted line), QMOM ( $\blacktriangleleft$ ), QMOM+SC ( $\triangleright$ ), QMOM+DC ( $\triangle$ ), oLBM (\*).

directly related to the fact that the equilibrium arises from the collision integral, approximated (and not exactly solved) by the quadrature rule. This error can however be corrected by the procedures proposed in this work (see Sec. 7.3.3).

The first static correction (QMOM+SC) fixes this problem by construction but presents one serious drawback. The approach to equilibrium is no more monotonic, in the sense that the macroscopic quantities  $\Phi_p$  cross the equilibrium value and after that they slowly relax to it. This is thermodynamically inconsistent because KEs must be characterised locally by a monotonic relaxation to equilibrium. Furthermore Fig. 7.5 shows that the static correction predicts a too fast dynamics, with a relaxation which is more than exponential. This error in the prediction of the dynamics cannot be seen in Fig. 7.4.

When the dynamical correction (QMOM+DC) is used QMOM becomes very accurate and close to the reference results. After some tests, it was found that the parameter  $h$  (in Eq. 7.35) must be chosen between one and two to preserve the correct approach to equilibrium. In particular we have considered here  $h = 1.5$ , resulting in very accurate results. This is clearly visible in Fig. 7.5 where, as already reported, the normalised moment relaxation rates are plotted in logarithmic scale.

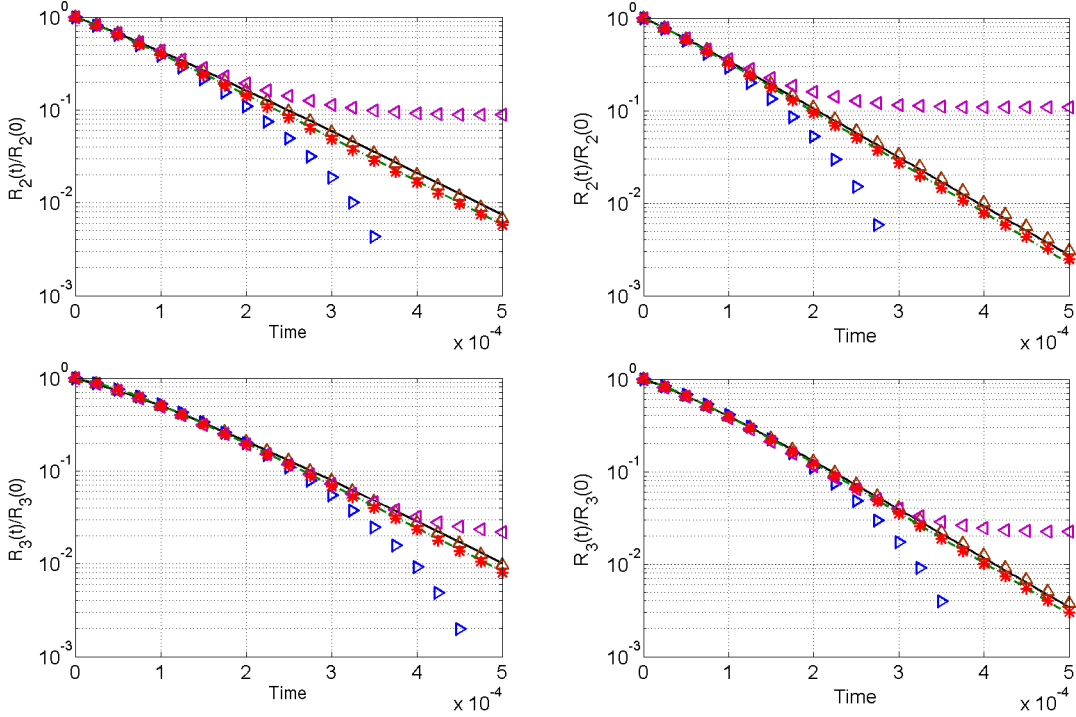


Figure 7.5: Evolution over time of the 2<sup>nd</sup> (top) and 3<sup>rd</sup> (bottom) moment normalised relaxation rates for test case T1 (left) and T2 (right). Reference DVM (continuous line), GM (dashed-dotted line), QMOM ( $\triangleleft$ ), QMOM+SC ( $\triangleright$ ), QMOM+DC ( $\triangle$ ), oLBM (\*).

In general GM and oLBM give very similar results because they are based on very similar assumptions (either Laguerre polynomials or Laguerre nodes) but, as we already discussed, oLBM introduces a small error in the approximation of collisions and does not relax exactly to the equilibrium. It should be also highlighted that although the predictions of  $R_p$  made by GM and oLBM in Figs. 7.4-7.5 seems good, the reconstruction of the distribution can lead to negative values during the evolution, especially far away from equilibrium. This inaccuracy in the initial part of the dynamics becomes more evident when analysing other quantities such as the relative errors or the equivalent relaxation times.

The relative error for each moment (with respect to the DVM reference solution), depicted in Fig. 7.6, demonstrates the very high accuracy of QMOM+DC that produces a relative error always very close to zero (below 0.3%) while the other methods fails either close to equilibrium (QMOM) or far away from it (oLBM, GRAD, QMOM+SC).

Fig. 7.7 shows the equivalent relaxation time, given by Eq. 7.20, normalised to the BGK frequency approximation, given by the DVM reference code as the relaxation

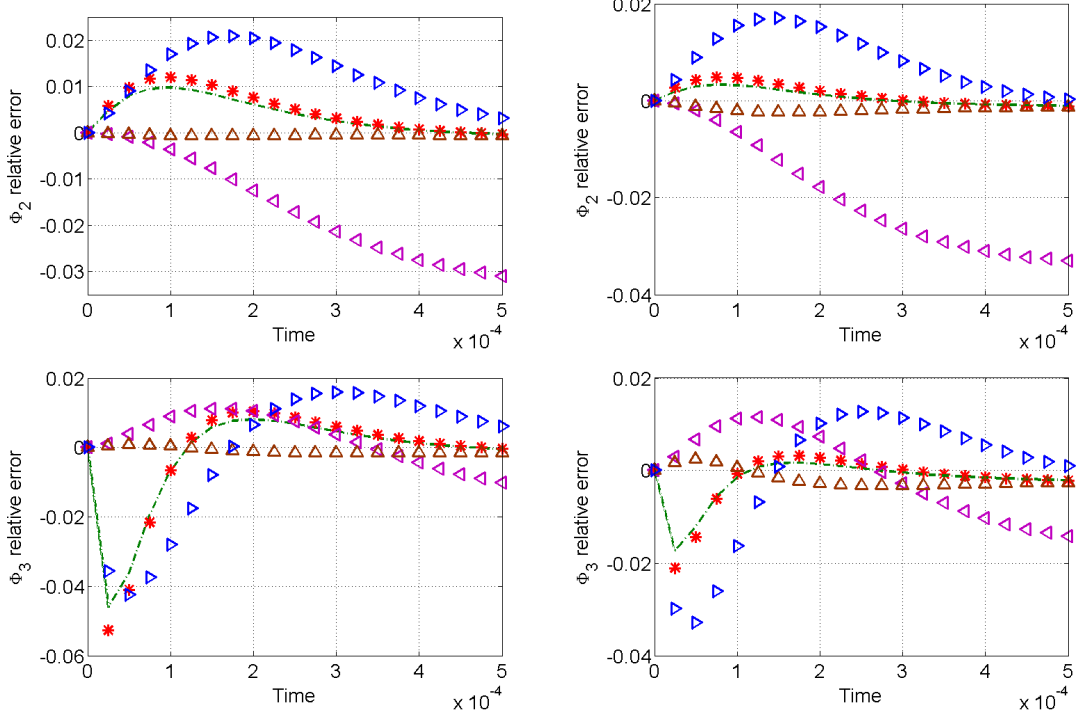


Figure 7.6: Relative errors of the 2<sup>nd</sup> (top) and 3<sup>rd</sup> (bottom) moments for test case T1 (left) and T2 (right). Reference DVM (continuous line), GM (dashed-dotted line), QMOM ( $\blacktriangleleft$ ), QMOM+SC ( $\blacktriangleright$ ), QMOM+DC ( $\blacktriangle$ ), oLBM (\*).

of the lowest discrete energy. Equation 7.20 shows that these quantities represent also the quadrature errors committed by the different methods, scaled with the distance from equilibrium. This means that the errors committed in the first part of the dynamics, when the distance from equilibrium is big, are less evident. One first comment is that the figure shows the inaccuracy of the BGK approximation, especially in the first part of the dynamics where the relaxation frequency cannot be approximated as constant. With QMOM the equivalent relaxation time goes quickly to zero, meaning that the system has reached the wrong equilibrium state. As we observed before, when the static correction is enabled the approach to equilibrium is no more monotonic and the equivalent time relaxation involves a division by zero. This means that at a certain time their derivatives change sign and the equivalent relaxation times go to infinity. As it is seen the static correction drives the frequency to infinity, leading to a non-physical behaviour. The correct behaviour instead is recovered with the dynamic correction. A more accurate analysis of this figure in the initial part of the dynamics reveals also the inaccuracy of the equilibrium assumption made by GM and oLBM, showing significant error from the reference solution that

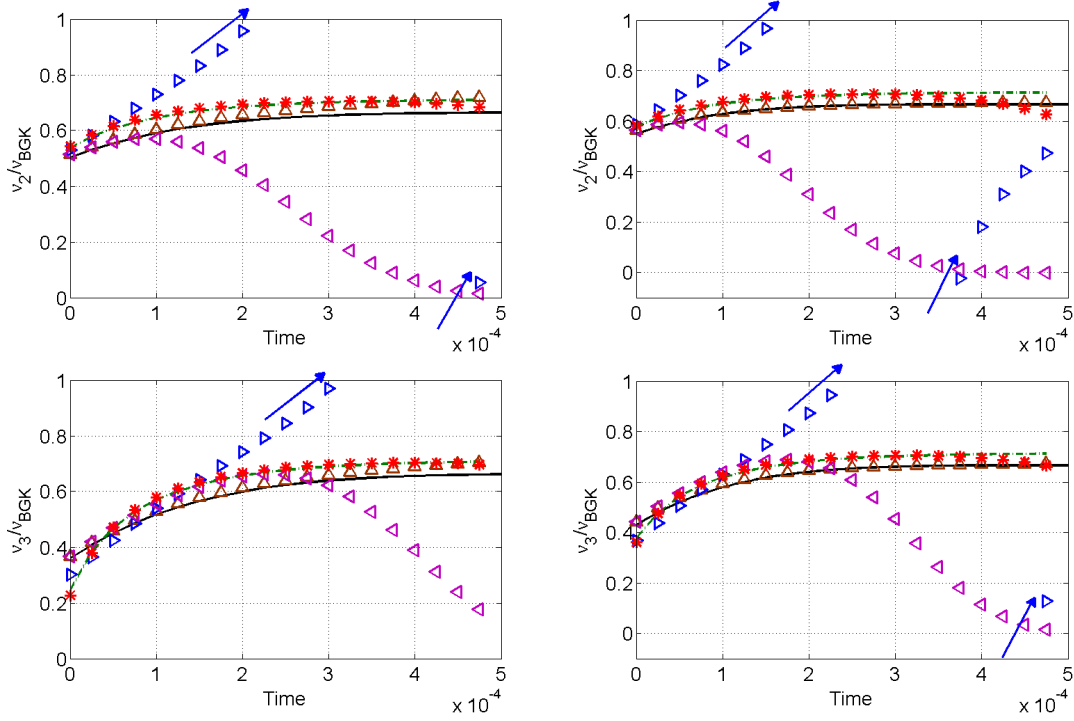


Figure 7.7: Evolution over time of the 2<sup>nd</sup> (top) and 3<sup>rd</sup> (bottom) moment equivalent relaxation time for test case T1 (left) and T2 (right). Reference DVM (continuous line), GM (dashed-dotted line), QMOM ( $\triangleleft$ ), QMOM+SC ( $\triangleright$ ), QMOM+DC ( $\triangle$ ), oLBM (\*); the arrows indicate the behaviour of QMOM+SC across the singularity.

is not present in QMOM+DC that can predict very accurately the early dynamics as much as the late dynamics.

## 7.6 Conclusions

In the framework of non-equilibrium flows, the Quadrature Method of Moments (QMOM) is tested as a closure for the Homogeneous Isotropic Boltzmann Equation (HIBE) with a hard-sphere elastic collisional kernel. Results are compared with other closures such as the Grad's moment Method (GM), the off-Lattice Boltzmann Method (oLBM), and with the solution obtained from a very accurate Discrete Velocity Method (DVM) as a reference.

QMOM is characterised by great flexibility and adaptivity; however a small but non negligible error in reproducing the Maxwellian equilibrium is evidenced. This problem can be only partially solved by increasing the number of moments tracked and consequently the quadrature order. In fact, a residual error in the approximation

clearpage  
of the equilibrium (and in the relaxation time and dynamics) remains because of the intrinsic structure of the method.

Analysing the steady state of the system, we can conclude that, as expected, GM provides the exact closure by construction since it is based on the hypothesis of small perturbation from equilibrium. Also oLBM provides an accurate closure of the steady state, with an error always below 0.03%, because it makes use of a quadrature purposely designed for the equilibrium state (Gauss-Laguerre in our case).

When considering instead distributions far from equilibrium (very important in the initial dynamics) QMOM better predicts the moments and their dynamics, with quadrature weights always positive or in other words, with a reconstructed distribution always valid. GM and oLBM instead, since they are based on equilibrium assumptions, produce significant errors and they can also predict non-physical negative values of the distribution. This can be a problem when considering spatial transport terms which will yield unrealisable moments.

Corrections to QMOM are proposed to increase the accuracy close to equilibrium, by including physically-based information, such as the a priori knowledge of the equilibrium state. In particular, a correction to the collisional integral, based on a distance from the equilibrium, is tested obtaining very accurate results comparable to the reference DVM solution, but at a much lower computational costs (i.e. solving only four instead of 400 differential equations). More generally, the idea of using a dynamically corrected QMOM, that is capable to exploit the equilibrium assumptions of the oLBM quadrature depending on the state of the system (together with initial condition and equilibrium condition) seems to be very promising.

## References

- V. V. Aristov. *Methods of direct solving the Boltzmann equation and study of nonequilibrium flows*. Kluwer Academic Publishers (Dordrecht), 1st edition, 2001.
- P. Asinari. Nonlinear Boltzmann equation for the homogeneous isotropic case: Minimal deterministic Matlab program. *Comput. Phys. Commun.*, 181(10):1776–1788, 2010.
- A. Bardow, I. V. Karlin, and A. A. Gusev. General characteristic-based algorithm for off-lattice boltzmann simulations. *Europhys. Lett.*, 75(3):434, 2006.
- N. Bellomo and M. Pulvirenti. *Modeling in applied sciences: a kinetic theory approach*. Modeling and simulation in science, engineering & technology. Birkhäuser, 2000.
- R. Benzi, S. Succi, and M. Vergassola. The lattice Boltzmann equation: theory and applications. *Phys. Reports*, 222(3):145–197, 1992.
- P. Bhatnagar, E. Gross, and M. Krook. A model for collision process in gases, I. Small amplitude processes in charged and neutral one-component system. *Phys. Rev.*, 94: 511–525, 1954.

- G. Bird. *Molecular Gas Dynamics and the Direct Simulation of Gas Flows*. Oxford University Press (Oxford), 2nd edition, 1994.
- J. E. Broadwell. Study of rarefied shear flow by the discrete velocity method. *J. Fluid Mech.*, 19(03):401–414, 1964.
- C. Cercignani. *The Boltzmann equation and its applications*. Applied mathematical sciences. Springer-Verlag, 1988.
- S. Chen and G. Doolen. Lattice Boltzmann method for fluid flows. *Annu. Rev. Fluid Mech.*, 30:329–364, 1998.
- S. S. Chikatamarla and I. V. Karlin. Entropy and Galilean invariance of lattice Boltzmann theories. *Phys. Rev. Lett.*, 97:190601, 2006.
- S. S. Chikatamarla, S. Asumali, and I. V. Karlin. Entropic lattice boltzmann models for hydrodynamics in three dimensions. *Phys. Rev. Lett.*, 97:010201, 2006.
- O. Desjardins, R. O. Fox, and P. Villedieu. A quadrature-based moment method for dilute fluid-particle flows. *J. Comput. Phys.*, 227(4):2514–2539, 2008.
- M. Ernst. Nonlinear model-boltzmann equations and exact solutions. *Phys. Rep.*, 78(1):1–171, 1981.
- R. O. Fox. A quadrature-based third-order moment method for dilute gas-particle flows. *J. Comput. Phys.*, 227(12):6313–6350, 2008.
- R. O. Fox. Higher-order quadrature-based moment methods for kinetic equations. *J. Comput. Phys.*, 228(20):7771–7791, 2009.
- R. O. Fox and P. Vedula. Quadrature-based moment model for moderately dense polydisperse gas-particle flows. *Ind. Eng. Chem. Res.*, 49(11):5174–5187, 2010.
- S. Friedlander. *Smoke, dust, and haze: fundamentals of aerosol dynamics*. Topics in chemical engineering. Oxford University Press, 2000.
- R. Gatignol. Kinetic theory for a discrete velocity gas and application to the shock structure. *Phys. Fluids*, 18(2):153–161, 1975.
- D. Gidaspow. *Multiphase flow and fluidization: continuum and kinetic theory descriptions*. Academic Press, 1994.
- H. Grad. On the kinetic theory of rarefied gases. *Commun. Pure Appl. Math.*, 2(4):331–407, 1949.
- X. He and L.-S. Luo. Theory of lattice Boltzmann mehtod: From the Boltzmann equation to the lattice Boltzmann equation. *Phys. Rev. E*, 56:6811–6817, 1997.
- M. Icardi, P. Asinari, D. L. Marchisio, S. Izquierdo, and R. O. Fox. Quadrature-based moment closures for non-equilibrium flows: hard-sphere collisions and approach to equilibrium. *J. Comput. Phys.*, Submitted.
- M. N. Kogan. Kinetic theory in aerothermodynamics. *Prog. Aerosp. Sci.*, 29(4):271–354, 1992.
- A. Passalacqua, J. Galvin, P. Vedula, C. Hrenya, and R. Fox. A quadrature-based kinetic model for dilute non-isothermal granular flows. *Communications in Computational Physics*, 10(1):216–252, 2011.

- L. Preziosi and E. Longo. On a conservative polar discretization of the boltzmann equation. *Jpn. J. Ind. Appl. Math.*, 14:399–435, 1997. 10.1007/BF03167391.
- Y. Qian, D. d'Humieres, and P. Lallemand. Lattice BGK Models for Navier-Stokes Equation. *Europhys. Lett.*, 17(6):479–484, 1992.
- D. Ramkrishna. *Population balances: theory and applications to particulate systems in engineering*. Chemical, Petrochemical & Process. Academic Press, 2000.
- V. Rasetto, D. L. Marchisio, D. Fissore, and A. A. Barresi. On the use of a dual-scale model to improve understanding of a pharmaceutical freeze-drying process. *J. Pharm. Sci.*, 99(10):4337–4350, 2010.
- J. Reese, M. Gallis, and D. Lockerby. New directions in fluid dynamics: Non-equilibrium aerodynamic and microsystem flows. *Philos. Trans. R. Soc. A*, 361(1813):2967–2988, 2003.
- M. V. Smoluchowski. Drei Vortrage über Diffusion, Brownsche Bewegung und Koagulation von Kolloidteilchen. *Z. Phys.*, 17:557–585, 1916.
- Y. Sone. *Kinetic theory and fluid dynamics*. Birkhäuser (Boston), first edition, 2002.
- Y. Sone and Y. Onishi. Kinetic theory of evaporation and condensation –hydrodynamic equation and slip boundary condition–. *J. Phys. Soc. Jpn.*, 44(6):1981–1994, 1978.
- H. Struchtrup. *Macroscopic transport equations for rarefied gas flow: approximation methods in Kinetic Theory*. Springer (Berlin), 2005.
- S. Succi. *The Lattice Boltzmann Equation for Fluid Dynamics and Beyond*. Oxford University Press (New York), first edition, 2001.
- V. Vikas, Z. Wang, A. Passalacqua, and R. Fox. Realizable high-order finite-volume schemes for quadrature-based moment methods. *J. Comput. Phys.*, 230(13):5328–5352, 2011.
- F. A. Williams. Spray combustion and atomization. *Phys. Fluids*, 1(6):541–545, 1958.
- D. A. Wolf-Gladrow. *Lattice-Gas Cellular Automata and Lattice Boltzmann Models. An Introduction*. Lecture Notes in Mathematics 1725. Springer (Berlin), first edition, 2000.

## 7.7 Appendices

### A. Analytical integration of Grad equations for HIBE

Let us consider the case  $M = 2$ . Applying Eq. 7.26 in Eq. 7.25, considering the collision operator described by Eqs. 7.3 and 7.4, we obtain, after performing a change of variables

$\psi = E/E_0$  and arranging terms, the following expression

$$\begin{aligned} \frac{\partial R_2}{\partial t} = & \frac{2\pi^2}{\Phi_2^{eq}} \left[ n_0 \left( \frac{1}{\pi E_0} \right)^{3/2} \right]^2 (2E_0)^{11/2} \int_0^\infty \psi^6 \exp(-2\psi) \int_0^\infty \psi_*^2 \exp(-2\psi_*) \int_{-1}^1 \int_{-1}^1 \\ & \left[ (1 + a_4 \mathcal{L}_2^{1/2}(\psi')) (1 + a_4 \mathcal{L}_2^{1/2}(\psi_*)) - (1 + a_4 \mathcal{L}_2^{1/2}(\psi)) (1 + a_4 \mathcal{L}_2^{1/2}(\psi_*)) \right] \\ & |\psi y - \psi_* x| dx dy d\psi_* d\psi. \end{aligned} \quad (7.39)$$

To obtain an analytical expression for Eq. 7.39 it is convenient to rewrite this equation in the following compact form:

$$\frac{\partial R_2}{\partial t} = \frac{2\pi^2}{\Phi_2^{eq}} \left[ n_0 \left( \frac{1}{\pi E_0} \right)^{3/2} \right]^2 (2E_0)^{11/2} [R_2(k_3 - k_1) + R_2^2(k_4 - k_2)]; \quad (7.40)$$

by defining the following integrals:

$$\begin{aligned} k_1 = & \int_0^\infty \psi^6 \exp(-2\psi) \int_0^\infty \psi_*^2 \exp(-2\psi_*) (\mathcal{L}_2^{1/2}(\psi_*) + \mathcal{L}_2^{1/2}(\psi)) \\ & \int_{-1}^1 \int_{-1}^1 |\psi y - \psi_* x| dx dy d\psi_* d\psi; \end{aligned} \quad (7.41)$$

$$\begin{aligned} k_2 = & \int_0^\infty \psi^6 \exp(-2\psi) \int_0^\infty \psi_*^2 \exp(-2\psi_*) (\mathcal{L}_2^{1/2}(\psi_*) \mathcal{L}_2^{1/2}(\psi)) \\ & \int_{-1}^1 \int_{-1}^1 |\psi y - \psi_* x| dx dy d\psi_* d\psi; \end{aligned} \quad (7.42)$$

$$\begin{aligned} k_3 = & \int_0^\infty \psi^6 \exp(-2\psi) \int_0^\infty \psi_*^2 \exp(-2\psi_*) \\ & \int_{-1}^1 \int_{-1}^1 (\mathcal{L}_2^{1/2}(\psi'_*) + \mathcal{L}_2^{1/2}(\psi')) |\psi y - \psi_* x| dx dy d\psi_* d\psi; \end{aligned} \quad (7.43)$$

$$\begin{aligned} k_4 = & \int_0^\infty \psi^6 \exp(-2\psi) \int_0^\infty \psi_*^2 \exp(-2\psi_*) \\ & \int_{-1}^1 \int_{-1}^1 (\mathcal{L}_2^{1/2}(\psi'_*) \mathcal{L}_2^{1/2}(\psi')) |\psi y - \psi_* x| dx dy d\psi_* d\psi. \end{aligned} \quad (7.44)$$

These quantities can be integrated analytically giving place to an explicit collision term for  $R_2$ , Eq. 7.27.

The same procedure can be applied for  $R_2$  and  $R_3$  in the case of  $M = 4$ . The compact

form of the evolutions equations is:

$$\begin{aligned} \frac{\partial R_2}{\partial t} = & \frac{2\pi^2}{\Phi_2^e} \left[ n_0 \left( \frac{1}{\pi E_0} \right)^{3/2} \right]^2 (2E_0)^{11/2} \\ & \left[ (-k_1 + k_3 - 3k_5 + 3k_9) R_2 + (k_5 - k_9) R_3 \right. \\ & + (6k_6 + k_7 + k_8 - 6k_{10} - k_{11} - k_{12}) R_3 R_2 \\ & + (-k_2 + k_4 - 9k_6 - 3k_7 - 3k_8 + 9k_{10} + 3k_{11} + 3k_{12}) R_2^2 \\ & \left. + (k_{10} - k_6) R_3^2 \right]; \end{aligned} \quad (7.45)$$

$$\begin{aligned} \frac{\partial R_3}{\partial t} = & \frac{2\pi^2}{\Phi_3^e} \left[ n_0 \left( \frac{1}{\pi E_0} \right)^{3/2} \right]^2 (2E_0)^{13/2} \\ & \left[ (-k_{b1} + k_{b3} - 3k_{b5} + 3k_{b9}) R_2 + (k_{b5} - k_{b9}) R_3 \right. \\ & + (6k_{b6} + k_{b7} + k_{b8} - 6k_{b10} - k_{b11} - k_{b12}) R_3 R_2 \\ & + (-k_{b2} + k_{b4} - 9k_{b6} - 3k_{b7} - 3k_{b8} + 9k_{b10} + 3k_{b11} + 3k_{b12}) R_2^2 \\ & \left. + (k_{b10} - k_{b6}) R_3^2 \right]; \end{aligned} \quad (7.46)$$

where the following additional integrals are introduced:

$$k_5 = \int_0^\infty \psi^6 \exp(-2\psi) \int_0^\infty \psi_\star^2 \exp(-2\psi_\star) (\mathcal{L}_3^{1/2}(\psi_\star) + \mathcal{L}_3^{1/2}(\psi)) \int_{-1}^1 \int_{-1}^1 |\psi y - \psi_\star x| dx dy d\psi_\star d\psi; \quad (7.47)$$

$$k_6 = \int_0^\infty \psi^6 \exp(-2\psi) \int_0^\infty \psi_\star^2 \exp(-2\psi_\star) (\mathcal{L}_3^{1/2}(\psi_\star) \mathcal{L}_3^{1/2}(\psi)) \int_{-1}^1 \int_{-1}^1 |\psi y - \psi_\star x| dx dy d\psi_\star d\psi; \quad (7.48)$$

$$k_7 = \int_0^\infty \psi^6 \exp(-2\psi) \int_0^\infty \psi_\star^2 \exp(-2\psi_\star) (\mathcal{L}_3^{1/2}(\psi_\star) \mathcal{L}_2^{1/2}(\psi)) \int_{-1}^1 \int_{-1}^1 |\psi y - \psi_\star x| dx dy d\psi_\star d\psi; \quad (7.49)$$

$$k_8 = \int_0^\infty \psi^6 \exp(-2\psi) \int_0^\infty \psi_\star^2 \exp(-2\psi_\star) (\mathcal{L}_2^{1/2}(\psi_\star) \mathcal{L}_3^{1/2}(\psi)) \int_{-1}^1 \int_{-1}^1 |\psi y - \psi_\star x| dx dy d\psi_\star d\psi; \quad (7.50)$$

$$k_9 = \int_0^\infty \psi^6 \exp(-2\psi) \int_0^\infty \psi_\star^2 \exp(-2\psi_\star) \\ \int_{-1}^1 \int_{-1}^1 \left( \mathcal{L}_3^{1/2}(\psi'_\star) + \mathcal{L}_3^{1/2}(\psi') \right) |\psi y - \psi_\star x| dx dy d\psi_\star d\psi; \quad (7.51)$$

$$k_{10} = \int_0^\infty \psi^6 \exp(-2\psi) \int_0^\infty \psi_\star^2 \exp(-2\psi_\star) \\ \int_{-1}^1 \int_{-1}^1 \left( \mathcal{L}_3^{1/2}(\psi'_\star) \mathcal{L}_3^{1/2}(\psi') \right) |\psi y - \psi_\star x| dx dy d\psi_\star d\psi; \quad (7.52)$$

$$k_{11} = \int_0^\infty \psi^6 \exp(-2\psi) \int_0^\infty \psi_\star^2 \exp(-2\psi_\star) \\ \int_{-1}^1 \int_{-1}^1 \left( \mathcal{L}_3^{1/2}(\psi'_\star) \mathcal{L}_2^{1/2}(\psi') \right) |\psi y - \psi_\star x| dx dy d\psi_\star d\psi; \quad (7.53)$$

$$k_{12} = \int_0^\infty \psi^6 \exp(-2\psi) \int_0^\infty \psi_\star^2 \exp(-2\psi_\star) \\ \int_{-1}^1 \int_{-1}^1 \left( \mathcal{L}_2^{1/2}(\psi'_\star) \mathcal{L}_3^{1/2}(\psi') \right) |\psi y - \psi_\star x| dx dy d\psi_\star d\psi. \quad (7.54)$$

Integrals  $(k_{b1}, \dots, k_{b12})$  are equal to integrals  $(k_1, \dots, k_{12})$  but replacing  $\psi^6$  by  $\psi^8$ . Integrating analytically Eqs. 7.45 and 7.46 we obtain Eq. 7.30.

## B. Analytical integration of QMOM equations for HIBE

In order to calculate analytically the integrals of Eq. 7.33 over the collisional parameters  $x$  and  $y$  let us define

$$\begin{aligned} \delta_{ij} &= \sqrt{E_j/E_i} \\ q_{ij} &= q(x, y, E_i, E_j) \\ C_{ij,p}^+ &= C_p^+(x, y, E_i, E_j) \\ C_{i,p}^- &= C_p^-(E_i) \\ \Lambda_{ij,p}^+ &= \int_{-1}^{+1} \int_{-1}^{+1} |q_{ij}| C_{ij,p}^+ dx dy \\ \Lambda_{ij,p}^- &= \int_{-1}^{+1} \int_{-1}^{+1} |q_{ij}| C_{i,p}^- dx dy \end{aligned} \quad (7.55)$$

It is possible to rewrite the above integrals by splitting the integration domain in four parts and using the symmetry properties of the integrands. It follows that

$$\begin{aligned}
 \Lambda_{ij,p}^+|_{E_i \geq E_j} &= 2 \left( \int_{-1}^{-\delta_{ij}} \int_{-1}^{+1} q_{ij} C_{ij,p}^+ dy dx + \int_{-\delta_{ij}}^{+\delta_{ij}} \int_{x\delta_{ji}}^{+1} q_{ij} C_{ij,p}^+ dy dx \right) \\
 &= 4 \sum_{\alpha=0}^p \binom{p}{\alpha} (-1)^\alpha \sum_{\beta=0}^{p-\alpha} \binom{p-\alpha}{\beta} E_i^{p-\beta} E_j^\beta \\
 &\quad \left[ \frac{\sqrt{E_i}}{2\beta+1} \left( \frac{1-\delta_{ij}^{2\alpha+2}}{2\alpha+2} + \frac{\delta_{ij}^{2\alpha+2}}{2\alpha+2\beta+3} \right) + \frac{\sqrt{E_j}}{2\beta+2} \left( \frac{\delta_{ij}^{2\alpha+1}}{2\alpha+1} - \frac{\delta_{ij}^{2\alpha+1}}{2\alpha+2\beta+3} \right) \right] \\
 \Lambda_{ij,p}^-|_{E_i \geq E_j} &= 2C_{ij,p}^- \left( \int_{-1}^{-\delta_{ij}} \int_{-1}^{+1} q_{ij} dy dx + \int_{-\delta_{ij}}^{+\delta_{ij}} \int_{x\delta_{ji}}^{+1} q_{ij} dy dx \right) = \\
 &= 2E_i^p \sqrt{E_i} \left( 1 + \frac{\delta_{ij}^2}{3} \right)
 \end{aligned} \tag{7.56}$$

if  $E_i \geq E_j$ , while for  $E_i < E_j$

$$\begin{aligned}
 \Lambda_{ij,p}^+|_{E_i < E_j} &= 2 \left( \int_{-1}^{-\delta_{ji}} \int_{-1}^{+1} q_{ij} C_{ij,p}^+ dy dx + \int_{-\delta_{ji}}^{+\delta_{ji}} \int_{\delta_{ij}y}^{+1} q_{ij} C_{ij,p}^+ dy dx \right) \\
 &= 4 \sum_{\alpha=0}^p (-1)^\alpha \binom{p}{\alpha} \sum_{\beta=0}^{p-\alpha} \binom{p-\alpha}{\beta} E_i^{p-\alpha} E_j^\alpha \\
 &\quad \left[ \frac{\sqrt{E_j}}{2\beta+1} \left( \frac{1-\delta_{ji}^{2\alpha+2}}{2\alpha+2} + \frac{\delta_{ji}^{2\alpha+2}}{2\alpha+2\beta+3} \right) + \frac{\sqrt{E_i}}{2\beta+2} \left( \frac{\delta_{ji}^{2\alpha+1}}{2\alpha+1} - \frac{\delta_{ji}^{2\alpha+1}}{2\alpha+2\beta+3} \right) \right] \\
 \Lambda_{ij,p}^-|_{E_i < E_j} &= 2C_{ij,p}^- \left( \int_{-1}^{-\delta_{ji}} \int_{-1}^{+1} q_{ij} dx dy + \int_{-\delta_{ji}}^{+\delta_{ji}} \int_{\delta_{ij}y}^{+1} q_{ij} dx dy \right) = \\
 &= 2E_i^p \sqrt{E_j} \left( 1 + \frac{\delta_{ji}^2}{3} \right)
 \end{aligned} \tag{7.57}$$

Assuming that the nodes are numbered such that  $E_M \geq \dots \geq E_j \geq \dots \geq E_1 \geq 0$  we can write Eq. 7.32 as

$$\begin{aligned}
 \frac{d\Phi_p}{dt} &= \frac{\pi}{\sqrt{2}} \left( \sum_{i=1}^{M/2} \sum_{j=i}^{M/2} w_i w_j (\Lambda_{ij,p}^+|_{E_i \geq E_j} - \Lambda_{ij,p}^-|_{E_i \geq E_j}) + \sum_{i=1}^{M/2} \sum_{j=1}^{i-1} w_i w_j (\Lambda_{ij,p}^+|_{E_i < E_j} - \Lambda_{ij,p}^-|_{E_i < E_j}) \right) \\
 &= \frac{\pi}{\sqrt{2}} \left( \sum_{i=1}^{M/2} \sum_{j=1}^{M/2} w_i w_j \Lambda_{ij,p}^+ - \sum_{i=1}^{M/2} \sum_{j=1}^{M/2} w_i w_j \Lambda_{ij,p}^- \right)
 \end{aligned} \tag{7.58}$$

and  $\Lambda_{ij,p}^\pm$  as

$$\begin{aligned}\Lambda_{ij,p}^+ &= 2E_i^p \sqrt{E_+} \sum_{\alpha=0}^p \binom{p}{\alpha} \sum_{\beta=0}^{p-\alpha} \binom{p-\alpha}{\beta} (-1)^{\gamma_{ij}} E_i^{-\beta-\alpha} E_+^\alpha E_-^\beta \\ &\quad \left[ \frac{2}{2\beta+1} \left( \frac{1-r_{ij}^{2\alpha+2}}{2\alpha+2} + \frac{r_{ij}^{2\alpha+2}}{2\alpha+2\beta+3} \right) + \frac{1}{\beta+1} \left( \frac{r_{ij}^{2\alpha+2}}{2\alpha+1} - \frac{r_{ij}^{2\alpha+2}}{2\alpha+2\beta+3} \right) \right] \quad (7.59) \\ \Lambda_{ij,p}^- &= 2E_i^p \sqrt{E_+} \left( 1 + \frac{r_{ij}^2}{3} \right)\end{aligned}$$

where  $E_+ = \max(E_i, E_j)$ ,  $E_- = \min(E_i, E_j)$ ,  $r_{ij} = \min\left(\sqrt{\frac{E_i}{E_j}}, \sqrt{\frac{E_j}{E_i}}\right)$  and

$$\gamma_{ij} = \begin{cases} \alpha & \text{if } E_i \geq E_j \\ \beta & \text{if } E_i < E_j \end{cases}$$

The derivation described here to compute the integrals over  $x$  and  $y$  can be easily extended to the continuous case (without quadrature approximation) giving place to a more general result.

The discrete (with QMOM approximation) equilibrium condition is univocally determined by the following  $M$  conditions on the  $M$  QMOM variables

$$\sum_{i=1}^{M/2} \sum_{j=1}^{M/2} w_i w_j \Lambda_{ij,p}^+ = \sum_{i=1}^{M/2} \sum_{j=1}^{M/2} w_i w_j \Lambda_{ij,p}^-, \quad \forall p \in [0, 2M-1] \quad (7.60)$$

## C. Explicit QMOM equations for HIBE with M=4

The explicit evolution equations for  $\Phi_{2-3}$  with QMOM considering  $M = 4$  are

$$\begin{aligned}\frac{d\Phi_2}{dt} &= \frac{\sqrt{2}\pi}{105\sqrt{E_2}} \left( 32\sqrt{E_1 E_2} E_1^2 w_1^2 - (13E_1^3 - 7E_1^2 E_2 - 105E_1 E_2^2 + 35E_2^3) w_1 w_2 + 32E_2^3 w_2^2 \right) \\ \frac{d\Phi_3}{dt} &= \frac{\sqrt{2}\pi}{70\sqrt{E_2}} \left( 64\sqrt{E_1 E_2} E_1^3 w_1^2 - (E_1 + E_2) (13E_1^3 - 7E_1^2 E_2 - 105E_1 E_2^2 + 35E_2^3) w_1 w_2 + 64E_2^4 w_2^2 \right) \quad (7.61)\end{aligned}$$

The source term for  $\Phi_0$  is clearly null because all the integrands vanish. The same thing happens for  $\Phi_1$  when the sum over the quadrature indexes is performed.

These equations are difficult to analyse qualitatively because the relation between macroscopic quantities (moments) and QMOM variables (nodes and weights) is highly non-linear.

DQMOM is a formulation of QMOM where evolution equations for quadrature weights and weighted nodes, instead of getting them at each time step by using specific algorithms (e.g. PD algorithm). The drawback of this formulation is that a linear system must be

solved to calculate the source terms of the equations. In the DQMOM formulation the above equation can be rewritten as

$$\begin{aligned} \frac{dw_1}{dt} &= \frac{32\sqrt{2}\pi}{35(E_1 - E_2)^2} \left( -\sqrt{E_1}E_1^2 w_1^2 + \sqrt{E_2}E_2^2 w_2^2 \right) \\ \frac{dw_2}{dt} &= -\frac{dw_1}{dt} \\ \frac{dE_1}{dt} &= \frac{\pi(-128\sqrt{E_1 E_2}E_1^2 w_1^2 + (13E_1^3 - 7E_1^2 E_2 - 105E_1 E_2^2 + 35E_2^3) w_1 w_2 + 64E_2^2 w_2^2)}{105\sqrt{2E_2}(E_2 - E_1)w_1} \\ \frac{dE_2}{dt} &= \frac{\pi(-64\sqrt{E_1 E_2}E_1^2 w_1^2 - (13E_1^3 - 7E_1^2 E_2 - 105E_1 E_2^2 + 35E_2^3) w_1 w_2 + 128E_2^2 w_2^2)}{105\sqrt{2E_2}(E_2 - E_1)w_2} \end{aligned} \quad (7.62)$$

To obtain a full QMOM formulation, Eq. 7.61 must be rewritten substituting the following values for the nodes and weights (calculated with P-D algorithm)

$$\begin{aligned} E_1 &= \frac{\Phi_1\Phi_2 - \Phi_0\Phi_3 + \sqrt{-3\Phi_1^2\Phi_2^2 + 4\Phi_0\Phi_2^3 - 4\Phi_1^3\Phi_3 - 6\Phi_0\Phi_1\Phi_2\Phi_3 + 2\Phi_0^2\Phi_3^3}}{2\Phi_1^2 - 2\Phi_0\Phi_2} \\ E_2 &= \frac{\Phi_1\Phi_2 - \Phi_0\Phi_3 - \sqrt{-3\Phi_1^2\Phi_2^2 + 4\Phi_0\Phi_2^3 - 4\Phi_1^3\Phi_3 - 6\Phi_0\Phi_1\Phi_2\Phi_3 + 2\Phi_0^2\Phi_3^3}}{2\Phi_1^2 - 2\Phi_0\Phi_2} \\ w_1 &= \frac{4\Phi_0(\Phi_1^2 - \Phi_0\Phi_2)^3}{4(\Phi_1^2 - \Phi_0\Phi_2)^3 - \left[ 2\Phi_1^3 - 3\Phi_0\Phi_1\Phi_2 + \Phi_0 \left( \Phi_0\Phi_3 + \sqrt{4\Phi_0\Phi_2^3 - 3\Phi_1^2\Phi_2^2 + 4\Phi_1^3\Phi_3 - 6\Phi_0\Phi_1\Phi_2\Phi_3 + \Phi_0^2\Phi_3^2} \right) \right]^2} \\ w_2 &= \frac{4\Phi_0(\Phi_1^2 - \Phi_0\Phi_2)^3}{4(\Phi_1^2 - \Phi_0\Phi_2)^3 - \left[ 2\Phi_1^3 - 3\Phi_0\Phi_1\Phi_2 + \Phi_0 \left( \Phi_0\Phi_3 - \sqrt{4\Phi_0\Phi_2^3 - 3\Phi_1^2\Phi_2^2 + 4\Phi_1^3\Phi_3 - 6\Phi_0\Phi_1\Phi_2\Phi_3 + \Phi_0^2\Phi_3^2} \right) \right]^2} \end{aligned} \quad (7.63)$$



# 8

## Conclusions and future perspectives

This thesis have investigated various aspects of multiphase poly-dispersed flows that arise when simulating particle production processes, together with some of the state-of-the-art mathematical models and computational methods for efficient numerical simulations. The main results can be summarised as follows:

- in Chap. 3 we have demonstrated the importance of coupling experimental techniques with detailed and computationally expensive numerical simulations, that are both needed to understand processes happening at small scales, such as the micro-mixer investigated in this work, or processes involving complex physics.
- This was particularly important for example to understand the proper boundary conditions of the simulation, that were not completely determined by the experimental parameters, because of the uncertainty and the high difficulty of the micro Particle Image Velocimetry ( $\mu$ PIV) technique.
- With the objective of finding efficient models to simulate a broad range of turbulent flow processes, a comprehensive study of Large Eddy Simulation (LES) models in our Computational Fluid Dynamics (CFD) platform has been performed in Chap. 4 for a well-known test case such as the turbulent periodic channel flow. This activity, carried out in the framework of the LESinItaly group, was also a possibility to compare the results with many other different CFD codes and models.
- These results and validations of LES have been then applied, together with the important findings of Chap. 3, for the simulation of the micro-mixer in a LES framework, which is much more interesting and efficient in terms of computational cost and makes possible the extension of this tool for other similar systems.
- The efficiency of LES has been coupled with specific models for poly-disperse multiphase flows in Chap. 6 where a turbulent channel seeded with finite-size particles is

studied to validate the LES model for dispersed phase, together with a Quadrature-Based Moment Method (QBMM) for particle poly-dispersity and an efficient algebraic models for particle relative velocity. This model represents a complex balance between an adequate description of the main phenomena involved in the deposition of particles in turbulent flows, and an efficient solution to be applied for more complex geometries such as the ones used for particle production processes.

- Finally a more theoretical activity, with important applications for micro- and nano-scale flows as well as rarefied flows, has been carried out in Chap. 7, where an approximated model of the Boltzmann Equation (BE) has been solved with QBMM. Particle collisions and non-equilibrium effects are studied in a framework that can be easily extended to general CFD models.

Also some critical comments can be made regarding the possible improvements and extensions of the work presented in this thesis:

- the cause and the effects of the pumps instability in the micro-mixer can be further investigated, with specific simulations of the feeding systems and the micro-mixing of chemical species;
- the LES models proposed for single and multiphase flows can be verified and extended for a broader range of Reynolds number and reactor geometries, to have a more general validation of the CFD tool;
- the Population Balance Equation (PBE) model can be solved with QBMM including particulate processes such as aggregation and breakage of particles;
- the proposed model for the simulation of the BE can be extended for inhomogeneous system and coupled with poly-dispersity model in a four-way coupled multiphase model;
- finally, most of the proposed methods can be applied with small modifications, to a broad range of similar flows such as gas-liquid or liquid-liquid system.

To conclude, we can state that the use of LES and QBMM made in this thesis, goes into the direction of overcome the most simplified physical models, based on rough macroscopic average, introducing more physical complexity, through the understanding of phenomena happening at different scales, and efficient numerical tools to make these approaches usable for real processes. This turns out to be a crucial issue for many chemical processes and engineering applications.